Synthesis and Catalytic Performance of Hierarchically Structured Zeolitic Materials

Abdul-Lateef Ajibade Adedigba

University College London

Thesis submitted in partial fulfilment of the requirements for the degree of doctor of Philosophy

Declaration

I, Adedigba Abdul-Lateef Ajibade, confirm that the work presented in this thesis is my own. Where information has been derived from other sources, I confirm that this has been indicated in the thesis.

Signed……

Abstract

The work presented in this dissertation involves the investigation of the synthesis methodology of hierarchically structured zeolite and their catalytic performances. To create these materials, an inert templating agent, chitosan, as macro-template was used along with microporous templating agent to produce titanosilicate, aluminosilicate and titano-aluminosilicate systems with MFI structure.

Firstly, synthesis of the titanosilicate (TS-1) system was carried out. It was found that, while the use of chitosan did not affect production of crystalline, phase pure TS-1, the preparation of precursors indeed is an important factor in the insertion of titanium in the silicalite structure. A range of characterisation methods were used to establish the nature of titanium species in the catalyst and also the nature of pore structures present in the system. The catalysts developed here were evaluated for liquid phase epoxidation of cyclohexene and styrene with their activities and selectivity correlated with the amount of chitosan included in the synthesis precursors.

Secondly, the chitosan was transformed into a rigid three dimensional structure (scaffold) and used as macro-template to form the alumino-silicate (ZSM-5) zeolite. Parameters such as the amount of zeolite precursor to chitosan scaffold and the ratio of silicon to aluminium in the starting precursor were found to influence the acidity, pore distribution and the crystal morphology. The selectivity and coke formation of these zeolites were evaluated for the methanol to hydrocarbon reaction.

Finally, a zeolite with both redox and acid sites was synthesised in the presence of chitosan. This catalyst was investigated for direct conversion of cyclohexanone to caprolactam in the liquid phase. The influence of the amount of chitosan in the

synthesis, reaction conditions and solvent medium on activity and selectivity was studied.

In summary, the project successfully investigated the use of chitosan in the production of hierarchical MFI type zeolite and evaluated the performance for a range of catalytic reactions

Table of Contents

List of Figures

List of tables

List of schemes

Acknowledgements

First, I would like to thank my supervisors, Professor Richard Catlow and Professor Gopinathan Sankar for their support, in-depth knowledge, guidance and encouragement during the past few years of my study.

I would like to thank everyone who has assisted me during my time at UCL, particularly all the support and technical staff who gave me training on the various characterization techniques employed during my studies. I would like to acknowledge Dr. Steve Firth for training me on the use of Raman, TGA, and SEM. Also deserving mention are Dr. Martin Vickers, Dr. Katsi Karu, Dr. Abil and Dr. Srinivas for training me on the use of the XRD, GC, NMR and BET instruments.

My appreciation also goes to Dr. Justin Hargreaves at the University of Glasgow and all the members of his research group, particularly Nicholas, for the opportunity given me to visit their lab to conduct part of my experiments. I would like to acknowledge all of my lab colleagues at UCL; Dr. Tom Daley, Dr. Husna Islam, Ian, Huw, Zarrin, Glen, Anastasia, Adam, Alex, Ekram, Feyza, and Arif for all the constructive discussions and help I received from you all. I would particularly like to thank Ian and Huw for proof reading my thesis and offering very useful suggestions.

I would like to thank my Parents for all the moral support they gave me during my studies, especially at the very tough periods of my work. Deserving special acknowledgement is my wife Zenab for her patience for the duration of my PhD and for taking good care of our three children; Aisha, Hameedah and little Maryam who are sources of joy, encouragement and hope to me all day long.

Finally, I would like to acknowledge the financial assistance from my sponsor, the Islamic Development Bank, which enabled me to undertake my studies.

Chapter 1: Introduction

1.1 Introduction to Catalysis

Catalysis is a chemical process whereby the rate of a chemical reaction is accelerated to equilibrium. When studying catalysis, we measure the formation and distribution of products in a given reaction in the presence of another substance known as the catalyst. The catalyst can exist in the same phase as the reactant (homogeneous-e.g. liquid-liquid) or in a different phase (heterogeneous-e.g. liquid-solid or gas-solid).

More generally, a catalyst is a substance which enhances the rate of disappearance of the reactant(s) or the rate of formation of the product(s), in a given reaction without being consumed. It is important to note that a catalyst cannot initiate a reaction which otherwise is thermodynamically infeasible. In reality, catalysts speed up the rate of thermodynamically feasible reactions by providing an alternative route with a lower activation energy.

In general, catalytic processes can be broadly classified as involving three distinct steps[1]. First is the adsorption of the reacting species on the catalyst surface, which commonly involves chemisorption, followed by bond rearrangement of the adsorbed species to form the products, which are then finally desorbed from the catalyst surface.

The application of catalysts and the development of catalytic process have occurred since time immemorial[2] probably beginning with the undocumented production of alcohol through the fermentation process. Since this time, catalytic processes have evolved into more defined methods of producing chemical products. These include the production of bulk chemicals such as fertilizer and explosives during the First

World War, production of synthetic fuel during world war two, production of polymers from petrochemical products and currently, the development of catalytic processes which are more benign to the environment.

1.2 Types of Catalysis

Catalysis is generally categorised into three broad types. The first two are defined by the phase in which the catalyst and the reacting species exists in the reacting medium, homogenous and heterogeneous catalysis. The third type, bio-catalysis, is effected by enzymes.

1.2.1 Homogeneous catalysis

Homogeneous catalysis occurs when the catalysing species and the reacting bodies are present in a single uniform phase, for example, liquid–liquid reactions. The main disadvantage of catalysis in the homogeneous phase is that the products and catalysts always remain in the same phase, which introduces an often expensive separating unit to the reactor.

In addition, homogeneous catalysts are often environmentally hazardous, corrosive, difficult-to-separate and often difficult to dispose. Common examples of homogeneous catalysts are mineral acids, organic and inorganic bases and toxic metallic compounds[3]. Nevertheless, homogeneous catalysis is extensively used in fine chemicals production.

1.2.2 Heterogeneous catalysis

Heterogeneous catalysis, on the other hand, is used to describe a catalytic process in which the reactants and the catalyst coexist in different phases for instance, liquid or gas reactants with a solid catalyst.

There are different types of industrially important heterogeneous catalysts, which include metals, metal oxides, sulfides, carbon and zeolites. For efficient catalyst performance, metals and metal oxides are often dispersed on supports to ensure better exposure of the metal surface to the reacting species. Commonly used supports include titania, zirconia, silica, alumina and activated carbons. The use of the support minimizes the rate of loss of the active metal catalyst, which is especially important for expensive precious metals such as platinum, palladium and gold. The use of supports for the immobilization of certain metals, oxides, carbides and sulphides has provided an alternative route to liquid phase reactions, which can sometimes be hazardous and involve expensive separation units. Also used in heterogeneous catalysis are mesoporous solids, membranes as well as zeolites.

Through well-tailored catalyst design, product selectivity and distribution may be greatly enhanced, while avoiding the toxic, corrosive and environmentally hazardous path of homogenous catalysis.

1.3 Zeolites as heterogeneous catalysts

Zeolites are a fascinating class of materials with exceptional molecular shape selective properties, ion exchange capability, high surface area and tuneable acidity**,** which makes them ideal for heterogeneous catalysis. Zeolites are defined as crystalline materials made up of silicon and aluminium atoms connected through

oxygen linkages. The term “zeolite” literally means “boiling stone” and was coined by the Swedish mineralogist Cronstedt[4]. The history of zeolite science dates back to as early as 1756 when the first zeolite, stilbite, was discovered in nature[5]. It was described as a new class of mineral, consisting of hydrated aluminosilicates of alkaline and alkaline earth metals.

Since the discovery of mineral zeolites, much effort have been devoted to producing synthetic zeolites which mirror the same properties as those found in naturally existing ones. The first such synthetic zeolite, levynite, was produced in 1862 by *St.* Claire Deville via a hydrothermal method[6]. To date, there are approximately 40 known natural zeolites and more than 200 synthetic zeolites have been developed. Zeolites may be classified based on different criteria such as their pore size and framework topology.

ABW	ACO	AEI	AEL	AEN	AET	AFG	AFI	AFN	AFO	AFR	AFS
AFT	AFV	AFX	AFY	AHT	ANA	APC	APD	AST	ASV	ATN	ATO
ATS	ATT	ATV	AVL	AWO	AWW	BCT	*BEA	BEC	BIK	BOF	BOG
BOZ	BPH	BRE	BSV	CAN	CAS	CDO	CFI	CGF	CGS	CHA	-CHI
-CLO	CON	CSV	CZP	DAC	DDR	DFO	DFT	DOH	DON	EAB	EDI
EEI	EMT	EON	EPI	ERI	ESV	ETR	EUO	*-EWT	EZT	FAR	FAU
FER	FRA	GIS	GIU	GME	GON	GOO	HEU	IFO	IFR	IFW	IFY
IHW	IMF	IRN	IRR	-IRY	ISV	ITE	ITG	ITH	*-ITN	ITR	ITT
-ITV	ITW	IWR	IWS	IWV	IWW	JBW	JNT	JOZ	JRY	JSN	JSR
JST	JSW	KFI	LAU	LEV	LIO	-LIT	LOS	LOV	LTA	LTF	LTJ
LTL	LTN	MAR	MAZ	MEI	MEL	MEP	MER	MFI	MFS	MON	MOR
MOZ	*MRE	MSE	MSO	MTF	MTN	MTT	MTW	MVY	MWW	NAB	NAT
NES	NON	NPO	NPT	NSI	OBW	OFF	OKO	OSI	OSO	OWE	-PAR
PAU	PCR	PHI	PON	POS	PSI	PUN	RHO	-RON	RRO	RSN	RTE
RTH	RUT	RWR	RWY	SAF	SAO	SAS	SAT	SAV	SBE	SBN	SBS
SBT	SEW	SFE	SFF	SFG	SFH	SFN	SFO	SFS	*SFV	SFW	SGT
SIV	SOD	SOF	SOS	SSF	*-SSO	SSY	STF	STI	*STO	STT	STW
-SVR	SVV	SZR	TER	THO	TOL	TON	TSC	TUN	UEI	UFI	UOS
UOV	UOZ	USI	UTL	UWY	VET	VFI	VNI	VSV	WEI	-WEN	YUG
ZON											

Figure 1.1: Approved zeolite framework types[7]. Each three letter code represents a distinct framework type

Based on their pore structure, zeolites are generally classified into three types - small, medium and large pore - stemming from the number of atoms in the ring system, e.g 8-, 10- and 12-member rings. Recently, there have been reports of zeolites with a larger ring unit consisting of 14-members. According to the international zeolite association, there are 229 approved zeolite framework types as of April 2015 (figure 1.1).

1.4 Structure and topology of zeolites

The starting point of zeolite structures is the primary building unit. This unit is made up of a central atom (T-atom) surrounded by four oxygen atoms to form a tetrahedron (see figure 1.2). From the primary unit, the secondary building blocks are formed, when two primary building units are connected through shared oxygen atom. This bridge connecting the two tetrahedrons is referred to as an oxygen bridge. Zeolite channels and cages are formed from different connections of the secondary building units. There are several configurations of the secondary unit, which are given in figure 1.3

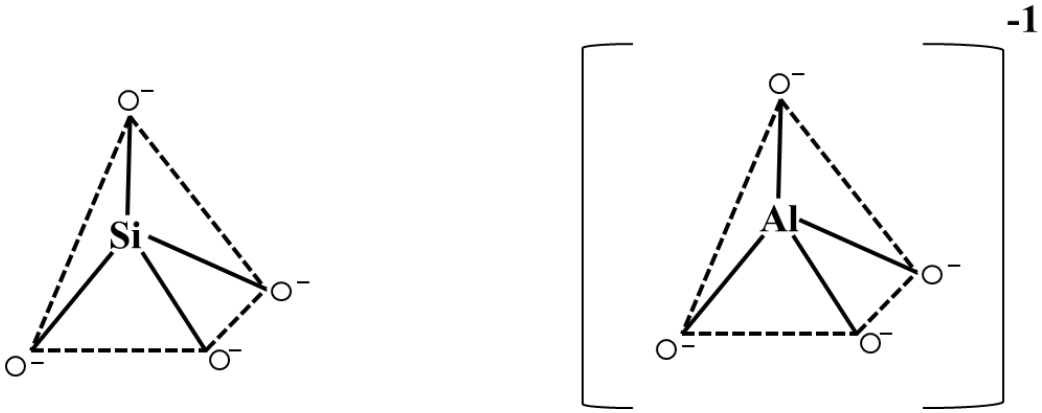

Figure 1.2: Primary building units made up of silicon tetrahedron (left) and aluminium tetrahedron (right)

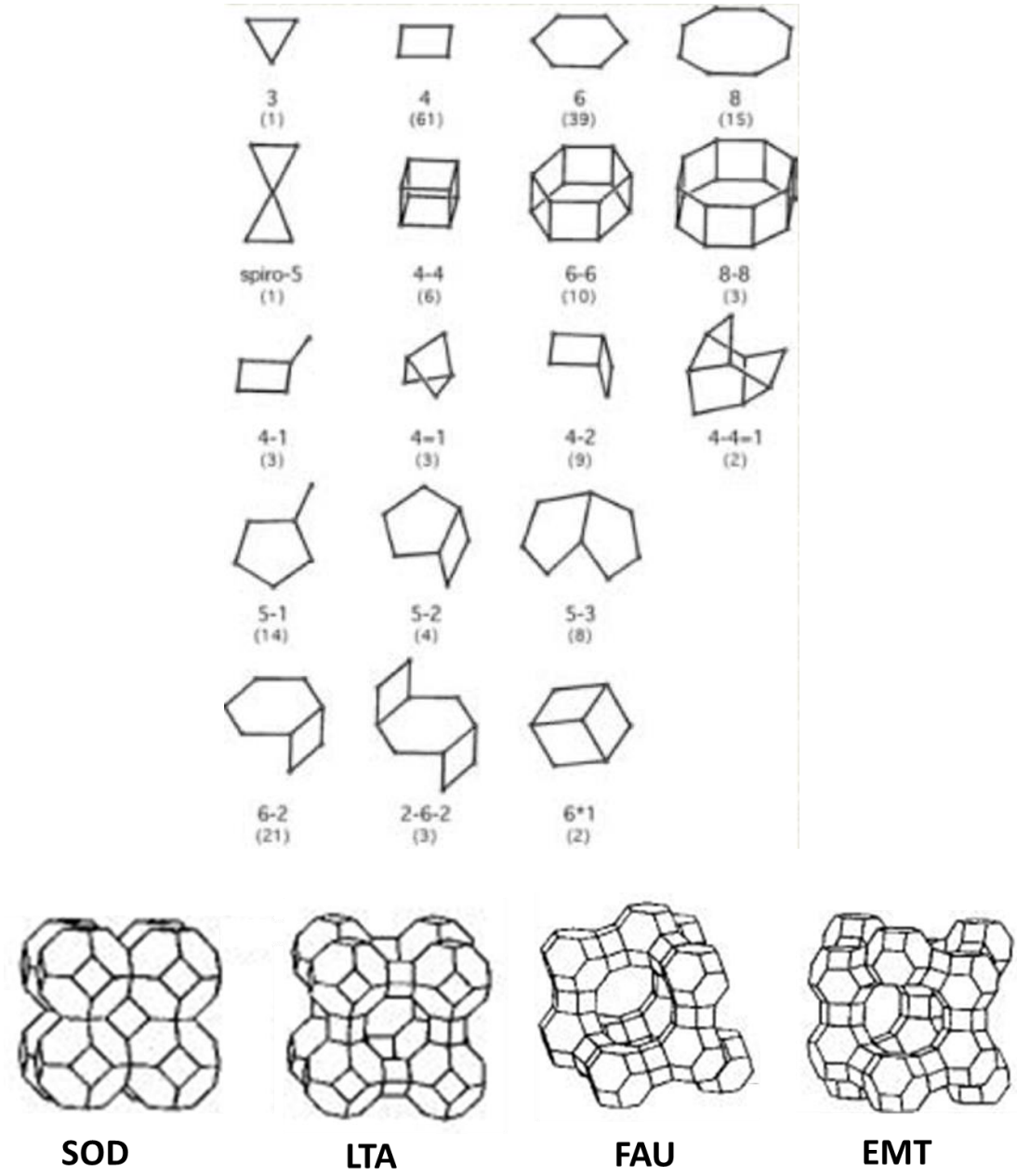

Figure 1.3: Secondary building units of zeolite framework and the 3D of four different zeolite cages . Schematic illustrations taken from ref [7]

In the case of ZSM-5, for instance, the framework is formed through eight five-membered rings tetrahedral, connected through their edges into a chain of tetrahedra. These chains are connected to form sheets, from which the three dimensional framework structure is formed (figure 1.4) [8].

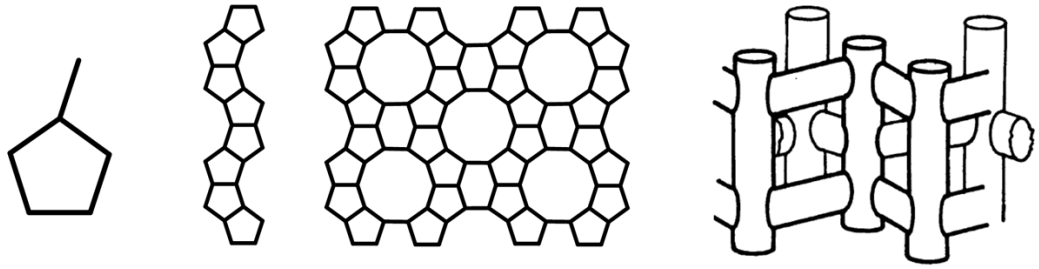

Figure 1.4: Structure of ZSM-5 zeolite. left to right; secondary building unit, building unit constructed into chains, ZSM-5 sheet and three dimensional ZSM-5 structure. Illustration adapted from ref [9]

1.5 Advantages of zeolites

Zeolites are a unique class of materials with outstanding properties that make them useful in a variety of applications. They have found good applications in ion-exchange and adsorption as well as in catalysis. The advantages of zeolites include product selectivity, high surface area and high hydrothermal stability, as well as tuneable acidity, which can be employed in catalytic reactions such as cracking and isomerization.

1.5.1 Selectivity in zeolite catalysis

Selectivity in zeolites is derived from their pore size and geometry [10-12]. Depending on the pore geometry of the zeolite, certain reactants can gain free access into the micropores, where catalysis takes place, and the escape of products to the surface of the catalyst from the micropore is also determined by the pore geometry. A typical example of reactant selectivity is dehydration of primary and secondary alcohols over, e.g., zeolites Ca-X and Ca-A, as illustrated in figure 1.5. Zeolite Ca-A has a pore width of approximately 5A, whereas the Ca-X pore width is 8A. This allows easy access by the primary alcohols which are linear, into both zeolites'

pores. However, due to pore size restrictions, secondary alcohols have very limited access to Ca-A[13].

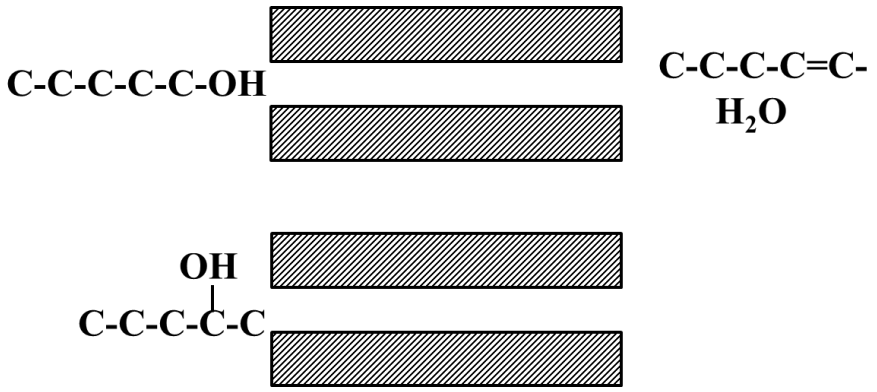

Figure 1.5: Illustration of reactant selectivity in alcohol dehydration over zeolite Ca-A[13]

In essence, molecules which are larger than the pore openings of the catalyst are screened out, while those smaller are able to access the active site. This phenomenon is widely employed in separation processes involving zeolites. The screening effect which allows the diffusion of certain products out of the catalyst pores while others are forced to undergo further reactions, is known as product selectivity, which sometimes, however, leads to deactivation of the catalyst via pore plugging. An illustration of product selectivity is given in figure 1.6.

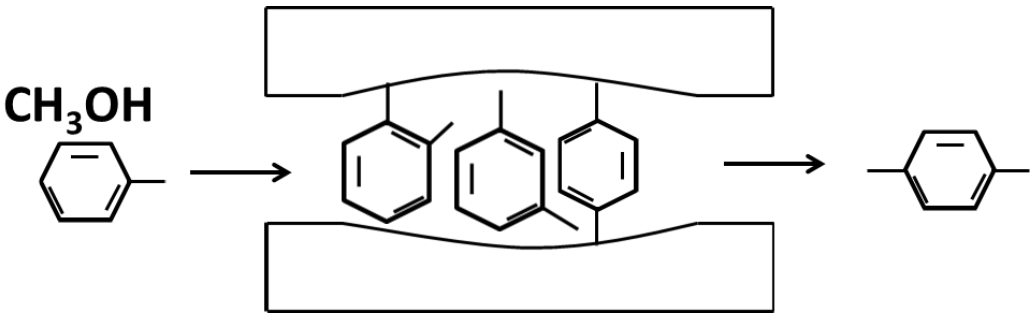

Figure 1.6: Illustration of product selectivity in zeolites[13]

1.5.2 Acidity in zeolites

Acidity in zeolites is derived from the unbalanced charge resulting from the isomorphous substitution of the trivalent atom, most commonly aluminium, for the

tetravalent silicon atoms in the zeolite framework structure. This substitution leaves a net negative charge on the zeolite structure. The negative charge is often compensated for by reactive alkaline or alkaline earth metals such as Na, Rb, K and Ca etc. These cations, which are always mobile, can be replaced and are the basis for the ion exchange capability of zeolites. Likewise, the cations can be replaced by protons (see figure 1.7) which behave as strong Brønsted acid sites. The strength of such acidity can be tuned by varying the silicon to aluminium ratio in the zeolite framework. In general, the higher the silicon to aluminium ratio, the lower is the acidity and vice-versa.

In addition to the combination of silicon and aluminium to produce acid sites in zeolites, a combination of other elements has been reported. The replacement of other trivalent atoms for silicon, in a silicate structure, will also yield acidity in zeolites. In ZSM-5, mordenite and beta zeolites, for instance, the isomorphous substitution of iron (Fe^{3+}), gallium (Ga^{3+}) and boron (B^{3+}) for silicon have been reported to produce acid sites. Similarly, using germanium instead of silicon and combining this with other trivalent atoms will also lead to acid sites in zeolites.

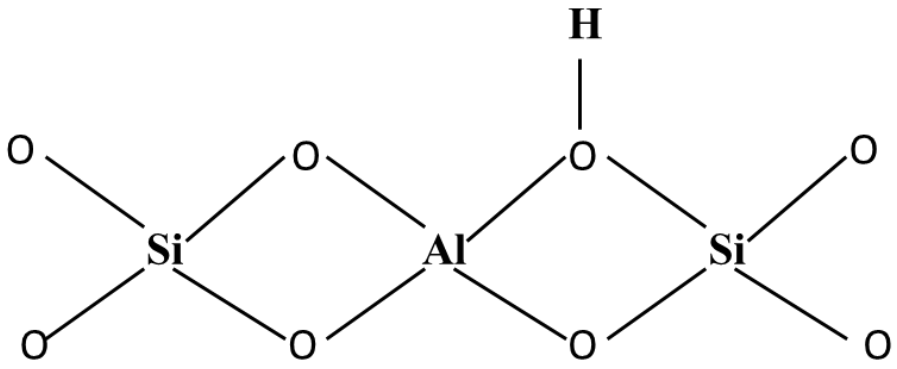

Figure 1.7: Illustration of Bronsted acidity in zeolites[20]

1.5.3 Redox functionality in zeolites

In addition to their use as acid catalysts, zeolites are also widely applied to the redox transformation of substrates to oxygenated products. In order for the zeolite to function in such a capacity, it must consist of active sites that are capable of causing a change in the oxidation state of the reactant by activating the oxidizing agent. Through several means, such active centres can be incorporated into zeolites. The most commonly used redox active centres are the transition metal ions. They can be incorporated into the zeolite structure through various techniques such as ion exchange, vapour phase substitution and isomorphous substitution.

In the early periods of investigating zeolites for redox reactions, transition metals were often substituted into the zeolite structure by ion exchange. The ion exchange technique was very useful for the incorporation of redox active centres into low silica zeolites. The most studied zeolites through this route are zeolites Y, X and beta. Indeed, Co-Y, Cu-Y, CuPd-Y and Co-X all have been prepared through ion exchange and reported to be effective for oxidation reactions. Although the ion exchange was the main technique used historically, it is still used for metal incorporation into zeolites - as demonstrated by some recent work, such as [14]. The greatest disadvantage of transition metal-zeolites prepared by ion exchange is the high possibility of the metal ion leaching into solution during liquid phase reactions [15, 16].

With the discovery of high silica zeolites (e.g MFI and MEL) comes the possibility to isomorphously incorporate redox active sites into the silicate structure. This is the ability to insert the transition metal ion in an isolated form (occupying a framework position) in the zeolite framework. In this regard, titanium containing zeolites have

been the most studied [15, 16] redox catalysts, with TS-1 (titanium containing silicate material with MFI topology) receiving the most attention. In addition to titanium, several other transition metals such as zirconium, vanadium, iron, cobalt, chromium and copper have also been isomorphously substituted into ZSM-5 zeolites and have been extensively investigated for redox reactions.

Of particular interest is the Fe-ZSM-5 system which has been investigated for a variety of oxidation reactions. In a recent series of studies, the Fe-ZSM-5 was employed for the direct conversion of methane to methanol using hydrogen peroxide as the terminal oxidant [14, 17, 18]. In those studies efforts were concentrated on elucidating the active centre in the catalyst system and in determining the reaction mechanism, through which the catalyst was able to directly convert methane to methanol. The authors showed that the active species in the system was the iron centre as oppose to the confinement effect of the catalyst pores and the aluminium sites [17, 18]. Furthermore, it was discovered that the presence of copper species in addition to the Fe centres significantly improve the selectivity of the reaction to methanol. The role of copper in this system was thought to be the prevention of over oxidation reaction by minimizing the presence of hydroxyl centres that initiate the consecutive conversion of methanol to formic acid [17]. In the concluding study of their work, the authors showed that the octahedral or extra-framework iron sites in the micropores of the zeolite are responsible for the activity of this system of catalyst in the direct conversion of methane to methanol. The increasing presence of the extra-framework species – as demonstrated by pre-treatment of the iron ZSM-5 at different temperatures – was also shown to have a positive influence on the methane conversion up to 700 ^{O}C.

1.6 Zeolite type materials (zeotype)

There are other materials with properties that closely resemble those of crystalline zeolite materials. These categories of materials are often referred to as zeotype (zeolite-type or zeolite-like) materials. There are two major classes of such materials, namely the aluminophosphate (AlPO) and the silicoaluminophosphate (SAPO).

Aluminophosphates are a class of crystalline, three dimensional materials, comprising aluminium and phosphorus in their framework structure in a similar fashion to silicon and aluminium in conventional zeolite materials. Since the first publication on the AlPO class of materials in 1982[19], there have been discoveries of many more materials of similar composition [20]. The aluminophosphate materials are often denoted as *$AlPO_4$-n*, where each *n* refers to a distinct crystallographic structure with the aluminium and phosphorus T-atoms always present in equal amount, i.e. the phosphorus to aluminium ratio is always equal to unity.

The isomorphous substitution of other metal elements for either the aluminium, phosphorus or even both in the framework of the $AlPO_4$ can lead to materials with distinct properties for applications in adsorption and catalysis as described earlier for the aluminosilicate zeolites. In the $AlPO_4$ structure, the substitution of aluminium or phosphorus by other metals is usually done during the synthesis.

Like alumnosilicate zeolites, the framework structure of $AlPO_4$ is also formed from primary building units of aluminium and phosphorus tetrahedra. Unlike conventional zeolites, $AlPO_4$s are strictly made of alternating aluminium and phosphorus T-atoms in the framework, which ensures framework neutrality. To impose some acid

functionality into this zeotype material, it is necessary to disturb this framework charge such that it can be balanced by a functional group.

Typical examples of this framework charge perturbation and functionality are illustrated by the substitution of divalent atoms for aluminium in the $AlPO_4$ structure or the substitution of a tetravalent atom for phosphorus. These substitutions will impose a net negative charge on the framework structure and the negative charge can then be balanced by a proton, which will impose an acid functionality. Rather than balancing the negative charge with a proton the charge may be compensated by other metal atoms of appropriate valency, resulting in ion-exchange capability.

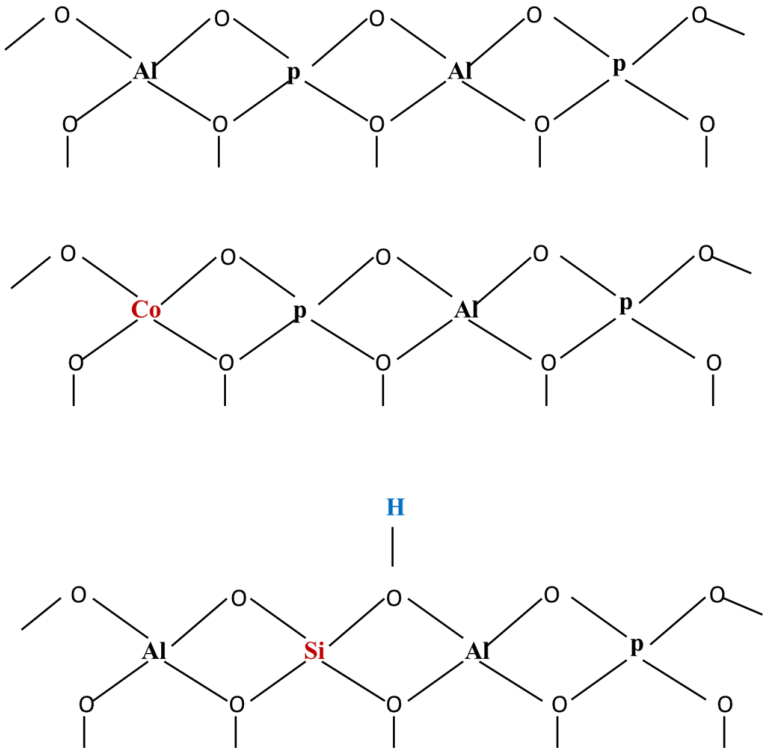

Figure 1.8: schematic illustration of $AlPO_4$ framework structure (top; neutral, middle; redox functionality, bottom; acid functionality)

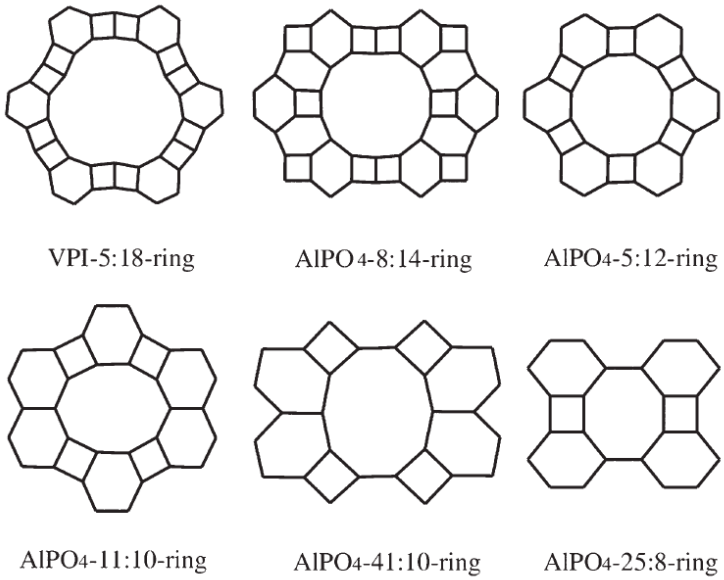

Figure 1.9: Typical structures of aluminophosphate zeolite-type materials with different pore sizes, taken from ref [21]

1.7 Factors limiting the applications of zeolites and zeotype materials

Though, zeolites have proven to be very useful in many applications in the petroleum and fine chemical industry, there are still certain limitations which greatly affect the full utilization of their potential. It is generally accepted that catalytic reactions in conventional zeolites take place within the micropores of the zeolite. Accessibility to these microporous sites have been identified as one of the key factors limiting their potential[22]. The fact that molecules with large kinetic diameters cannot access these pores, which are smaller than their molecular diameters, ensures that only molecules of certain kinetic diameter can be accommodated, which has therefore limited the range of reactants which can be processed with certain zeolites and the range of desirable products that can be obtained.

Diffusion to and from the micropores of the zeolite are other limiting factors in zeolite catalysis. The rate at which reactants and products diffuse in and out of the

zeolite micropore greatly affects the activity and selectivity of such catalysts. If the path the product has to journey through, before emerging from the pore, is too long conversion of the product to secondary or by-products which greatly impacts negatively on product selectivity, may occur.

1.8 Solutions to the factors limiting the applications of zeolites

Much effort is being devoted to the modification of zeolite structures and morphology so as to make the most of their outstanding characteristic properties, including the optimization of the acidity, structural stability and pore configuration and geometry.

Alhough strongly acidic zeolites are often desired in reactions such as cracking it is important to optimise the acidity for maximum efficiency, since a catalyst with too strong an acidity will be readily deactivated due to coke formation on the catalyst active sites, reducing the catalyst life time and activity. One way of regulating the acid strength in zeolites is by dealumination.

To overcome diffusion hindrance of reactants and products in and out of zeolite pores many routes have been exploited. These include the synthesis of very large pore zeolites, such as the VPI family (18MR pore), as well as the creation of zeolites with a hierarchy of porosity. Synthesis of nano-size zeolites has also been suggested as a way of reducing the intrinsic diffusion path of reactants and products through the zeolite pore. Using carefully chosen synthesis conditions, gel formulation and the addition of crystal growth inhibitors, such as polyethylene glycol and non-ionic surfactant (e.g polyoxyethlene lauryl ether)[23], nano-size zeolites have been

reported. However, the difficulty involved in the handling of such nano-size materials, and the difficulty to separate them from solution, has limited their application to the laboratory scale [22].

1.9 Hierarchical zeolites

Hierarchical zeolites can be defined as those zeolites or zeotype materials having more than one kind of porosity, which could be a two-way connection such as micro-meso, micro-macro, meso-macro or even three way micro-meso-macro pore configurations. Ideally, zeolites are mono-porous materials with micropore structures. These micropores often hinder the accessibility of bulky chemical feedstocks or the formation of bulky products[24]. To enhance the accessibility, efforts have been devoted to the incorporation of either the meso or macro pore to the characteristic micropores of the zeolite. The coexistence of the mesopore ensures greater and faster access to the micropores while the shape selectivity of the zeolite is still maintained. The size and nature of the induced extra porosity depends significantly on the synthesis strategy employed [25]. In this thesis these synthesis strategies are classified into two groups namely the post synthesis methods and the one-pot extra-templating techniques, which are discussed in the following sections.

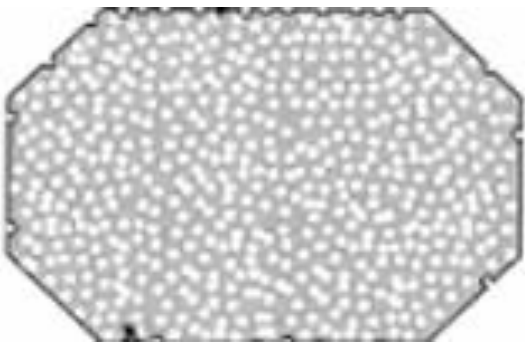

Figure 1.10: Schematic illustration of a zeolite with hierarchical pore structure. Image taken from ref[24]

1.10 Post synthesis creation of extra porosity in zeolites

The demetallation technique is a common and established procedure use for inducing secondary porosity in synthesized zeolites. It involves the selective removal of T-atoms from the zeolite framework. The voids left behind by the expunged T-atom act as sources of extra porosity in the framework. This approach is often referred to as a destructive method as it results in significant loss of the zeolite mass. Depending on which T-atom is preferentially removed from the framework, the process can be termed either as dealumination (removal of aluminium) or desilication (removal of silicon).

1.10.1 Dealumination

Through steaming or acid treatment, aluminium T-atoms have been selectively removed from zeolite frameworks, which is particularly useful in zeolites with low Si/Al ratios. Even though it was not immediately appreciated, the existence of mesopores was first observed in zeolite samples with low silica content which were subjected to dealumination treatment as a way to raise the silicon to aluminium ratio. In addition to creating extra porosity, steaming of high aluminium containing zeolites also contributes to their structural stability, a common example of which is the steaming of zeolite Y to yield ultra-stable Y (USY) zeolite which is commonly employed in the fluid catalytic cracking unit. USY has been found to have high thermal stability, as well as strong resistance to deactivation by coking[13]. This approach of creating mesoporosity in zeolites, however powerful, suffers from poor interconnectivity of the pores, as well as inducing considerable damage to the microporosity and crystallinity of the zeolite under severe treatments [24, 25]. Partial

pore blocking could also arise from the deposited amorphous debris that may arise from the dealumination process[24]. Loss of active sites, as well as a change in the nature of the acid sites, are other problems that are associated with the dealumination technique.

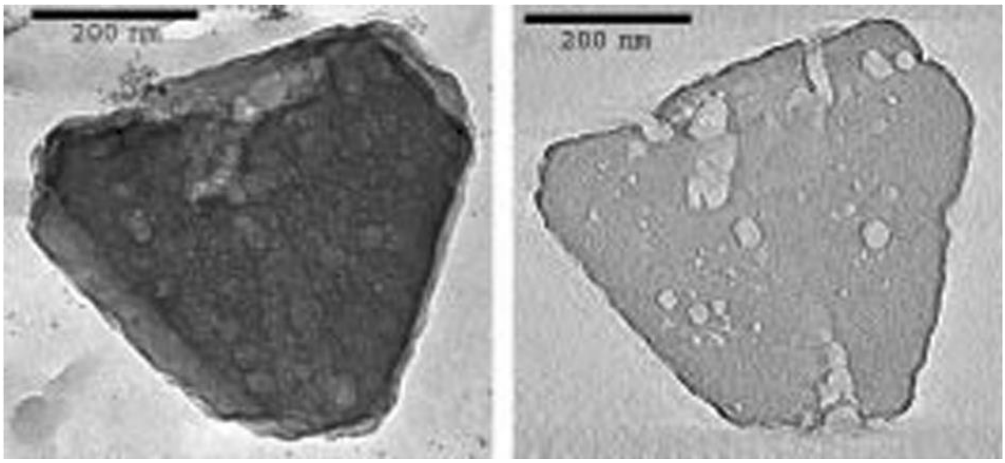

Figure 1.11: TEM image of steamed and acid leached ammonium –Y zeolite. image fom ref[24]

In addition to steaming, acid leaching is another technique which has been widely used in selective dealumination. Mild acid leaching results in the removal of aluminium from T-sites. Unlike steaming, the use of acid leaching leads to a significant increase in the framework Si/Al ratio, which eventually leads to loss of catalytic activity. Therefore, it is always difficult to distinguish between the effect of the induced mesopore arising from this process and that of the altered Si/Al ratio. One positive effect of acid leaching, however, comes when it is used in combination with the steaming technique. The use of acid leaching, post-steaming, is capable of dissolving the amorphous debris deposited during that process[24]. Figure 1.11 is a typical TEM image of a steamed and an acid leached ammonium-Y zeolite.

1.10.2 Desilication

Desilication as a means of mesopore creation is often applicable to highly siliceous zeolites or zeotype materials. It involves the treatment of the zeolite material in an alkaline medium, under controlled conditions, to selectively remove silicon atoms from the zeolite framework. The cavities left then become a source of secondary porosity. One significant importance of this method is that the degree of desilication can be controlled by a combination of factors, such as the strength of the alkaline medium, treatment time and temperature. The approach leads to a decrease in the Si/Al ratio of the zeolite and often impacts on the hydrophobic or hydrophilic nature of the crystal. In contrast to dealumination, desilication exerts less influence on the crystallinity[25] of the zeolite, thereby preserving it. However, it results in considerable loss of microporosity in the zeolite[25].

1.11 One-Pot secondary templating synthesis of hierarchical zeolites

In this technique, the mesopore is created in the microporous zeolite during the synthesis steps. In direct synthesis of zeolites with a hierarchy of pore structures, two main approaches have been followed in the literature. The concept entails the addition of an inert template to the amorphous zeolite gel and subsequently removing the template after the synthesis process [26, 27]. These secondary templates are often inert and rarely play any chemical role in the synthesis of the crystals. The technique also gives higher degree of freedom to fine-tune the mesopore shape, size and connectivity. Unlike the leaching technique, this method has no influence on the framework Si/Al ratio of the synthesized zeolite, ensuring higher control of the

active site. Depending on the nature of the inert template, the process can be termed soft or hard templating.

1.11.1 Soft templating

Polymers are commonly employed as secondary templates in the direct synthesis of hierarchical zeolites. The zeolite gel is mixed with the polymer and the resulting precursor is hydrothermally treated to crystallize the zeolite. The polymeric phase is subsequently removed by high temperature calcination in air or via chemical treatment.

Several polymeric materials have been employed in the search for hierarchical zeolites using polymers as templates. Those commonly employed are polystyrene spheres[28, 29], cellulose acetate filter membranes[30], polyurethane beads[31], natural starch[32] and latex beads[33]. The main drawback of this method, however, is the glass transition temperature of the polymers[25], which can severely limit the hydrothermal crystallization temperature of the zeolite.

1.11.2 Hard templating

The most common form of hard templating in hierarchical zeolite synthesis is the use of carbon based materials. The idea involves the incorporation of the carbon based materials into the zeolite gel and allowing the zeolite crystals to nucleate round the carbon particles, after which the matrix is subjected to thermal treatment for zeolite crystallization. Subsequently, the carbon is burnt off at a temperature of about 550 ^{O}C-700^{O}C, leaving behind cavities which act as sources of extra porosity in the zeolite (see figure 1.12). Carbon black[26, 34] and carbon nanotubes[27] or carbon

nano-fibres[35-37] are common carbon based materials which have been widely used.

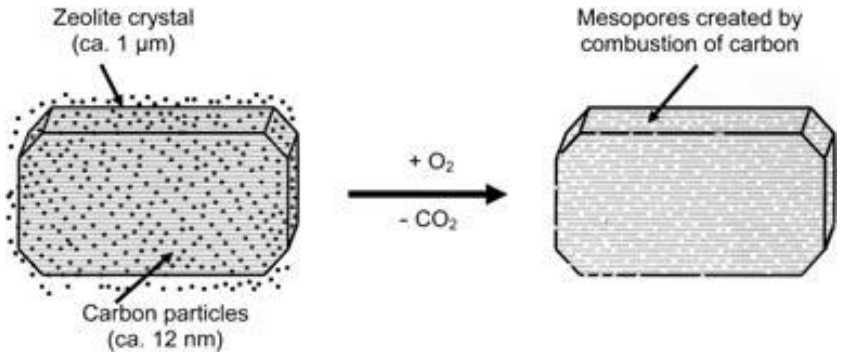

Figure 1.12: Concept of carbon hard templating in zeolites. Image taken from ref[20]

1.12 Chitosan

Chitosan is a naturally occurring, alkaline, hydrophilic, non-toxic and biodegradable copolymer which is obtained via deacetylation of chitin[38]. It is a widely occurring polysaccharide and has been described as the second most abundant polysaccharide found on earth, after cellulose[39]. It is described chemically as (1, 4)-2-amino-2-deoxy-β-D-glucosamine (see fig. 1.13) and is widely used in many important sectors such as the pharmaceutical, food[40, 41], medical[42] and textile industries[43-45]. In addition, chitosan has also been used extensively in catalysis for the immobilization of enzymes and as a support for precious and transition metals, which can be directly attributed to the high stability and the sorption capacities of metal anions in chitosan, in addition to the physical and chemical versatility of the chitosan polymer itself[46].

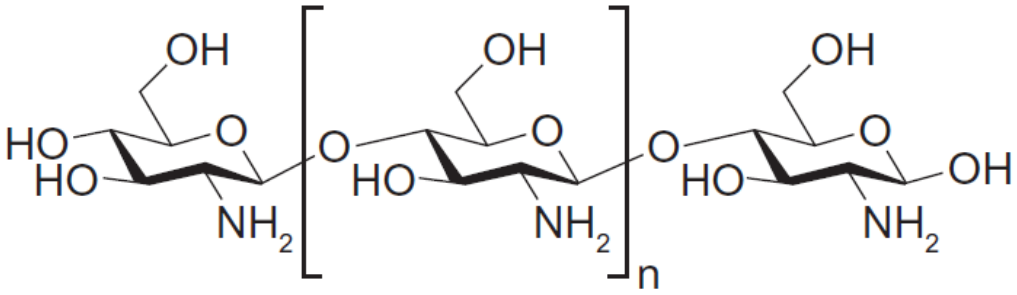

Figure 1.13: Chitosan structure with its repeating unit. Taken from ref[46]

1.12.1 Chitosan in heterogeneous catalysis

Significant enhancement has been reported in the reaction of iodobenzene with n-butyl acrylate in the presence of a palladium metal catalyst supported on a chitosan microsphere modified with a pearl shell[47]. Similarly, the utilization of copper immobilized on the surface of chitosan[48], by simple stirring of an aqueous suspension of chitosan in water with copper sulphate, in the azide–alkyne cycloaddition in aqueous media displayed good performance. In another development novel, chitosan-supported cinchona alkaloids were developed for heterogeneous catalysis for the enantioselective Michael reaction[49], for which high efficiency was observed. Chitosan has also been employed as a bio-template in the synthesis of nano-sized gold/palladium[50] particulates which displayed excellent catalytic activity in the aerobic oxidation of benzyl alcohol to benzaldehyde.

1.12.2 Chitosan for medical applications

The use of chitosan for medical and biomedical applications has also been studied extensively. Chitosan has been applied as a carrier for heparin [51, 52] for application in wound treatment. The results showed that the heparin-chitosan membrane exhibited faster wound healing compared to a matrix of heparin on other supports. Similarly, the effect of chitosan properties, such as the degree of

deacetylation and their molecular weight, have also been studied and found to affect the rate of wound healing[53]. Chitosans with a high degree of deacetylation and lower molecular weight were found to have better performance. Due to their biodegradable and biocompatible nature, nano-sized chitosan particles have also gained wide applications in drug delivery systems [54-56].

Tissue engineering and regeneration is another medical aspect where chitosan is also widely used. For tissue engineering, the chitosan is always preferred in three dimensional (3D) forms to mimic the damaged tissue structure[57]. Chitosan is a polymer with surface amino groups, which make it insoluble in alkaline solutions. However, upon protonation of the amino group, the chitosan can be rendered soluble in mild acidic solutions with a pH of less than 7, which gives chitosan the ability to be fabricated into 3D porous, stand-alone scaffolds of different shape and size. Figure 1.14 is a typical SEM image of a porous 3D chitosan scaffold for tissue regeneration.

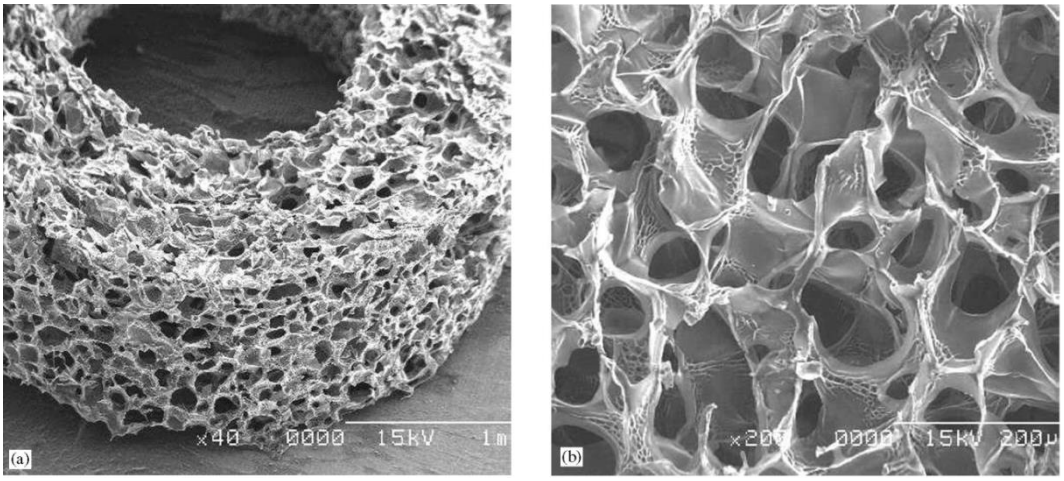

Figure 1.14: SEM images of a circular 3D chitosan scaffold[57]

1.12.3 Chitosan for water treatment

Due to their high sorption for metal ions chitosans have also been widely used for water treatment, which is possible because of the amino groups on the chitosan surface that can form various metal complexes. In addition, it has been found to be an effective chelating polymer for binding heavy metals[58]. The sorption ability of chitosan for the removal of heavy metals such as silver, cadmium, copper, lead and zinc ions has been well studied and reported[59, 60].

1.12.4 Chitosan as a source of carbon

Carbons for different applications have been derived from chitosan by subjecting it to varying treatment methods; including hydrothermal treatment for the generation of amino functional carbon particles for application in bio-imaging[61]. Through this technique, nanocarbons[62] have also been achieved for production of electrodes that are used in electrochemical sensing.

1.12.5 Chitosan as an inert template for hierarchical zeolites

Considering the vast abundance of chitosan, its low cost, non-toxicity and biodegradability, as well as the possible ease of elimination by simple thermal treatment in oxygen or in air stream, it can be considered as a good replacement for carbon or carbon nanotubes in the production of hierarchical zeolites via the hard templating route. This is even more important considering the high degree of toxicity presented by the carbon based materials that are currently being used in the synthesis of hierarchical pores in zeolite and zeotype materials.

To date, there are hardly any materials in the open literature where chitosan or its derivatives have been used directly as hard templates in hierarchical zeolite synthesis. This work, which is based on the direct use of commercial chitosan as a hard template in the synthesis of different zeolites will, therefore, present the first such application of chitosan.

1.13 Objective and scope

As discussed earlier in many publications, the use of zeolites with combined micro and mesopores has been suggested as the most viable way to mitigate against the diffusion and mass transfer problems in zeolites. To achieve this end, many techniques have been proposed and the advantages and draw backs of each were as discussed in the preceding sections of this chapter.

The most widely used and well regarded method, however, is the templating method; with carbon based materials the preferred candidates. With the high cost of carbon nanotubes and carbon nanofibres, their commercial use in this technique is far from realization. Recently, carbon black below a certain particle size has also been reported to have some degree of toxicity to humans.

Hence, the overall objective of this work is to investigate the suitability and possible use of chitosan (which is biodegradable, cost effective, hydrophilic, non-toxic and highly abundant) as an *insitu* carbon source in macro-templating for hierarchical zeolite synthesis. The influence of the chitosan on the crystallinity, phase purity and structural properties of the zeolites, and the effect of the created mesopore on the catalytic performance of the zeolite will be investigated.

The investigation was conducted on three different systems. In the first, the chitosan was used in the as-received powder form for the synthesis of hierarchical titano-silicate zeolites, and the obtained zeolites were investigated for liquid phase epoxidation of cyclohexene and styrene. In the second, the chitosan powder was transformed into a three dimensional porous scaffold and the scaffold was used to template the growth of the alumino-silicate zeolite. The resulting zeolite from this process was investigated for gas-phase methanol to hydrocarbon conversion. The final system investigated involves the use of the powder chitosan as an inert template in the synthesis of a bifunctional aluminium-titano-silicate zeolite. This system was investigated for low temperature liquid phase cyclohexanone to caprolactam conversion, gas-phase methanol to hydrocarbon conversion and Beckmann rearrangement of cyclohexanone oxime to caprolactam.

References

1. C.N. Satterfield, *Heterogeneous catalysis in industrial practice*, Second edition, McGraw-Hill, **1991**

2. J. Wisniak, *Educ. quím*, **2010**, *21*, 60-69

3. I. Fechete, Y. Wang, J.C. Védrine, *Catalysis Today*, **2012**, *189*, 2-27

4. S. Kulprathipanja, *Zeolites in industrial separation and catalysis*, Wiley interscience, **2010**.

5. A.F. Cronstedt, *Akad. Handl. Stockholm*, **1756**, *18*, 120-130

6. H. St Claire Deville, *Comptes Rendus Acad. Sci.*, **1862**, *54*, 324

7. C. Baerlocher, L.B. Mccusker, D.H. Olson, *Atlas of Zeolite Framework Types*

8. S. Bhatia, *Zeolite catalysis : Principles and applications*, CRC Press, **1990**

9. G.T. Kokotailo, S.L. Lawton, D.H. Olson, W.M. Meeier, *Nature*, **M*arch 30 1978***, *272*, 437-438

10. M.A. Uguina, D.P. Serrano, R. Van Grieken, S. Vènes, *Applied Catalysis A: General*, **1993**, *99*, 97-113

11. C.B. Khouw, M.E. Davis, *Shape-selective catalysis with zeolites and molecular sieves*, in *Selectivity in catalysis*, *American Chemical Society*, **1993**, p. 206-221.

12. A.M. Kareem, S. Chand, I.M. Mishra, *Journal of scientific and industrial research*, **2001**, *60*, 319-327

13. S.M. Csicsery, *Zeolites*, **1984**, *4*, 202-213

14. C. Hammond, N. Dimitratos, R.L. Jenkins, J.A. Lopez-Sanchez, S.A. Kondrat, M. Hasbi Ab Rahim, M.M. Forde, A. Thetford, S.H. Taylor, H.

Hagen, E.E. Stangland, J.H. Kang, J.M. Moulijn, D.J. Willock, G.J. Hutchings, *ACS Catalysis*, **2013**, *3*, 689-699

15. G. Bellussi, M.S. Rigutto, *Chapter 19 metal ions associated to molecular sieve frameworks as catalytic sites for selective oxidation reactions*, in *Studies in surface science and catalysis*, Elsevier, **2001**, pp. 911-955.

16. A.W. Chester, E.G. Derouane, *Zeolite characterization and catalysis*, Springer**, 2009**

17. C. Hammond, M.M. Forde, M.H. Ab Rahim, A. Thetford, Q. He, R.L. Jenkins, N. Dimitratos, J.A. Lopez-Sanchez, N.F. Dummer, D.M. Murphy, A.F. Carley, S.H. Taylor, D.J. Willock, E.E. Stangland, J. Kang, H. Hagen, C.J. Kiely, G.J. Hutchings, *Angewandte Chemie International Edition*, **2012**, *51*, 5129-5133

18. C. Hammond, N. Dimitratos, R.L. Jenkins, J.A. Lopez-Sanchez, S.A. Kondrat, M. Hasbi Ab Rahim, M.M. Forde, A. Thetford, S.H. Taylor, H. Hagen, E.E. Stangland, J.H. Kang, J.M. Moulijn, D.J. Willock, G.J. Hutchings, *Chemistry – A European Journal*, **2012**, *18*, 15735-15745

19. S.T. Wilson, B.M. Lok, C.A. Messina, T.R. Cannan, E.M. Flanigen, *Journal of the American Chemical Society*, **1982**, *104*, 1146-1147

20. J. Weitkamp, L. Puppe, *Catalysis and zeolites : Fundamentals and applications*, Springer**, 1999**.

21. J. Yu, R. Xu, *Chem Soc Rev*, **2006**, *35*, 593-604

22. M. Hartmann, *Angewandte Chemie International Edition*, **2004**, *43*, 5880-5882

23. H. Hosokawa, K. Oki, *Chemistry Letters*, **2003**, *32*, 586-587

24. S.Van Donk, A.H. Janssen, J.H. Bitter, K.P. De Jong, *Catalysis Reviews*, **2003**, *45*, 297-319

25. D.P. Serrano, J.M. Escola, P. Pizarro, *Chemical Society Reviews*, **2013**, *42*, 4004-4035

26. C.J.H. Jacobsen, C. Madsen, J. Houzvicka, I. Schmidt, A. Carlsson, *Journal of the American Chemical Society*, **2000**, *122*, 7116-7117

27. I. Schmidt, A. Boisen, E. Gustavsson, K. Ståhl, S. Pehrson, S. Dahl, A. Carlsson, C.J.H. Jacobsen, *Chemistry of Materials*, **2001**, *13*, 4416-4418

28. T.B. Holland, L. Abrams, A. Stein, *Journal of the American Chemical Society*, **1999**, *121*, 4308-4309

29. L. Xu, S. Wu, J. Guan, H. Wang, Y. Ma, K. Song, H. Xu, H. Xing, C. Xu, Z. Wang, Q. Kan, *Catalysis Communications*, **2008**, *9*, 1272-1276

30. Y. Wang, Y. Tang, A. Dong, X. Wang, N. Ren, W. Shan, Z. Gao, *Advanced Materials*, **2002**, *14*, 994-997

31. Y.J. Lee, J.S. Lee, Y.S. Park, K.B. Yoon, *Advanced Materials*, **2001**, *13*, 1259-1263

32. Y. Liu, W. Zhang, Z. Liu, S. Xu, Y. Wang, Z. Xie, X. Han, X. Bao, *The Journal of Physical Chemistry C*, **2008**, *112*, 15375-15381

33. S.P. Naik, A.S.T. Chiang, H. Sasakura, Y. Yamaguchi, T. Okubo, *Chemistry Letters*, **2005**, *34*, 982-983

34. I. Schmidt, A. Krogh, K. Wienberg, A. Carlsson, M. Brorson, C.J.H. Jacobsen, *Chemical Communications*, **2000**, 2157-2158

35. F. Schmidt, S. Paasch, E. Brunner, S. Kaskel, *Microporous and Mesoporous Materials*, **2012**, *164*, 214-221

36. A.H. Janssen, I. Schmidt, C.J.H. Jacobsen, A.J. Koster, K.P. De Jong, *Microporous and Mesoporous Materials*, **2003**, *65*, 59-75

37. A. Boisen, I. Schmidt, A. Carlsson, S. Dahl, M. Brorson, C.J.H. Jacobsen, *Chemical Communications*, **2003**, 958-959

38. H. Yi, L. Wu, W.E. Bentley, R. Ghodssi, G.W. Rubloff, J.N. Culver, G.F. Payne, *Biomacromolecules*, **2005**, *6*, 2881-2894

39. S.H. Lim, S.M. Hudson, *Journal of Macromolecular Science, Part C*, **2003**, *43*, 223-269

40. A.M. Papineau, D.G. Hoover, D. Knorr, D.F. Farkas, *Food Biotechnology*, **1991**, *5*, 45-57

41. S.W. Fang, C.F. Li, D.Y.C. Shih, *Journal of Food Protection*, **1994**, *57*, 136-140

42. J. Berger, M. Reist, J.M. Mayer, O. Felt, N.A, Peppas, R. Gurny, *European Journal of Pharmaceutics and Biopharmaceutics*, **2004**, *57*, 19-34

43. K. Kurita, M. Kamiya, S. Nishimura, *Carbohydrate Polymers*, **1991**, *16*, 83-92

44. M.N.V.R, Kumar, *Bull. Mater. Sci.*, **1999**, *22*, 905-915

45. J.A. Rippon, *Journal of the Society of Dyers and Colourists*, **1984**, *100*, 298-303

46. E. Guibal, *Progress in Polymer Science*, **2005**, *30*, 71-109

47. M. Zeng, C. Qi, X. Zhang, *International Journal of Biological Macromolecules*, **2013**, *55*, 240-245

48. R.B.N. Baig, R.S. Varma, *Green Chemistry*, **2013**, *15*, 1839-1843

49. Y. Qin, W. Zhao, L. Yang, X. Zhang, Y. Cui, *Chirality*, **2012**, *24*, 640-645

50. S.R. Hall, A.M. Collins, N.J. Wood, W. Ogasawara, M. Morad, P.J. Miedziak, M. Sankar, D.W. Knight, G.J. Hutchings, *RSC Advances*, **2012**, *2*, 2217-2220

51. G. Kratz, C. Arnander, J. Swedenborg, M. Back, C. Falk, I. Gouda, O. Larm, *Scandinavian Journal of Plastic and Reconstructive Surgery and Hand Surgery*, **1997**, *31*, 119-123

52. D.K. Kweon, S.B. Song, Y.Y. Park, *Biomaterials*, **2003**, *24*, 1595-1601

53. T. Minagawa, Y. Okamura, Y. Shigemasa, S. Minami, Y. Okamoto, *Carbohydrate Polymers*, **2007**, *67*, 640-644

54. J. Wang, Z. Zeng, R. Xiao, T. Xie, G. Zhou, X. Zhan, S. Wang, *International journal of nanomedicine*, **2011**, *6*, 765-74

55. M.P. Patel, R.R. Patel, J.K. Patel, *J Pharm Pharm Sci*, **2010**, *13*, 536-57

56. M. Amidi, E. Mastrobattista, W. Jiskoot, W.E. Hennink, *Advanced Drug Delivery Reviews*, **2010**, *62*, 59-82

57. F. Croisier, C. Jérôme, *European Polymer Journal*, **2013**, *49*, 780-792

58. H.K. No, S.P. Meyers, *Rev Environ Contam Toxicol*, **2000**, *163*, 1-27

59. A. Kamari, I.D. Pulford, J.S.J. Hargreaves, *Journal of Environmental Management*, **2011**, *92*, 2675-2682

60. A. Kamari, I.D. Pulford, J.S.J. Hargreaves, *Colloids and Surfaces B: Biointerfaces*, **2011**, *82*, 71-80

61. Y. Yang, J. Cui, M. Zheng, C. Hu, S. Tan, Y. Xiao, Q. Yang, Y. Liu, *Chem Commun*, **2012**, *48*, 380-2

62. F. Xia, M. Pan, S. Mu, M.D. Jones, D. Wolverson, F. Marken, *Electroanalysis*, **2012**, *24*, 1703-1708

Chapter 2: Experimental techniques and methodologies

Chapter overview

This chapter gives the detailed description of the experimental techniques and procedures used throughout this study. The chapter opens with a brief discussion of the techniques used for the synthesis of zeolites followed by a more detailed analysis of each of the synthesis methods and their advantages. This is followed with a discussion of the techniques used for the characterization of the zeolite samples synthesized during this project. A brief discussion of the working principles and the benefits of each characterization techniques are given. Where applicable and practically possible, a schematic illustration of each method is included and a photographic image of the experimental set up is also added for visual appreciation of the description. The experimental procedure specifically used during this work for each technique is then described.

Following the discussion of the characterization and synthesis techniques, we give a discussion of the set-ups used for catalytic evaluation of the synthesized zeolites. Discussion of the individual reactions is omitted here, but included in the relevant chapters.

2.1 Zeolite synthesis techniques

The hydrothermal method, described by Milton and co-workers in the 1940s, for the synthesis of zeolites consists of the mixing of reactive alkali metal cations with aluminosilicate gels at high pH; these mixtures are then crystallized at low

temperature and pressure. Nowadays, however, hydrothermal synthesis of zeolites includes high temperature crystallization of aluminosilicate/metalosilicate gels at higher temperature and pressure. While the hydrothermal method is still very much in use today, other routes have been developed for zeolite crystallization.

In general, three different methods have been described for the synthesis of zeolites. These include the conventional hydrothermal technique, the steam assisted method and the vapour phase crystallization method.

2.1.1 Hydrothermal synthesis technique

Hydrothermal synthesis refers to the formation of materials in a primarily aqueous solvent[1]. This technique involves the preparation of the zeolite precursor, consisting of the aluminium/silicon/phosphorus sources, structure directing agent, water and a source of the alkali metal cation. Typically, the precursor composition determines the type of zeolite formed. The amorphous gel, in contact with the solvent phase, is thus transferred to an autoclave, which is filled to a maximum of 60-70% volumetric capacity for safety reasons. The autoclave is sealed and heated at a pre-set temperature. The crystallization is then carried out under autogenous pressure, generated by the liquid in the autoclave (see figure 2.1 for schematic illustration). After the crystallization has been completed, the zeolite material is retrieved from solution by filtration or centrifugation.

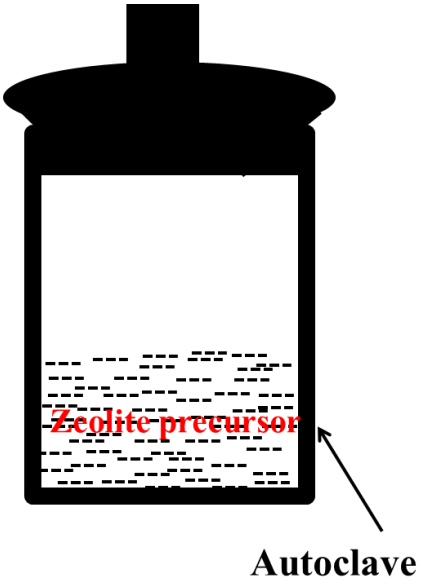

Figure 2.1: Schematic illustration of the hydrothermal technique

2.1.2 Steam assisted crystallization (SAC)

This method was first developed in 1990 by Wenyang Xu et al[2] for the preparation of ZSM-5 zeolite. It involves the preparation of an amorphous gel of the zeolite without the organic structure directing agent (OSDA). The amorphous gel is filtered, washed and dried. The dry gel is then placed in a specially made autoclave containing a porous sieve. The OSDA is mixed with water and placed in the bottom of the autoclave. The autoclave is then heated at a predetermined temperature. The steam containing the organic structure directing agent mixes with the amorphous phase to initiate crystallization.

The striking feature of this technique is that the amorphous gel is not in direct contact with the liquid phase which allows for the OSDA in solution to be reused for another synthesis batch.

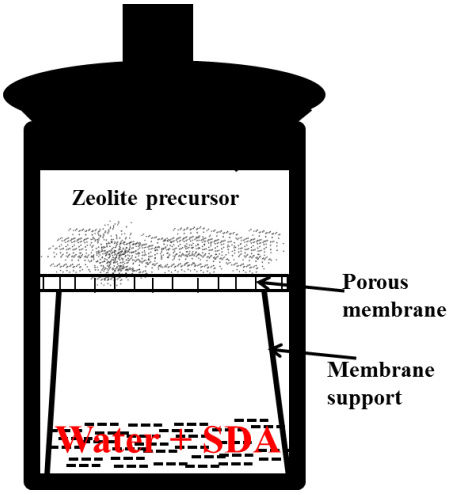

Figure 2.2: Typical set-up for zeolite crystallization via the steam assisted crystallization technique. Adapted from ref[2]

2.1.3 Vapour phase crystallization (VPC)

This technique is similar to the steam assisted method. The only difference between the two is that the structure directing agent is always included during the precursor preparation for the VPC. The water is then dried off to obtain dry powder. The powder is placed in a modified autoclave of the kind used in the SAC method as illustrated in figure 2.3. In this method, however, water is placed into the bottom of the autoclave, contrary to SAC method where the template-water mixture was used.

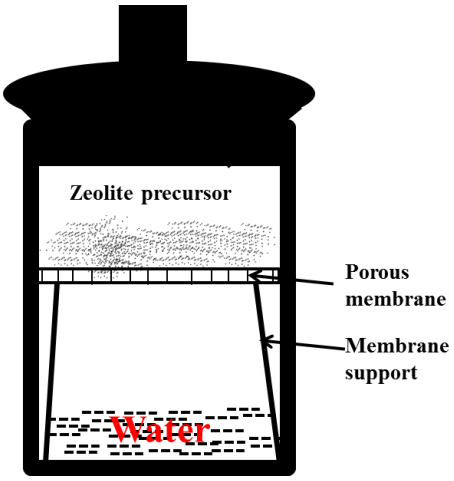

Figure 2.3: Illustration of zeolite crystallization by the vapour phase method

2.1.4 Hybrid method of crystallization

During preparation of hierarchical zeolites through the hard templating route, there has always been the problem of the additional inert templating agent separating out of the liquid phase, thereby resulting in poor utilization of such templates. To overcome this problem the SAC method has often been used. In this work a new method described as a 'hybrid' method was employed.

This approach includes the preparation of the amorphous zeolite gel containing the hard template in water and heating the solution to complete dryness. The dry amorphous gel is subsequently mixed with the organic templating agent and the resulting moist powder is then sealed in a Teflon lined conventional steel autoclave, as illustrated in figure 2.4. Crystallization takes place at a predetermined temperature under autogenous pressure. It was envisaged that this method will ensure maximum contact between the amorphous zeolite gel and the inert templating agent.

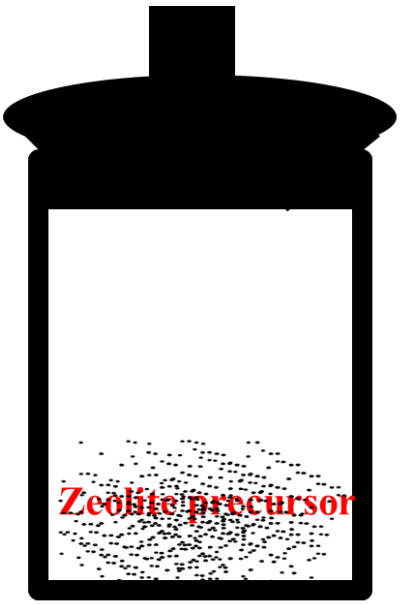

Figure 2.4: Schematic illustration of the hybrid technique described above

2.2 Advantages of SAC synthesis techniques

Phase separation has always been a major concern in the hydrothermal synthesis of hard templated hierarchical zeolites. This problem has been conveniently solved to some degree by the steam assisted method. In addition, the steaming method also produces zeolites of uniform size distribution and controlled growth – this is due to the elimination of the temperature gradient, which easily occurs in the hydrothermal technique. In the SAC method, the amorphous gel is heated by the saturated steam, which is envisaged to be at uniform temperature. The SAC method can also be considered as an economical route since the expensive organic template can be reused for another batch of synthesis, since it is not in direct contact with the amorphous gel[2].

2.3 Characterization techniques

There are a number of factors which dictate the type of zeolite formed. These range from the gel composition, crystallization temperature and time, and the choice of organic template, which has necessitated the need to carry out comprehensive characterization of the materials obtained after the crystallization period. This procedure is often followed to ascertain the zeolite phase and purity, crystal size and morphology and coordination state of the T-atoms as well as the acidity. Since there is no one single technique which can give all these required information the synthesised zeolite must be taken through a series of techniques to obtain the information required. Some of these techniques, which are employed in this thesis, are discussed below.

2.3.1 Phase identification by X-Ray diffraction technique

The X-ray diffraction (XRD) technique is a well-established method of identifying structure, phase and purity of crystalline solid materials. The diffraction resulting from the crystalline phase is always unique, and this has been used as a “finger print” for phase identification in zeolites[3] and other crystalline solids. In zeolite phase identification, by comparing the diffraction patterns of a sample with standard patterns available in the atlas of materials, the purity of the material as well as phase of the material can be determined. The presence of any additional peak in the obtained diffraction pattern is always an indication of the presence of an impurity phase in the synthesized material.

The degree of crystallinity may sometimes be determined from the XRD patterns by simple inspection of the diffraction peak intensity, or more precisely through refinement techniques such as Rietveld refinement. The nature of the base line in the diffraction pattern of a crystalline material can reveal information about the presence of amorphous material in the solid[4]. It is important to note, however, that the degree of packing can influence the intensity of the diffraction pattern in powder diffraction analysis, therefore simple peak inspection might not be ideal for crystallinity measurement. The crystal size of the material can also be deduced from X-ray diffraction patterns using the relationship derived by Scherrer. According to the Scherrer equation, the width of the diffraction peak is inversely proportional to the crystallite size.

2.3.2 Phase purity

A slight change in one or more parameter(s) during zeolite gel preparation or the crystallization step can result in a completely different phase of material than intended. For instance, the hydrothermal synthesis of ZSM-22 with TON topology in the presence of Na^+ or K^+ cations can only be achieved in the pure form if the precursor is stirred at speed of at least 400rpm during hydrothermal crystallization[5]. At a lesser speed, the ZSM-22 will coexist with the ZSM-5 MFI phase and, under static crystallization conditions, ZSM-5 is produced as the main product, with a small amount of dense phase cristobalite[5] (see figure 2.5). This further stresses the need to characterize the zeolite for phase purity.

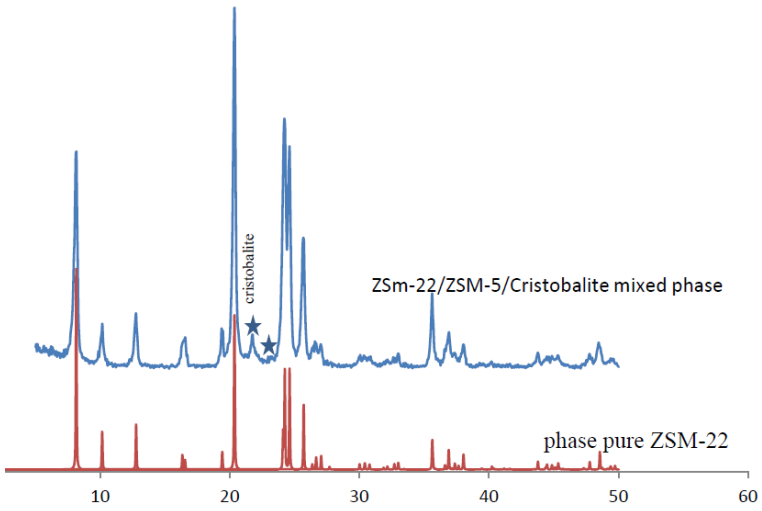

Figure 2.5: XRD pattern of synthesized ZSM-22; illustration of phase purity (star is ZSM-5 & cristobalite phases)

2.3.3 Sample preparation and procedure for X-ray diffraction measurement

The flat plate powder X-ray diffraction technique was used for phase identification of all samples synthesised in this work. The instrument used was a Bruker D4 X-ray diffractometer using Cu Kα target and a nickel filter. Plastic holders were used and

powder patterns were collected from 5 to 50^{O} 2θ angle. Prior to pattern collection, the zeolite samples were dried overnight at 110^{O}C after which they were crushed to obtain a very fine powder. An appropriate quantity of the fine powder thus obtained was tightly and uniformly packed into the plastic holder to produce a flat smooth surface. All measurements were done at room temperature.

2.4 Textural properties and pore characterization

Surface area, pore size, pore size distribution, pore volume and the nature of porosity are some of the textural properties of zeolites that require careful characterization. Though, the Brunauer-Emmett-Teller (BET) technique is the most widely used method for surface area determination, other methods such as mercury porosimetry have been used for the determination of the pore size and size distribution. The adsorption of a particular molecular species from a gas onto the surface of the porous zeolite is the primary method of measuring total surface area[6]. Commonly used gases in surface area measurement include nitrogen, argon and krypton.

The porosity of the zeolite material can be determined from the physical adsorption isotherms which have been classified into five types, generally known as the BET classification[6]. These adsorption isotherms, illustrated schematically in figure 2.6, also indicate the shape of the pore [7]. The type I isotherm is characteristic of microporous materials with relatively small external surface area. Adsorption on this type of materials typically takes place at low relative pressure, due to the strong interaction between the adsorbate and the material pore walls[8]. The type II adsorption isotherm, which is sigmoid or S-shaped, is commonly observed for macroporous materials. The type III isotherm arises from materials possessing

relatively weak adsorption, such that their surface is not wetted by the adsorbate. Materials with a mesoporous pore structure are characterized by the type IV isotherm - these exhibit a hysteresis effect at high relative pressure, from which pore size distribution can be estimated.

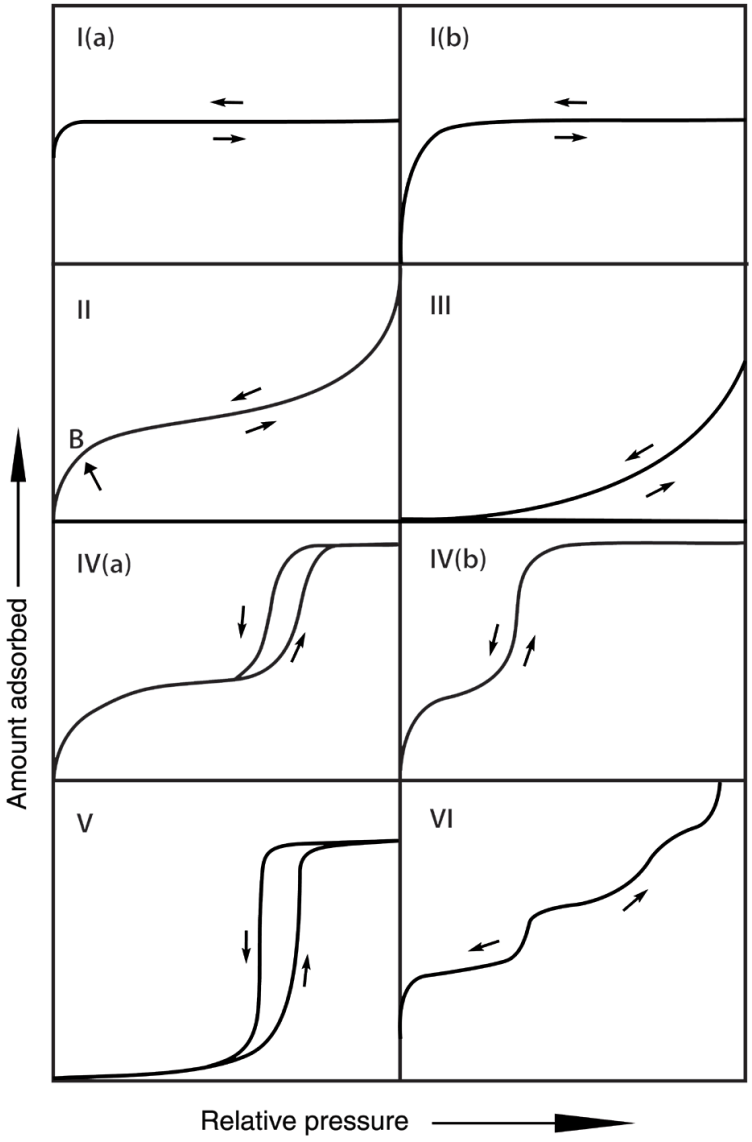

Figure 2.6: Different nitrogen adsorption isotherms[9]

The shape of the hysteresis curve exhibited by a porous material gives useful information on the nature of the pores within the material. These hysteresis, which were previously classified into four groups, have recently been reclassified by the IUPAC into six groups, and are illustrated in figure 2.7 below.

The type H1 hysteresis is typical of particles made up of nearly cylindrical channels or agglomerates of spherical particles; materials exhibiting this type of hysteresis are characterized by uniform pore size and shapes. The H2 loop is closely related to that of H1, except that the pores in materials that exhibit this kind of hysteresis are composed of non-uniform size and shape. Unlike types H1 and H2, where the make-up is that of agglomerated spheroidal particles, types H3 and H4 indicate aggregated particles formed into slit shaped pores. These pores are of uniform size and shape in the case of type H3 and non-uniform in type H4[8].

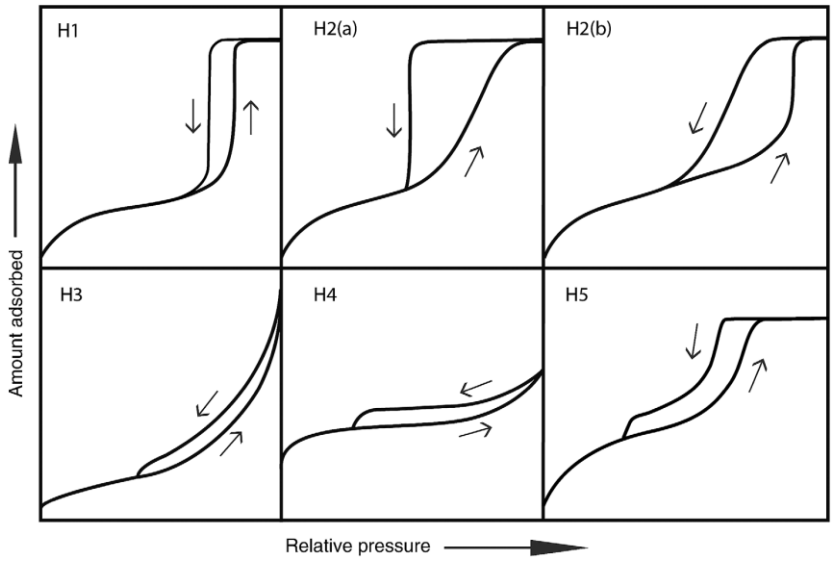

Figure 2.7: Types of hysteresis exhibited by different types of porous materials. Taken from ref[9]

2.4.1 Sample preparation for BET surface area determination

To measure the surface area of zeolites accurately, using the BET technique, it is important to ensure that all the zeolite pores are available for gas adsorption. For this reason, the sample is thermally treated at a temperature of between 120^{O}C to 350^{O}C for 4 to 12 hours under vacuum or inert atmosphere. This ensures the complete removal of any adsorbed moisture and stray gases from the zeolite pores and is

known as degassing. For highly microporous zeolites, subsequent degassing is necessary at the sample analysis port, though for a shorter period of time.

The surface area and pore volume were obtained from nitrogen adsorption-desorption isotherms, measured at 77 K on Quantachrome Autosorb-iQC. The sample was degassed at $300^{O}C$ overnight under dynamic vacuum prior to the adsorption measurement. The specific surface area was measured from the desorption isotherm in the relative pressure range between 0.005 and 0.3, according to the BET method. The pore size distribution was estimated using the density function theory (DFT) model inbuilt in the instrument software. The total pore volume was calculated from the amount of N_2 adsorbed at a relative pressure of 0.99.

2.5 Acid characterization of zeolite samples - FTIR approach

Infrared spectroscopy is widely applied in zeolite characterization. It is commonly applied for the determination of various zeolite features including structure, framework features, zeolite-adsorbate interaction, silicon to aluminium (Si/Al) ratio, hydroxyl groups and acidity. Commonly available infrared spectrometers measure the absorption of radiation in the mid-infrared region of electromagnetic spectrum[1] ($4000\text{-}400cm^{-1}$). Qualitative information about the acidity of zeolites can be obtained by investigating the hydroxyl group in the protonated zeolite using this technique; this is particularly useful because the protons which are responsible for the zeolite acidity are present as bridging hydroxyl groups in the zeolite framework[1]. The use of probe molecules such as ammonia and pyridine can, however, permit the quantitative determination of acidity via the FTIR technique. Though FTIR is also a

useful technique for gathering information about zeolite formation, framework vibrations, surface properties, catalysis and adsorption[10], it was employed in this work as a tool for qualitative determination of the zeolite acidity.

2.5.1 Sample preparation for FTIR measurement

Each powdered sample was pelletized into a circular disc which can easily fit into the KBr window of our cell. Approximately 7 mg of very fine powder of each sample was pelletized to yield a very transparent disc of sample. The sample was placed in the instrument KBr window and thermally treated *in situ* from room temperature to 550 ^{O}C at a heating rate of 10 ^{O}C/min in a nitrogen flow stream; this was done to remove adsorbed water from the zeolite as water displays very strong adsorption bands in the OH region of interest. Data were collected in the transmission mode between 4000 and 400cm^{-1}. Information about the acidity of the samples was deduced from the intensity of the peaks at around 3610 cm^{-1} and 3740 cm^{-1}, which correspond to the strong Si-OH-Al in the zeolite super cage and the very weak Si-OH external silanol respectively, as illustrated in figure 2.8

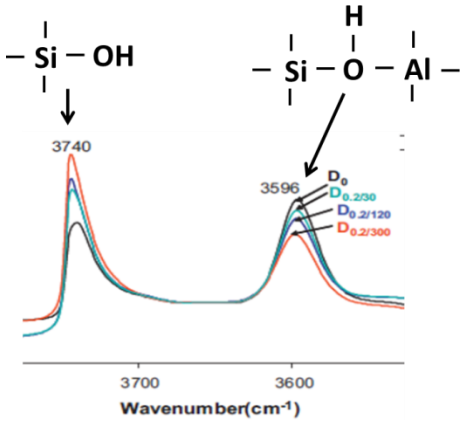

Figure 2.8: FTIR spectra of TON zeolites treated with NaOH for different durations[11]

2.6 Morphological characterization - Electron microscopy

Size, shape and surface properties are fundamental properties of synthesized zeolites which are always determined via electron microscopy. Generally, for crystal morphologies, the secondary electrons produced in the scanning electron microscope are used [12, 13]. These are low energy electrons which are generated just a few nanometres from the surface of the material, which makes contrast in the secondary electron imaging highly dependent on the crystallite morphology[10]. Application of secondary electrons in SEM has been used to reveal information on the zeolite surface roughness, shape and size such as given in figure 2.9.

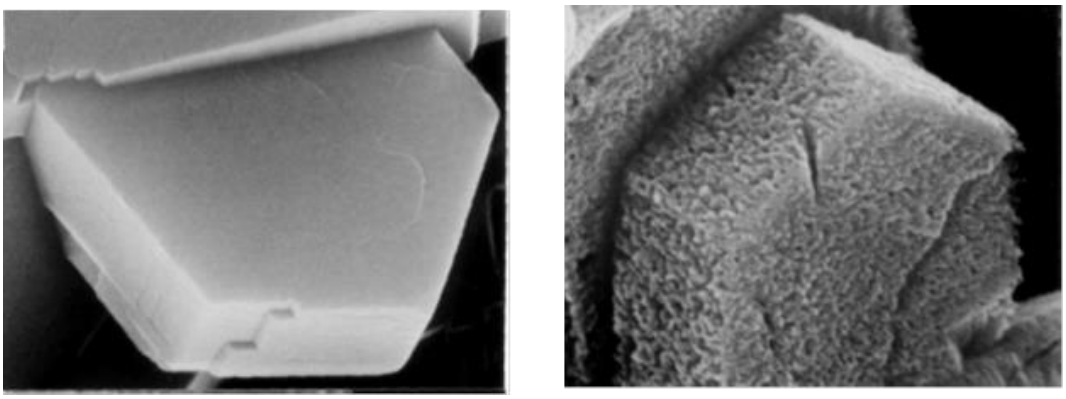

Figure 2.9: SEM micrograph showing surface properties of ZSM-5 (Left; As prepared, Right; modified). Image taken fom ref [14]

2.6.1 Working principle of the SEM

In a typical SEM instrument, the electrons are generated and emitted from a heated pointed cathode that serves as an electron gun[6]. These generated electrons are then permitted to accelerate through two electrodes, one of which is an anode. Subsequently, the accelerated electrons pass sequentially through a condenser system, the sample and a system of magnetic lens. The condenser collects and focuses the electrons on a small spot of the specimen while the magnetic lens system

collects, magnifies and transmits the signals from the specimen to a detector. Figure 2.10 gives a pictorial representation of the working principle of an SEM.

For accurate analysis, it is necessary to ensure the specimen to be analysed is stable under vacuum, as the instrument operates under a high vacuum. SEM data interpretation may be obscured and misleading if the sample surface is contaminated with impurities such as dust, hence it is imperative to avoid this during sample preparation.

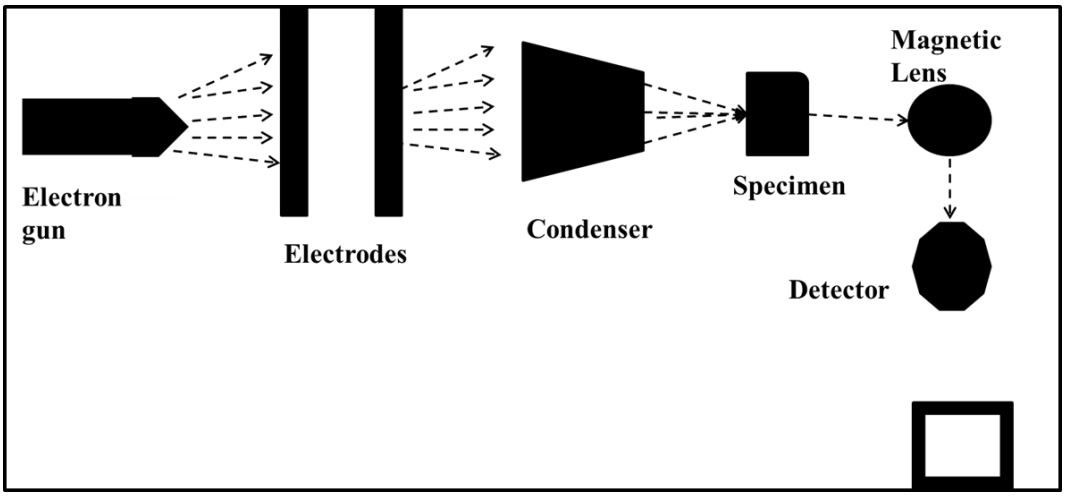

Figure 2.10: Schematic illustration of the working principle of an SEM

2.6.2 Sample preparation for SEM analysis

A very small amount of finely crushed powder was dispersed on one side of a piece of double sided carbon tape affixed to the surface of a standard SEM sample stub. To enhance the electrical conductivity and induce charge dissipation, the samples were coated with a thin layer of carbon/gold under a high vacuum environment. Images were taken on a JOEL (JSM-6301F) field emission scanning electron microscope. The working voltage was 5KV with a working distance of approximately 9mm. Images were taken at different magnifications and from different spots of the specimen.

2.7 Location & coordination state of T-atoms in zeolite frameworks - Raman spectroscopy technique

Crystallographic measurement is normally used to obtain information about the location of cations in zeolites[10]. Where this is not possible, however, the Raman and IR techniques have proven to be valuable alternatives [10]. In this work, the Raman spectroscopy technique was used to determine the presence and coordination state of titanium in all the titanium bearing zeolites. The use of resonance UV-Raman to determine the presence and position of titanium in the titanium-silicalite-1 framework has been reported by Can Li et.al[15]. In their work, they proved the resonance Raman influence on selective enhancement of the Raman bands associated with framework titanium atoms. Use of the UV-Raman method in cation identification has also been reported to reduce the fluorescence interference from the zeolite sample, thereby improving the Raman spectra considerably [16, 17]. Several literature reports[15, 18-20] have associated the Raman bands at 960 cm^{-1} and 1125 cm^{-1} with the framework associated titanium species, while the Raman band at 695 cm^{-1}, which occurs upon excitation of the zeolite with a 266nm laser, was attributed to the octahedral TiO_6 species[18]. Typical Raman spectra of two TS-1 zeolite samples are given in figure 2.11.

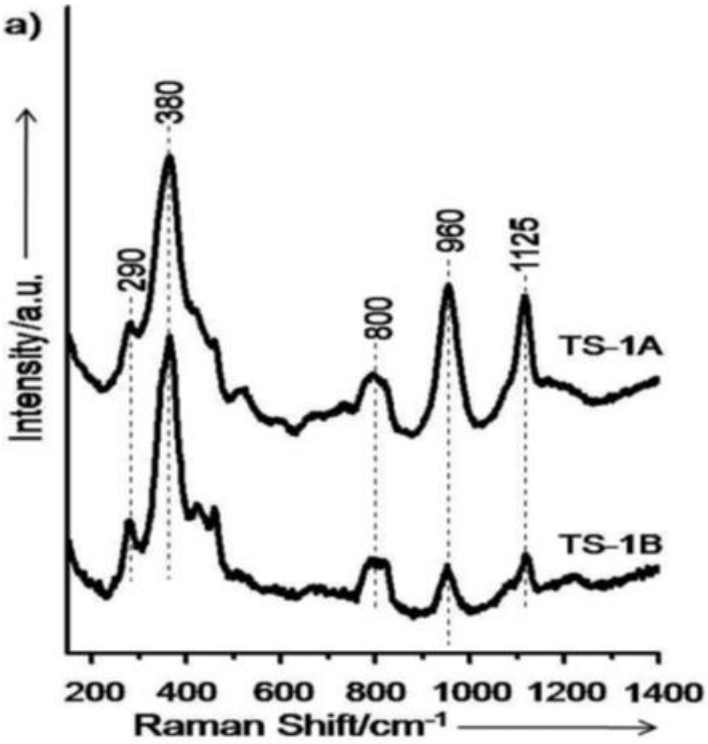

Figure 2.11: UV-Raman spectra of two TS-1 samples with peaks at 960 cm^{-1} and 1125cm^{-1} indicating the presence of framework titanium[18]

2.7.1 Sample preparation for Raman analysis

To maintain uniform sample thickness for all samples, approximately 50 mg of each sample was pelletized into a circular disk using a laboratory bench top pelletizer. Each pellet was in turn placed on a glass slide which was mounted onto the Raman sample holder. Data were recorded on a multiline Renishaw Invia Raman microscope using a laser wave length of 325 nm. An average of 30 scans was accumulated for each sample at a spectra resolution of 4cm^{-1}.

2.8 X-ray absorption spectroscopy (XAS)

The X-ray absorption spectroscopy technique refers to the way atoms absorb X-rays at energies near and above the binding energies of the atom's core levels. XAS measurement usually requires an intense source of X-rays with tuneable energy, as

provided by a synchrotron. A synchrotron is a light source that produces high energy radiation, which is used to study the structural and chemical properties of materials at a molecular level. The chemical state and local atomic structure of selected elements can be determined by this technique because XAS spectra are sensitive to the oxidation state and coordination chemistry of the selected element. It is also sensitive to the coordination number, as well as the distances and species immediately neighbouring the element of interest. In practice, the main interest in XAS measurements is the measure of the variation (intensity) of the absorption coefficient with varying X-ray energy at and above the binding energy of a known core level of a chosen atomic species. The absorption coefficient is a measure of the likelihood of an X-ray being absorbed in accordance with Beer's law (below):

$$I = I_O e^{-\mu t} \quad \ldots\ldots\ldots\

coordination chemistry and oxidation state of the absorbing atom can be determined. The second region, the extended X-ray absorption fine-structure (EXAFS), is particularly useful for quantitative analysis. For instance, the determination of the distances, coordination number and species of the absorbing atom's immediate neighbours can be determined from the EXAFS analysis.

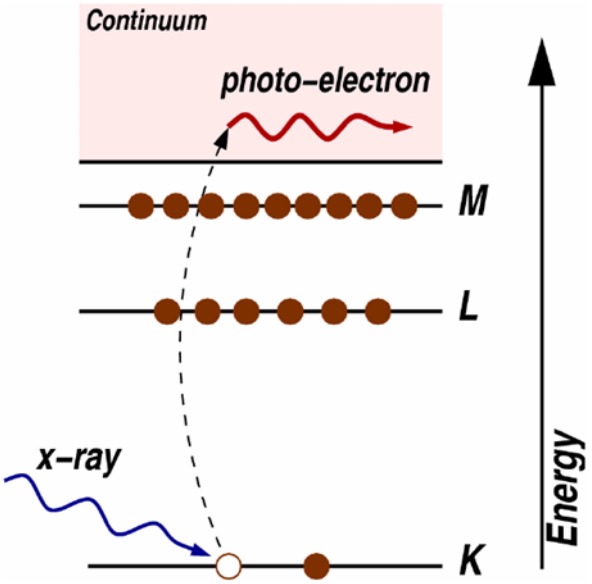

Figure 2.12: Illustration of X-ray absorption and the excitation of a core level electron [21]

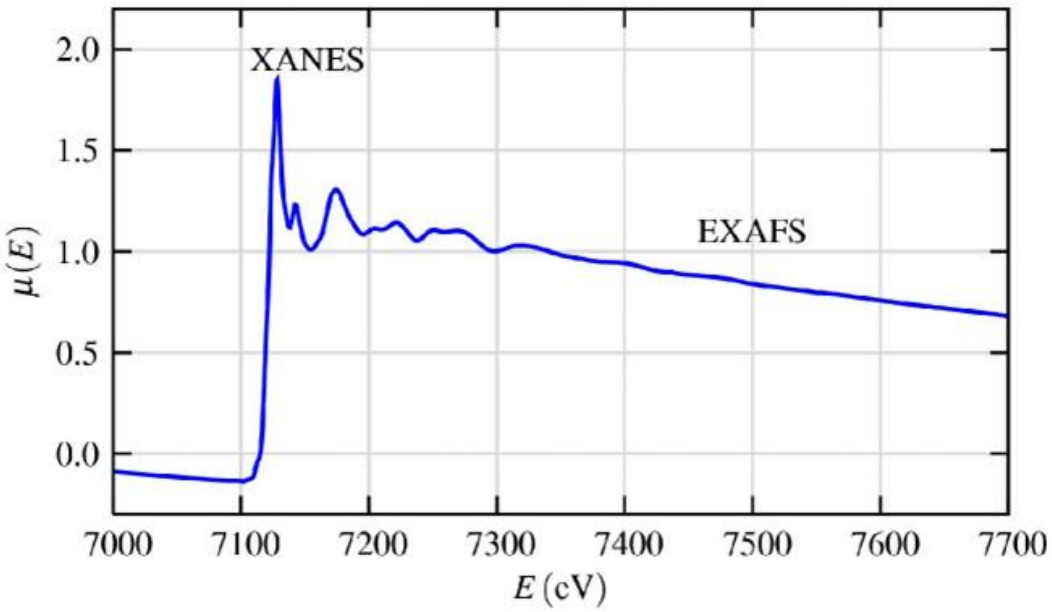

Figure 2.13: Typical XAS spectra of FeO showing the XANES and EXAFS region[21]

2.8.1 Sample preparation and procedure for XAS measurements

The coordination geometry of the titanium in the TS-1 structure was determined by Ti K-edge XAS analysis; in particular Ti K-edge XANES data were used to extract information on the coordination environment around titanium in these materials. Ti K-edge XANES data were collected at the XAFCA beam line at the Singapore synchrotron light source (SSLS), which operates at 0.9 GeV. In a typical experiment, pellets of the sample were loaded into the *in situ* cell and heated in vacuum to 773K. The data were recorded before and during the heating process to evaluate any structural changes that take place during the removal of adsorbed water. The measurement was repeated upon cooling down to room temperature. Typical scan time of about 20 minutes per scan was used. The XAS data were collected in the fluorescence mode using a VORTEX detector. $Ti(OSiPh_3)_4$ and ETS-10 were used as standards to evaluate the coordination environment of the titanium centres in TS-1 catalysts, following the procedure detailed previously[22].

2.9 Thermogravimetric analyzer

The thermogravimetric analysis technique, otherwise commonly referred to as TGA, follows the mass loss of a sample in response to a pre-set temperature ramp profile. The mass loss could be as a result of one or more thermal event(s) such as evaporation, degradation or decomposition of the material, or of a certain component in the material. It is always essential that the temperature program is ramped at constant rates. The measurement is often conducted under specific conditions, such as under an inert or reactive gas. The mass lost or gained by the sample under analysis is measured by an ultra-sensitive balance which is coupled to the TGA

instrument. This technique is very convenient in determining the percentage composition of a compound, filler contents in polymers, the thermal stability and degradation of polymers, adsorption-desorption behaviour of a material and the influence of reactive gases on a compound, as well as the stoichiometry of a reaction.

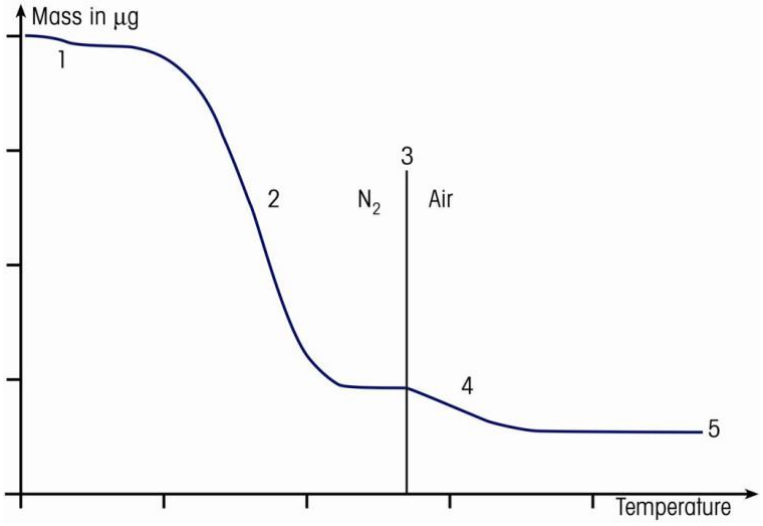

Figure 2.14: Typical TGA thermograph showing different possible thermal events taking place during a TGA experiment[23]

The data output from the TGA is capable of yielding information on the type of thermal event taking place under a certain temperature profile and specific environment. For instance, figure 2.14 gives a typical thermograph from a TGA experiment in which different thermal events can be observed. Sections 1 to 3 of the thermograph describe the thermal response of a polymeric material in an inert (nitrogen) environment. Region 1 is typical of the evolution of moisture and volatile components (gas, solvent) of the material and region 2 is an indication of degradation of the material. A switch from the inert conditions to air results in another thermal response (region 3 and 4), which is oxidation/combustion of the carbon components. The final step, which is depicted as region 5, is the residue left after the thermal treatment.

2.9.1 Sample preparation for TGA analysis

Prior to experimental measurements, two alumina crucibles were obtained and thoroughly cleaned to ensure they were free of any contaminants. The two crucibles were then placed on a sample pan, one on the reference pan and the other on the sample pan. The measure weight of these two crucibles was then tared. The sample (about 10 to 15 mg) was then put into the sample crucible. The mass was allowed to stabilize and recorded into the instrument control software.

The temperature profile used for the analysis includes ramping from room temperature to 1000 ^{O}C at a rate of 10 K/minute. The experiment was conducted under air. Once the program was input into the system, the crucible weights were tared again before initiating the program. Mass loss was recorded against temperature change.

2.10 Other techniques employed

Apart from the techniques described in detail above, others were used to a limited extent for characterization in this work. One of these is the UV-Vis spectroscopy. This technique was used as a complementary tool to validate the coordination state of titanium in the synthesized titano-silicate materials. It is capable of distinguishing between octahedral and tetrahedral titanium species in zeolites and other materials. Sample preparation involved powder zeolite being pressed into a circular disc of about 5mm thickness and 25mm diameter. This zeolite disc was placed in the cell and the measurement taken in the reflective mode. Data were recorded from 800nm to 200nm wavelength.

2.11 Catalytic reactions and reactor setups

Three reactions were investigated in this project. They include the liquid phase epoxidation of bulky alkenes to epoxide, gas phase methanol to hydrocarbons and the Beckmann rearrangement of cyclohexanone to caprolactam. The detailed description of each of these reactions is given in the specific chapters corresponding to each. In the following section, the experimental setup used for the execution of each reaction is described in detail.

2.11.1 Epoxidation reactor setup

For this liquid phase reaction, a simple set up comprising a single-neck 50ml round bottom flask, a stirrer, a stirrer-heater, oil bath and a reflux condenser was used. The reaction was typically conducted at a temperature of between 40 – 60 ^{O}C for varying durations. Acetonitrile and acetone were used as the solvents in the reaction and the products were analysed on a gas chromatograph following the method and technique describe in section 2.13. Figure 2.15 is a typical reactor setup for this reaction.

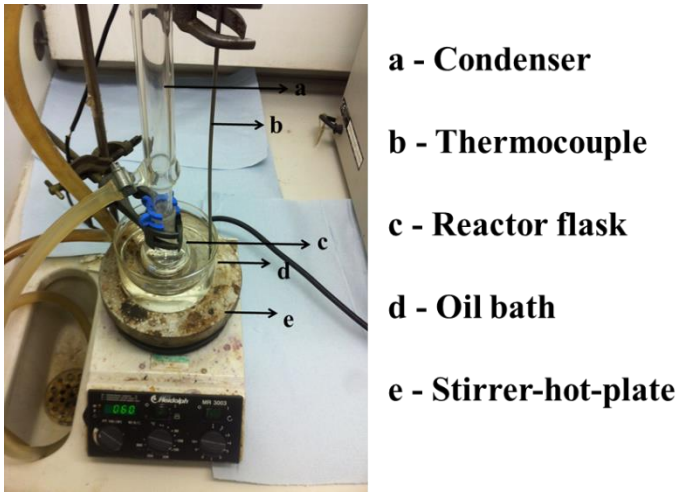

Figure 2.15: Typical reactor set-up for the liquid phase epoxidation reaction

2.11.2 Liquid phase ammoximation of cyclohexanone to caprolactam

This reaction was conducted in a reactor setup consisting of a specially designed double neck 50ml reactor, a reflux condenser, oil bath, magnetic heater stirrer, a septum, syringe and a syringe driver (figure 2.16). The reactor was designed to allow slow injection of the peroxide into the reaction mixture.

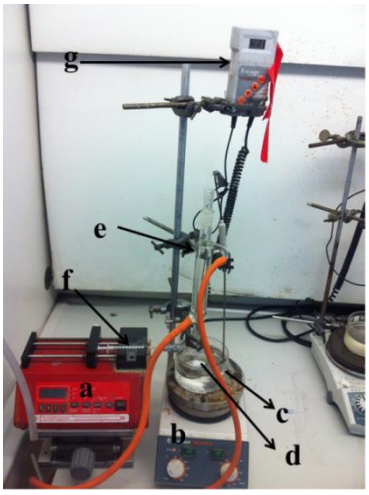

KEY
a- syringe pump
b- hot-plate- stirrer
c- oil bath
d- reactor flask
e- reflux condenser
f- syringe
g- temperature read-out

Figure 2.16: Typical reactor set-up for the liquid phase ammoximation of cyclohexanone

2.12 Gas phase reactor

The gas phase reactions investigated in the project are the methanol to hydrocarbon reaction and the Beckmann rearrangement of cyclohexanone oxime. Typical procedures for both experiments are given in the respective sections. In general, these reactions involve the catalyst being loaded on the reactor bed and activated at a pre-set temperature under inert atmosphere before the reaction.

The reactor set-up includes a Pyrex cylindrical tube approximately 150mm long and 9mm in diameter. The tube is open at both ends to allow input and output of the feed and products. A circular quartz frith infused at the centre of the reactor tube supports

the catalyst and acts as the catalyst bed. The reactor lines consist mainly of stainless steel pipes of ¼" diameter. The feed was fed at a constant rate to the reactor through a lab scale syringe driver, and is directly driven to a three-way valve where it is carried through to the reactor by a nitrogen stream. The product stream was connected to a bubbler which was placed in an ice bath for product collection. Figure 2.17 and 2.18 respectively gives the flow chart and the picture of the gas-phase reactor.

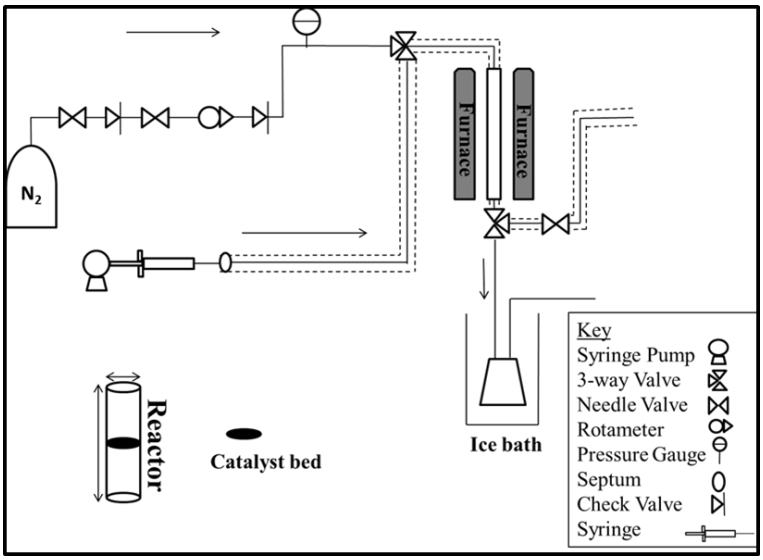

Figure 2.17: Schematic representation of the gas-phase reactor

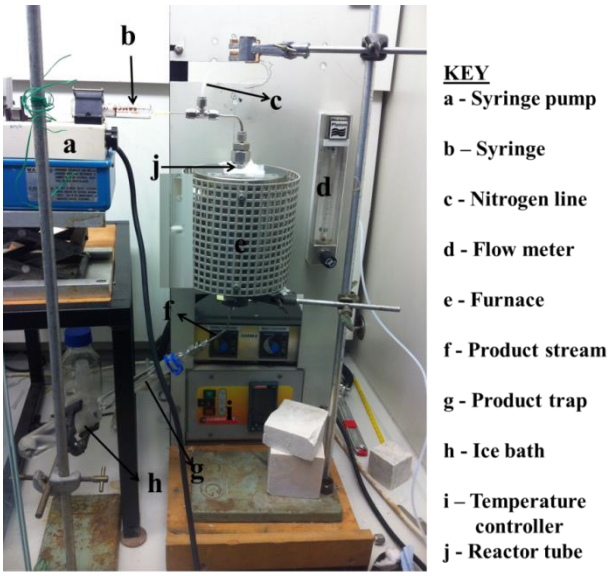

Figure 2.18: Photographic image of the gas phase reactor set-up

2.13 Product analysis by gas chromatography (GC)

Gas chromatography is an analytical technique used in chemistry for the separation and analysis of compounds or mixture of products and reactants. For a mixture or compound to be suitable for analysis by this technique, it must be vaporisable and also stable at the vaporization conditions without decomposing. Compounds which do not conform to these requirements may be analysed by other chromatography techniques, such as liquid chromatography. The GC is generally composed of a column within which the phase separation takes place based on the component boiling point or vapour pressure. The column wall is usually lined with an inert stationary phase(s) which differs from column to column. The column is placed in a heating chamber. A detector connected to the exit of the column analyses the egressing components of the mixture. Ideally, the components of the mixture/compound exit the column at different time over a pre-set temperature program. The time at which a component exits the column is referred to as the retention time of that component. In case of liquid samples, these are introduced into the column by means of a syringe. The injected sample is carried through to the column by a gas stream known as carrier gas, which is always a high purity inert gas, usually helium.

2.14 Product analysis method

In practice, the detector, connected to the column exit analyses the exiting components and produces a peak whose area (A) is proportional to the number of mole (n) of that fraction in the whole mixture. Quantitatively, this can be written as a mathematical relation thus:

$$A \propto n$$

This relationship can be transformed into a mathematical equation by introducing a constant of proportionality:

$$A = Kn \ldots\ldots\ldots\ldots\ldots\ldots\ldots\ldots\ldots\ldots\ldots\ldots (2.2)$$

Given that,

$$n = M * V \ldots\ldots\ldots\ldots\ldots\ldots\ldots\ldots\ldots\ldots\ldots\ldots (2.3)$$

Where *M* is the molar concentration and *V* is the volume of the solution

Equation 2.2 becomes,

$$A = K * M * V \ldots\ldots\ldots\ldots\ldots\ldots\ldots\ldots\ldots\ldots\ldots\ldots (2.4)$$

For two components (1 and 2) in the same mixture we have,

$$A_1 = K_1 * M_1 * V_1 \ldots\ldots\ldots\ldots\ldots\ldots\ldots\ldots\ldots\ldots\ldots\ldots (2.5)$$

$$A_2 = K_2 * M_2 * V_2 \ldots\ldots\ldots\ldots\ldots\ldots\ldots\ldots\ldots\ldots\ldots\ldots (2.6)$$

Dividing both equations 2.5 and 2.6, with the realization that V_1=V_2 (as both components are in the same solution) results in,

$$\frac{K_1}{K_2} = \frac{A_1 * M_2}{A_2 * M_1} = F \ldots\ldots\ldots\ldots\ldots\ldots\ldots\ldots\ldots\ldots\ldots\ldots (2.7)$$

Where the ratio of the two constants is referred to as the response factor, F

In a mixture where we know the concentration of one of the components, the concentration of the other components can be obtained by rearranging equation 2.7 into the form

$$y = mx + c \quad \text{.....(2.8)}$$

$$where\ y = \frac{M_2}{M_1}, m = \frac{K_1}{K_2} and\ x = \frac{A_2}{A_1}$$

From equation 2.7, it is clear that the equation is that of a straight line with the intercept at the origin and the slope is the ratio of the two constants - the response factor.

2.15 Calibration

From equation 2.8, the slope resulting from the straight line will give the response factor between the two components. For calibration purposes, standard solutions of the reacting components, and of the expected products, from each reaction investigated in this study were prepared. An inert component which will not take part in the reactions was introduced at a known concentration and acts as the internal standard. The response factors of all other components relative to this standard were then obtained.

For this reaction, mesitylene was used as the reference (internal standard) to which other components were normalized. Standard solutions of the reactants involved in these reactions were prepared and the calibration lines presented in the Appendix. By re-writing the straight line equation 2.8, a formula can be derived from which the concentration of each component emerging from the GC can be derived.

$$M_2 = \left(m * \frac{A_2}{A_1}\right) * M_1 \ldots\ldots\ldots\ldots\ldots\ldots\ldots\ldots\ldots (2.9)$$

Where M_2 is the new component, m is the slope determined from the calibration curve, A_1 and A_2 are the GC peak areas of components 1 and 2 and M_1 is the known concentration of the internal standard. Following the same procedure, the calibration lines for the other reactions were also obtained.

The formulae derived from the calibration lines for each component in all the reactions investigated in this work are given in table 2.1 to table 2.4

Table 2.1: Formulae obtained from calibration curves of the components of the cyclohexene epoxidation reaction

Components	Formulae
Cyclohexene	$M_{CH} = 1.61 * \frac{A_{CH}}{A_m} * 0.31$
Cyclohexene oxide	$M_{CHO} = 1.75 * \frac{A_{CHO}}{A_m} * 0.31$
2-cyclohexen-1-one	$M_{CO} = 2.08 * \frac{A_{CO}}{A_m} * 0.31$
1,2-Cyclohexane diol	$M_{CD} = 3.32 * \frac{A_{CD}}{A_m} * 0.31$

Table 2.2: Formulae obtained from calibration curves of the components of the styrene epoxidation reaction

Components	Formulae
Styrene	$M_{St} = 1.17 * \frac{A_{st}}{A_m} * 0.24$
Styrene oxide	$M_{Sto} = 2.12 * \frac{A_{Sto}}{A_m} * 0.24$
Benzaldehyde	$M_{BH} = 1.52 * \frac{A_{BH}}{A_m} * 0.24$
Phenyl acetaldehyde	$M_{Ph} = 1.13 * \frac{A_{Ph}}{A_m} * 0.24$

Table 2.3: Formulae obtained from calibration curves of the components of the methanol to hydrocarbon reactions

Components	Formulae
M+P- Xylene	$\mathbf{M_{m+p-xylene} = 0.41 * \frac{A_{m+p-xylene}}{A_{cyclohexene}} * 0.2}$
O-Xylene	$\mathbf{M_{O-xylene} = 0.96 * \frac{A_{o-xylene}}{A_{cyclohexene}} * 0.2}$
P-Ethyltoluene	$\mathbf{M_{p-ethyltoluene} = 0.74 * \frac{A_{p-ethyltoluene}}{A_{cyclohexene}} * 0.2}$
m-Ethyltoluene	$\mathbf{M_{m-ethyltoluene} = 0.58 * \frac{A_{m-ethyltoluene}}{A_{cyclohexene}} * 0.2}$
m- Diethylbenzene	$\mathbf{M_{m-Diethylbenzene} = 0.51 * \frac{A_{m-Diethylbenzene}}{A_{cyclohexene}} * 0.2}$
p-Diethylbenzene	$\mathbf{M_{p-Diethylbenzene} = 0.54 * \frac{A_{p-Diethylbenzene}}{A_{cyclohexene}} * 0.2}$
1,2,4-Trimethylbenzene	$\mathbf{M_{1,2,4-trimethylbenzene} = 0.82 * \frac{A_{1,2,4-trmethylbenzene}}{A_{cyclohexene}} * 0.2}$
Durene	$\mathbf{M_{Durene} = 0.62 * \frac{A_{Durene}}{A_{cyclohexene}} * 0.2}$

Table 2.4: Formulae obtained from calibration curves of the components of the Beckmann rearrangement of cyclohexanone oxime to caprolactam

Components	Formulae
Cyclohexanone	$\mathbf{M_{Cycohexanone} = 1.92 * \frac{A_{cyclohexanonee}}{A_{mesitylene}} * 0.72}$
Cyclohexanone oxime	$\mathbf{M_{Cyclohexanone\ Oxime} = 1.75 * \frac{A_{Cyclohexanone\ oxime}}{A_{mesitylene}} * 0.72}$
Caprolactam	$\mathbf{M_{Caprolactame} = 1.99 * \frac{A_{Caprolactam}}{A_{mesitylene}} * 0.72}$
2-cyclohexen-1-one	$\mathbf{M_{2-cyclohexen-1-one} = 1.97 * \frac{A_{2-cyclohexen-1-one}}{A_{mesitylene}} * 0.72}$
Hexanitrile	$\mathbf{M_{Hexanitrile} = 1.74 * \frac{A_{Hexanitrile}}{A_{mesitylene}} * 0.72}$
Aniline	$\mathbf{M_{Aniline} = 1.66 * \frac{A_{Aniline}}{A_{mesitylene}} * 0.72}$

Reference

1. S. Kulprathipanja, *Zeolites in industrial separation and catalysis*, Wiley interscience, **2010**.

2. W. Xu, J. Dong, J. Li, J. Li, F. Wu, *Journal of the Chemical Society, Chemical Communications*, **1990**, 755-756

3. J. Weitkamp, L. Puppe, *Catalysis and zeolites : Fundamentals and applications*, Springer, **1999**.

4. S. Bhatia, *Zeolite catalysis : Principles and applications*, CRC Press, **1990**.

5. D. Masih, T. Kobayashi, T. Baba, *Chemical Communications*, **2007**, 3303-3305

6. C.N. Satterfield, *Heterogeneous catalysis in industrial practice*, Second edition, McGraw-Hill, **1991**

7. J. Cejka, A. Corma, S. Zones, *Zeolites and catalysis : Synthesis, reactions and applications*, Vol. 1, Wiley interscience, **2010**.

8. W. Xu, J. Dong, J. Li, J. Li, F. Wu; *J.chem. soc. Chem. Commun*, **1990,** *10*, 755-756

9. M. Thommes, K. Kaneko, A.V. Neimark, J.P. Olivier, F. Rodriguez-Reinoso, J. Rouquerol, K.S.W. Sing, *Pure and Applied Chemistry*, **2015**, *87*, 1051-1069

10. A.W. Chester, E.G. Derouane, *Zeolite characterization and catalysis*, Springer, **2009**.

11. P. Matias, C. Sá Couto, I. Graça, J.M. Lopes, A.P. Carvalho, R.F. Ramôa, M. Guisnet, *Applied Catalysis A: General*, **2011**, *399*, 100-109

12. I.Y. Chan, P.A. Labun, M. Pan, S.I. Zones, *Microporous Materials*, **1995**, *3*, 409-418

13. O. Terasaki, T. Ohsuna, *Catalysis Today*, **1995**, *23*, 201-218

14. M. Ogura, S. Shinomiya, J. Tateno, Y. Nara, E. Kikuchi, M. Matsukata, *Chemistry Letters*, **2000**, *29*, 882-883

15. C. Li, G. Xiong, Q. Xin, J. Liu, P. Ying, Z. Feng, J. Li, W. Yang, Y. Wang, G. Wang, X. Liu, M. Lin, X. Wang, E. Min, *Angewandte Chemie International Edition*, **1999**, *38*, 2220-2222

16. P.C. Stair, C. Li, *J.Vac.Sci.Technol. A*, **1997**, *15*, 1679-1684

17. C. Li, P.C. Stair, *An advance in raman studies of catalysts: Ultraviolet resonance raman spectroscopy*, in *Studies in surface science and catalysis*, Elsevier, **1996**, pp. 881-890.

18. Q. Guo, K. Sun, Z. Feng, G. Li, M. Guo, F. Fan, C. Li, *Chemistry - A European Journal*, **2012**, *18*, 13854-13860

19. S. Bordiga, A. Damin, F. Bonino, G. Ricchiardi, A. Zecchina, R. Tagliapietra, C. Lamberti, *Physical Chemistry Chemical Physics*, **2003**, *5*, 4390-4393

20. F.Z. Zhang, X.W. Guo, X.S. Wang, G. Li, J.C. Zhou, J.Q. Yu, C. Li, *Catalysis Letters*, **2001**, *72*, 235-239

21. N. Matthew, *Consortium for Advanced radiation sources, University of Chicago, Chicago, Il*, **2004**,

22. G. Sankar, J.M. Thomas, C.R.A. Catlow, C.M. Barker, D. Gleeson, N. Kaltsoyannis, *The Journal of Physical Chemistry B*, **2001**, *105*, 9028-9030

23. Http://Qub.Ac.Uk/Schools/Schoolofchemistryandchemicalengineering/Filestore/Internalforms/Asepanalyticalservicesandenvironmentalprojects/Tga/Filetoupload, 404697, En.Pdf,

Chapter 3: Effect of structure and hierarchical pores on the catalytic properties of TS-1

Chapter overview

In this chapter, the possible use of chitosan as a macrotemplating agent for the synthesis of hierarchical zeolitic materials was investigated. The study was carried out on a titanosilicate zeolite with the MFI framework topology. The amount of chitosan in the synthesis medium was varied and the impact on the properties of the zeolites was monitored. During the synthesis steps, two different methods were employed which were observed to be important to achieving the insertion of titanium into the silicate structure. The catalysts developed here were evaluated for liquid phase epoxidation of cyclohexene and styrene; their activities and selectivity were correlated with the amount of chitosan included in the synthesis, as well as the method employed during the synthesis step.

3.1 Introduction

As discussed in chapter one, zeolites are highly desired catalysts for the production of many important raw materials as they offer high product selectivity, regenerability and environmentally benign reaction routes. In the petrochemical and fine chemicals industry, oxygenated starting materials are of particular importance. The discovery of titano-silicate molecular sieves opened up a new chapter in the selective oxidation of several substrates. The titano-silicate molecular sieve, TS-1, with the MFI framework topology is of high importance for the selective synthesis of these oxygenates under mild conditions using aqueous hydrogen peroxide as an oxidant. However, owing to the intrinsic pore geometry of TS-1, there is a considerable limit to the range of substrates which can be processed over the material [1]. Attempts to process substrates of kinetic diameters larger than the pore width of TS-1 could result in pore blocking, which ultimately leads to deactivation of the catalyst. Another problem which could be encountered from such an attempt is diffusion limitation that culminates in secondary reactions, yeilding secondary and often undesired products.

Due to the importance and desire for further applications of TS-1, there have been increased efforts to find ways around these limitations. In an attempt to reduce the diffusional path of substrates through the pore of this catalyst, the synthesis of nano-sized TS-1 has been attempted. Although much success has been reported in this field, interest in this direction has since cooled as the separation of the synthesized material from solution is often problematic.

The use of titanium based mesoporous molecular sieves[1-5], such as SBA, MCM, Beta and KIT, has also been attempted and widely studied. As a result of the

increased pore size of these materials, they are able to process a promising range of large substrates. Disappointingly, however, this class of materials have shown very poor catalytic activity when H_2O_2 is used as the oxidizing agent due to the production of unwanted oxidation products, which implies the organic oxidant TBHP must be used as the oxidant, which is less environmentally benign.

The limitations of nano-sized TS-1 and of the titanium based large pore zeolites have led to the need for a hybrid material made from the original parent TS-1. This latter approach will ensure the MFI topology is still maintained but, in addition to the micropores inherent in it, creation of meso- or macro pores will be induced [6-9], i.e. a hierarchical-pore molecular sieve, as described in chapter one.

As noted in chapter one, there has been an intense effort to optimise the synthesis routes to produce zeolites with a hierarchy of pores. Zhou *et al* [10] have successfully synthesized TS-1 with hierarchical pores using the steam assisted synthesis method. The zeolite obtained through this method boasts of prolonged catalytic life time in a reaction involving trimethylphenol. In addition, the authors attributed the catalyst stability to the additional tetraethanolamine used in the synthesis, which acts as a rigid guide against the collapse of the created mesoporous wall.

Using a specially prepared bifunctional surfactant as the structural directing agent, a multi-layered TS-1 consisting of TS-1 sheets of about 2 nm has been synthesized[11]. The resulting catalyst, with an intra crystal mesopore diameter of about 3 nm, displayed improved catalytic performance in the oxidation of both linear and cyclic alkenes. The TS-1, however, showed retarded activity (selectivity and conversion) when applied in the presence of hydrogen peroxide. Chemical treatment for selective desilication has also been studied and reported [12]. Hydroxides of

sodium, potassium, lithium, caesium and even organic tetrapropyl ammonium hydroxide have all been found to be capable of inducing mesoporosity in TS-1, with caesium having an excessive desilication effect and leading to some framework collapse [12].

Other methods of generating mesoporosity in TS-1 include the use of additional inert templating materials which can be easily removed by post synthesis thermal treatment in air/oxygen or via chemical treatment. Direct sucrose templating of TS-1 gel was explored and resulted in a TS-1 zeolite with induced mesoporosity, which showed better performance in the removal of thiophene and benzothiophene sulphur compounds [7]. As discussed in chapter one, commonly used carbon based materials, are carbon black [13, 14], carbon nanotubes (CNT) and carbon nanofibres (CNF)[15-18]. The use of these inert materials as a templating agent offers better control on the size and connectivity of the mesopore that can be generated, which can be achieved by choosing the size of the inert template. However, due to the toxic nature of carbon black [19], and the high cost of CNT and CNF, alternative materials which are less toxic and more cost effective are highly desired.

For this reason, we focus on the use of chitosan, which as discussed in chapter one, has been widely used in catalysis. Although, previous studies have focused on the preparation of chitosan-zeolite composites[20, 21], in this chapter the focus is on the direct use of chitosan as a secondary macro-template in the one-pot synthesis of hierarchical TS-1 zeolite.

3.2 Experimental

This section describes the detailed synthesis techniques adopted in the preparation of the hierarchical TS-1 in this work, followed by the detailed characterization of the samples as well as the catalytic evaluation of the catalyst.

3.2.1 Materials

All chemicals utilized in this study were sourced commercially. Tetraethyl orthosilicate (TEOS, research grade, 98%) and tetraethyl orthotitanate (TEOT, technical grade) used respectively as the silica and titanium sources, respectively, were obtained from Sigma-Aldrich. Tetrapropyl ammonium hydroxide (TPAOH, 25wt% in H_2O) purchased from Acros Organics was used as the structure directing agent. Chitosan (ground coarse and fine powder) was used as the inert templating agent and was obtained from Sigma-Aldrich. All chemicals were used as received without further purification or modification

3.2.2 Synthesis technique

Two approaches were used for the synthesis of the hierarchical TS-1. The first is designated as the fully dried method (FD) while the second, a modified version of the FD method, is denoted as the partially dried method (PD).

3.2.2.1 The fully dried route

The preparation of the initial gel followed that of the original patent [22] with slight modifications. In a typical synthesis gel, 0.5 g TEOT was slowly added to 22.85g of TEOS, under vigorous stirring at room temperature, over an hour to form a silica-titania solution. To this solution, 4.45 g of TPAOH (25 wt% in H_2O) was

added dropwise over a period of 15-20 minutes, with stirring, to obtain the zeolite precursor. Stirring of the precursor was maintained for another hour, after which the Teflon beaker containing the resulting solution was suspended in an oil bath placed on a hotplate-stirrer and maintained at 45 ^{O}C for 2 hours. After this, a measured amount of chitosan was added to the synthesis gel and the beaker uncapped, while keeping the oil bath at 45 ^{O}C for another 3 hours to evaporate the liberated alcohol. Subsequently the temperature was increased to 80 ^{O}C to drive off all the liquids completely. The beaker was kept in the heating bath until a dry powder was obtained.

In the crystallization step, the dry powder obtained was crushed into a fine powder and mixed thoroughly with 10.6 g of TPAOH (25 wt% in H_2O). The amorphous powder mixed with the organic template was directly placed in the Teflon lined autoclave with no additional water. Crystallization was conducted under static conditions in an oven maintained at 170 ^{O}C for 2 days. This procedure is illustrated in scheme 3-1.

Upon completion of the crystallization, the solid material was dispersed in deionized water and separated by centrifugation. This procedure was repeated until the pH of the solution was below 7.5, and followed by drying at 110 ^{O}C overnight. The samples were subsequently calcined at 650 ^{O}C over 12 hours.

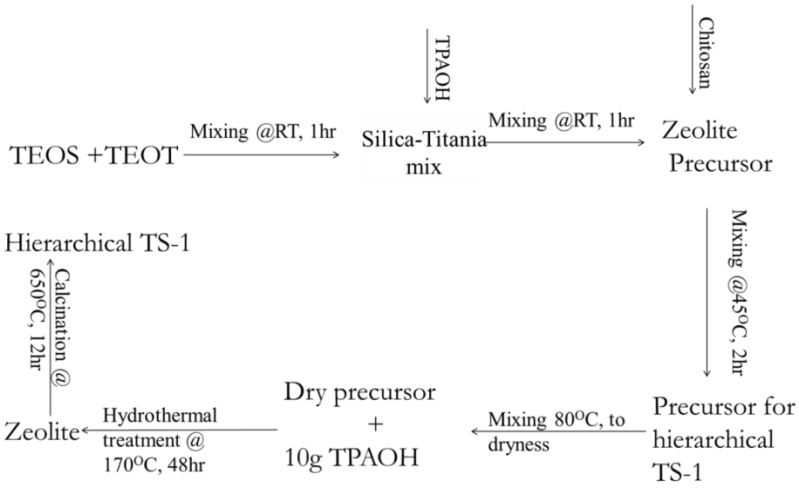

Scheme 3-1: Illustration of the fully dried synthesis technique

3.2.2.2 Partially dried route

This method was derived to improve on some properties of the resulting material from the FD method. In this technique, the procedure was maintained as for the FD method except that, rather than completely drying the zeolite precursor, it was only subjected to partial drying. The rest of the procedure, including the crystallization steps and the post synthesis treatment, was maintained as in the FD method.

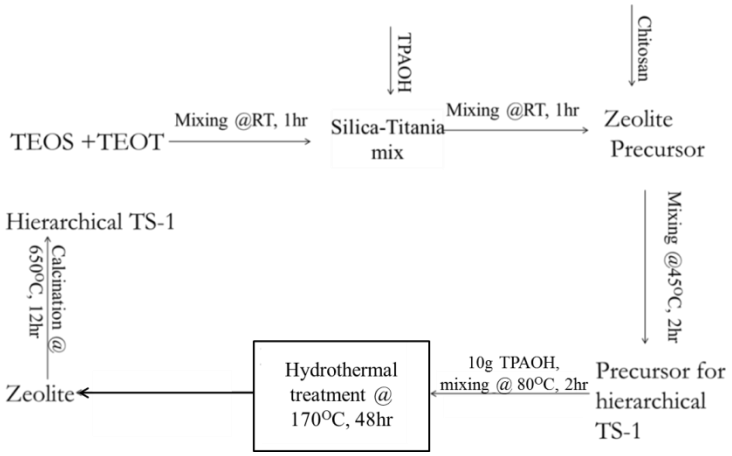

Scheme 3-2: Illustration of the partially dried synthesis technique

3.2.3 Characterization

The phase, purity and the degree of crystallinity of the synthesized materials were evaluated via the powder XRD technique. Diffraction data were recorded in the

range 5-50^{O} 2θ angle on a Bruker D4 X-ray diffractometer using Cu-Kα radiation, with a nickel filter, operated at 40KV and 50mA.

The coordination state of the titanium atoms in the TS-1 framework was elucidated by four different techniques, including the use of Raman and FTIR spectroscopies, UV-Vis and X-ray absorption spectroscopy. Morphological characteristics of the samples, including the particle shape and size were observed via scanning electron microscopy.

The details and sample preparation steps for each of these techniques are as described in chapter two.

3.2.4 Catalytic evaluation

3.2.4.1 Cyclohexene epoxidation

Catalytic epoxidation of cyclohexene was carried out in a 50 ml reactor as described in chapter two. In a typical reaction set up, 6 mmol of cyclohexene (analytical standard, Sigma Aldrich), 6 mmol of H_2O_2 (30 wt% in H_2O), 10 mL acetonitrile as the solvent and 0.5 mL mesitylene, used as the internal standard, were charged into the reactor. The reaction mixture was thoroughly stirred at room temperature before 100 mg of the catalyst was added. The set-up was then suspended in an oil bath, maintained at specified temperatures ranging from 313 K to 333 K, and the reaction carried out for a fixed time at 400rpm magnetic stirring.

Upon completion of the reaction, the reactor was allowed to cool overnight after which the solid catalyst was separated by centrifugation. Analysis was carried out on a gas chromatograph (Perkin Elmer Clarus 500 GC) equipped with a flame ionization detector (FID) with an Elite 1 (30 m*0.32 mm*3 μm) capillary column. Product analysis was done following the procedure detailed in chapter two.

3.2.4.2 Styrene epoxidation

Styrene epoxidation reaction was conducted using the same reactor set-up as in the cyclohexene epoxidation. The reaction mixture consisted of 6 mmol of styrene (analytical standard, Fluka), 6 mmol of H_2O_2 (30 wt% in H_2O), 10 mL solvent (acetonitrile or acetone), 0.5 mL mesitylene and 100 mg of the catalyst. The remainder of the steps were as described above in the cyclohexene epoxidation.

3.3 Results and discussions

3.3.1 Phase and phase purity by PXRD

The powder X-ray diffraction patterns of all the samples synthesized with chitosan in their precursors were compared to that of a standard TS-1 sample synthesized without chitosan in the precursor (See Fig.3.1). The diffraction patterns of all the samples synthesised with chitosan agree well with that of the standard sample. Notably, no extra peak was detected - clearly showing that the presence of chitosan in the synthesis gels did not inhibit the formation of the MFI framework based TS-1. Furthermore, all diffraction patterns agree well with the simulated MFI powder diffraction pattern. Therefore, it can be safely inferred that no extra phase formation was induced as a result of chitosan in the synthesis medium.

3.3.2 Morphological characterization using SEM

Scanning electron micrographs of all the synthesized samples displayed well-formed cubic shaped particles of relatively uniform size. These micrographs, presented in figure 3.2, show various degrees of surface roughness for the chitosan templated

systems. This surface roughness can be taken as an indication of extra porosity in the zeolite samples, as previously reported by several authors [17, 23-27].

The particle size distributions, estimated by taking an average of 50 measured particles from the SEM micrographs show a reduction in the crystallite size from approximately 250 nm for the standard samples (TS-1 with 0% chitosan) to 150 nm for the samples synthesized with 10% chitosan content. This observation can be attributed to the principle of "confined space growth" which has been reported with carbon templated growth of ZSM-5 [28, 29]. "Confined space growth", it will be recalled is the principle whereby zeolite crystal growth is restricted to the void of the inert templating material.

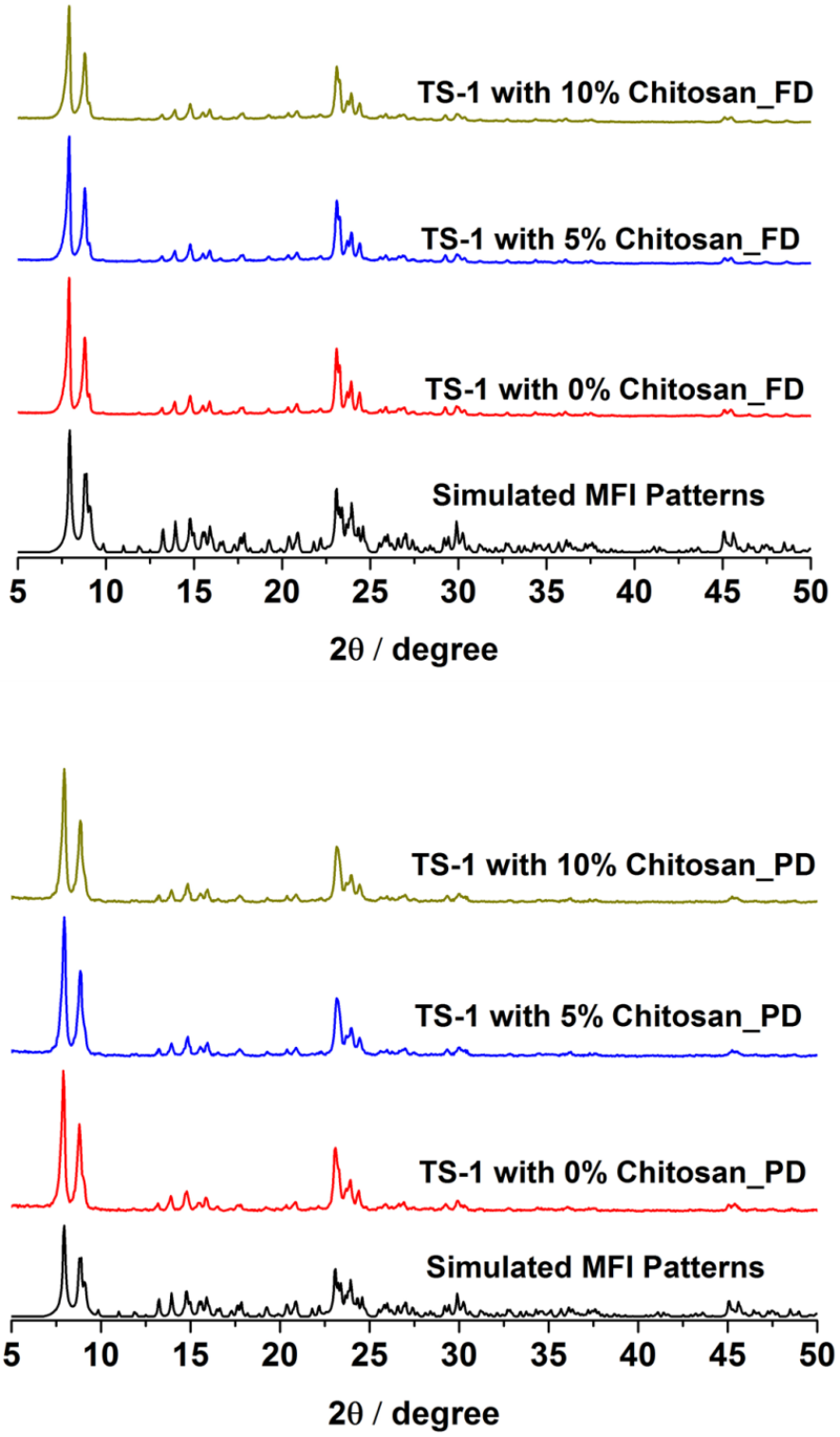

Figure 3.1: XRD patterns of TS-1 zeolites synthesized through the PD and FD methods

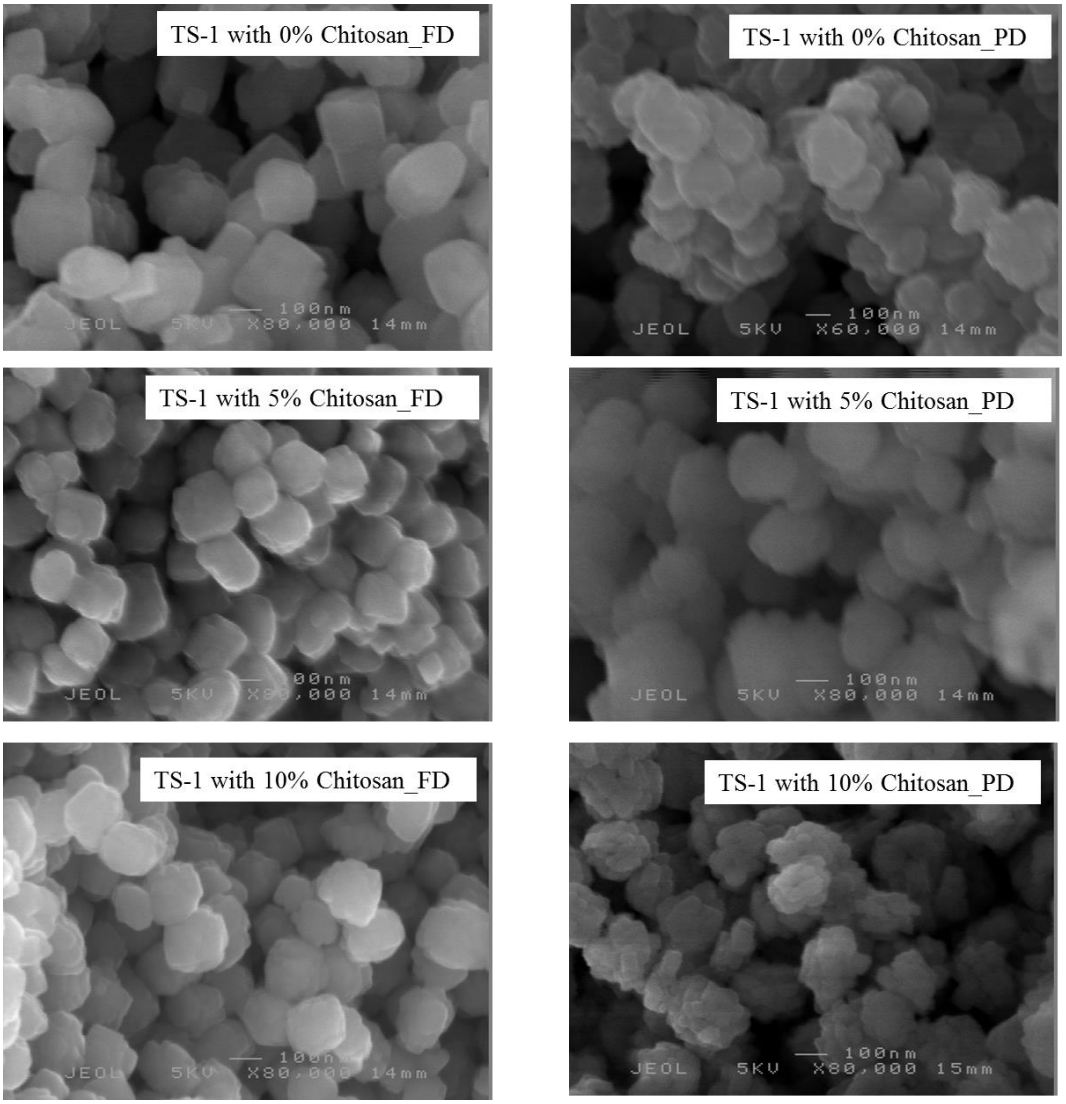

Figure 3.2: SEM micrographs showing the morphology of all samples

3.3.3 FTIR, Raman and UV-Vis investigation of the coordination state of titanium

FTIR spectroscopy is widely used to characterize titanosilicate materials including TS-1. It is typically done by comparing the spectra of the titanosilicate material with that of pure silicalite and recording the difference in the spectra of both materials. The observed vibration band at ca 960 cm^{-1}, which was absent in the silicalite analogue, is attributed to the framework titanium in the TS-1 [22]. The intensity of

this band is also observed to change with respect to the titanium content of the sample [22].

The FTIR spectra of samples synthesized in this work and presented in figure 3.3 show strong vibration bands at ca 960 cm^{-1}, indicative of the tetrahedral titanium species in the TS-1 framework. This conclusion was strengthened by the absence of such a peak in the silicalite samples, as can be seen in figure 3.3.

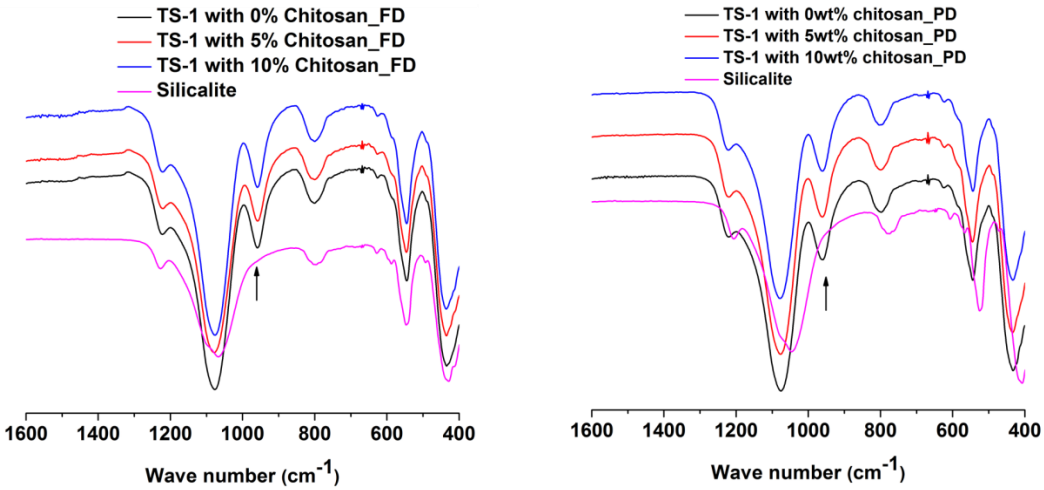

Figure 3.3: FTIR spectra of synthesized samples. The arrow shows the position of the framework titanium vibration

Raman spectroscopy is also widely used to investigate the coordination state of titanium in zeolites, and the presence of Raman peaks at 960 cm^{-1} and 1125 cm^{-1} is generally accepted as an indication of the presence of tetrahedrally coordinated titanium species [30-33]. As shown in figure 3.4, all samples - with and without chitosan in the synthesis gel - clearly show strong peaks at both 960 cm^{-1} and 1125 cm^{-1}. The presence of these peaks demonstrates that chitosan does not prevent the incorporation of titanium in the zeolite framework, and does not prevent their incorporation in the tetrahedral state.

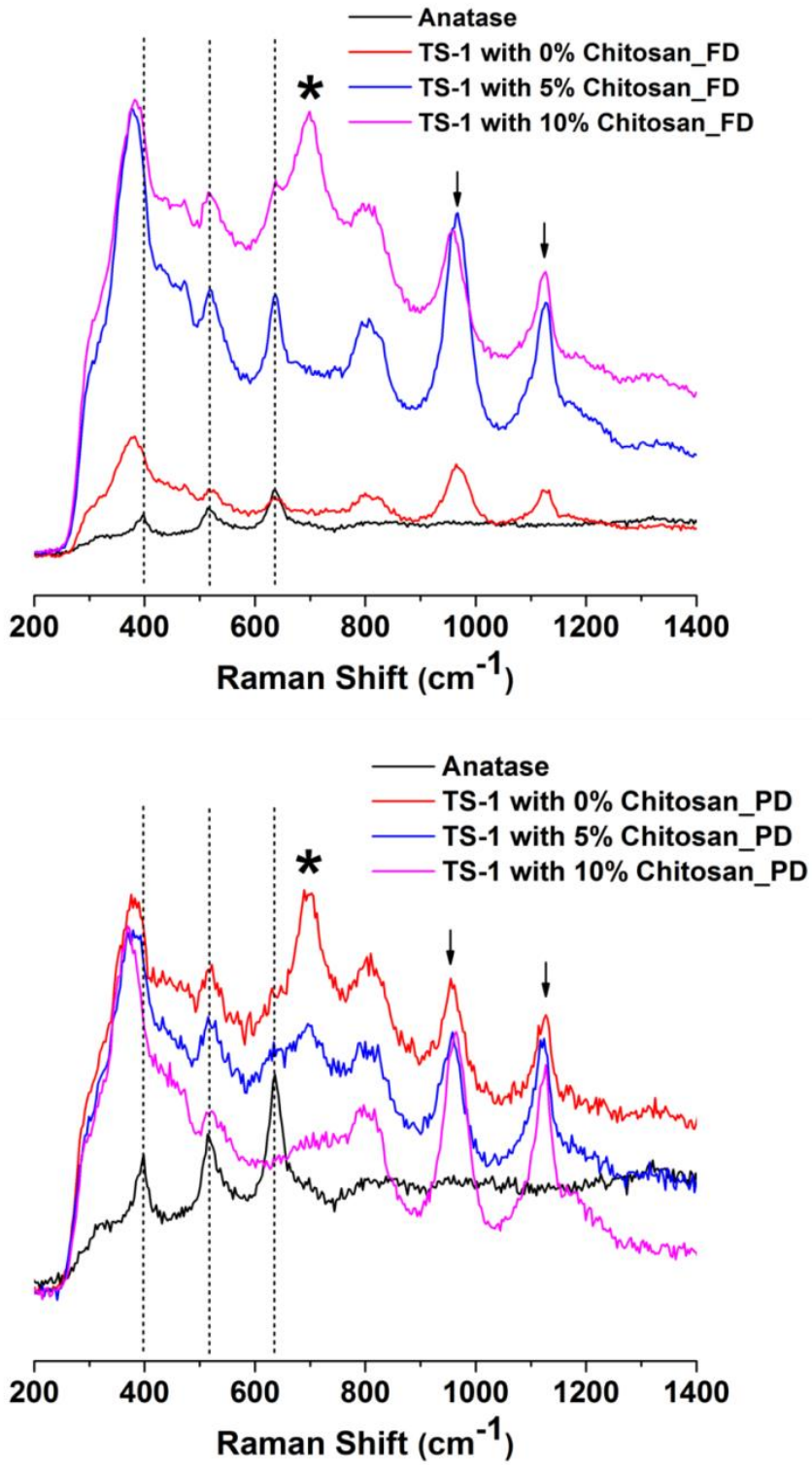

Figure 3.4: Raman spectra of all synthesized samples showing the tetrahedrally coordinated titanium vibration bands at 960 cm^{-1} and 1125 cm^{-1} (arrowed) and octahedrally coordinated titanium (broken lines)

Further evidence on the coordination state of the incorporated titanium was sought by subjecting the samples to UV-Vis spectroscopic analysis. Figure 3.5 shows the spectra of all samples compared to that of anatase, with known octahedral coordination. The main peak appears at about 215 nm for the standard samples - assigned to tetrahedral titanium - as well as that synthesised with 5% chitosan concentration, while that with 10% chitosan has this peak appearing further down at about 230 nm, which is close to the first observed peak of anatase at 240 nm. This observation is an indication of the presence of some extra framework titanium species, probably a dense phase titanium oxide which may not be anatase or rutile due to the absence of the 325 nm peak which is the major band for these phases, as in figure 3.5.

This observation was the main reason for the modification of the synthesis methodology, which resulted in the desired impact of incorporating more of the titanium in the framework and the elimination of the presence of the extra phase of titanium oxide. Upon the synthesis process modification, as in the PD series, only the 215 nm peak is now observable for all the samples.

This observation suggests that the extra framework titanium results from the synthesis methodology rather than due to the presence of chitosan in the precursor. Another possible source of this extra framework titanium could be from the calcination step. At high calcination temperature and high chitosan content there is the possibility of having a localized isothermal environment. This higher heat environment may result in the ejection of the titanium atom from the framework positions.

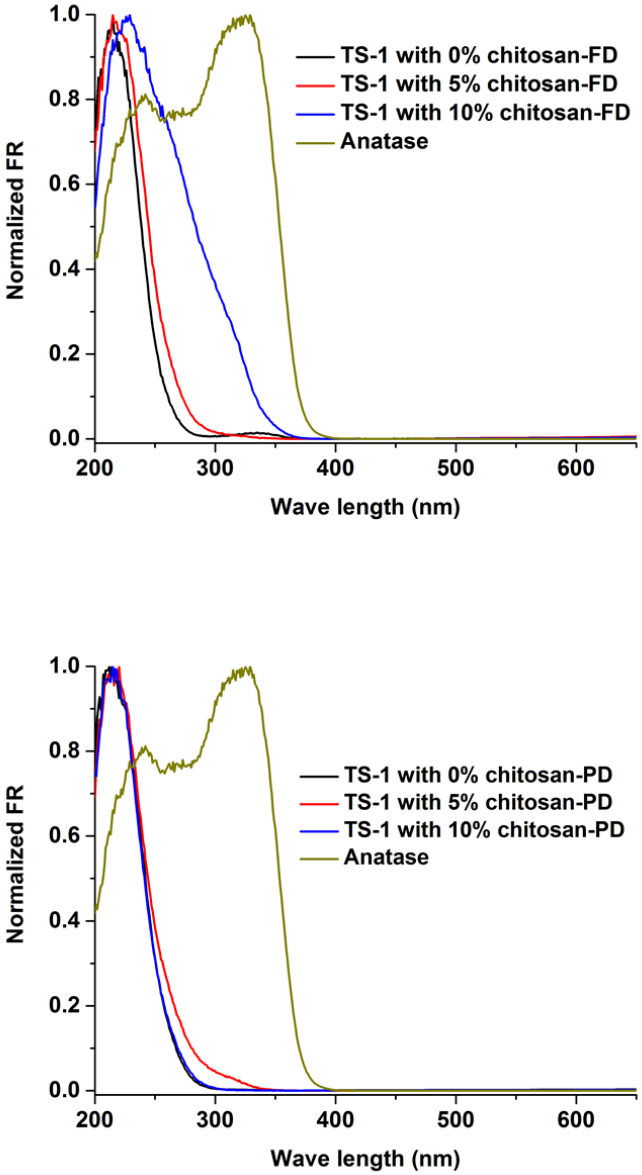

Figure 3.5: UV-Vis spectra of samples synthesized through FD and PD routes

3.3.4 X-ray absorption spectroscopy measurement

Further investigation of the electronic structure of titanium in the framework of the synthesized samples was carried out using high resolution X-ray absorption spectroscopy at the Ti K-edge. The spectra of these samples were compared to two reference samples of known coordination environments - ETS-10 with octahedral coordination, and $Ti(OSiPh_3)_4$, with perfect tetrahedral coordination [34].

From the spectra in figure 3.6, it can be seen that the synthesized samples have the pre-edge feature similar to that of the tetrahedral reference material. In addition, the energy position of the pre-edge peak of these samples is comparable to that of the tetrahedrally coordinated reference sample, which is at a lower energy position compared to that of ETS-10. These observations imply that the titanium in these samples is present in a lower coordination state than ETS-10. The intensity of the pre-edge peak is a further evidence to conclude that the samples exist in tetrahedral form. It has been reported that the pre-edge intensity is an inverse function of the coordination state of the metal.

It is, however, important to point out the slight decrease in the pre-edge intensity of the samples as the chitosan content was increased, particularly, for the FD series. This observation can be rationalised as a consequence of two possibilities, the first of which could be the presence of extra framework titanium species and, secondly, it could be as a result of the coordination of framework titanium with water molecules, leading to a distorted tetrahedral structure. The first possibility has been proved to be partially true by the result of the UV-Vis spectroscopy described earlier. However, in order to elucidate the second possibility further, *in situ* XAS studies were carried out using the procedure described in chapter two.

Here, the samples were dehydrated in an inert atmosphere, and data collected before and after dehydration. Figures 3.7 and 3.8 show the spectra of the *in situ* experiments. As expected, the pre-edge intensity increased upon dehydration, confirming the presence of a water coordinated titanium environment. However, for this proposal to be valid, the pre-edge intensity would be expected to remain at the same level upon cooling, as long as the sample atmosphere remains dry. The observation in these samples was, however, different from such expectations. The

pre-edge intensity was observed to reduce back to the initial state after cooling to room temperature. This observation implies that, although water coordination with the titanium environment might be contributing to the noticed reduction in the pre-edge intensity, this cannot be the absolute reason.

A combination of the observations from the UV-Vis, Raman spectroscopy and the XAS analysis reveals that synthesis through the FD method yield TS-1 zeolites with some degree of anatase and dense phase titanium species, probably nano-phase titanium oxide. The formation of anatase and dense phase titanium oxide appears to have been minimized by using the PD technique. In addition to the previously enumerated techniques above, further evidence of this can be seen in the difference in the pre-edge intensity of both series, figure 3.9. In the FD series, there is a significantly larger difference between the intensity of the untemplated sample and that of the chitosan templated one, whereas for the PD series this difference is only marginal.

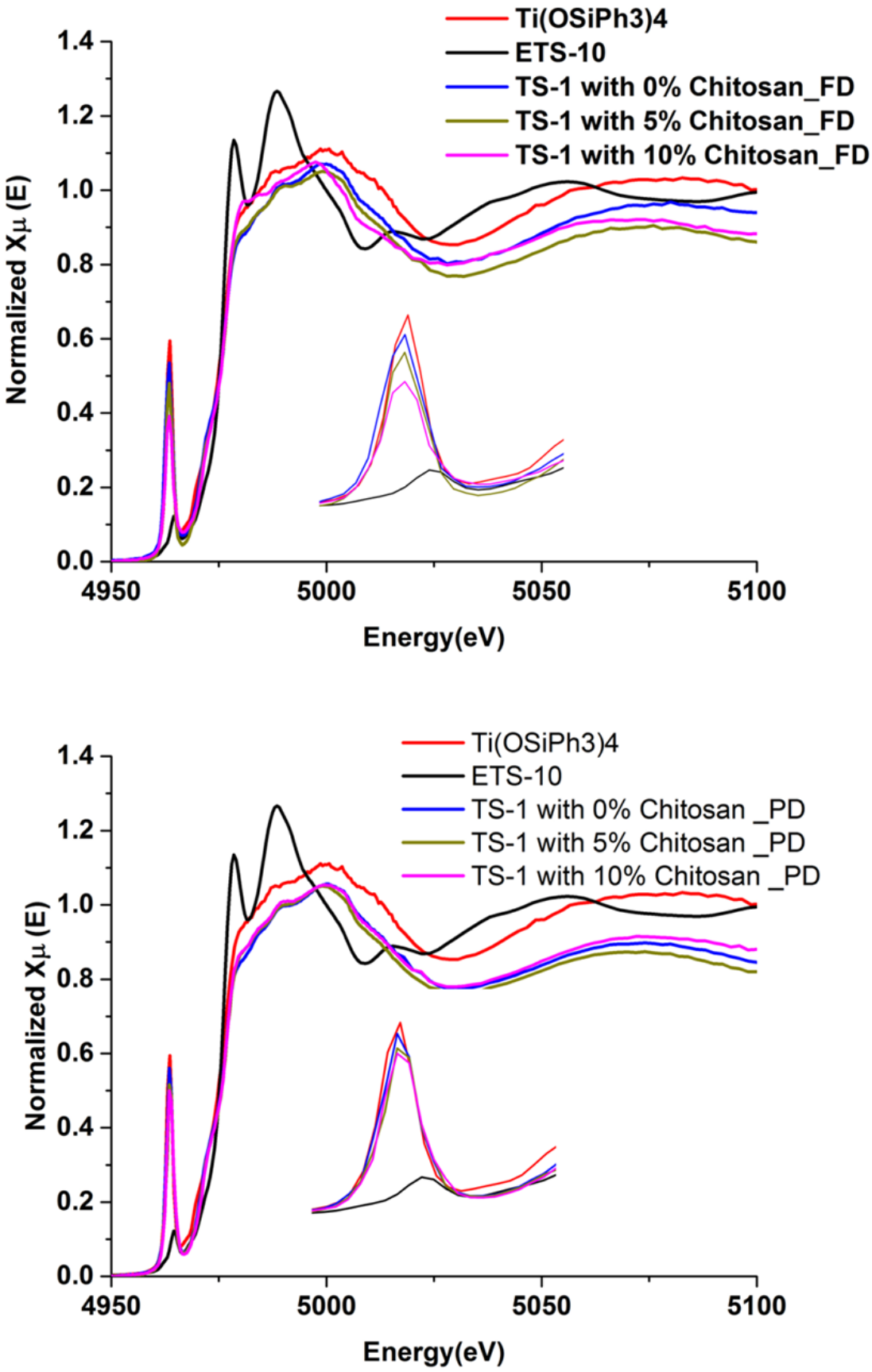

Figure 3.6: Titanium K-edge XANES of all the synthesized samples showing pre-edge peak that allows the determination of the coordination state of titanium in the zeolite framework. Inset is the expanded pre-edge region for clearity.

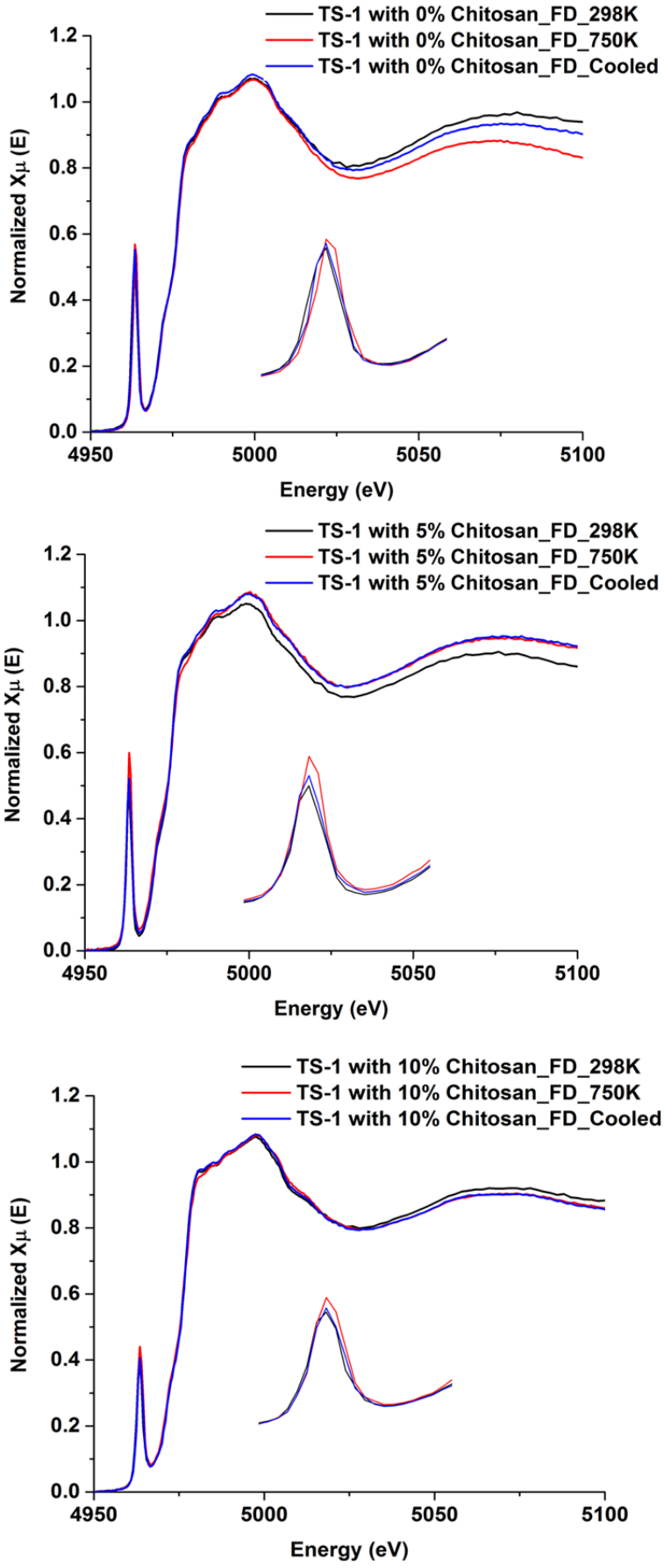

Figure 3.7: ***In situ*** **XANES of samples synthesized through the FD method showing the response of pre-edge intensity to temperature. Inset is the expanded pre-edge intensity**

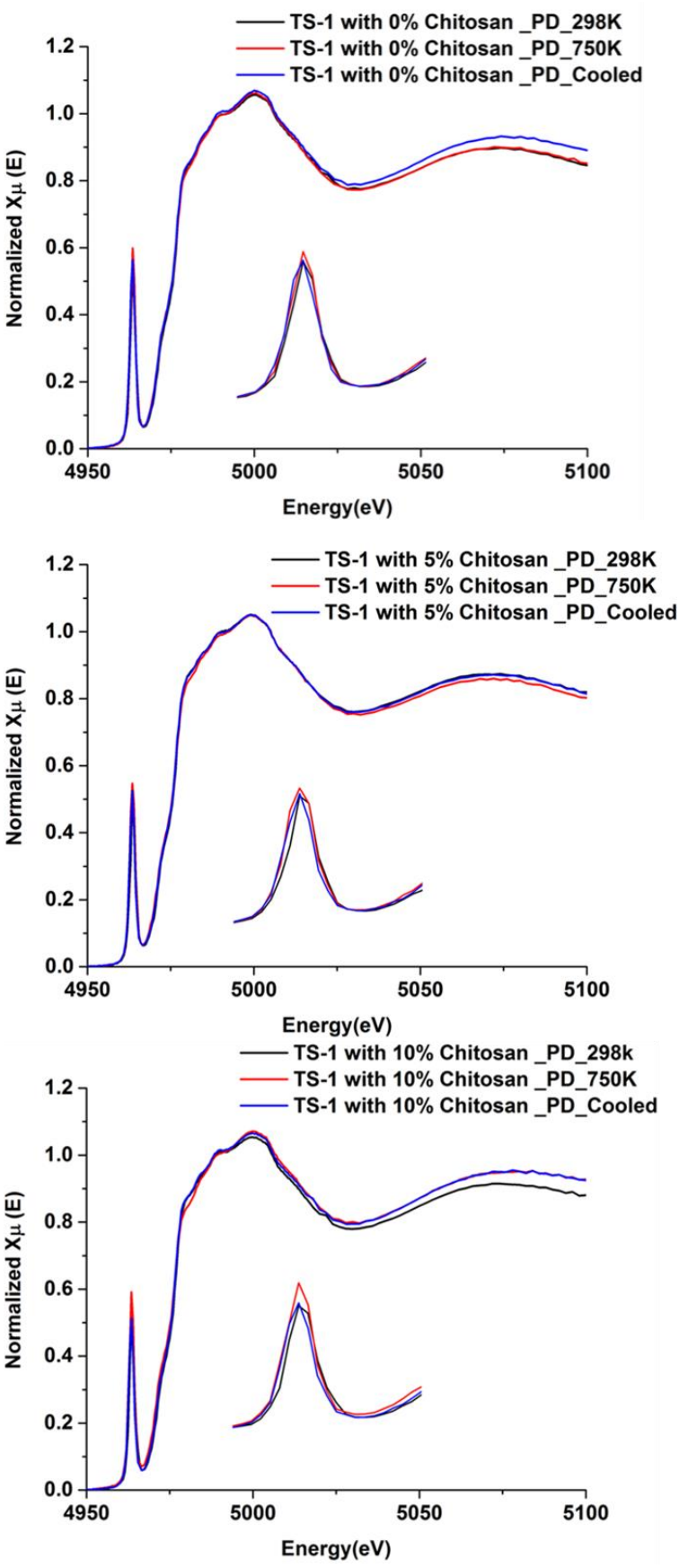

Figure 3.8: ***In situ*** **XANES of samplessynthesized through the PD method showing the response of pre-edge intensity to temperature. Inset is the expanded pre-edge region**

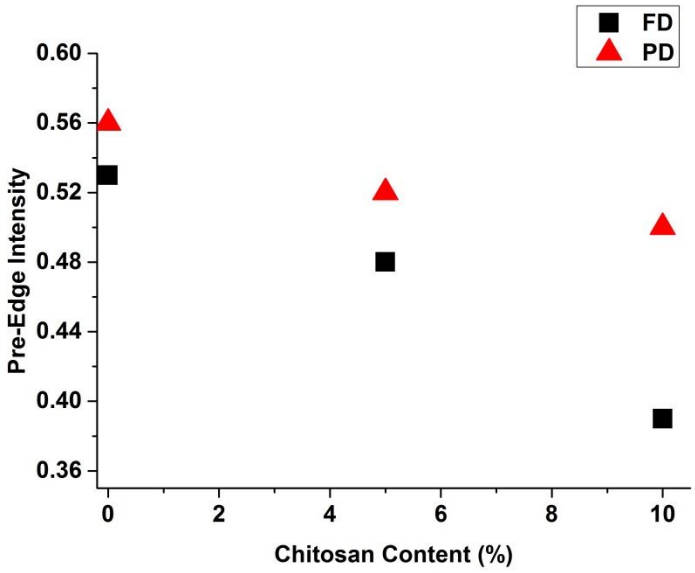

Figure 3.9: Pre-edge intensity as a function of chitosan concentration for FD and PD sample series

3.3.5 Pore characteristics

The nitrogen adsorption isotherms, and the corresponding pore size distributions, for both the FD and PD samples are given in figure 3.10. The isotherms are typically sigmoid or S-shaped, which signifies the micro-macropore nature of these samples. All samples exhibited an initial adsorption that is characteristic of the micropore region. The second major region of the pore occurs beyond 200 Å. Above this point a wide size distribution in the meso and macropore regions can be seen for the samples templated with 5 and 10% chitosan, especially for the FD samples. In all of the cases, the pore volumes and surface area of the samples synthesized through the PD route display higher values than those obtained from the FD method. These pore volumes can be further appreciated when the adsorption isotherms of samples from both methods are compared.

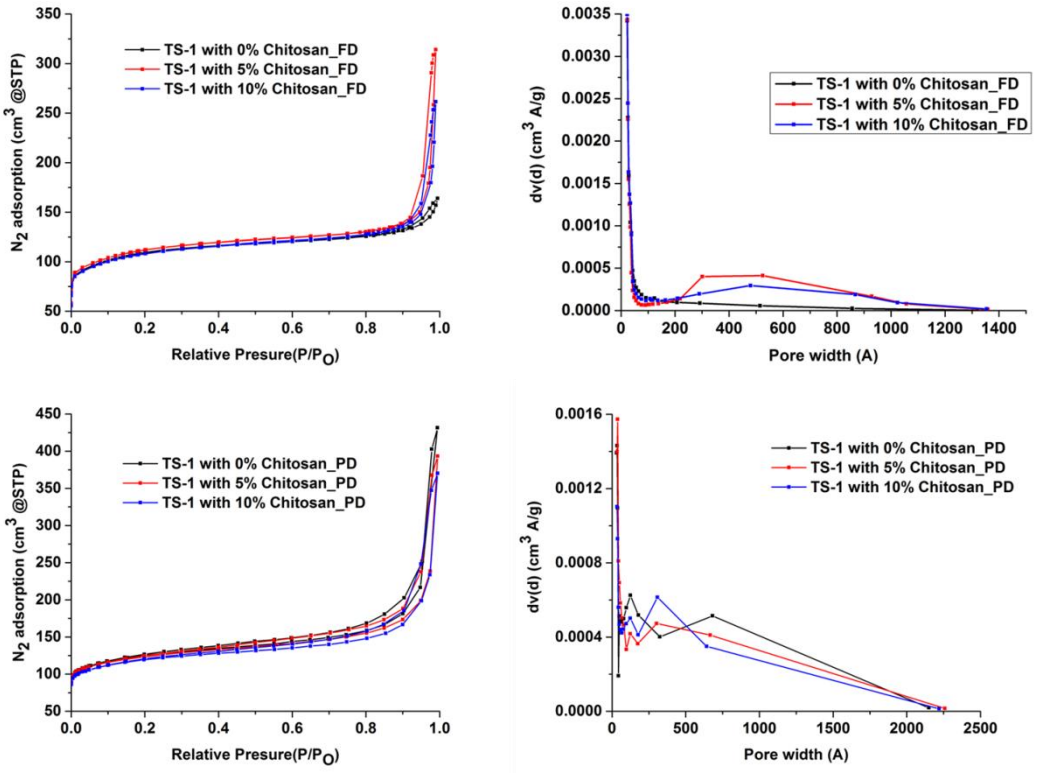

Figure 3.10: Nitrogen adsorption isotherms (left) and pore size distribution (right) of synthesized samples

Table 3.1: Physical properties of samples synthesis through the FD and PD methods

Chitosan content (%)	BET Surface Area (m^2/g)		Total Pore volume (cm^3/g)	
	FD	PD	FD	PD
0%	363	464	0.25	0.67
5%	373	458	0.48	0.61
10%	360	442	0.41	0.58

3.4 Catalytic evaluation of catalysts

All synthesized samples were evaluated for catalysis in the epoxidation of cyclohexene and styrene.

3.4.1 Epoxidation of cyclohexene

Figure 3.11 shows the effect of chitosan content in the synthesis gel on the catalytic performance of the resulting catalyst. The conversion of cyclohexene increased with

increasing chitosan content, which can be attributed to the induced extra porosity enabling easier access of the cyclohexene into the active sites. The selectivity to epoxide, on the other hand displays, an inverse response to chitosan concentration in the synthesis medium. This observation was initially thought to be a consequence of the zeolite titanium environment having strong coordination with water, as the loss of selectivity to the epoxide was accompanied by increase in cyclohexane diol which is a secondary product resulting from hydrolysis of cyclohexene epoxide.

Relying on the observed trend in the *insitu* XAS experiment, this hypothesis was rejected and, based on the spectroscopy data, it was concluded that the loss of selectivity must be due to the presence of extra framework species in the catalyst. This conclusion was further supported by the result of the catalysis of the samples synthesized through the PD method. Samples from this route show no UV-Vis vibrational peaks attributable to an extra-framework titanium phase, while the catalytic results of the samples as in figure 3.12, displayed improvement in the selectivity to the epoxide product. Figure 3.13 shows the comparison in selectivity to cyclohexene epoxide as a function of the preparation method.

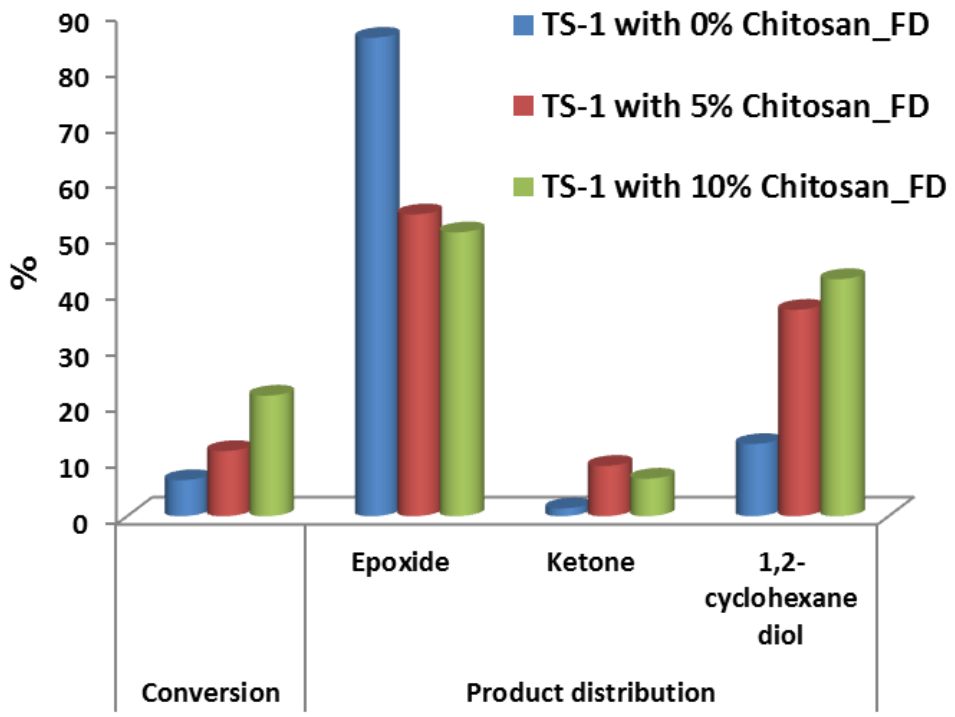

Figure 3.11: Influence of chitosan concentration on conversion and product distribution for fully dried catalysts (Reaction conditions: Temp - 333K, Time - 6hr)

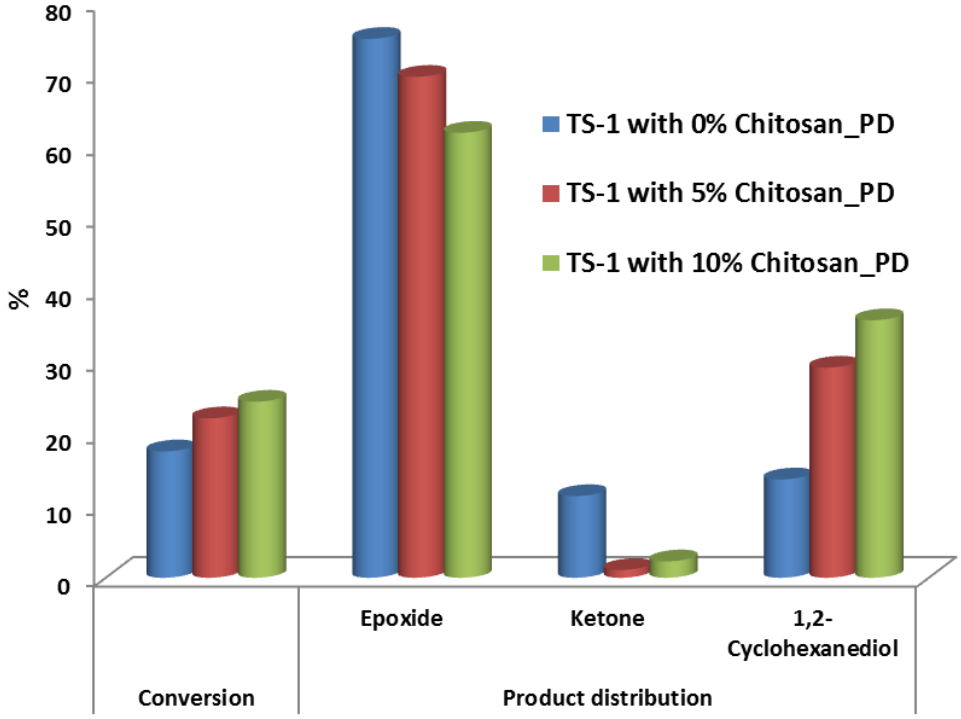

Figure 3.12: Influene of chitosan concentration on conversion and product distribution for the partially dried catalysts (Reaction conditions: Temp - 333K, Time - 6hr)

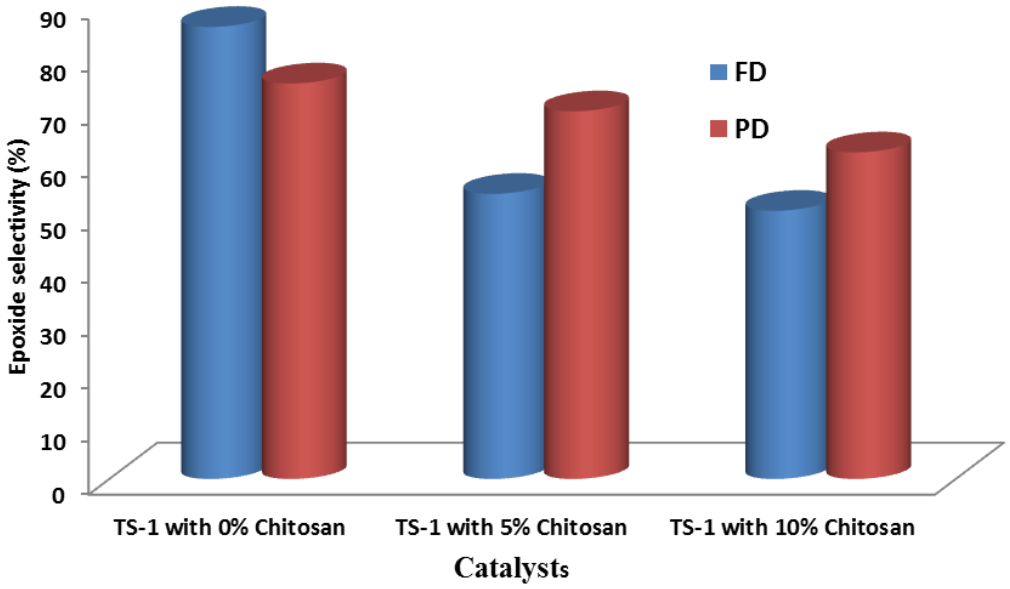

Figure 3.13: Effect of method of preparation on the selectivity to epoxide product

3.4.2 Optimization of the reaction conditions

Although the selectivity of cyclohexene epoxide showed a decreasing trend with chitosan concentration it is probable that a careful choice of reaction conditions might be able to shift this trend.

For instance, investigation of the effect of reaction temperature on conversion and product distribution shows that, at a higher temperature, there is a possibility of obtaining a high conversion percentage at the expense of epoxide selectivity. As can be seen in figure 3.14, which is a case study of the temperature effect on the performance of TS-1 synthesized with 10% chitosan concentration through the FD method, there was no significant increase in conversion from 313 K to 323 K. As the temperature was further increased to 333 K conversion increased by almost 100% from 10.51% at 313 K to 21.58%. Selectivity, on the other hand, progressively decreased as the temperature was increased, which may be attributable to the higher rate of degradation of the peroxide at higher temperatures [35].

The role of reaction time on the product distribution was demonstrated over the same catalyst by varying the reaction time from 2 to 6 hours. As shown in figure 3.15, it is clear that conversion of the substrate increased with reaction time. However, not so large an increase was achieved from 4 to 6 hours. The shorter reaction time appears to favour the production of more epoxide product, as compared to the longer time, which can also be explained in terms of the hydrogen peroxide still remaining very fresh and available to oxidize the substrate to epoxide at shorter reaction time, whereas there is the possibility of degradation of the peroxide over longer reaction times which might culminate into lower epoxide selectivity.

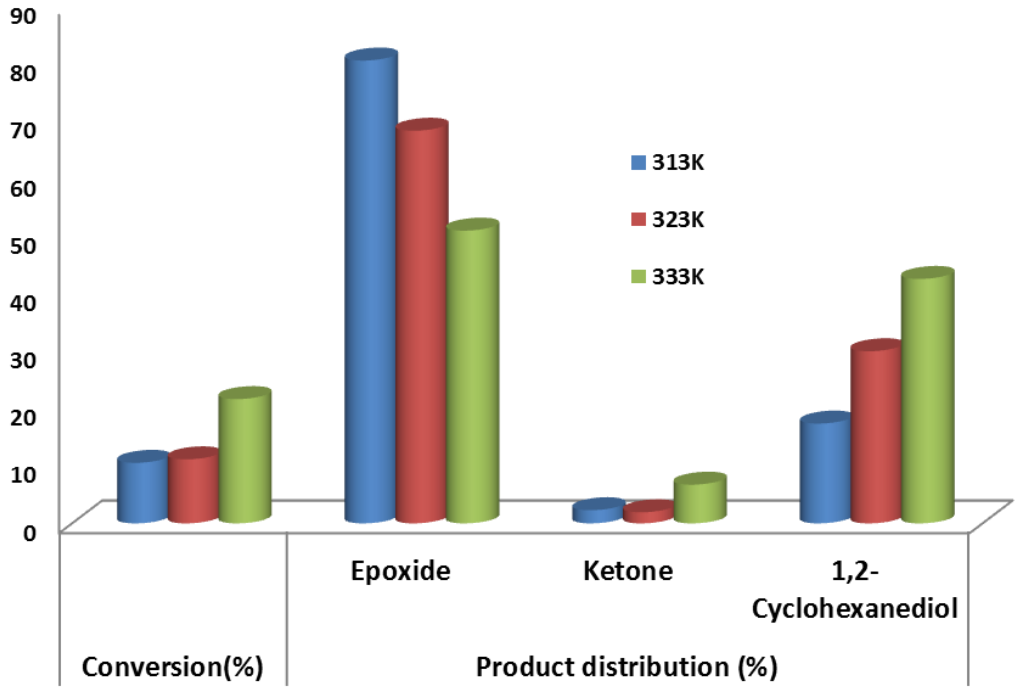

Figure 3.14: Influence of reaction temperature on the conversion and product distribution (Catalyst; TS-1 with 10% Chitosan_FD)

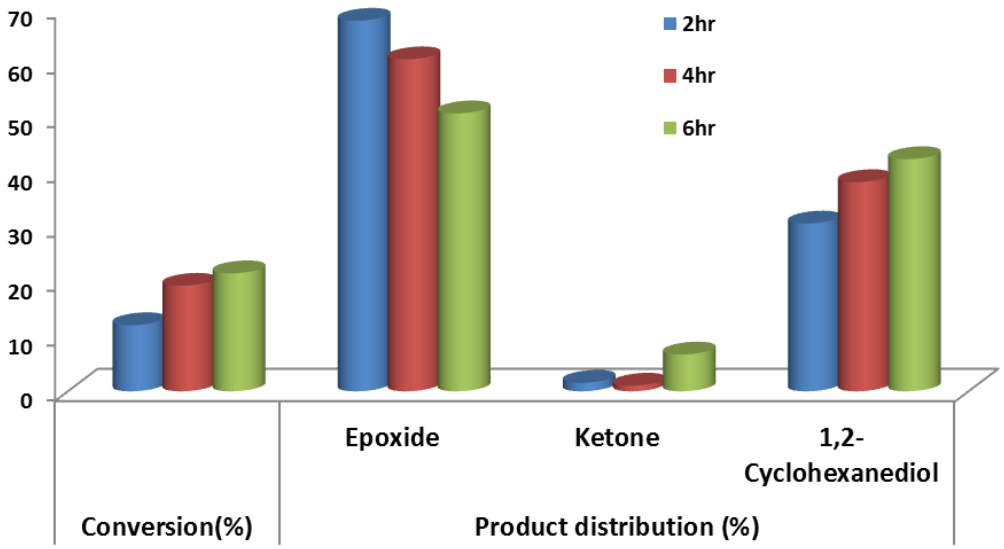

Figure 3.15: Influence of reaction time on the conversion and product distribution (Catalyst; TS-1 with 10% Chitosan_FD)

3.4.3 Styrene epoxidation

In order to investigate the effect of the mesopores further, a substrate with slightly higher kinetic diameter than cyclohexene was investigated. Styrene, with a kinetic diameter of approximately 6.0 Å as compared to 5.8 Å for cyclohexene, was used.

As presented in figure 3.16, there was very little difference in the conversion of this substrate versus chitosan concentration. Nonetheless, the catalysts templated with chitosan still display slightly higher conversion than that without.

The reaction was conducted in acetonitrile (figure 3.16) and acetone (figure 3.17) and the conversion of styrene showed virtually no dependence on the solvent, whereas, the product selectivity was predominantly a function of solvent.

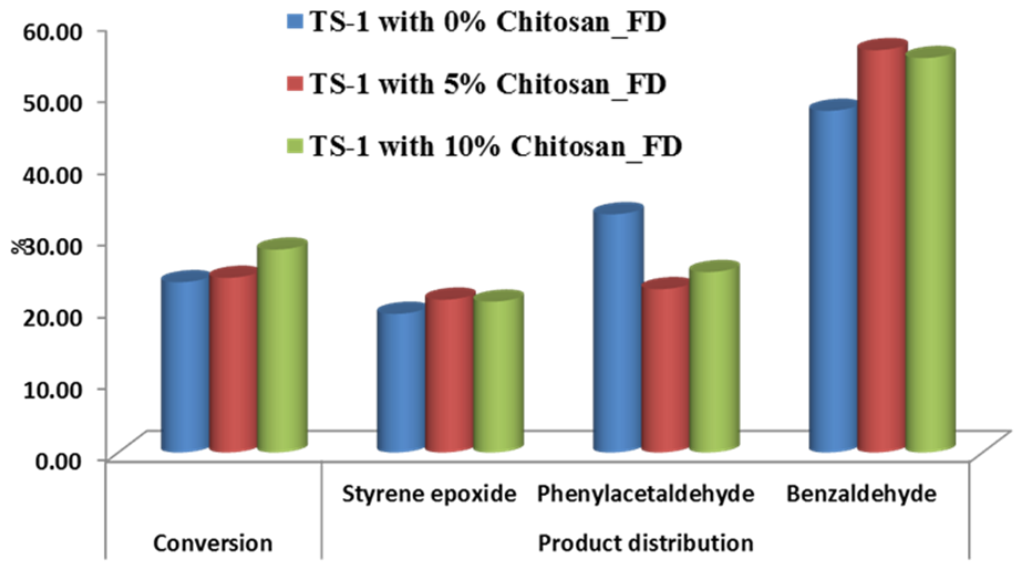

Figure 3.16: Effect of chitosan concentration on the conversion and product distribution of styrene (Solvent; Acetonitrile)

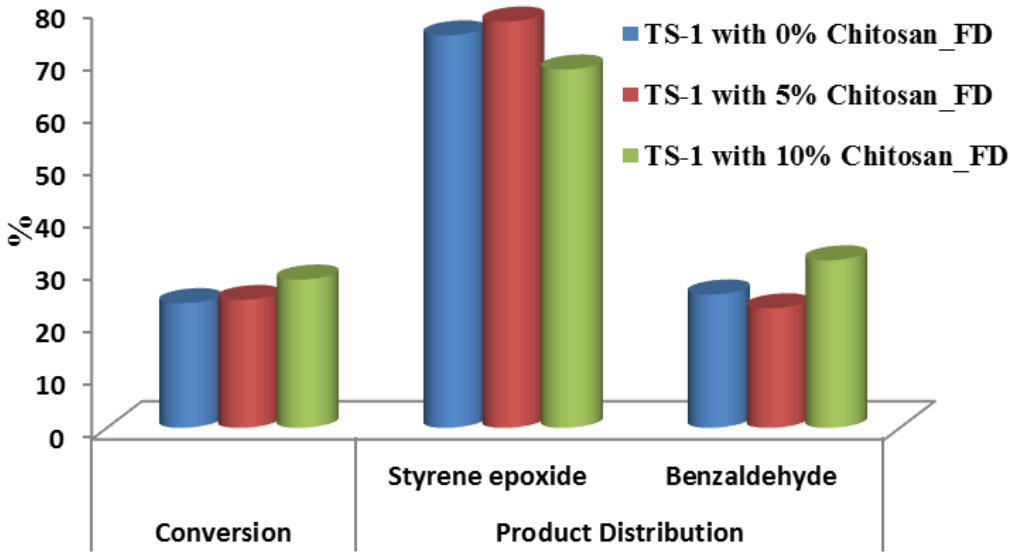

Figure 3.17: Effect of chitosan concentration on the conversion and product distribution of styrene (Solvent; Acetone)

While three products were observed in the reactions conducted in acetonitrile - styrene epoxide, phenyl acetaldehyde and benzaldehyde - only styrene epoxide and benzaldehyde were observed in acetone. A shift in selectivity from benzaldehyde to styrene epoxide was also obvious as the solvent was changed from acetonitrile to acetone.

3.5 Conclusions

The potential use of chitosan as an inert macro templating agent in the one-pot synthesis of TS-1 was successfully demonstrated. Chitosan was found to have no adverse effect on the crystallinity and phase purity of the synthesized TS-1. The structure of the TS-1 was still maintained even with chitosan in the synthesis formulation. Furthermore, the incorporation of the titanium atoms in the TS-1 framework was also unaffected by the presence of chitosan. The samples derived from the partially dried synthesis technique showed better selectivity to epoxide in the cyclohexene oxidation reaction. The lower selectivity to cyclohexene epoxide at high chitosan concentration was attributed to the presence of extra framework titanium clusters, which was evident from a series of characterization techniques. Reactions conducted at lower temperature, or for short time, resulted in improved selectivity to epoxide. During epoxidation of styrene, the selectivity was observed to strongly depend on the solvent. Acetonitrile tends to favour selectivity to benzaldehyde, while acetone favours styrene oxide. The results suggest that chitosan can be effective in synthesizing samples of TS-1 which will extend the range of oxidation reactions that can be catalysed by this material.

References

1. Z. Wenzhong, F. Michael, W. Jialiang, T.T. Peter, W. Joe, P.J. Thomas, *Journal of the American Chemical Society*, **1996**, *118*, 9164-9171

2. W. Zhan, J. Yao, Z. Xiao, Y. Guo, Y. Wang, Y. Guo, G. Lu, *Microporous and Mesoporous Materials*, **2014**, *183*, 150-155

3. D. He, C. Bai, C. Jiang, T. Zhou, *Powder Technology*, **2013**, *249*, 151-156

4. A. Bhaumik, T. Tatsumi, *Journal of Catalysis*, **2000**, *189*, 31-39

5. Y. Fang, H. Hu, *Catalysis Communications*, **2007**, *8*, 817-820

6. Z. Kang, G. Fang, Q. Ke, J. Hu, T. Tang, *ChemCatChem*, **2013**, *5*, 2191-2194

7. X. Wang, G. Li, W. Wang, C. Jin, Y. Chen, *Microporous and Mesoporous Materials*, **2011**, *142*, 494-502

8. Y. Cheneviere, F. Chieux, V. Caps, A. Tuel, *Journal of Catalysis*, **2010**, *269*, 161-168

9. X. Ke, L. Xu, C. Zeng, L. Zhang, N. Xu, *Microporous and Mesoporous Materials*, **2007**, *106*, 68-75

10. J. Zhou, Z. Hua, X. Cui, Z. Ye, F. Cui, J. Shi, *Chem Commun*, **2010**, *46*, 4994-6

11. J. Wang, L. Xu, K. Zhang, H. Peng, H. Wu, J. Jiang, Y. Liu, P. Wu, *Journal of Catalysis*, **2012**, *288*, 16-23

12. P. Chao, S. Tsai, T. Tsai, J. Mao,X. Guo, *Topics in Catalysis*, **2009**, *52*, 185-192

13. C. J. H. Jacobsen, C. Madsen, J. Houzvicka, I. Schmidt, A. Carlsson, *Journal of the American Chemical Society*, **2000**, *122*, 7116-7117

14. I. Schmidt, A. Krogh, K. Wienberg, A. Carlsson, M. Brorson, C.J.H. Jacobsen, *Chem Commun*, **2000**, 2157-2158

15. F. Schmidt, S. Paasch, E. Brunner, S. Kaskel, *Microporous and Mesoporous Materials*, **2012**, *164*, 214-221

16. I. Schmidt, A. Boisen, E. Gustavsson, K. Ståhl, S. Pehrson, S. Dahl, A. Carlsson, C.J.H. Jacobsen, *Chemistry of materials*, **2001**, *13*, 4416-4418

17. A.H. Janssen, I. Schmidt, C.J.H. Jacobsen, A.J. Koster, K.P. De Jong, *Microporous and Mesoporous Materials*, **2003**, *65*, 59-75

18. A. Boisen, I. Schmidt, A. Carlsson, S. Dahl, M. Brorson, C.J.H. Jacobsen, *Chem Commun*, **2003**, 958-959

19. D. Sahu, G.M. Kannan, R. Vijayaraghavan, *Int J Inflam*, **2014**, *2014*, 1-11

20. X. Chen, H. Yang, Z. Gu, Z. Shao, *Journal of Applied Polymer Science*, **2001**, *79*, 1144-1149

21. W. S. Wan Ngah, L. C. Teong, M. A. K. M. Hanafiah, *Carbohydrate Polymers*, **2011**, *83*, 1446-1456

22. M. Taramasso, G. Perego, B. Notari, *Preparation of porous crystalline synthetic material comprised of silicon and titanium oxides, United states patent*, **1983**

23. M. Ogura, S. Shinomiya, J. Tateno, Y. Nara, E. Kikuchi, M. Matsukata, *chemistry Letters*, **2000**, *29*, 882-883

24. X. Li, R. Prins, J.A. Van Bokhoven, *Journal of Catalysis*, **2009**, *262*, 257-265

25. J.B. Koo, N. Jiang, S. Saravanamurugan, M. Bejblová, Z. Musilová, J. Čejka, S.E. Park, *Journal of Catalysis*, **2010**, *276*, 327-334

26. M. Ogura, S. Shinomiya, J. Tateno, Y. Nara, M. Nomura, E. Kikuchi, M. Matsukata, *Applied Catalysis A: General*, **2001**, *219*, 33-43

27. R. Giudici, H.W. Kouwenhoven, R. Prins, *Applied Catalysis A: General*, **2000**, *203*, 101-110

28. I. Schmidt, C. Madsen, C.J.H. Jacobsen, *Inorganic chemistry*, **2000**, *39*, 2279-2283

29. C. Madsena, C.J.H. Jacobsen, *Chem Commun*, **1999**, 673–674

30. C. Li, G. Xiong, Q. Xin, J. Liu, P. Ying, Z. Feng, J. Li, W. Yang, Y. Wang, G. Wang, X. Liu, M. Lin, X. Wang, E. Min, *Angewandte Chemie International Edition*, **1999**, *38*, 2219-2221

31. Q. Guo, K. Sun, Z. Feng, G. Li, M. Guo, F. Fan, C. Li, *Chemistry*, **2012**, *18*, 13854-13860

32. S. Bordiga, A. Damin, F. Bonino, G. Ricchiardi, A. Zecchina, R. Tagliapietra, C. Lamberti, *Physical Chemistry Chemical Physics*, **2003**, *5*, 4390

33. F.Z. Zhang , X.W. Guo, X.S. Wang, G. Li, J.C. Zhou, J.Q. Yu, C. Li, *Catalysis Letters*, **2001**, *72*, 235-239

34. G. Sankar, J.M. Thomas, C.R.A. Catlow, C.M. Barker, D. Gleeson, N. Kaltsoyannis, *The Journal of Physical Chemistry B*, **2001**, *105*, 9028-9030

35. M. Anilkumar,W. F. Hoelderich, *Applied Catalysis B: Environmental*, **2015**, *165*, 87-93

Chapter 4: Chitosan scaffold templated ZSM-5 and application in methanol to hydrocarbon reaction

Chapter overview

In this chapter, the chitosan was transformed into a rigid three dimensional structure (scaffold) and used as a macro-template to form the alumino-silicate (ZSM-5) zeolite. Parameters such as the amount of zeolite precursor to chitosan scaffold, the mass of chitosan in each scaffold and the ratio of silicon to aluminium in the starting precursor were found to influence the acidity, pore distribution and the crystal morphology. The selectivity and coke formation of these scaffold-templated ZSM-5 zeolites were investigated for the methanol to hydrocarbon reaction.

4.1 Introduction

Since it was first discovered by researchers at Mobil, the methanol to hydrocarbon (MTH) reaction has proven to be an important chemical process. The reaction was first carried out over the acid zeolite catalyst HZSM-5 in the mid-1970s [1] and was ultimately commercialized for the production of gasoline products in 1986. The commercial plant was, however, discontinued due to a boom in the global oil market. However, the MTH process is again gathering attention in the academic and industrial worlds, partly due to the perceived depletion in the proven global oil reserves.

Natural gas and coal are sources of energy which are very abundant with natural gas reserves currently estimated to be more than that of crude oil, however, since the direct use of coal is no longer an attractive energy source, coal is often converted into synthesis gas which can subsequently be transformed to liquid fuels and other chemical raw materials. Methanol from synthesis gas is an attractive product which can be converted into liquid fuel through the methanol to hydrocarbon or the Fischer-Tropsch processes.

Several authors have devoted significant research efforts to the MTH process in order to better understand the intermediate steps involve in this process [1-7], as well as to garner more details on how the product selectivity is influenced by factors such as the catalyst features, reaction conditions and reactor parameters.

Catalyst properties, such as the acidity, acid site density, pore size, topology and morphology, have been well studied and all of these have been found to have some influence on product selectivity in the MTH reaction. The medium pore ZSM-5 zeolite, which was the first catalyst tested for the methanol to gasoline (MTG)

reaction, has been widely studied with a view to improving the catalytic life and to shift selectivity towards certain products, e.g. olefin, paraffin or gasoline.

The zeolite crystal size has been found to have a strong influence on the product distribution of the MTH reaction [8, 9]; the tendency to obtain bulky aromatic products is higher for strongly acidic catalysts compared to those with weak or moderate acid sites [10, 11]. Hence, the acid site is often modified either through demetalation, by silination or by substitution at the aluminium sites. Iron substituted ZSM-5 was investigated for the conversion of ethanol to hydrocarbons and was reported to have better ethanol conversion at low iron loading [12, 13]. Similarly, other elemental substitution such as gallium [14-16], boron [17] and zinc [18, 19] have also given rise to more stable catalysts and higher yields of liquid products during the MTH reactions.

Depending on the ultimate objective of the reaction, the methanol to hydrocarbon reaction may be described more specifically as the methanol to olefin (MTO) or methanol to gasoline (MTG) reaction and the catalyst used always has great influence on the product selectivity, as described in scheme 4-1. The MTH reaction typically occurs within the zeolite pores, which make a product range that is very dependent on the catalyst pore size. The MTO reaction is aimed at obtaining light olefins, such as ethylene, propylene and butylene, which are subsequently used for petrochemical applications. In tailoring this reaction towards these light olefins, catalysts with small pores are generally required as they prevent the formation of larger sized or liquid products. It is therefore of little surprise that the commercial MTO reactor operated by UOP is primarily based on the silicoaluminophosphate material (SAPO-34) [20] with pore dimensions of *ca* 3.8*3.8 Å. This catalyst is highly selective towards the C_2 and C_3 hydrocarbons [21].

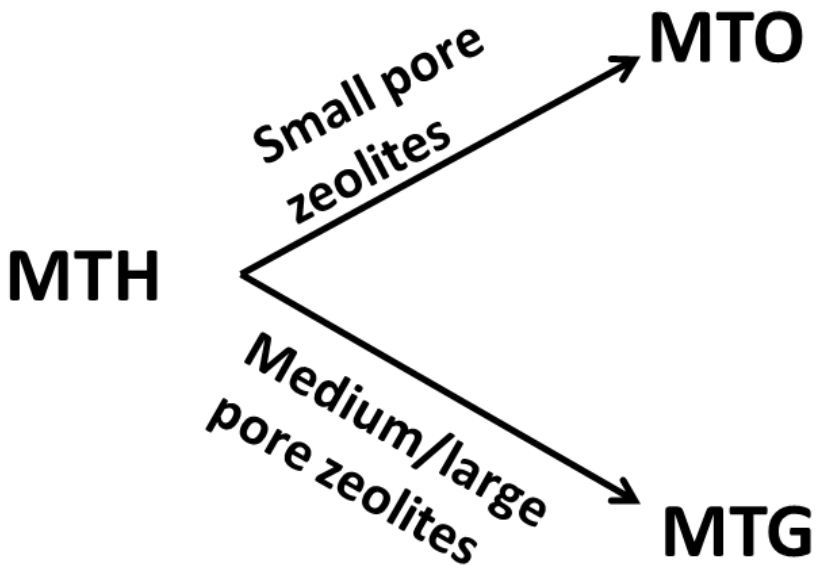

Scheme 4-1: Illustration of the dependence of catalyst pore size on product distribution

In the MTG process, the primary aim is to convert the methanol feed into gasoline range products; these high molecular weight hydrocarbons are predominantly liquids. The first catalyst used for this reaction was the ZSM-5 zeolite, and it has been the most widely studied for this process ever since. This zeolite is made up of three dimensional framework structure with pore openings of about 5.6 Å in diameter. This pore diameter is intermediate between large pore zeolites, such as faujasite (9 - 10 Å) and small pore zeolites with a pore diameter of less than 5 Å. In the MTG reaction over the ZSM-5 zeolite catalyst, a sharp cut-off is often observed in the product distribution - this has been attributed to the diffusion and steric constraints imposed by the pore size of the zeolite. These constraints prevent the formation of substituted benzenes greater than 10 carbon atoms; to overcome these diffusion and steric effects, many researchers have suggested the use of the ZSM-5 zeolite with a hierarchical pore structure, which implies the ZSM-5 zeolite will consist of mesopores or macropores coexisting with its intrinsic microporous

structure. The hierarchical pore geometry will ensure large size products, predominantly in the liquid range, can be effectively produced with the catalyst.

Much work has been reported on the synthesis and use of hierarchical ZSM-5. In their work, Bjørgen *et al* [22] reported the improved catalytic performance of ZSM-5 treated with NaOH. As an alternative to NaOH, Vennestrom *et al* [23] employed a guanidinium base in mesopore creation and the catalytic activity in the MTH reaction was compared to that of the NaOH treated materials. The influence of the created mesopore on product selectivity was demonstrated by the yield of large aromatic compounds, which were absent from the same reaction on an untreated ZSM-5 catalyst. A combined treatment in NaOH and tetrapropylammonium hydroxide [24] was also recently reported to yield high propylene selectivity and a longer catalyst life time, at an optimum organic base ratio of 0.4. In their work, Kim and coworkers [25] showed a linear relationship between the catalyst life and the amount of mesoporosity induced on HZSM-5 zeolite. Other recent works [26-28], investigating the roles of mesoporosity on catalysts longevity, have attributed the more durable performance of the mesoporous HZSM-5 to a reduced rate of coke formation.

Hierarchical ZSM-5 has also been achieved using other facile methods. For instance, three dimensional monoliths of ZSM-5 have been synthesized using different methods and a variety of macro-templates [29-33]. Using microspheres as a template, silicalite-1 zeolite (an isomorph of ZSM-5) was synthesized using the steam assisted technique. The zeolite obtained was found to have hollow structure that allowed macropore access [29]. A simple method involving the self-assembly of a silicalite nanoparticle has also been reported [30]. Song et al [31] have also reported on the synthesis of hollow ZSM-5. In their approach, hollow mesoporous

silica was prepared first, followed by subsequent conversion to aluminium containing ZSM-5. Using macroporous polyurethane foam, large silicalite-1[32] and ZSM-5[33] monoliths have been successfully synthesized. The monolith structure is capable of inducing an inter-crystal macropore, which can lead to a significant reduction in the pressure drop and mass transfer limitations.

The focus of this chapter is, therefore, the investigation of the potential use of the chitosan scaffold as a macroporous three dimensional template for the synthesis of a self-supporting ZSM-5 monolith. The zeolites obtained were characterized using a series of lab based characterization techniques, and their potential as a MTH catalyst was investigated.

4.2 Methanol to hydrocarbon reaction steps

During the reaction of methanol to hydrocarbon over a solid acid catalyst, such as zeolites, several reaction paths have been reported. The most widely regarded of these, however, is the hydrocarbon pool mechanism which includes five overall reaction steps [1]. The first step involves the dehydration of methanol to form dimethyl ether (DME); equilibrium is eventually attained between the methanol, DME and water in this step. The methanol dehydration step is followed by a kinetic induction loop which precedes the formation of the hydrocarbon pool, which is then followed by the formation of the first hydrocarbon products from the combination of methanol and DME. The first sets of hydrocarbon products are mainly lower olefins. The fourth stage comprises the conversion of the primary olefin products to a mixture of higher hydrocarbons through a series of secondary reaction steps; such as alkylation, cracking and hydrogen transfer. The extent of these secondary reactions

is often governed by a variety of factors, including the catalyst acidity, topology, crystal size and process conditions [1]. Scheme 4-2 gives the overall reaction paths that may be involved in the conversion of methanol to hydrocarbon products. The final steps involve the catalyst deactivation which ultimately terminates the reaction.

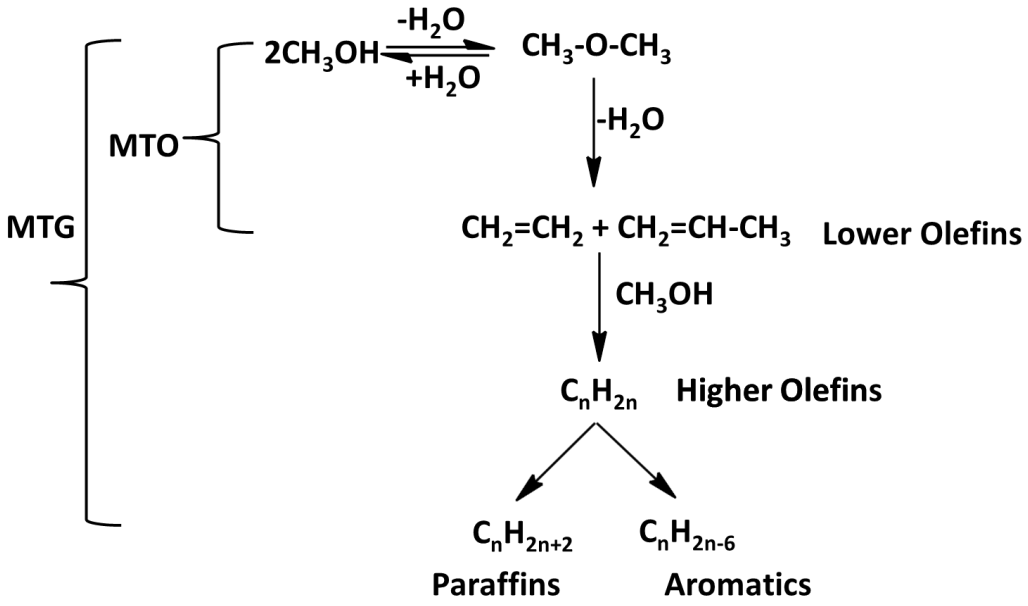

Scheme 4-2: Schematic representation of the overall reaction steps involved in the conversion of methanol to hydrocarbon. Adapted with modifications from [34, 35]

4.3 Experimental techniques

4.3.1 Scaffold preparation

The chitosan scaffold was prepared by following procedures available elsewhere [36, 37]. Typically, different amounts of chitosan powder were dissolved in 0.3M acetic acid. The mixture was mixed thoroughly using a spatula, covered and then maintained overnight at room temperature. After 24 hours, the viscous solution was poured into a cylindrical centrifuge tube acting as a mould and subjected to centrifugation at 4000 rpm for 10 minutes to remove any trapped air bubbles. The tube was then frozen in an ultra-cool freezer at -80 ^{O}C for 24 hours. Subsequently,

the frozen solution was freeze dried at -20 ^{O}C. When fully dried the scaffold was soaked in 0.1 M sodium hydroxide solution for 24 hours, to neutralize the acetic acid, and washed with deionized water until the filtrate was neutral and the freeze drying cycle then repeated. Following this procedure, different scaffolds of varying chitosan concentration were prepared. Table 4.1 gives the composition of each scaffold.

Table 4.1: Summary of mass composition for each scaffold

Total weight (g)	Acid weight (g)	Chitosan mass (g)	Scaffold wt%
25	24.25	0.75	3
18.75	18	0.75	4
15	14.25	0.75	5
50	48.5	1.5	3
50	48	2.0	4
50	47.5	2.5	5

4.3.2 Zeolite gel preparation

The zeolite precursor was prepared from a clear solution of silica-alumina solution. In a typical procedure the aluminium source, sodium aluminate, was dissolved in distilled water and stirred until completely dissolved. To this aluminate solution, the organic structure directing agent, tetra propyl ammonium hydroxide (25 wt%), was added and stirred for 30 minutes. Subsequently the silica source, tetraethyl orthosilicate, was added and the resulting clear solution was allowed to age at room temperature for 3 hours (see table 4.2 for mass composition of the precursor), resulting in a clear solution with the following composition:

SiO_2: 0.125TPAOH: 41.25H_2O: yAl_2O_3 (where y is either 0.04 or 0.08)

To vary the aluminium content in the zeolite, the amount of aluminium source added to the precursor was varied resulting in gels with two Si to aluminium ratio as given in table 4.2 - gel A with Si/Al of 50 and gel B with Si/Al of 25.

Table 4.2: Zeolite gel composition

Gel	TEOS (g)	$NaAlO_2$ (g)	TPAOH (g)	H_2O (g)	Si/Al (g)
A	17	0.13	8.10	51	50
B	17	0.26	8.10	51	25

4.3.3 Scaffold filling and crystallization

Measured amounts of the above solution were added to a centrifuge tube containing the prepared scaffold and then centrifuged to allow impregnation of the scaffold with the solution, and to remove any trapped air bubbles from the scaffold.

The solution-impregnated scaffold was placed in a Teflon-lined autoclave with the remaining free solution and subjected to hydrothermal crystallization at 170 ^{O}C for 64 hours, under static conditions. Once the crystallization was complete, the resulting scaffolded zeolite was washed with copious amount of distilled water and then dried at 120 ^{O}C overnight. Calcination was carried out at 650 ^{O}C in air. The calcination furnace was slowly ramped at a rate of 2 ^{O}C /min and held at 650 ^{O}C for 12 hours

The effect of different parameters, such as the amount of chitosan, amount of zeolite solution to scaffold and silicon to aluminium ratio, on the resulting scaffolded zeolite was studied. The variation of these parameters is given in the table 4.3 below.

Table 4.3: Composition of the scaffold-zeolite precursor

Chitosan mass (g)	Scaffold wt%	Si/Al	Volume of solution	Sample notation
0.75	3	50	32ml	HRS-0.75-3wt%-32ml
0.75	4	50	32ml	HRS-0.75-4wt%-32ml
0.75	5	50	32ml	HRS-0.75-5wt%-32ml
0.75	3	50	16ml	HRS-0.75-3wt%-16ml
0.75	4	50	16ml	HRS-0.75-4wt%-16ml
0.75	5	50	16ml	HRS-0.75-5wt%-16ml
0.75	3	25	32ml	HRS-0.75-3wt%-SiAl25
0.75	4	25	32ml	HRS-0.75-4wt%-SiAl25
0.75	5	25	32ml	HRS-0.75-5wt%-SiAl25
1.5	3	50	32ml	HRS-1.5-3wt%-SiAl50
2	4	50	32ml	HRS-2.0-4wt%- SiAl50
2.5	5	50	32ml	HRS-2.5-5wt%- SiAl50

4.3.4 Characterization

4.3.4.1 Phase, purity and crystallinity

Powder X-ray diffraction was used to investigate the phase and purity of the synthesized samples. The diffraction patterns of the scaffold templated samples were compared with that of a standard sample that was synthesized without chitosan. To conduct the diffraction experiment, each sample was first crushed and ground into a fine powder. The powdered samples were tightly and smoothly packed onto a flat sample holder and loaded into the diffractometer as describe in chapter two. The diffraction patterns were recorded for each sample from 5 to 50 degrees two theta angle at a step size of 0.05^{O} and 2 seconds per step.

4.3.4.2 Morphological investigation

Scanning electron microscopy (SEM) was used to observe the morphology of the synthesized samples. The procedure described in chapter two was adopted for

sample preparation and measurement. Images were taken from different areas of the specimen and at different magnifications.

4.3.4.3 Investigation of the acid site

FTIR spectroscopy was used to investigate the nature of the acidity of the samples. About 1.6 mg of each sample was pressed into a transparent thin pellet. The pellet was loaded into the pellet window of the FTIR *in situ* cell. The samples were heated from room temperature to 550 ^{O}C. Data was recorded at every 100 ^{O}C rise in temperature.

4.3.4.4 Nitrogen physisorption

Physical adsorption isotherms were measured on a Quantachrome Autosorb-iQC. The surface area was estimated using the BET method, while the pore size distribution was obtained by the DFT method. Prior to measurement, about 100 mg of the powder sample was degassed at 250 ^{O}C in vacuum for 12 hours.

4.3.5 Catalytic reactions

The synthesized catalysts were evaluated for the methanol to hydrocarbon reaction. This gas phase reaction was carried out using the reactor described in chapter two. Typically, 200 mg of the catalyst preformed into 212-300 micron sized particles, were loaded onto the centre of the reactor tube. Prior to flowing the methanol feed, catalyst activation was done at 500 ^{O}C under a nitrogen flow of 30 ml/min. The reactor was heated at a rate of 10 ^{O}C/min and held at 500 ^{O}C for an hour, after which it was cooled to the reaction temperature of 350 ^{O}C.

The methanol was fed at a rate of 2 ml/hr, and nitrogen fed at 30 mL/min was used as the carrier gas. The reaction was carried out for 5 hours and the cumulative liquid

products over the course of the reaction was collected in a test tube placed in an ice bath and connected to the effluent stream of the reactor.

For product analysis, upon completion of the reaction, the product was collected and the organic products separated from the water phase. A solution consisting of 0.05 ml of the organic product phase was diluted in a 5 ml standard flask with dichloromethane. Cyclohexene was used as the internal standard for quantification.

4.4 Results and discussions

4.4.1 Morphology of scaffolds

The morphological features of the chitosan scaffolds were first investigated. Photographic images of the resulting scaffolds are given in figure 4.1. The spongy nature of the scaffold can be appreciated from the internal cross section of a fractured surface as shown in figure 4.1d.

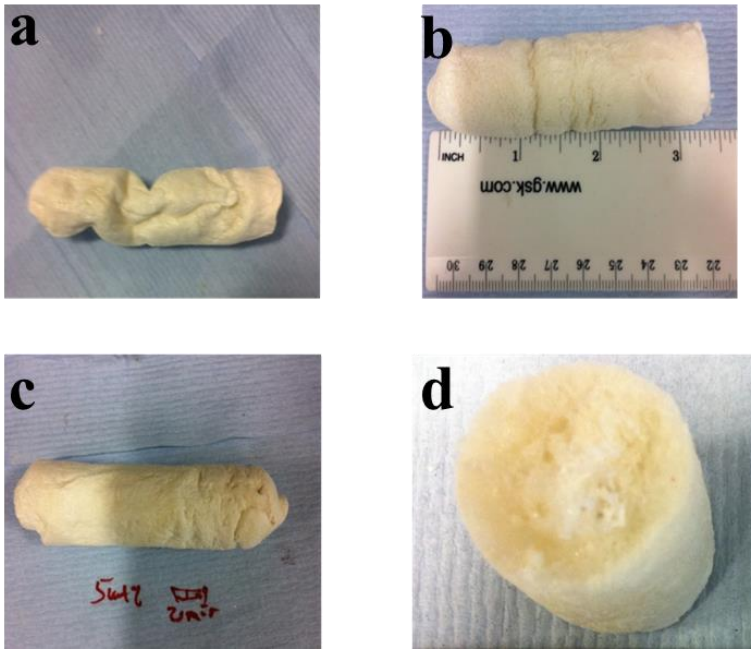

Figure 4.1: Representative images of chitosan scaffolds at different percentage concentrations (a) 3wt%, (b) 4wt% (c) 5wt% and (d) internal cross section of a fractured surface

The SEM micrographs of the scaffolds (figure 4.2) confirm the porosity and pore connectivity of the scaffolds. The pore width of the scaffolds can be seen to shrink on increasing the percentage chitosan concentration. Likewise, the individual pores became less distinct, with some pores observed to have cracked or collapsed as the concentration of chitosan was increased.

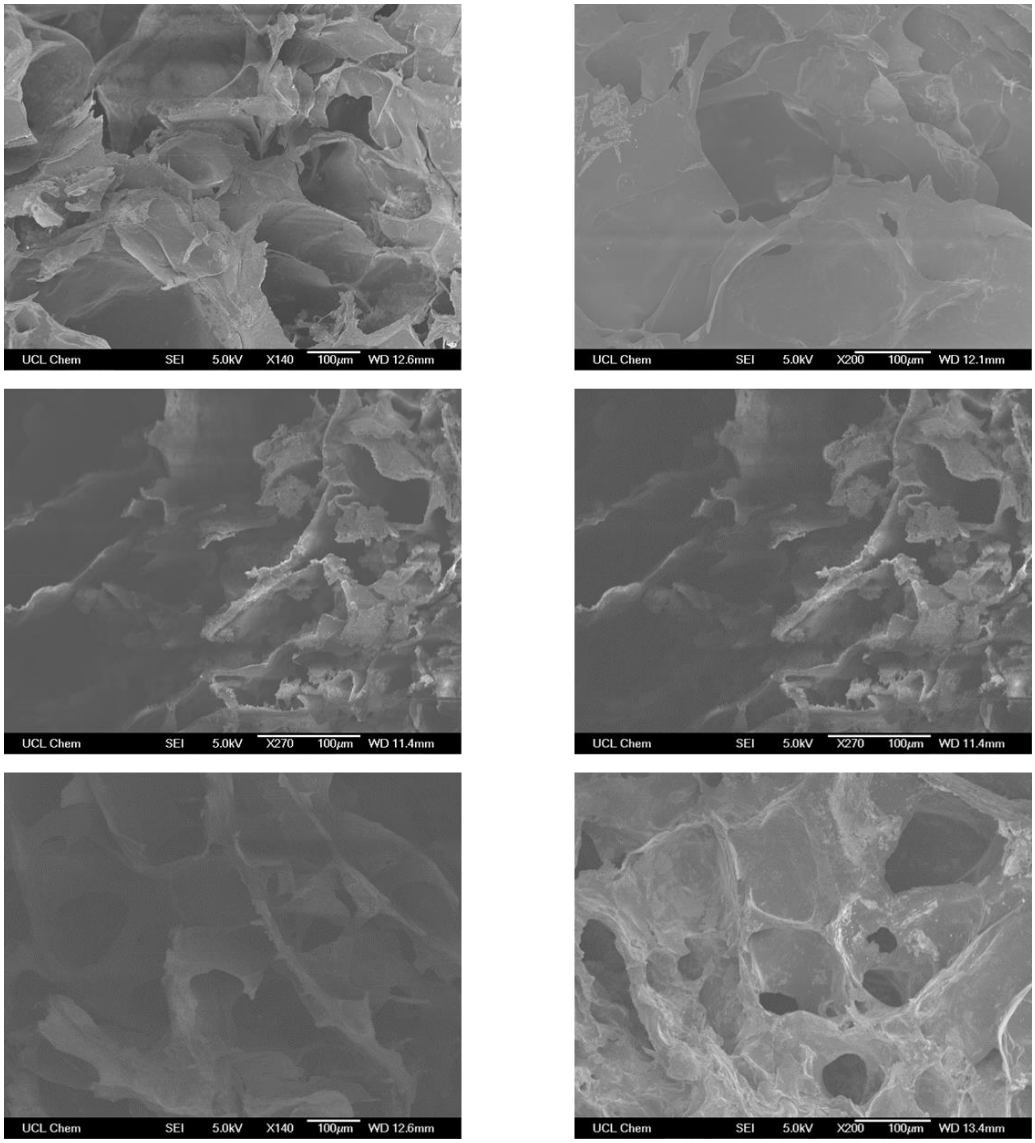

Figure 4.2: SEM micrographs of chitosan scaffolds at different percentage concentrations. Top to bottom 3wt%, 4wt% and 5wt%. Left and right are at different magnifications

4.4.2 Post synthesis observation

A comparison of the chitosan scaffold before and after it was subjected to the hydrothermal process is given in figure 4.3. Figure 4.3b shows the chitosan scaffold with the zeolite embedded in its pores after hydrothermal treatment and before calcination. This observation is the first proof that the zeolite crystallization took place inside and within the pores of the scaffold. The scaffold can be seen to have diminished in length and shrunk in width after hydrothermal process. This observation can be attributed to the thermal effect of the generated steam during the hydrothermal process, which could have led to some carbonization and flaking off of the weakly bound portions of the scaffold. The hydrothermal carbonization technique, we recall, is often employed in the densification of biomass materials [38-41].

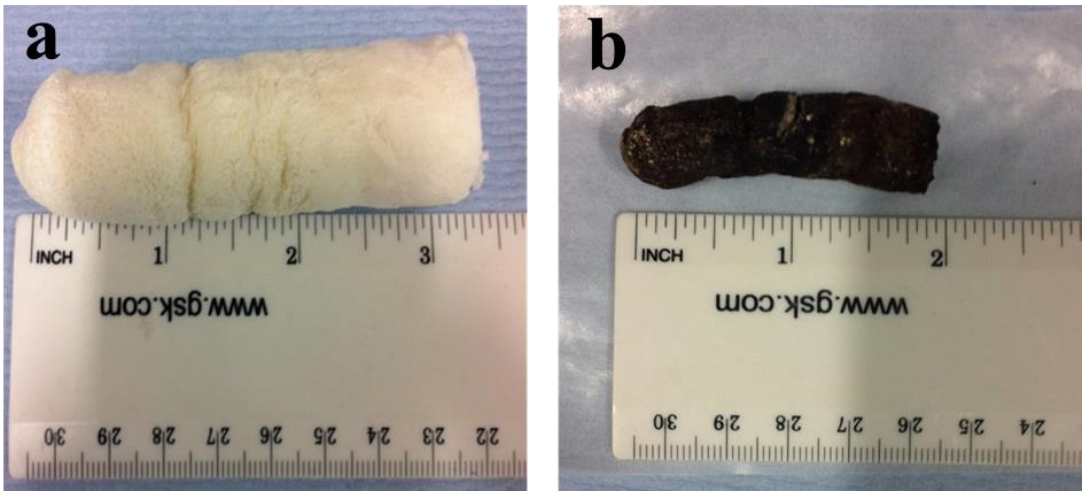

Figure 4.3: Photographic images comparing a representative chitosan scaffold before (a) and after (b) hydrothermal treatment.

The removal of the scaffold frame, however, resulted in the collapse of this scaffolded zeolite, which may be attributed to the soft nature of the scaffold material. Another possible reason could be that the zeolite was unable to form walls thick

enough to maintain the three dimensional skeletal frame of the scaffold once it has been removed.

4.4.3 Phase identification

The diffraction patterns of all the samples synthesized during this work were compared to that of a reference sample that was synthesized without chitosan, in order to identify any effect the chitosan might have on the phase and phase purity of the resulting samples.

Figure 4.4 shows the XRD patterns of the samples synthesized by impregnating 3wt%, 4wt% and 5wt% of chitosan scaffold with 32 ml of zeolite precursor. These chitosan scaffolds were prepared with 0.75 g of chitosan powder, as enumerated in table 4.3. The Si to Al ratio of the zeolite gel was 50. The diffraction patterns of all the templated zeolites match well with that of the reference, and they all display a typical MFI framework diffraction pattern. The diffraction peak positions and the relative ratios of all the peaks also compare well with that of the reference sample, which implies that the resulting zeolites from the scaffold templates are of good crystallinity. Furthermore, as no extra peaks can be observed in the templated samples, we can conclude that these materials are of good phase purity.

The volume of zeolite precursor impregnated into the scaffold was also investigated. In contrast to figure 4.4, where each scaffold was impregnated with 32 ml of zeolite precursor, the diffraction patterns in figure 4.5 are those of the zeolites obtained from scaffolds impregnated with 16 ml of precursor. These diffraction patterns also compare well with that of the reference with no extra peaks detected, implying that the zeolites were phase pure.

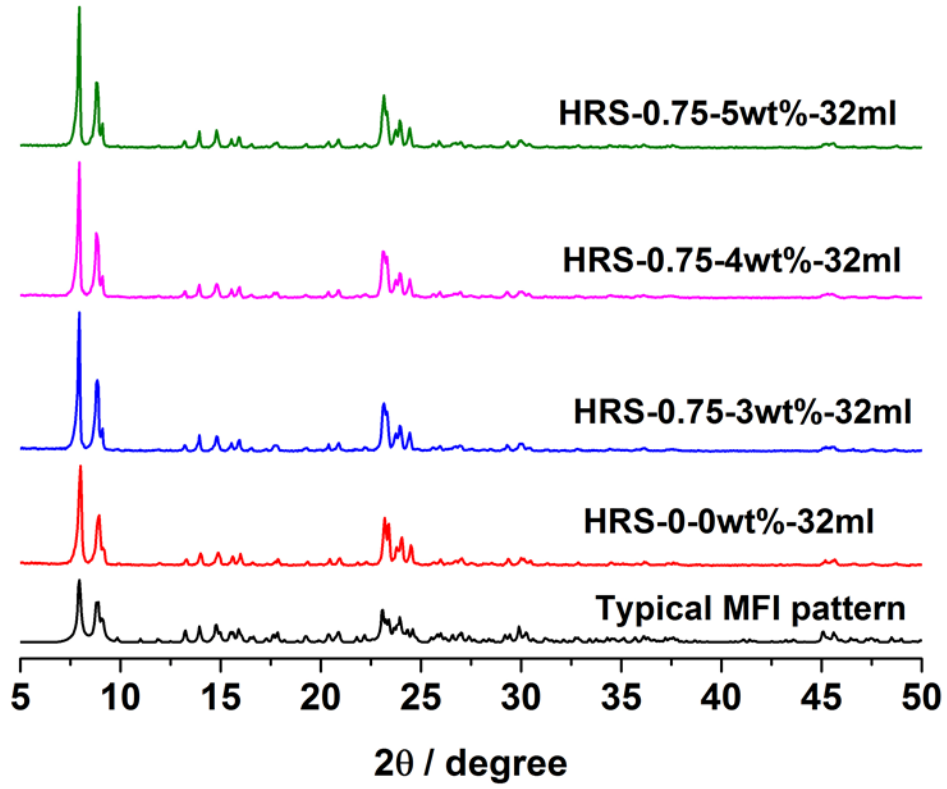

Figure 4.4: Powder X-ray diffraction patterns of scaffold templated zeolites. (Zeolite gel composition: Si/Al=50, volume of gel: 32ml)

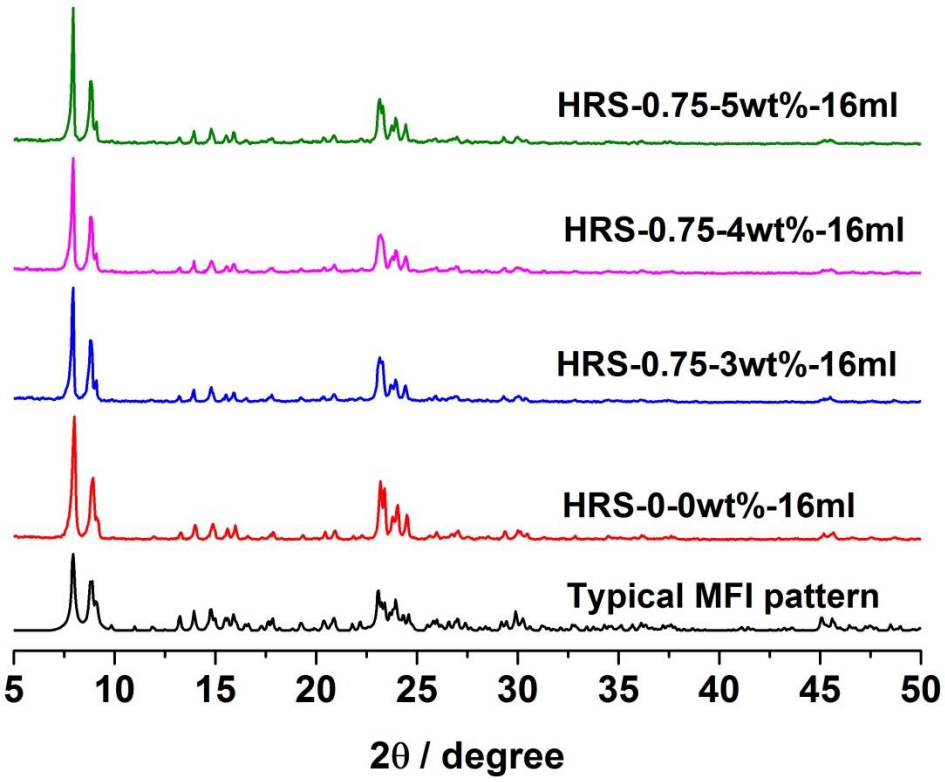

Figure 4.5: Powder X-ray diffraction patterns of scaffold templated zeolites.(Zeolite gel composition: Si/Al=50, volume of gel: 16ml)

We also probed the amount of chitosan powder used to prepare each scaffold to discern the influence of chitosan on the crystallinity and phase purity of the resulting zeolite. As is clear in figure 4.6, there are no differences between the diffraction patterns of these samples and those with less chitosan, indicating that chitosan on its own has no effect on the phase, purity or crystallinity of the zeolite.

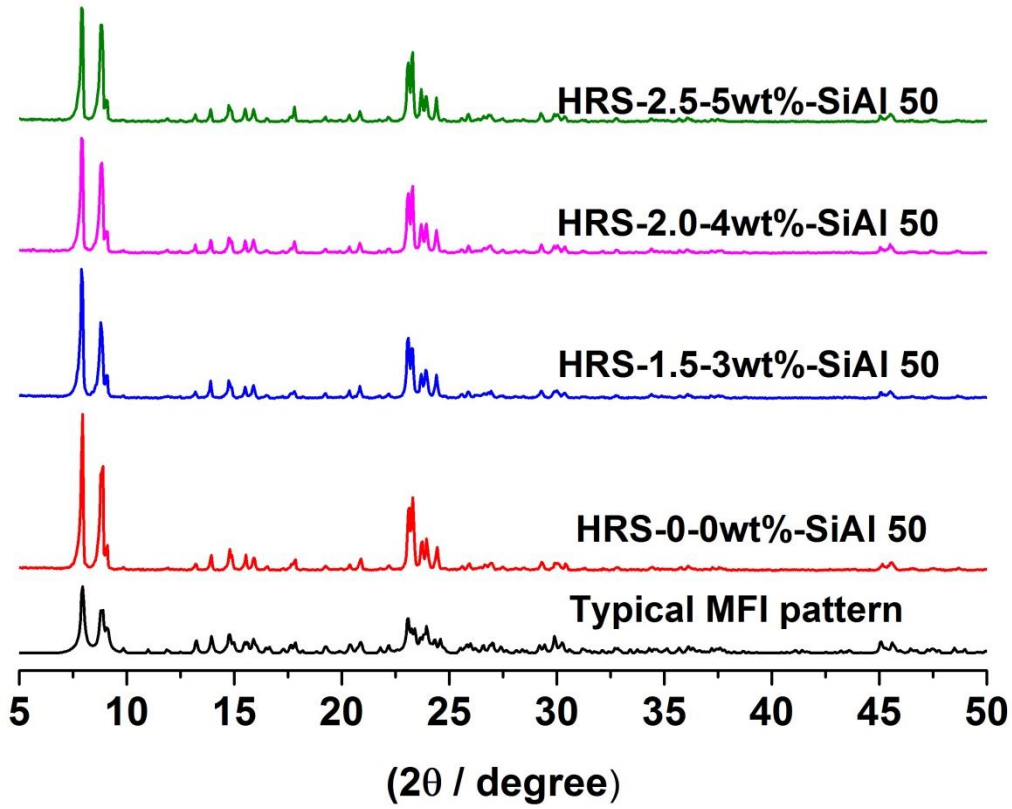

Figure 4.6: Powder X-ray diffraction patterns of scaffold templated zeolites. (Zeolite gel composition: Si/Al=50, chitosan content in scaffold varied from 1.5g to 2.5g)

The silicon to aluminium ratio of the zeolite precursor also showed no influence on the phase purity and degree of crystallinity, as demonstrated by the diffraction patterns in figure 4.7. The diffraction patterns in figure 4.7 are those of zeolites obtained from a precursor with a silicon to aluminium ratio of 25, in contrast to the previous ones with a silicon to aluminium ratio of 50.

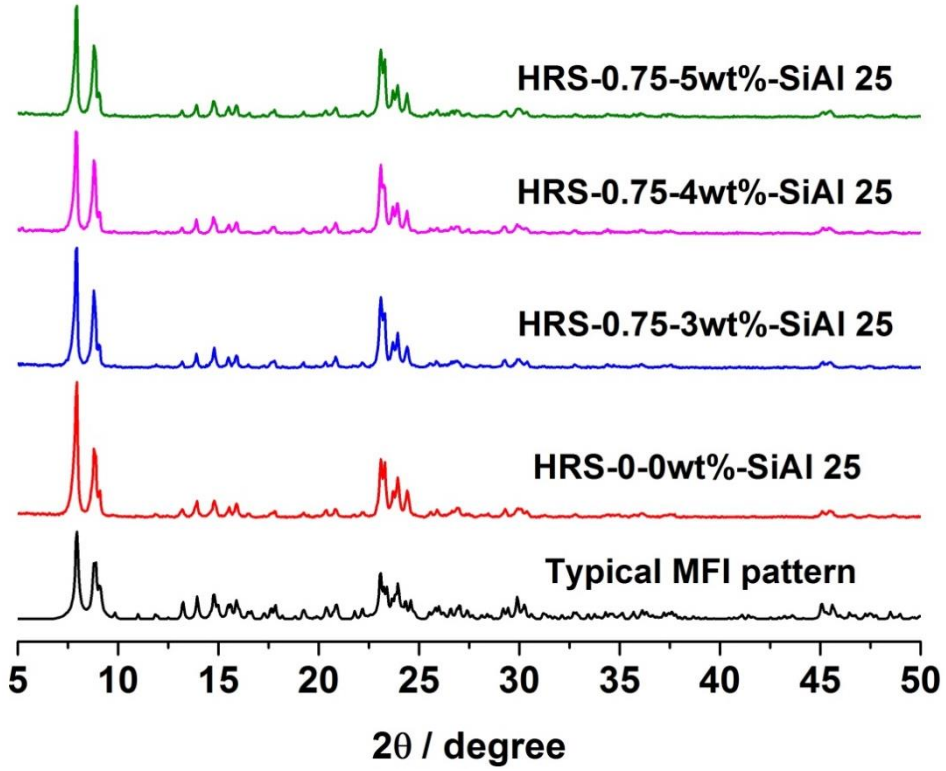

Figure 4.7: Powder X-ray diffraction patterns of scaffold templated zeolites. (Zeolite gel composition: Si/Al=25, volume of gel: 32ml)

4.4.4 FTIR characterization

The FTIR Spectra for all the scaffold templated zeolites, recorded during *in situ* dehydration in nitrogen, are presented in figures 4.8 to 4.10. These figures show the response of the bands at approximately 3600 cm^{-1} and 3700 cm^{-1}, which are indicative of the Brønsted and Lewis acid sites [35] to increasing dehydration temperature. These peaks grew in intensity as the temperature was increased from 298 K to 823 K - this is due to the removal of adsorbed water, which displays an FTIR band at the same wavelength as the hydroxyl group responsible for the acid sites [42]. The adsorbed water is also responsible for the broad band observed at low temperature in these OH regions. No significant increase in the acid site bands was noticeable beyond 773 K explaining why zeolite catalyst activation is mostly done at just beyond this point e.g. 823 K during gas-phase reactions.

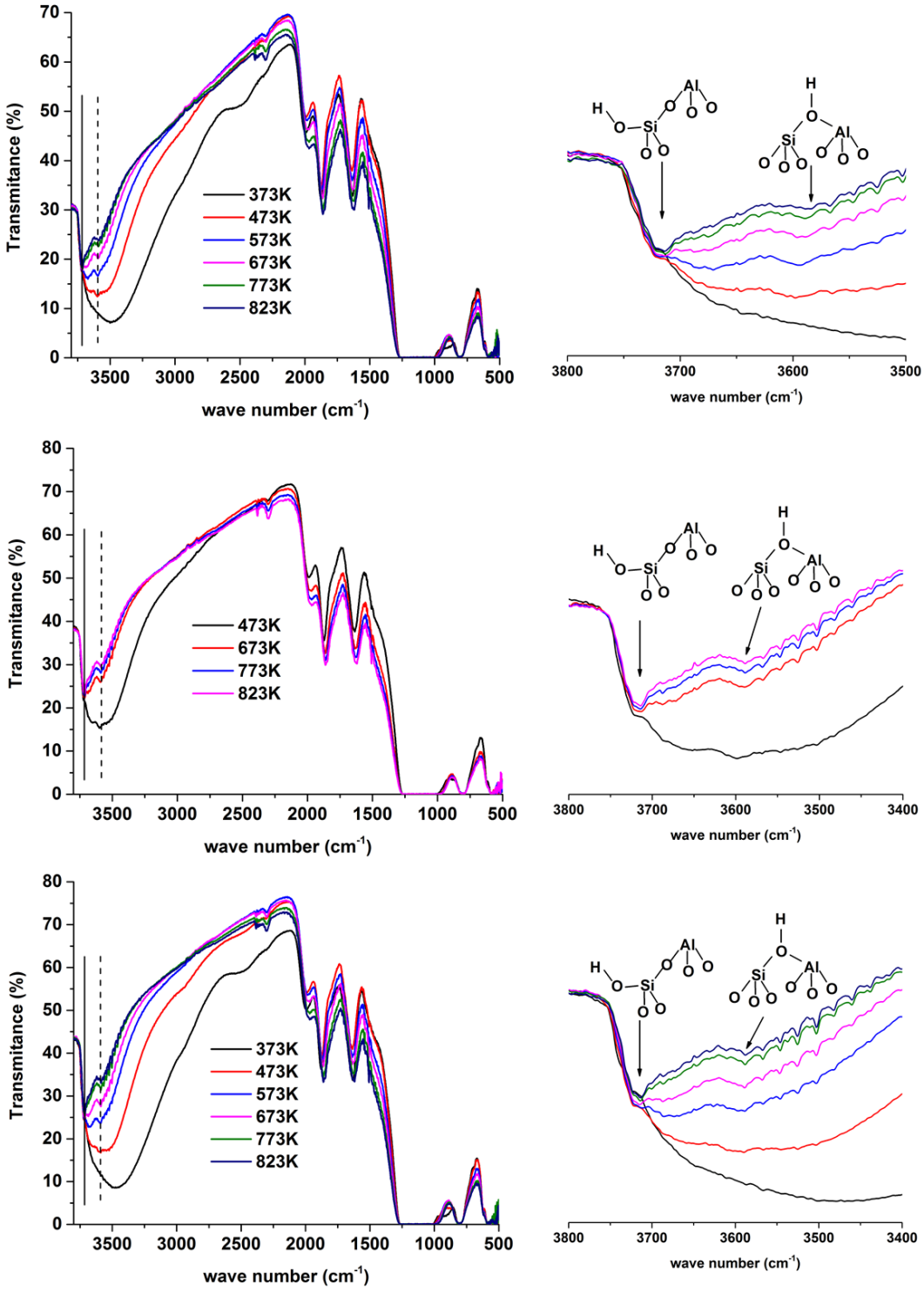

Figure 4.8: FTIR spectra of scaffold templated zeolites showing response of the OH band to temperature. Synthesized with different scaffold concentrations impregnated with 32 ml of gel of Si:Al= 50 (from top to bottom: 3wt%, 4wt% and 5wt% scaffold, the right column is a magnification of the OH region for clarity)

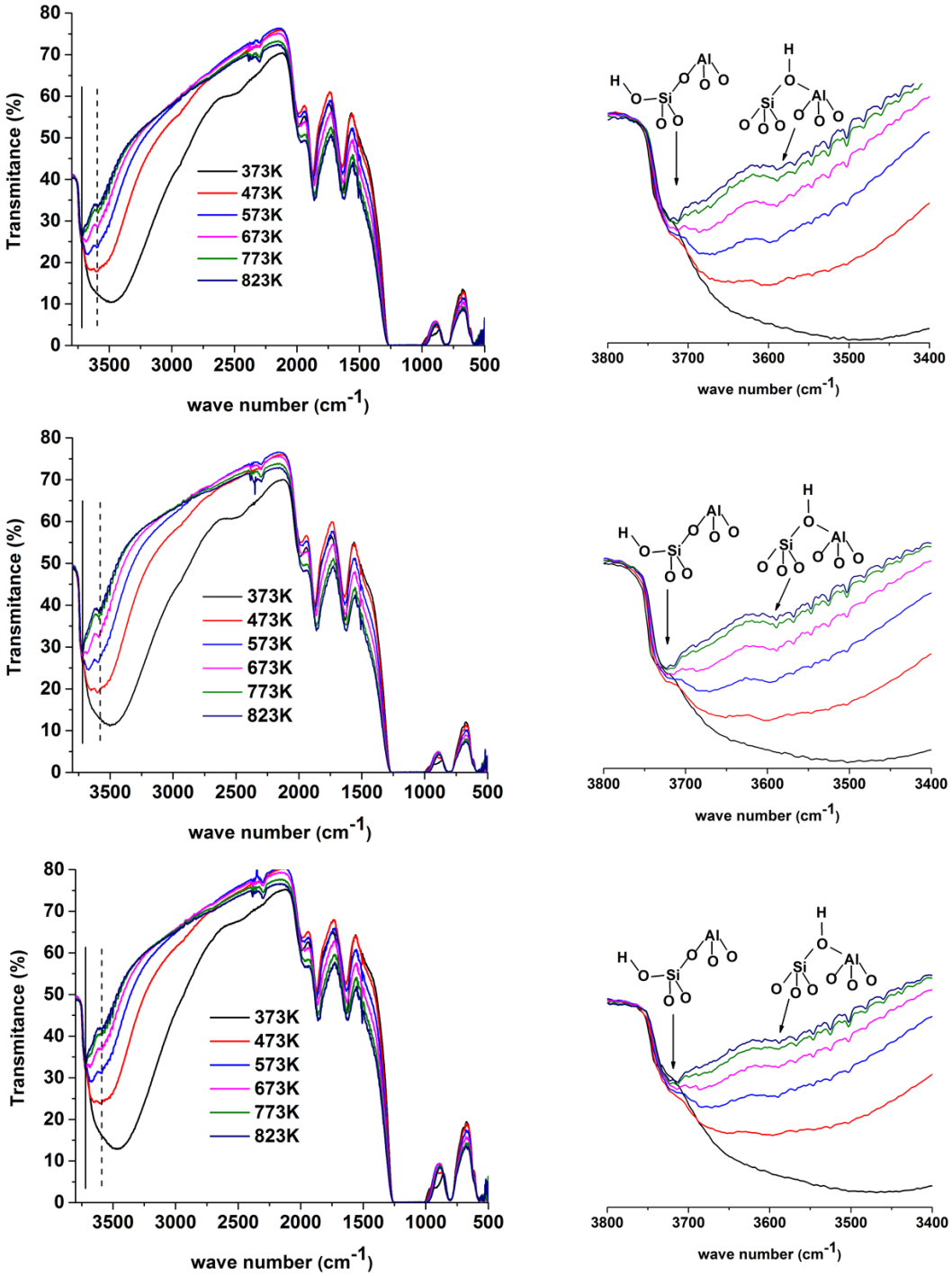

Figure 4.9: FTIR spectra of scaffold templated zeolites showing the response of the OH band to temperature. Synthesized with different scaffold concentrations impregnated with 16ml of gel of Si:Al= 50 (from top to bottom: 3wt%, 4wt% and 5wt% scaffold, the right column is a magnification of the OH region for clarity)

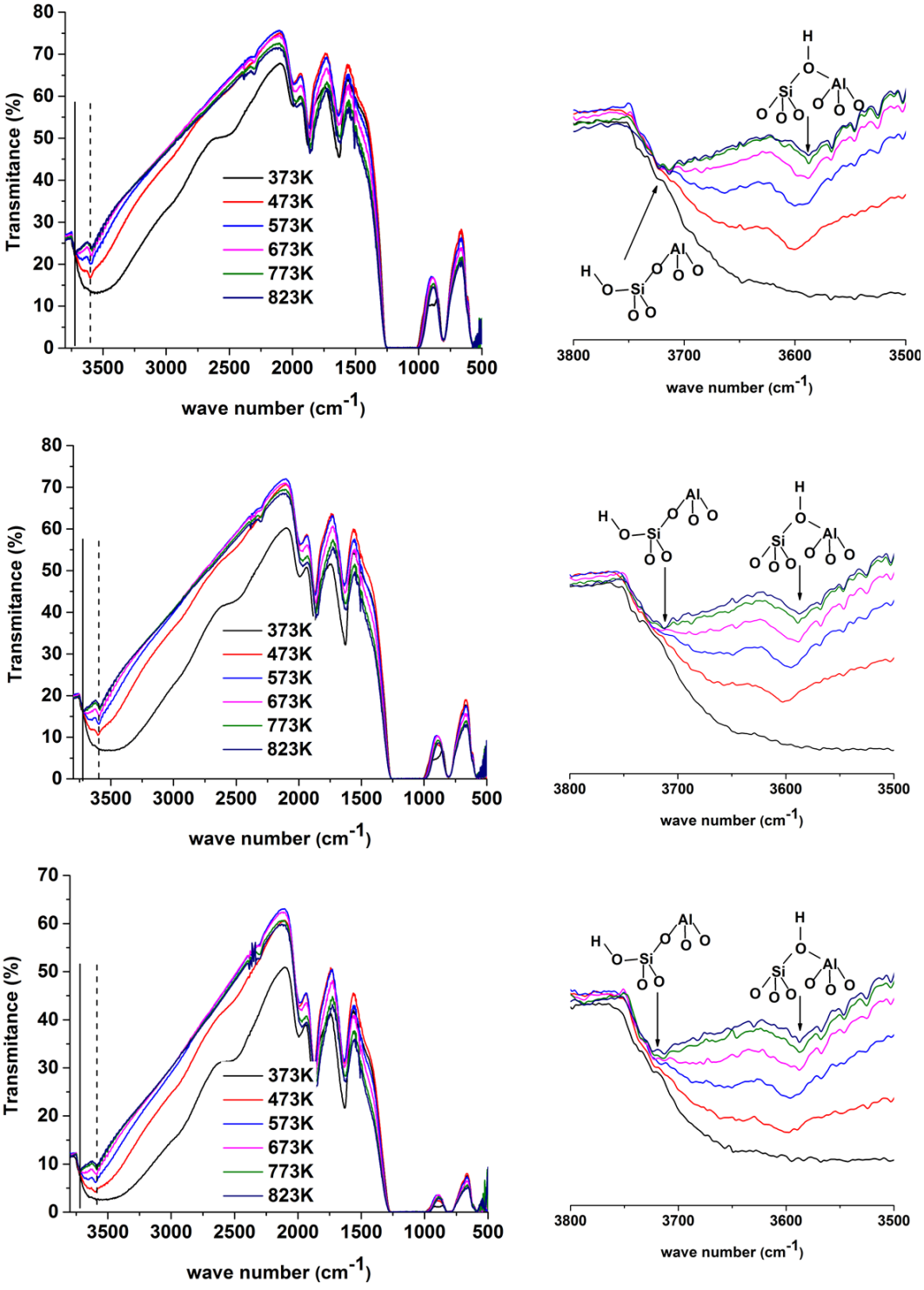

Figure 4.10: FTIR spectra of scaffold templated zeolites showing the response of the OH band to temperature. Synthesized with different scaffold concentrations impregnated with gel of Si:Al=25 (from top to bottom: 3wt%, 4wt% and 5wt% scaffold, the right column is a magnification of the OH region for clarity)

Next we compare the FTIR spectra of all the samples upon *in situ* dehydration in nitrogen at 823 K. Each batch is compared to a reference sample synthesized without scaffold templating. The first batch of samples, in figure 4.11, is that of samples

prepared by impregnating different chitosan scaffolds with 32 ml of zeolite precursor. All samples in this batch show distinct peaks at approximately 3600 and 3700 cm^{-1}. The intensity of the Lewis acid site (*ca* 3700 cm^{-1}) is, however, greater than that of the Brønsted and framework associated OH groups (*ca* 3600 cm^{-1}).

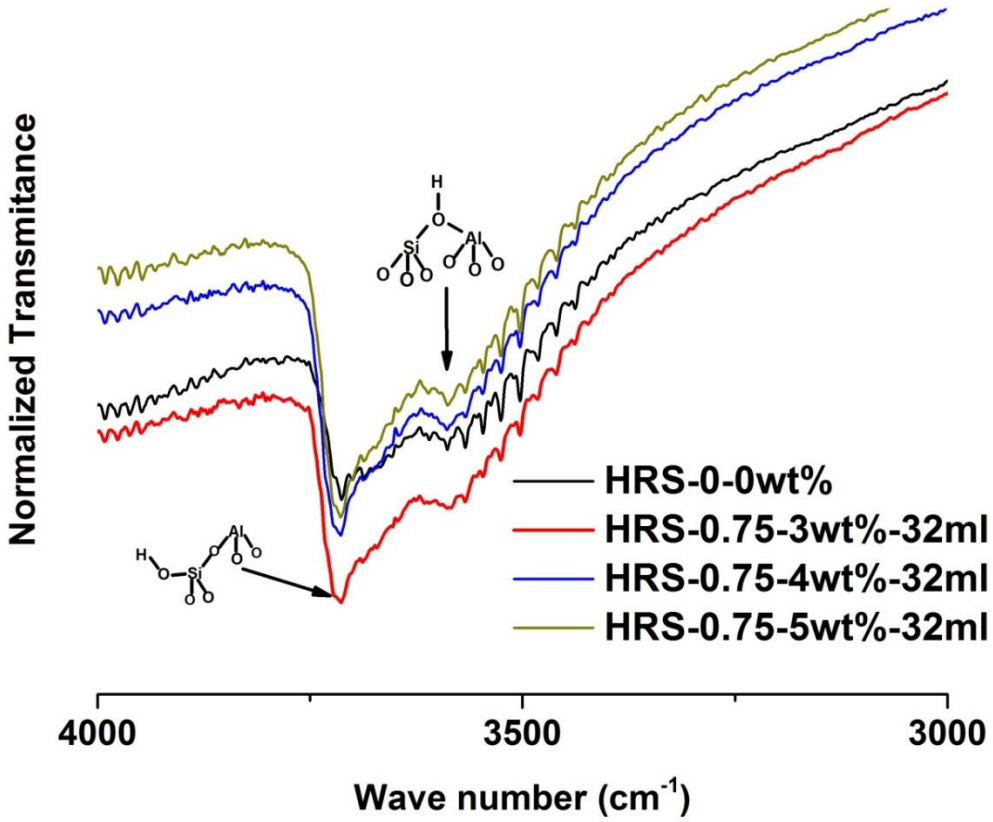

Figure 4.11: Comparison of FTIR spectra of zeolites synthesized in the presence of scaffolds of different weight concentrations that were impregnated with 32 ml of precursor

As the amount of zeolite gel impregnated into the scaffolds was decreased from 32 ml to 16 ml the intensity of the band at 3600cm^{-1} decreased further, with a concomitant increase in the 3700 cm^{-1} band, figure 4.12, implying that more defective sites are being created in the zeolite with decreasing gel presence. This observation seems to imply that, with more chitosan in the synthesis medium, less Brønsted acidity and more defective sites (terminal silanol) are created to ascertain which, 3wt% and 4wt% of chitosan scaffold with 1.5 g and 2.0 g chitosan powder

were used, rather than 0.75 g (see table 4.3) and filled with 32 ml of zeolite precursor with an Si/Al ratio of 50. The FTIR spectra of these samples, which is given in figure 4.13, indeed confirms this proposition.

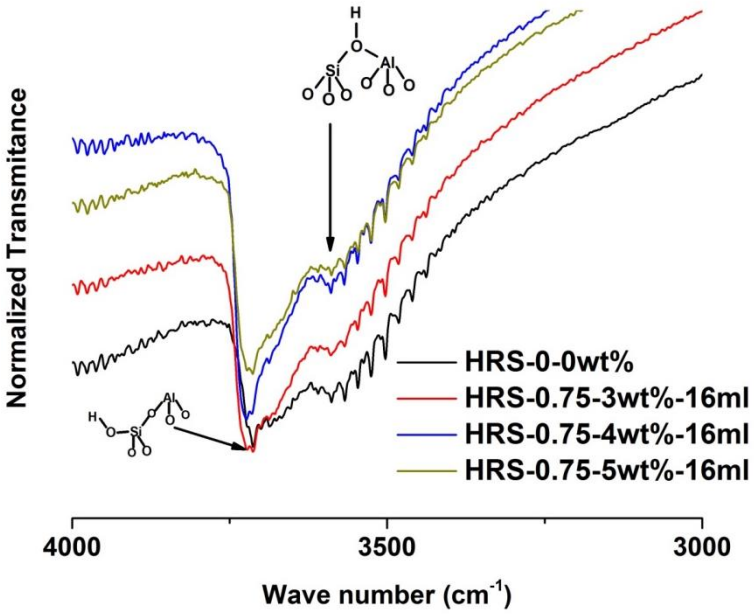

Figure 4.12: Comparison of FTIR spectra of zeolites synthesized in the presence of scaffolds of different weight concentration which were impregnated with 16ml of precursor.

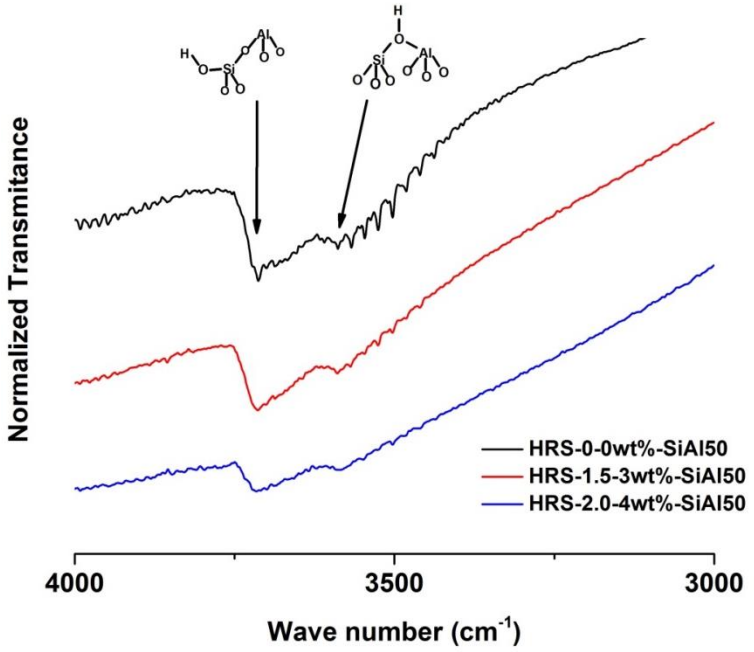

Figure 4.13: Comparison of FTIR spectra of zeolites synthesized in the presence of scaffolds of different weight concentration that were impreganated with a precursor of Si/Al ratio of 50

Figure 4.14 is the FTIR spectra of samples synthesized with a precursor gel of Si/Al ratio of 25, which shows FTIR bands representative of the Brønsted and Lewis sites with an almost equal intensity. It appears from this result that the defective acid sites resulting from the presence of chitosan during synthesis, can be reduced to a large extent with higher aluminium content in the zeolite precursor, which will consequently result in improved acidity.

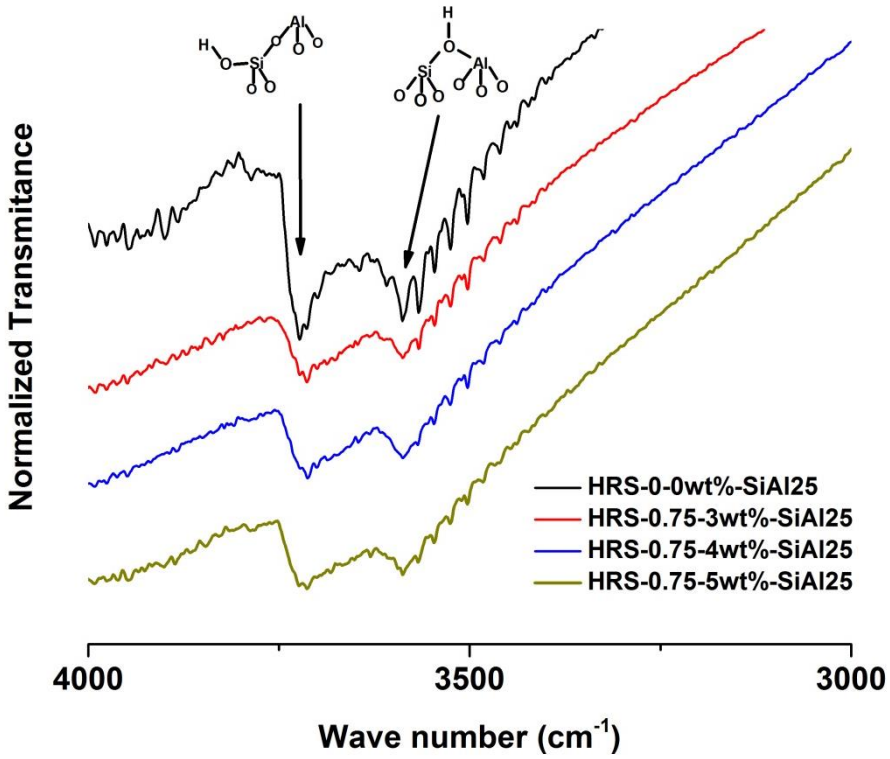

Figure 4.14: Comparison of FTIR spectra of zeolites synthesized in the presence of scaffolds of different weight concentration that were impregnated with a precursor of Si/Al ratio of 25

4.4.5 Morphological investigation by SEM

Figure 4.15 shows the shape and physical features of the samples synthesized in this work. The samples obtained in the absence of chitosan scaffold (0 wt%) clearly show the distinct and freely existing coffin-shape crystal morphologies that are typical of MFI zeolites. The particle size can also be observed to vary widely.

On the other hand, the samples obtained by using the chitosan scaffolds as macro-templates show relatively uniform size distribution. More significantly they display crystals with step growth. The step growth became increasingly smaller as the percentage chitosan concentration increased. A possible explanation for the observed morphology of the scaffolded samples could be that the pores of the scaffolds acted as micro-reaction sites, constraining the growth of individual particles to that pore space.

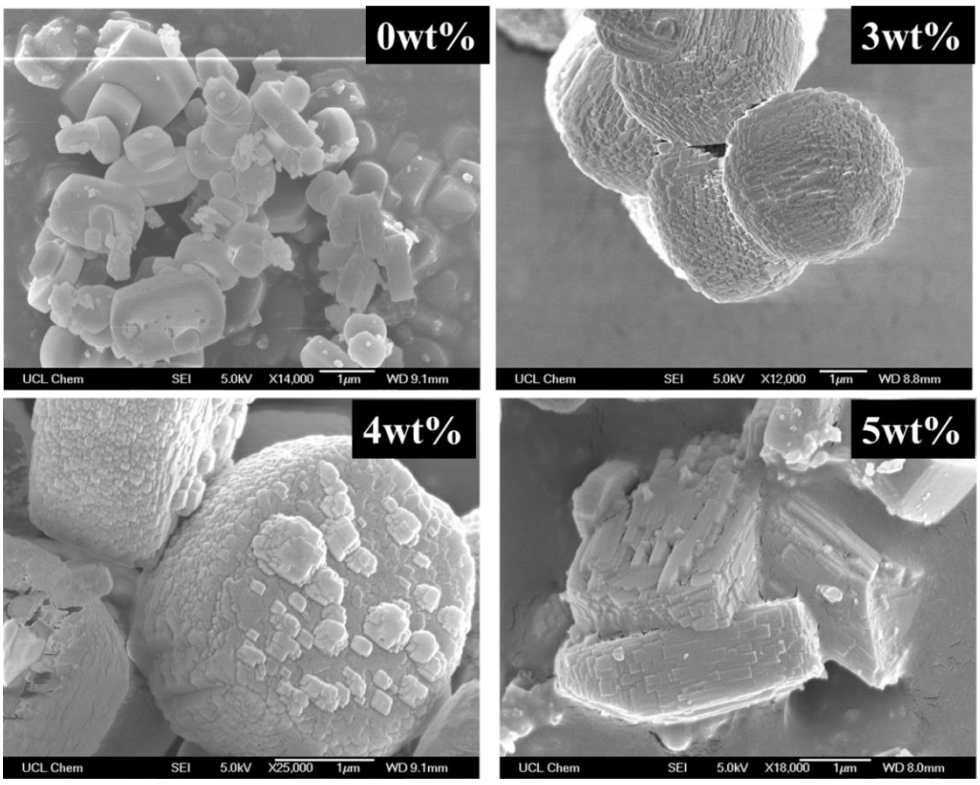

Figure 4.15: SEM micrographs of zeolites obtained from scaffolds impregnated with 32ml of zeolite precursor (precursor Si/Al = 50; chitosan weight of 0.75g)

As the volume of the zeolite precursor filled on the scaffold was reduced to 16 ml (figure 4.16), the particles grew smaller and the shape became less distinctive, which can be ascribed to restriction in the crystal growth as the pores of the scaffolds were probably not completely filled, and there was limited nutrient for the continuous crystal growth in the individual scaffold pores.

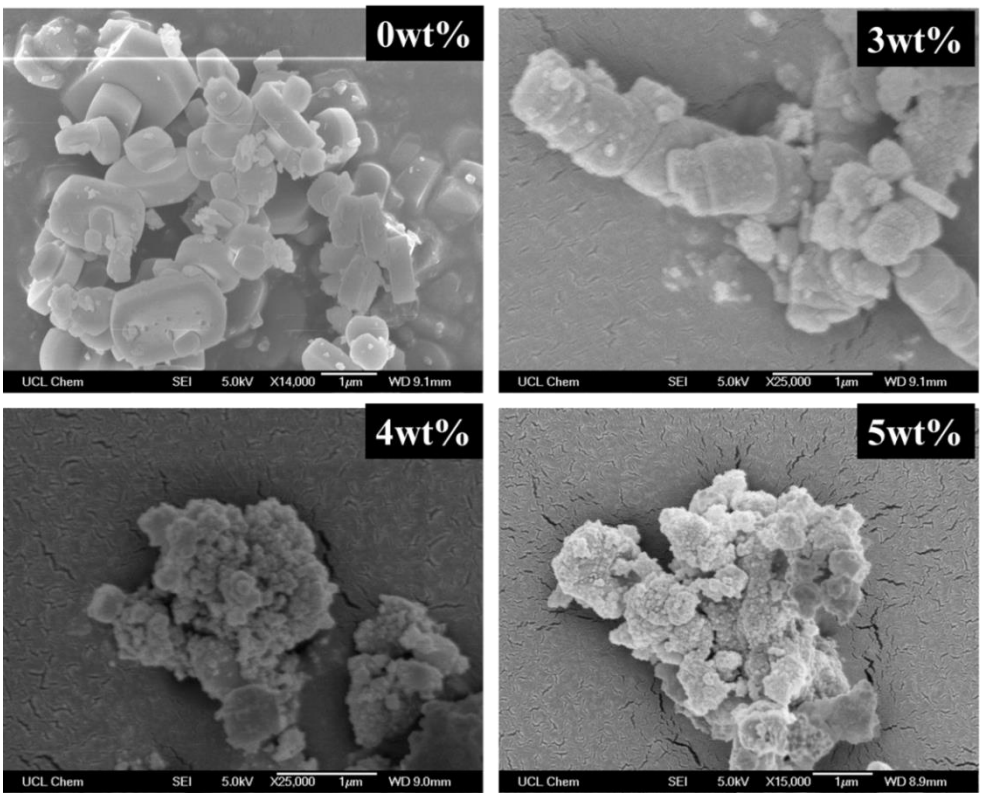

Figure 4.16: SEM micrographs of zeolites obtained from scaffolds impregnated with 16ml of precursor (precursor Si/Al = 50; chitosan weight of 0.75g)

The effect of the Si/Al ratio of the zeolite precursor on the morphology of the resulting zeolite was also investigated. Figure 4.17 shows that the sample without chitosan (0 wt%) also has some step growth, but to a minimal degree. In contrast, the scaffold templated samples display particles with uniform layered growth with the steps appearing smaller than observed in the samples with an Si/Al ratio of 50.

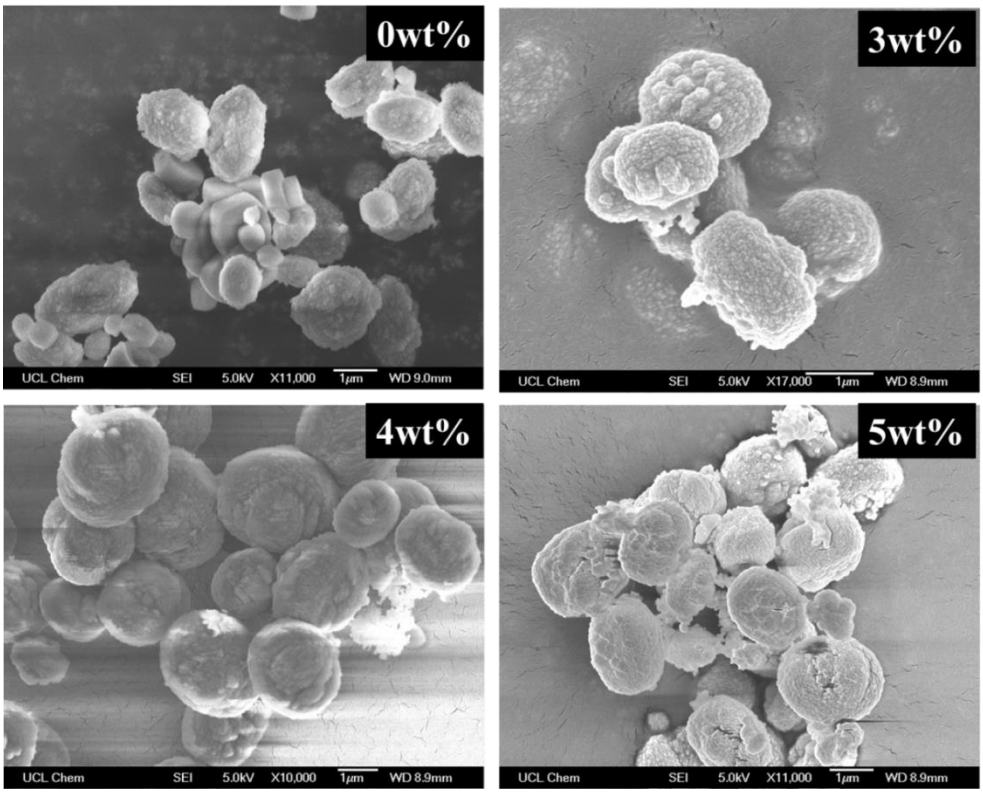

Figure 4.17: SEM micrographs of zeolites obtained from scaffolds impregnated with 32ml of zeolite precursor (Precursor Si/Al = 25; chitosan weight of 0.75g)

4.4.6 Textural characterization

Figure 4.18 gives the isotherms and pore size distribution of the samples with an Si/Al ratio of 50. The isotherms for samples synthesized in the scaffold pores display type IV hysteresis loop in the high relative pressure region, which is typical of materials with coexisting micro-mesopores; this is confirmed by the pore size distribution, which shows peaks at approximately 20 Å (micropore) and 50 Å (mesopore). The isotherm of the samples synthesized without scaffold (0 wt%) typifies that of materials with a predominantly microporous structure.

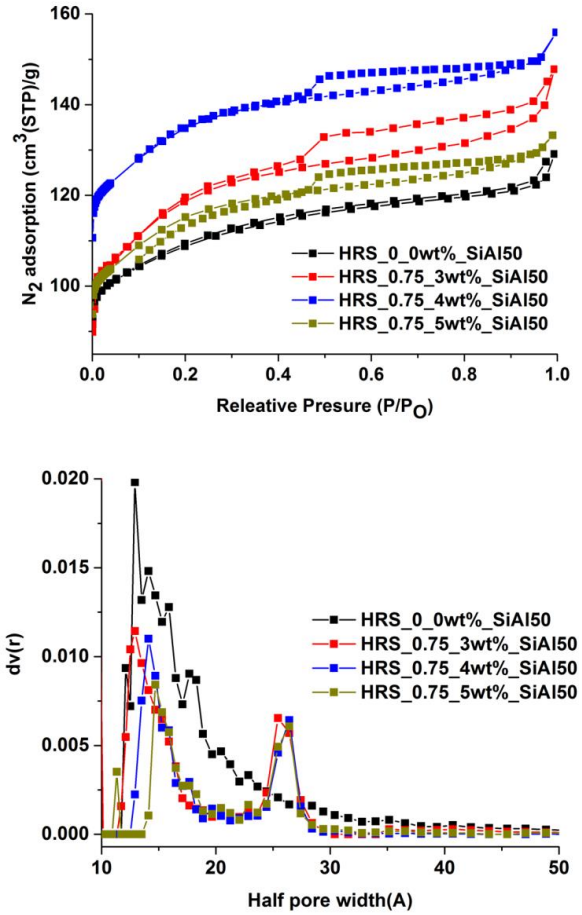

Figure 4.18: Nitrogen adsorption isotherms (top) and pore size distributions (bottom) of samples synthesized from a precursor with an Si/Al of 50

The effect of the silicon to aluminium ratio on the pore distribution is illustrated in figure 4.19. Upon doubling the aluminium content in the starting gel, a wide hysteresis was exhibited by the sample synthesized without chitosan. The reason for this is as yet unclear, but hints from the SEM micrographs of this sample suggest this may be a result of the small particle size and the step growth, to which inter-crystal void can be a contributory factor.

When the zeolite gel filled into each scaffold was decreased to 16 ml, the pore distribution showed a decrease in the intensity (figure 4.20) of the pore at 50 Å with a concomitant increase in the micropore volume, suggesting a decrease in the number of mesopores. The adsorption isotherm, however, suggests these samples still possess dual modal pore composition.

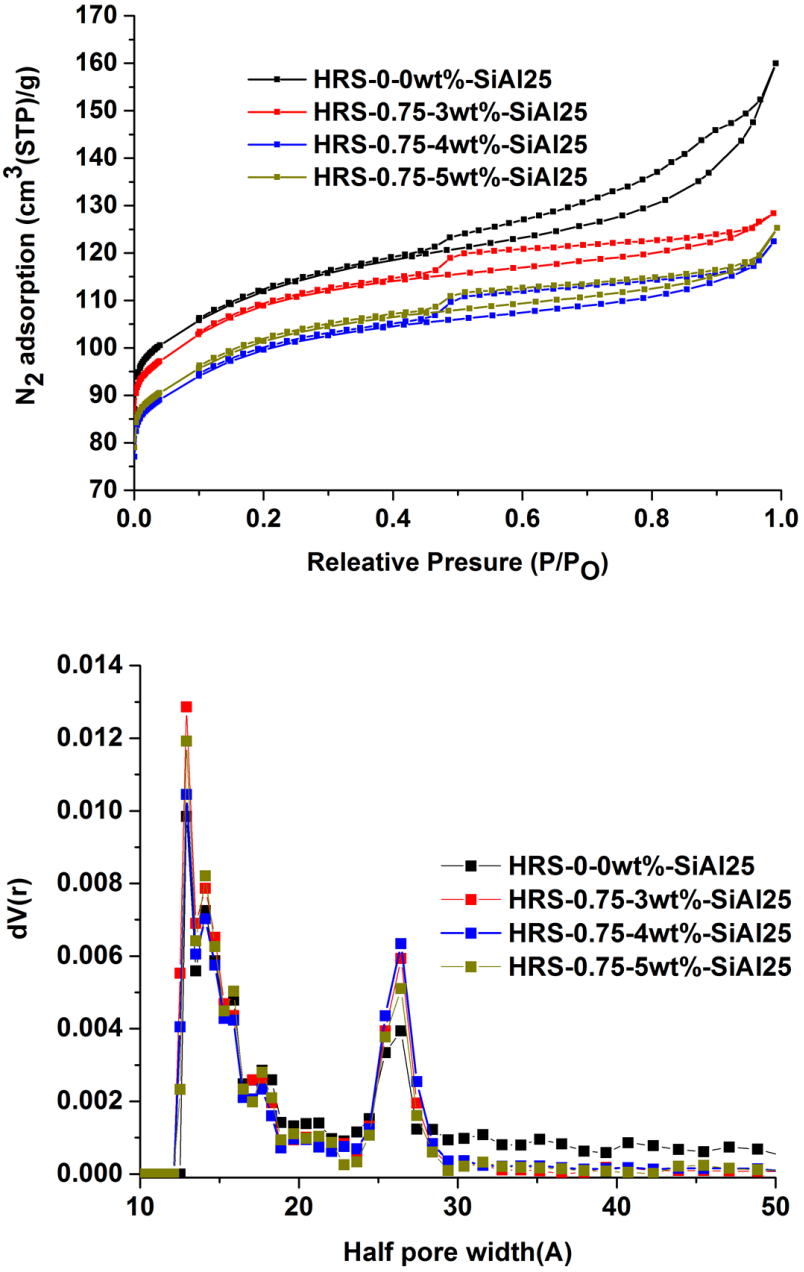

Figure 4.19: Nitrogen adsorption isotherms (top) and pore size distributions (bottom) of samples synthesized from a precursor with an Si/Al ratio of 25

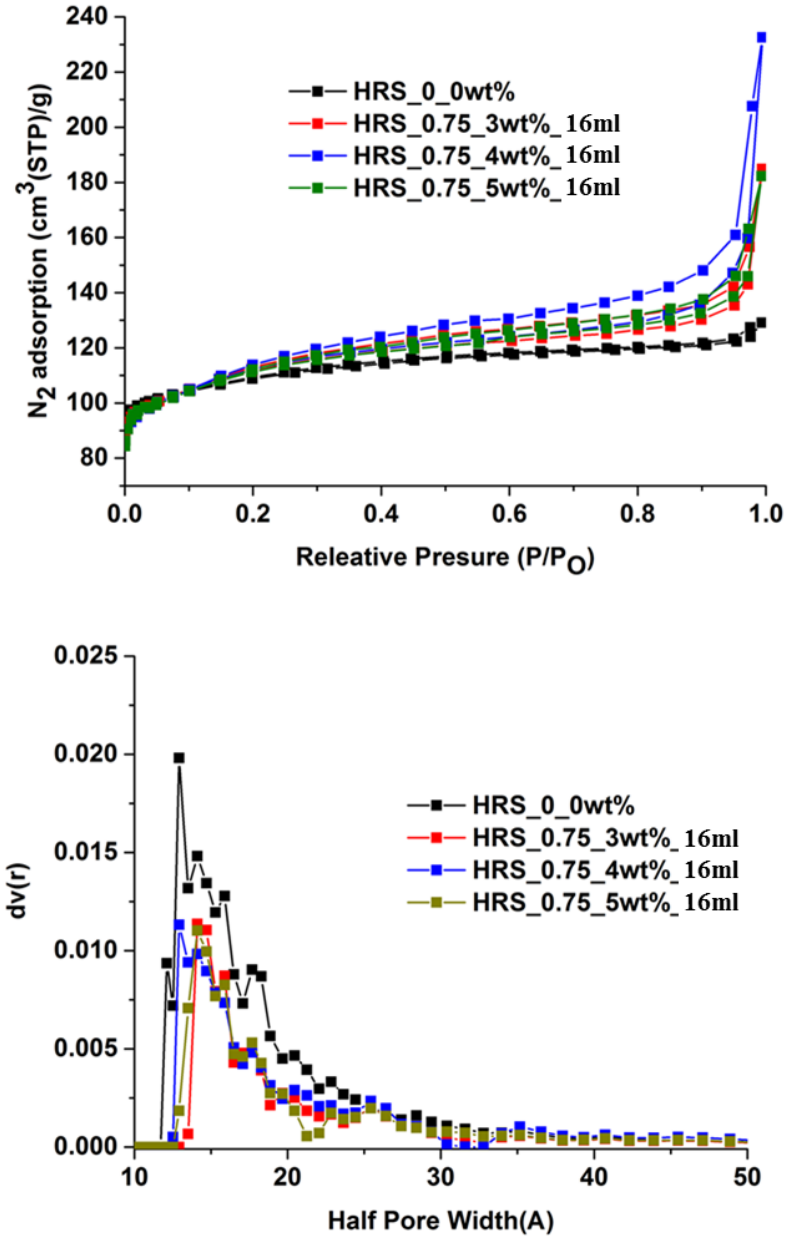

Figure 4.20: Nitrogen adsorption isotherms (top) and pore size distributions (bottom) of samples synthesized with 16 ml of precursor with an Si/Al ratio of 50

4.4.7 Location of T-atoms

The environment of the aluminium and silicon atoms in the zeolite structure was investigated by solid state NMR. All of the samples synthesised in this chapter show two characteristic silicon environments from ^{29}Si NMR. The first silicon environment corresponds to that of a silicon atom that is coordinated by four other silicon tetrahedra through oxygen linkages (Q0 environment) while the second corresponds to a silicon atom that is coordinated by three silicon tetrahedra and an aluminium tetrahedron (Q1 environment) [43, 44]. The main peak at the chemical shift of *ca* -115ppm corresponds to the Q0 environment, which is to be expected for a highly siliceous zeolite like ZSM-5[44]. The second peak, which centres at about -105 ppm, is that of the Q1 silicon environment, and is the environment that is mainly responsible for the acidity of the zeolite. The intensity of this peak increased with the aluminium concentration in the zeolite precursor, as presented in figure 4.21. This peak also became less broad as the aluminium concentration in the starting precursor was doubled.

The nature of the aluminium environment was elucidated by ^{27}Al NMR. In all of the samples investigated here, again, two main peaks were observed. The peak at *ca* 60 ppm chemical shift is indicative of aluminium in tetrahedral coordination, (framework associated) while that at 0 ppm signifies the existence of extra framework aluminium species [44]. Notably, in all the samples, the aluminium exists predominantly in the desired tetrahedral environment. Samples synthesized from a starting gel of higher aluminium composition exhibit more of the extra framework species (figure 4.22) compared to those obtained from a lower aluminium concentration.

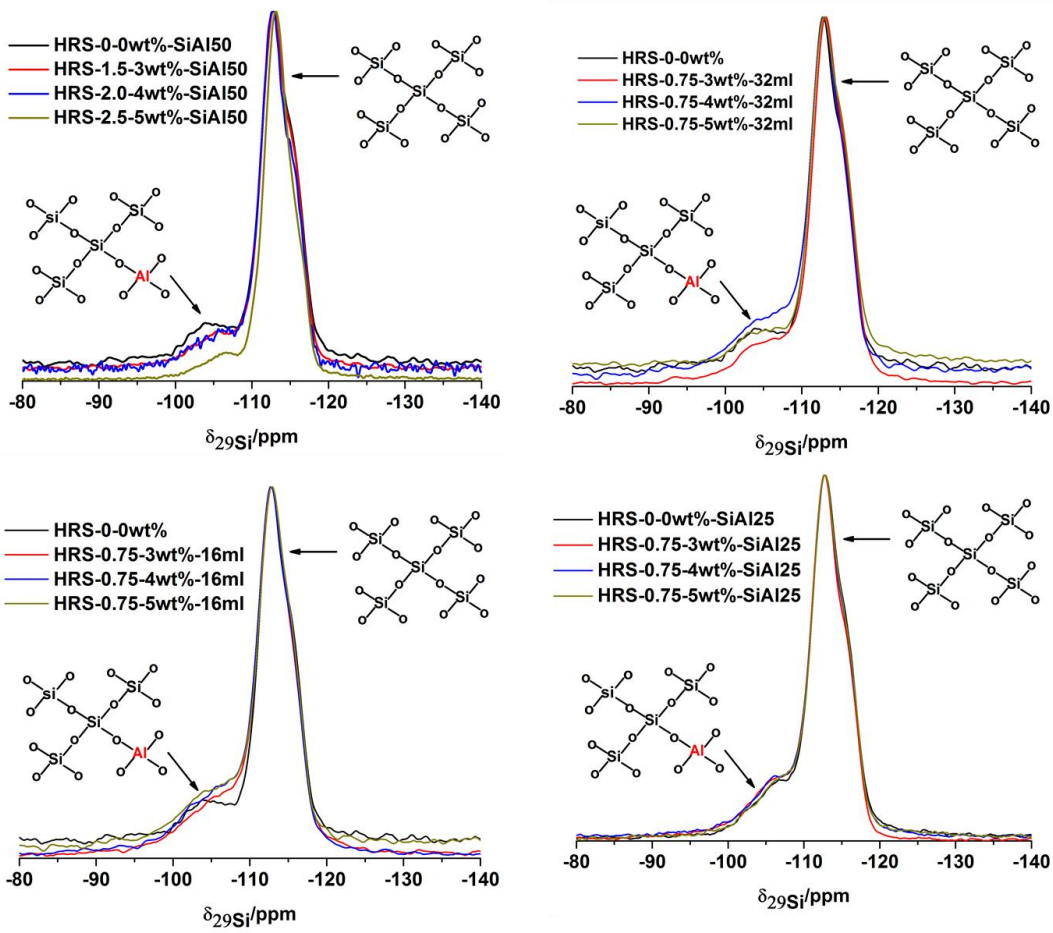

Figure 4.21: Solid state ^{29}Si NMR showing the silicon environments in all the synthesized samples

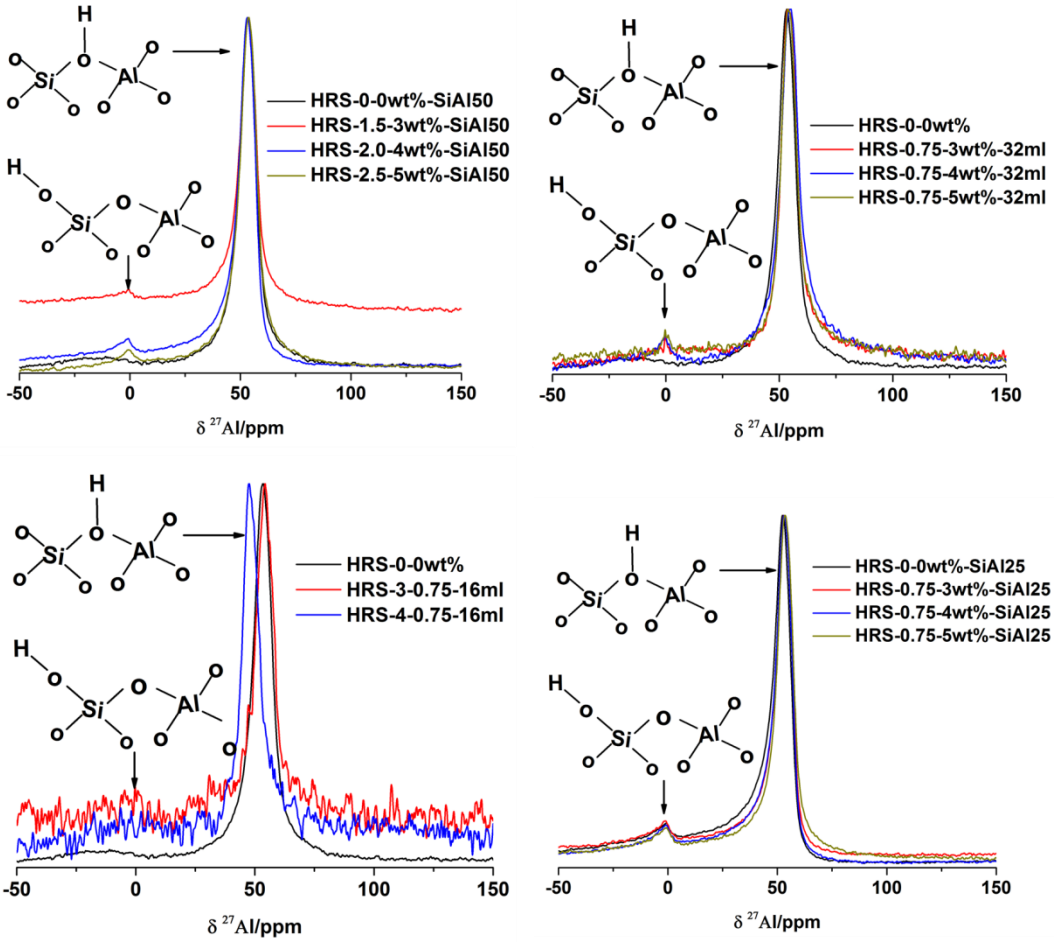

Figure 4.22: Solid state NMR showing the aluminium environments in all the synthesized samples

4.4.8 Catalytic evaluations

The predominant components of the organic phase of the reaction products from the methanol to hydrocarbon reaction are summarized in figure 4.23. These components are basically five different aromatic products (xylene, ethyltoluene, diethylbenzene, trimethylbenzene and tetramethylbenzene) and their isomers. The composition of

these products, and the ratio or dominance of any particular isomer, was correlated to the structural properties of the catalysts.

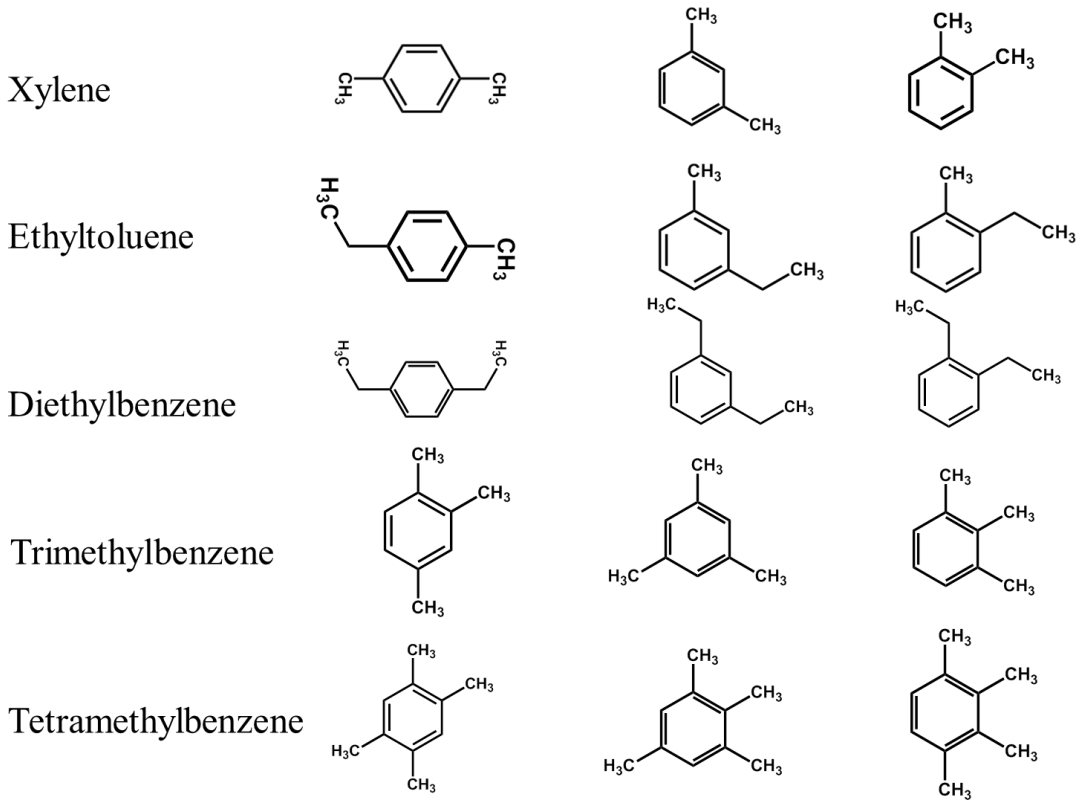

Figure 4.23: Main reaction products from the liquid phase of the MTH reaction carried out over the samples synthesized in this work

To gain insight into the composition of these products, the GC chromatogram of the catalytic products from each sample is compared. In each, the two dominant product peaks are those with retention times of 9.66 and 12.41 minutes. The 9.66 minute peak corresponds to a combination of meta- and para-xylene isomers, while the peak at 12.41 minute is of 1,2,4-trimethylbenzene. In all of the product mixtures there is no noticeable difference in the intensity of the meta- and para-xylene isomers; except for the 4 wt% at 32 ml precursor loading, which has a lower peak intensity for the meta- and para-xylenes as compared to the other catalysts. The intensity of the 1,2,4-trimethylbenzene signal shows a very distinct response to the chitosan concentration in the starting gel.

Beginning with figure 4.24 and table 4.4, which are respectively the chromatogram and normalized distribution of reaction products obtained over samples synthesized by impregnating the chitosan scaffolds with 32 ml of zeolite precursor, all the scaffold templated samples have higher 1,2,4-trimethylbenzene isomer concentration than the sample synthesized without the scaffold. The peak at a retention time of 10.23 min is that of ortho-xylene isomer. This is the bulkiest of the three isomers of xylene, and the three templated zeolites have a higher peak response for this isomer compared to the reference sample, which implies that these templated zeolites have pores that are large enough to allow the formation of this bulky isomer.

Another interesting shift in product isomer is that of the ethyltoluene. These products emerge from the GC column at retention times of 11.68 to 11.76 minutes. The untemplated sample showed selectivity to the para-ethyltoluene isomer, while the sample templated with 3 wt% scaffold displayed virtually no preferred selectivity since both the meta-ethyltoluene and para-ethyltoluene isomers have equal intensity. The samples templated with 4 wt% and 5 wt% scaffolds, however, showed higher selectivity to the meta-ethyltoluene isomer. The ortho-ethyltoluene isomer was not observed for any of the catalysts in this series. Table 4.4 gives the normalized distribution of the major products from this

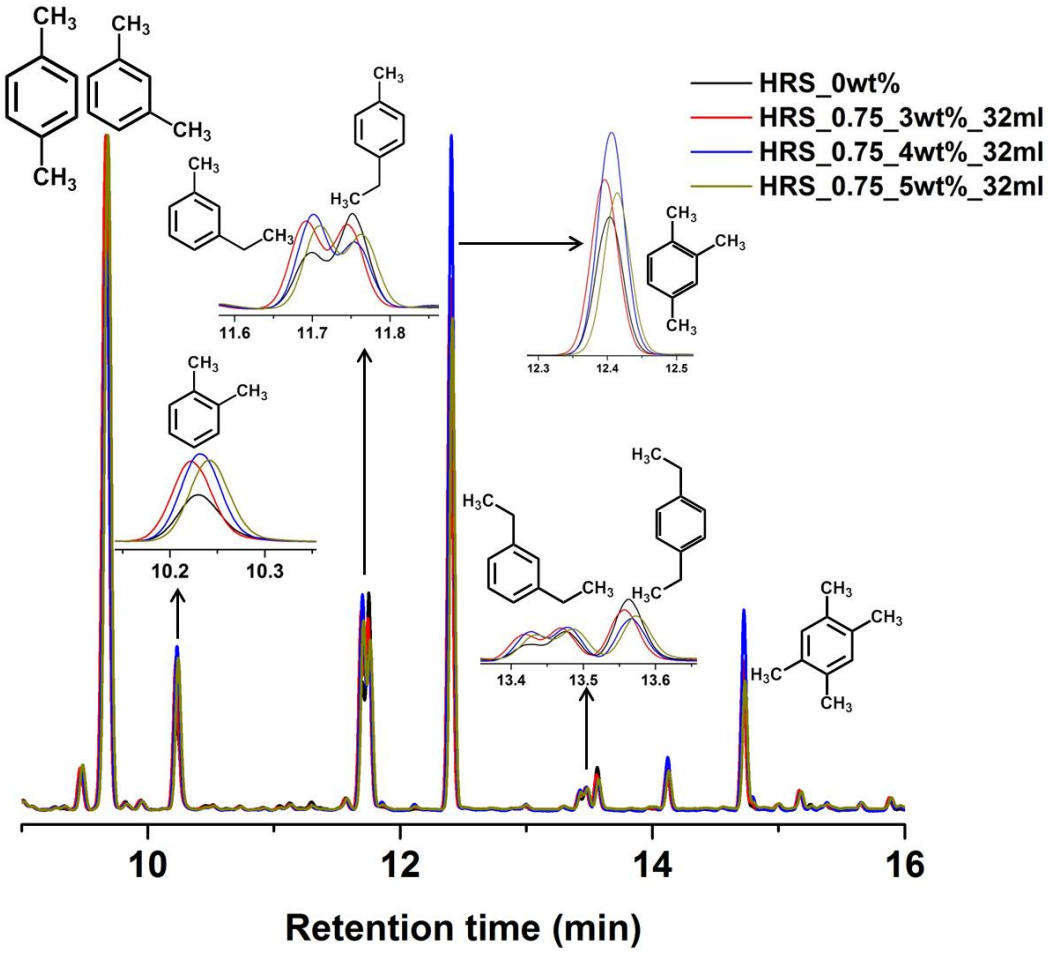

Figure 4.24: Normalized GC chromatogram of reaction products over zeolites obtained from scaffolds templated with 32ml of zeolite precursor with Si:Al = 50

Table 4.4: Normalized composition of the major aromatic products (catalyst batch: 0.75g scaffold impregnated with 32ml of the zeolite precursor, Si/Al=50)

	HRS-0-0wt%-50	HRS-0.75-3wt%-32ml	HRS-0.75-4wt%-32ml	HRS-0.75-5wt%-32ml
		Normalized Composition (%)		
xylene				
p+m	31.05	27.37	22.06	29.25
O	8.07	11.20	12.20	12.64
E-toluene				
P	14.62	10.30	7.60	9.63
M	5.73	8.53	9.19	8.49
O				
DEB				
M	1.17	1.32	0.68	0.22
P	2.85	2.00	1.12	1.57
TMB	30.45	33.18	39.24	32.13
Durene	6.06	6.10	7.91	6.07

Figure 4.25 is the normalized GC chromatogram of the products obtained over samples synthesized by impregnating the chitosan scaffolds with 16 ml of the zeolite precursor. The product distribution over these samples showed a different trend compared to those with 32 ml precursor in the scaffold (figure 4.24). As can be seen in figure 4.25 and summarized in table 4.5, the sample obtained from the 4wt% scaffold displayed higher selectivity for the meta-ethyltoluene isomer, while the 0 wt% and 3 wt% samples showed more preference for the para-ethyltoluene isomer. Similarly, the response of the 4 wt% sample for the ortho-xylene isomer is higher than those of 0 wt% and 3 wt% samples.

Figure 4.26 illustrates the distinct influence of the chitosan on the physical and chemical features of the resulting zeolite, and its role in shifting product selectivity. The scaffolds used here were prepared with higher amounts of chitosan (1.5 g and 2.0 g) compared to 0.75 g of chitosan used for other scaffolds. For the first time in this study, and contrary to figure 4.24 and 4.25, the intensity of the ethyltoluene isomers was seen to outweigh that of the trimethylbenzene product for the templated samples; the ortho-xylene isomer (10.2 - 10.3 min retention time) is also observed to have significantly diminished in intensity. As is clear from table 4.6, this set of catalysts can be said to be highly selective towards the para-ethyltoluene isomer.

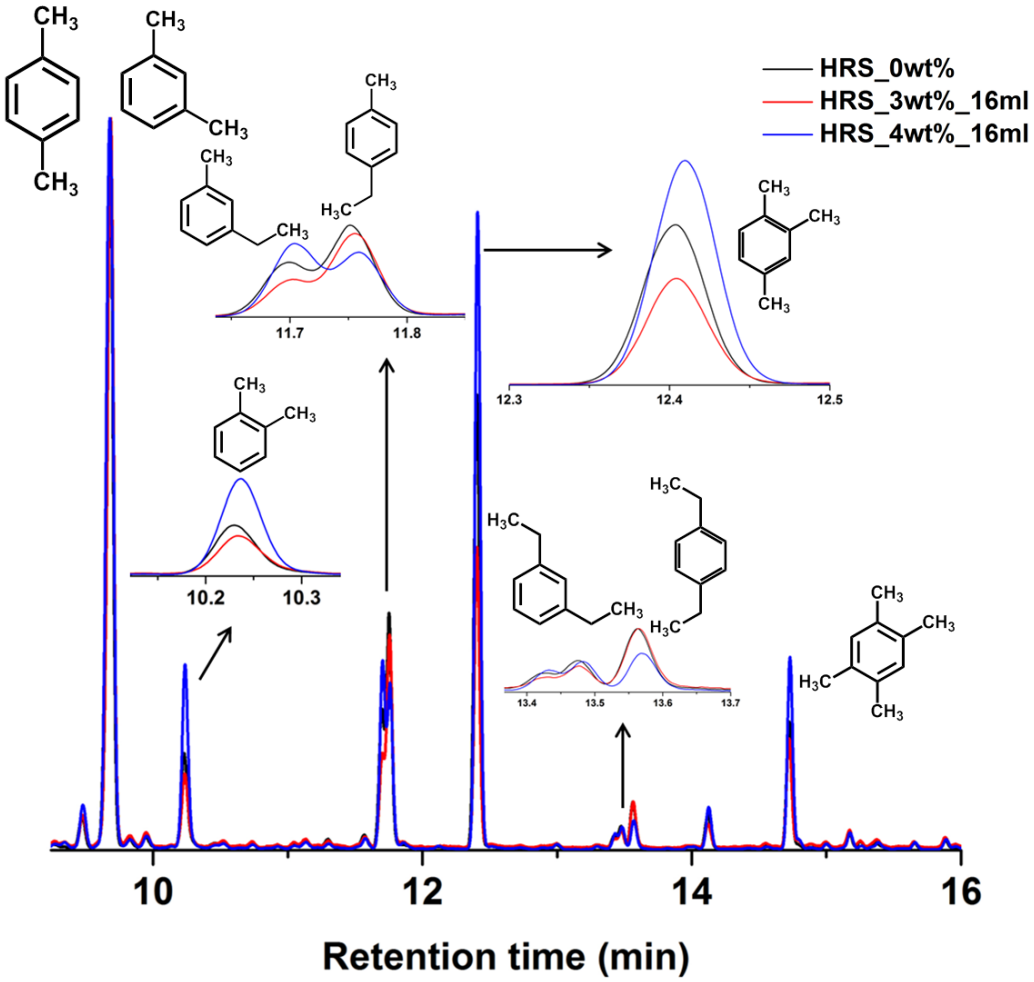

Figure 4.25: Normalized GC chromatogram of reaction products over zeolites obtained from scaffold templated with 16ml of zeolite precursor with SiAl =50

Table 4.5: Normalized composition of the major aromatic products (catalyst batch: 0.75g scaffold impregnated with 16ml of the zeolite precursor; Si/Al=50)

	HRS-0-0wt%-50	HRS-0.75-3wt%-16ml	HRS-0.75-4wt%-16ml
	Normalized Composition (%)		
xylene			
p+m	31.05	37.71	27.23
O	8.07	7.51	13.03
E-toluene			
P	14.62	16.04	7.31
M	5.73	4.32	7.82
O			
DEB			
M	1.17	0.00	0.74
P	2.85	3.64	1.19
TMB	30.45	24.56	35.16
Durene	6.06	6.22	7.52

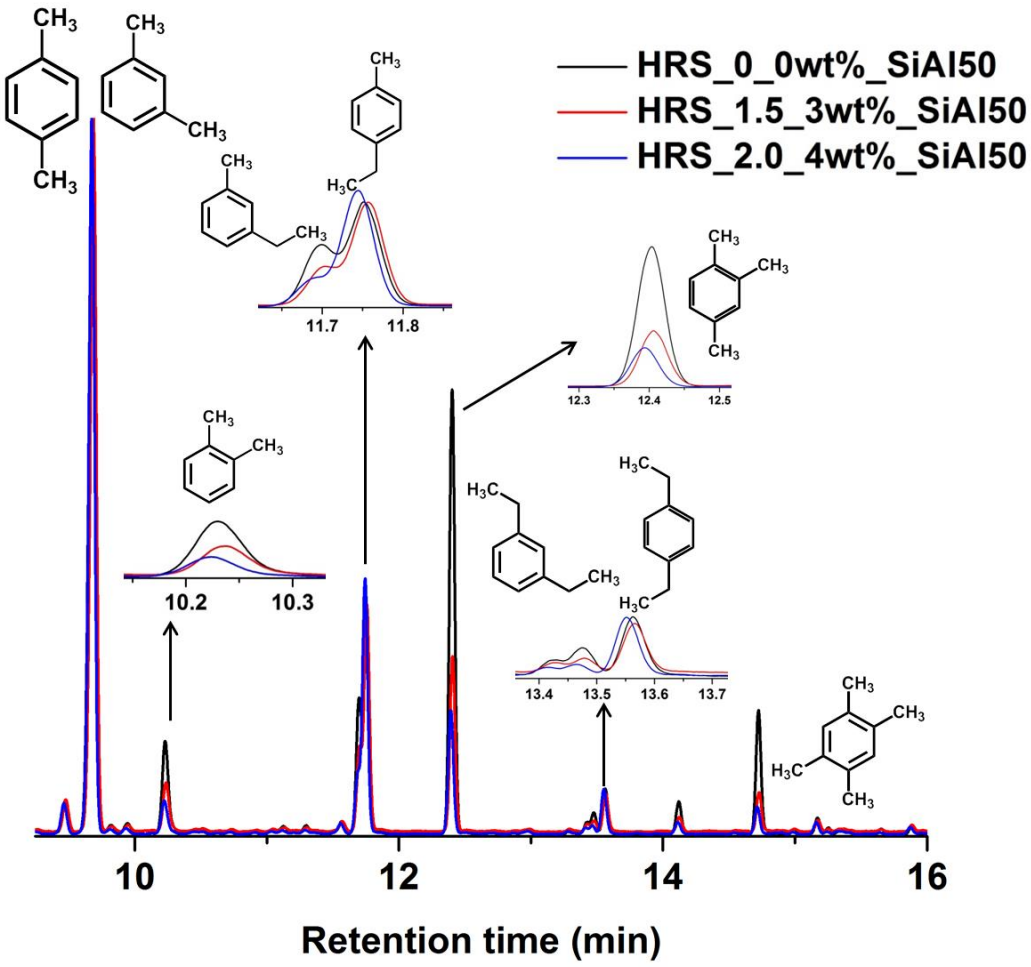

Figure 4.26: Normalized GC chromatogram of reaction products over zeolites obtained from scaffold templated zeolite (Scaffolds prepared with different mass of chitosan powder) Gel SiAl =50

Table 4.6: Normalized composition of the major aromatic products (catalyst batch:1.5g and 2.0g scaffold)

	HRS-0-0wt%-50	HRS-1.5g-3wt%-SiAl50	HRS-2.0-4wt%-SiAl50
	Normalized Composition (%)		
xylene			
p+m	31.05	40.33	42.50
O	8.07	6.53	4.60
E-toluene			
P	14.62	27.90	31.01
M	5.73	0.53	0.56
O			
DEB			
M	1.17		
P	2.85	3.97	5.48
TMB	30.45	17.79	13.68
Durene	6.06	2.95	2.17

The influence of the aluminium content in the starting synthesis precursor on the product distribution is illustrated in figure 4.27 (see table 4.7 for normalized distribution). The most significant observation for these series of samples is the shift in the selectivity of the untemplated sample (0 wt%) from para-ethyltoluene to meta-ethyltoluene. This observation may be attributed to two possibilities: first is the presence of larger pores in this sample, as demonstrated by the pore size distribution in figure 4.19, the second could be the strength of the acid sites, as there are now more Brønsted acid sites available, as seen in the FTIR spectra of figure 4.14

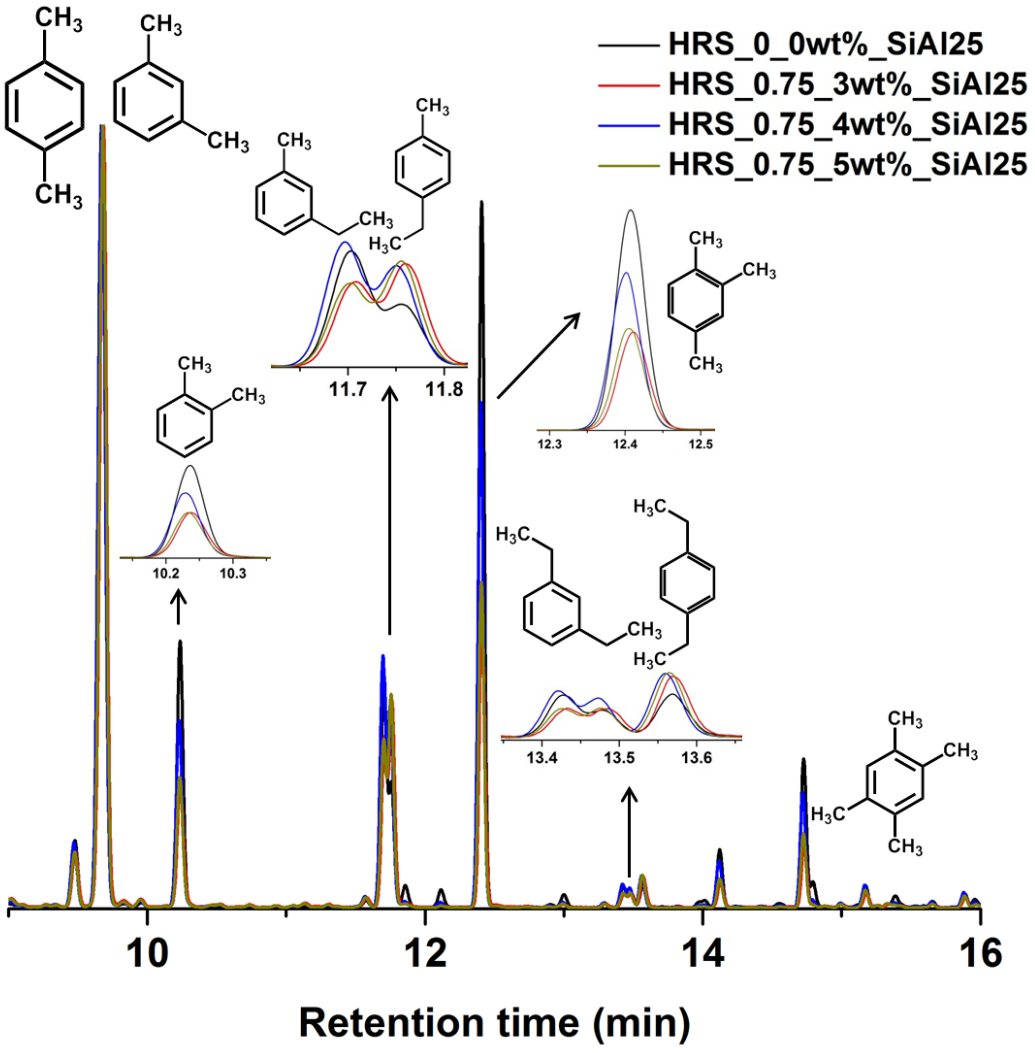

Figure 4.27: Normalized GC chromatogram of reaction products over zeolites obtained from scaffolds templated with 32ml of zeolite precursor with SiAl =25

Table 4.7: Normalized composition of the major aromatic products (catalyst batch: 0.75g scaffold impregnated with 32ml of zeolite Precursor; Si/Al=25)

	HRS-0-0wt%-25	HRS-0.75-3wt%-SiAl25	HRS-0.75-4wt%-SiAl25	HRS-0.75-5wt%-SiAl25
xylene				
p+m	26.74	37.29	30.03	35.74
O	16.79	12.14	13.39	12.09
E-toluene				
P	5.21	13.51	10.36	13.87
M	9.01	8.07	10.62	8.25
O				
DEB				
M	0.33	0.24	0.37	0.23
P	0.88	2.07	1.53	2.23
TMB	36.04	23.16	29.03	23.76
Durene	5.00	3.52	4.67	3.83

4.4.9 Coke analysis

The coke analysis of the spent catalysts was conducted by two different techniques. The amount of coke deposited on the catalysts during the course of the reaction was estimated by thermal analysis, while Raman spectroscopy was used to determine the nature of the cokes deposited on the catalysts during the reaction.

4.4.9.1 Thermal analysis

About 12 to 15mg of each used catalyst was treated in a TGA instrument. The sample was heated to 1000 ^{O}C at 10 K/min. The amount of coke was determined by taking the mass of sample before and after the thermal treatment, from which the total coke formed in a 200mg catalyst (200 mg is the mass of catalyst used in the reaction) was calculated.

The summary of the amount of coke formed on each catalyst from each batch is presented in tables 4.8 - 4.11. In all of the batches, the samples with 4 wt% chitosan

generated the least amount of coke, which can imply that the 4 wt% scaffold composition is the optimum to achieve the most stable sample.

Furthermore, the samples with less aluminium content (less acidity) also generated less coke during the reaction as compared to those with higher aluminium concentration. The high acidity of these samples may have resulted in excessive cracking, leading to the generation of more soot.

In all of the catalysts, the coke was completely removed after thermal treatment in air at about 600 ^{O}C. This is particularly important as it implies that the catalysts can be reused upon regeneration. Evidence of complete removal of the deposited coke can be seen from the TGA thermograph in figure 4.28. Raman spectra of each samples, (figure 4.30) taken after the spent catalysts have been thermally treated in the TGA also supports this conclusion, as the spectra showed no bands attributable to carbon.

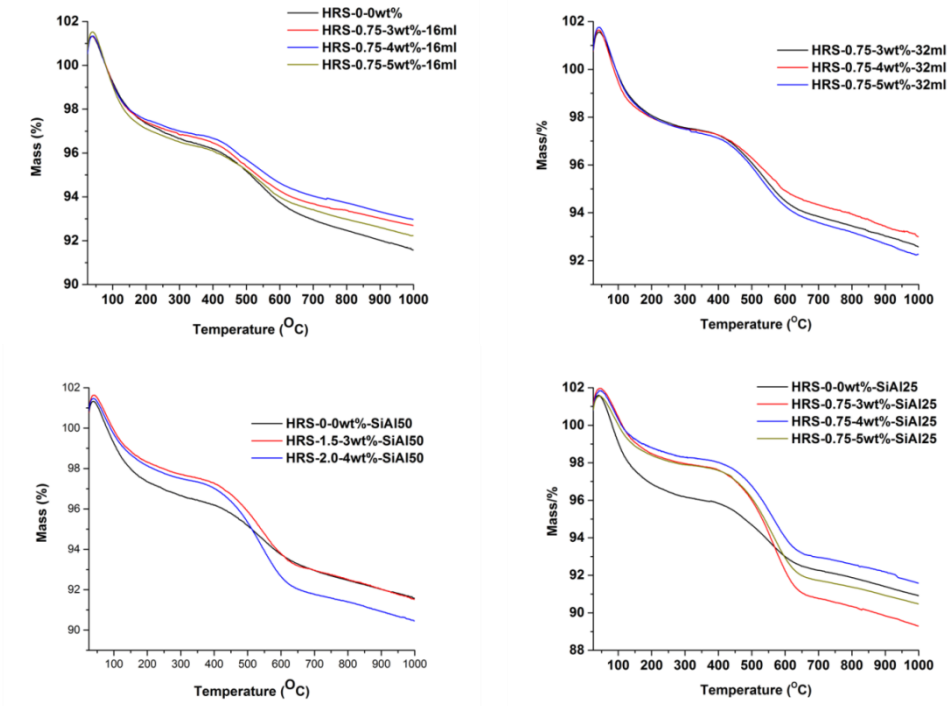

Figure 4.28: TGA thermograph of post reaction catalysts

4.4.9.2 Nature of coke

Figure 4.29 shows the Raman spectra of coked post reaction catalysts. In all of the samples two distinct Raman bands can be observed, with each corresponding to different carbon species. Generally, the Raman band at 1580 cm^{-1} is characteristic of highly ordered graphitic carbon, while that at around 1360 cm^{-1} is the defective or imperfect carbon band [45, 46]. In this analysis, the band at 1614 cm^{-1} can be seen to account for most of the deposited coke component. The source of this deposit should be the bulky aromatic hydrocarbons, probably mono- or di-benzene and alkylated aromatics, which were formed but could not diffuse out of the catalyst pores and channels. This proposal is supported by an earlier report[47] that ascribes the band in the 1600 cm^{-1} region to hydrogen deficient carbonaceous species. This carbon species is often referred to as hard coke, and can be said to be responsible for the second and major weight loss observed in the TGA plots of figure 4.28 (300 – 600 ^{O}C region). The Raman band at approximately 1390cm^{-1} has been assigned to olefinic carbonaceous species. This band is very broad, with less intensity, and may signify a series of olefinic coke species [47, 48]. These carbon species are less hydrogen deficient and can easily be removed at lower temperatures compared to the more hydrogen deficient aromatic carbonaceous species.

Table 4.8: Summary of coke analysis of zeolites synthesized with 16 ml zeolite gel impregnated into each scaffold

	Initial catalyst (mg)	Final catalyst (mg)	Coke (mg)	Coke per mg	Total coke (mg)
HRS-0-0wt%-50	14.01	12.83	1.18	0.08	16.85
HRS-0.75-3wt%-16ml	14.67	13.59	1.07	0.07	14.61
HRS-0.75-4wt%-16ml	14.76	13.72	1.04	0.07	14.06
HRS-0.75-5wt%-16ml	13.19	12.17	1.03	0.08	15.54

Table 4.9: Summary of coke analysis of zeolites synthesized with 32 ml zeolite gel impregnated into each scaffold

	Initial catalyst (mg)	Final catalyst (mg)	Coke (mg)	coke per mg	Total coke (mg)
HRS-0-0wt%-50	14.01	12.83	1.18	0.08	16.85
HRS-0.75-3wt%-32ml	13.58	12.57	1.01	0.07	14.85
HRS-0.75-4wt%-32ml	12.71	11.82	0.89	0.07	14.00
HRS-0.75-5wt%-32ml	12.07	11.14	0.93	0.08	15.47

Table 4.10: Summary of coke analysis of zeolites synthesized from gel of Si/Al =50

	Initial catalyst (mg)	Final catalyst (mg)	Coke (mg)	coke per mg	Total coke (mg)
HRS-0-0wt%-50	14.01	12.83	1.18	0.08	16.85
HRS-1.5-3wt%-SiAl50	12.01	10.99	1.02	0.08	16.97
HRS-2.0-4wt%-SiAl50	13.62	12.32	1.30	0.1	19.10

Table 4.11: Summary of coke analysis of zeolites synthesized from gel of Si/Al =25

	Initial catalyst (mg)	Final catalyst (mg)	Coke (mg)	coke per mg	Total coke (mg)
HRS-0-0-25	13.74	12.49	1.25	0.09	18.16
HRS-0.75-3wt%-SiAl25	11.67	10.42	1.25	0.11	21.41
HRS-0.75-4wt%-SiAl25	12.67	11.61	1.07	0.08	16.84
HRS-0.75-5wt%-SiAl25	14.45	13.07	1.38	0.10	19.05

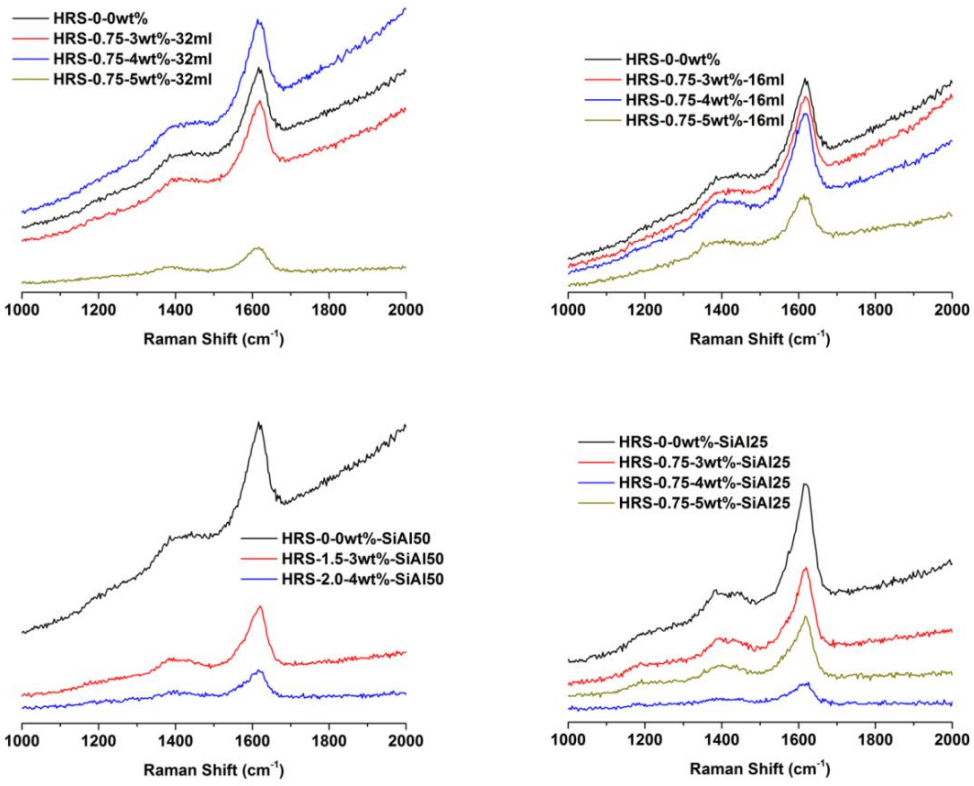

Figure 4.29: Raman spectra of spent catalysts taken after the reaction

To ascertain the level of coke removal after thermal treatment in the TGA, the Raman spectra of the batch of zeolite with a silicon to aluminium ratio of 25 was repeated and presented in figure 4.30. These sets of samples were chosen as the TGA analysis reveals they produced the highest amount of coke amongst all other samples. The Raman spectra of the thermally treated samples showed no vibration bands in the two carbon regions described earlier. The absence of these bands signifies no carbon species were present in the thermally treated samples and proves that these sets of catalysts can be regenerated to be subsequently reused in another batch reaction. It also implies that the cokes formed on these catalysts are not the very chemically stable that are difficult to remove even after oxidative treatment in air. Furthermore, the bands characteristic of the MFI framework can be seen to have been restored upon this thermal regeneration, indicating the zeolite framework structure is well preserved.

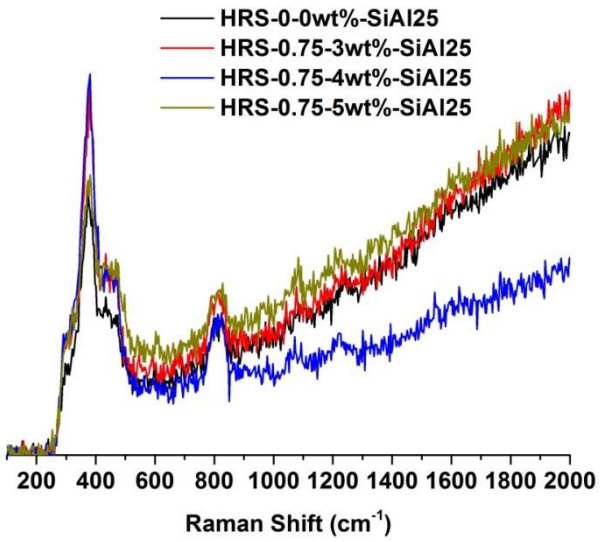

Figure 4.30: Raman spectra of catalysts taken after thermal treatment at 1000^{O}C

4.5 Discussion and conclusions

Aromatics are of significant importance in the chemical industry and they serve as raw materials for the production of several high-value finished products. However, not all aromatics are available in the form desired by the chemical processes. Important feedstocks such as xylene and ethyl benzene are produced through alkylation of benzene, while ethyl toluene is a product of ethylation of toluene. These reactions occur on solid acid catalysts such as ZSM-5, and often results in a mixture of isomers. To attain a satisfactory level of component selectivity the catalyst is often subjected to post synthesis modifications such as silanation [49], selective deactivation [50] and metal loading [51-54] to name a few.

The results presented in this chapter show that the catalyst can be tailored towards particular isomers. This one-pot preparation will go a long way to preserve the catalyst properties and save cost and time which otherwise would have been spent on the post synthesis modification. These sets of catalysts could also be very useful in the upgrading of the octane rating of gasolines that contain considerable amounts of benzene. Alkylation of benzene has been reported as a key process [55] to achieving a high octane number from fuels with high benzene content. The reaction of such fuel on these catalysts can ensure the conversion of the benzene into alkylated products, which will invariably reduce the benzene content of the fuel.

In conclusion, a chitosan scaffold was successfully prepared and applied as a macro-template in the synthesis of zeolite ZSM-5. The zeolite crystallization occurred within the pores of the chitosan scaffold, but the three dimensional zeolite-embedded scaffold collapsed during post synthesis calcination. The scaffold templated zeolites showed step growth morphology, while that synthesized without the scaffold

displayed typical coffin-shaped crystal morphology. FTIR characterization proved that the samples with higher chitosan concentration have lower Brønsted acid strength. Pores of about 50 Å were successfully created on the zeolites using the chitosan scaffold.

The aluminium atoms are present predominantly in tetrahedral coordination, with minor extra framework aluminium species detected in all of the scaffold templated samples. All of the samples synthesized showed good catalytic activity in the methanol to hydrocarbon reactions. The product selectivity differs from sample to sample and showed some correlation with the concentration of the chitosan scaffold. Post reaction thermal analysis showed that the samples synthesized in the 4 wt% scaffold produced the least amount of coke in the same reaction, and over the same reaction times. Two main carbon bands were detected on the spent catalysts from Raman analysis. The entire set of samples show a very sharp peak at 1614 cm^{-1}, indicative of trapped polyaromatic species, and a broad peak at 1390 cm^{-1}, which was attributed to the presence of an olefinic coke component. The catalysts were also shown to be reusable by subjecting to thermal treatment.

References

1. J. F. Haw, W. Song, D.M. Marcus, J.B. Nicholas, *Acc. Chem. Res.*, **2003**, *36*, 317-326

2. S. Ilias, A. Bhan, *Journal of Catalysis*, **2014**, *311*, 6-16

3. Y. Li, M. Zhang, D. Wang, F. Wei, Y. Wang, *Journal of Catalysis*, **2014**, *311*, 281-287

4. D. M. Mccann, D. Lesthaeghe, P. W. Kletnieks, D. R. Guenther, M. J. Hayman, V. Van Speybroeck, M.Waroquier, J. F. Haw, *Angew Chem Int Ed Engl*, **2008**, *47*, 5179-82

5. U. Olsbye, M. Bjørgen, S. Svelle, K. Lillerud, S. Kolboe, *Catalysis Today*, **2005**, *106*, 108-111

6. M. Bjorgen, Ms. Svelle, F. Joensen, J. Nerlov, S. Kolboe, F. Bonino, L. Palumbo, S. Bordiga, U. Olsbye, *Journal of Catalysis*, **2007**, *249*, 195-207

7. H. Schulz, *Catalysis Today*, **2010**, *154*, 183-194

8. A.A. Rownaghi, J. Hedlund, *Industrial & Engineering Chemistry Research*, **2011**, *50*, 11872-11878

9. A.A. Rownaghi, F. Rezaei, J. Hedlund, *Catalysis Communications*, **2011**, *14*, 37-41

10. Z. Xue, T. Zhang, J. Ma, H. Miao, W. Fan, Y. Zhang, R. Li, *Microporous and Mesoporous Materials*, **2012**, *151*, 271-276

11. M. Westgård Erichsen, S. Svelle, U. Olsbye, *Catalysis Today*, **2013**, *215*, 216-223

12. N. Regina Camargo Fernandes Machado, V. Calsavara, N. Guilherme Castelli Astrath, A. Medina Neto, M. Luciano Baesso, *Applied Catalysis A: General*, **2006**, *311*, 193-198

13. V. Calsavara, M.L. Baesso, N.R.C. Fernandes-Machado, *Fuel*, **2008**, *87*, 1628-1636

14. U.V. Mentzel, K.T. Højholt, M.S. Holm, R. Fehrmann, P. Beato, *Applied Catalysis A: General*, **2012**, *417-418*, 290-297

15. D. Ma, Y. Shu, C. Zhang, W. Zhang, X. Han, Y. Xu, X. Bao, *Journal of Molecular Catalysis A: Chemical*, **2001**, *168*, 139–146

16. K. Van Der Borght, V.V. Galvita, G.B. Marin, *Applied Catalysis A: General*, **2015**, *492*, 117-126

17. F. Yaripour, Z. Shariatinia, S. Sahebdelfar, A. Irandoukht, *Microporous and Mesoporous Materials*, **2015**, *203*, 41-53

18. Y. Ni, A. Sun, X. Wu, G. Hai, J. Hu, T. Li, G. Li, *Journal of Natural Gas Chemistry*, **2011**, *20*, 237-242

19. X. Wang, X. Gao, M. Dong, H. Zhao, W. Huang, *Journal of Energy Chemistry*, **2015**,

20. J.Q. Chen, A. Bozzano, B. Glover, T. Fuglerud, S. Kvisle, *Catalysis Today*, **2005**, *106*, 103-107

21. S. Teketel, W. Skistad, S. Benard, U. Olsbye, K. P. Lillerud, P. Beato, S. Svelle, *ACS Catal.*, **2012**, *2*, 26–37

22. M. Bjørgen, F. Joensen, M. Spangsberg Holm U. Olsbye, K. Lillerud, S. Svelle,, *Applied Catalysis A: General*, **2008**, *345*, 43-50

23. P.N.R. Vennestrøm, M. Grill, M. Kustova, K. Egeblad, L.F. Lundegaard, F. Joensen, C.H. Christensen, P. Beato, *Catalysis Today*, **2011**, *168*, 71-79

24. J. Ahmadpour, M. Taghizadeh, *Comptes Rendus Chimie*, **2015**, *18*, 834-847

25. J. Kim, M. Choi, R. Ryoo, *Journal of Catalysis*, **2010**, *269*, 219-228

26. L. Wu, V. Degirmenci, P.C.M.M. Magusin, N.J.H.G.M. Lousberg, E.J.M. Hensen, *Journal of Catalysis*, **2013**, *298*, 27-40

27. H. Li, S. He, K. Ma, Q. Wu, Q. Jiao, K. Sun, *Applied Catalysis A: General*, **2013**, *450*, 152-159

28. Z. Di, C. Yang, X. Jiao, J. Li, J. Wu, D. Zhang, *Fuel*, **2013**, *104*, 878-881

29. A. Dong, Y. Wang, D. Wang, W. Yang, Y. Zhang, N. Ren, Z. Gao,Y. Tang, *Microporous and Mesoporous Materials*, **2003**, *64*, 69-81

30. S. P. Naik, A. S. T. Chiang, R. W. Thompson, F. C. Huang, *Chem. Mater.*, **2003**, *15*, 787-792

31. W. Song, R. Kanthasamy, V.H. Grassian, S.C. Larsen, *Chem Commun*, **2004**, 1920-1

32. Y. J. Lee, J. S. Lee, Y.S Park, K.B. Yoon, *Adv. Mater.*, **2001**, *13*, 1259-1263

33. V.K. Saini, J. Pires, *Journal of Chemical Education*, **2012**, *89*, 276-279

34. C.N, Satterfield, *Heterogeneous catalysis in industrial practice*,Second edition, McGraw-Hill, **1991**

35. J. Weitkamp, L. Puppe, *Catalysis and zeolites : Fundamentals and applications*, Springer, **2009**

36. Z.Y. Gu, P.H. Xue and W.J. Li, -*Polym. Adv. Technol*, **2001**, *12*, 665-669

37. S. Jana, S.J. Florczyk, M. Leung, M. Zhang, *Journal of Materials Chemistry*, **2012**, *22*, 6291

38. F. Xia, M. Pan, S. Mu, M.D. Jones, D. Wolverson, F. Marken, *Electroanalysis*, **2012**, *24*, 1703-1708

39. L. Wei, M. Sevilla, A.B. Fuertes, R. Mokaya, G. Yushin, *Advanced Energy Materials*, **2011**, *1*, 356-361

40. Y. Yang, J. Cui, M. Zheng, C. Hu, S. Tan, Y. Xiao, Q. Yang, Y. Liu, *Chem Commun*, **2012**, *48*, 380-382

41. G. Pari, S. Darmawan, B. Prihandoko, *Procedia Environmental Sciences*, **2014**, *20*, 342-351

42. S. Kulprathipanja, *Zeolites in industrial separation and catalysis*, Wiley interscience, **2010**,

43. E. Lippmaa, M. Magi, A. Samoson, M. Tarmak, and G. Engelbardt, *J. Am. Chem. Soc.*, **1981,** *103*, 4992-4996

44. J. Klinoswki, *Progress in NMR Spectroscopy*, **1984**, *16*, 237-309

45. A. Shamsi, J.P. Baltrus, J.J. Spivey, *Applied Catalysis A: General*, **2005**, *293*, 145-152

46. F. Fan, Z. Feng, C. Li, *Characterization of SolidMaterials and Heterogeneous Catalysts: From Structure to Surface Reactivity*, First Edition, Wiley, **2012,** pp 49-84

47. C. Li , P. C. Stair, *Catalysis Today*, **1997**, *33*, 353-360

48. J. Li, G. Xiong, Z. Feng, Z. Liu, Q. Xin, C. Li, *Microporous and Mesoporous Materials*, **2000**, *39*, 275-28

49. W. Tan, M. Liu, Y. Zhao, K. Hou, H. Wu, A. Zhang, H. Liu, Y. Wang, C. Song, X. Guo, *Microporous and Mesoporous Materials*, **2014**, *196*, 18-30

50. S. Rabiu, S. Al-Khattaf, *Ind. Eng. Chem. Res.*, **2008**, *47*, 39-47

51. Y. Sugi, Y. Kubota, K. Komura, N. Sugiyama, M. Hayashi, J.H. Kim, G. Seo, *Applied Catalysis A: General*, **2006**, *299*, 157-166

52. J. Gao, L. Zhang, J. Hu, W. Li, J. Wang, *Catalysis Communications*, **2009**, *10*, 1615-1619

53. S. Todorova, B. Su, *Catalysis Today*, **2004**, *93-95*, 417-424

54. Y. Zhao, W. Tan, H. Wu, A. Zhang, M. Liu, G. Li, X. Wang, C. Song, X. Guo, *Catalysis Today*, **2011**, *160*, 179-183

55. T. Odedairo, S. Al-Khattaf, *Catalysis Today*, **2013**, *204*, 73-84

Chapter 5: Bifunctional zeolite and application to liquid phase conversion of cyclohexanone to caprolactam

Chapter overview

The work presented in this chapter includes the design and investigation of a bifunctional catalyst with two distinct catalytic active sites. The possibility of creating a multipore structure on the bifunctional catalyst using chitosan as a macrotemplate was also explored. The bifunctional catalyst was based on a zeolite material with the MFI framework topology. The acid site was created by substitution of trivalent aluminium atom for tetravalent silicon, while the redox site was created by substituting titanium for silicon atoms. The catalytic performance of the synthesized bifunctional catalysts was investigated for the conversion of cyclohexanone to caprolactam in a liquid medium at low reaction temperatures. The gas-phase activities of the catalysts were investigated for methanol to hydrocarbon conversion. The role of the chitosan as a macrotemplate on the properties of the zeolites was also studied and correlated with their catalytic activities.

5.1 Introduction to dual functional catalysts

In certain reactions of industrial interest the conversion of the feed to the final product proceeds through several reaction steps and each of these steps might require different distinct catalytic active sites. A typical example of such a process is the catalytic reforming of hydrocarbons: during catalytic reforming any of hydrogenation, dehydrogenation and isomerization reactions can take place.

Hydrogenation and dehydrogenation typically occur on metallic sites, while isomerization takes place on acid sites; implying that, for the three reactions to occur on a single catalyst, both the metallic and the acidic sites must be present on the surface of the catalyst, leading to the conception of a dual/bifunctional catalyst. Hence a bifunctional catalyst can be described as one which consists of two distinctly different kinds of catalytically active sites. An illustration of the general concept of dual functional catalyis, the reforming of cyclohexane, is represented in scheme 5-1.

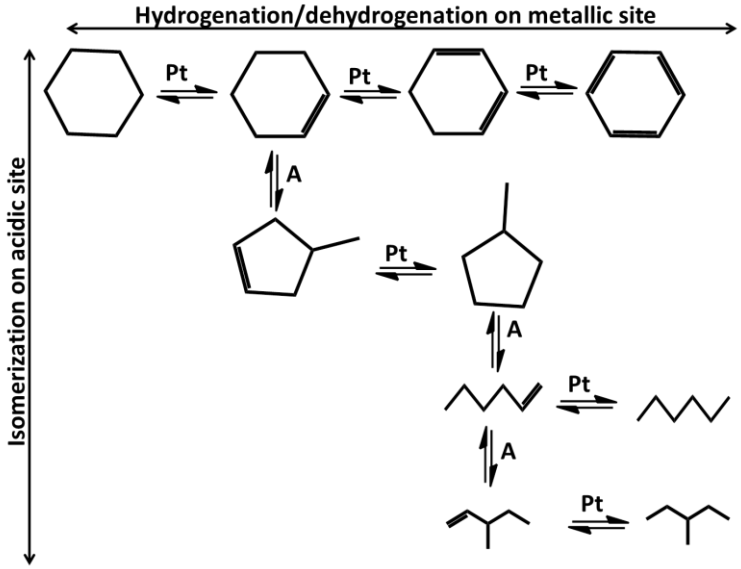

Scheme 5-1: Schematic illustration of the concept of bifunctional catalysis in cyclohexane reforming. Adapted with modification from ref [1, 2]

Another reaction of industrial importance is the conversion of cyclohexanone to caprolactam. This reaction involves two distinct reaction steps that require two distinct catalytic active sites. Caprolactam is a very useful raw material for the production of nylon 6, which is in turn used for textile and fibre products. The current industrial process for the production of caprolactam involves a series of chemical reactions starting with cyclohexanone as the feed.

The cyclohexanone is converted to cyclohexanone oxime through reaction with hydroxylamine sulfate in a buffer condition [3]. The cyclohexanone oxime is subsequently transformed to caprolactam through the Beckmann rearrangement, using oleum as a liquid acid catalyst. Oleum is a corrosive chemical [4] that needs replacing in the production process. The final step of this process involves separation of the caprolactam by addition of ammonia. On a commercial scale this step generates ammonium sulfate waste, typically of 2 to 5 times the amount of the caprolactam produced[3].

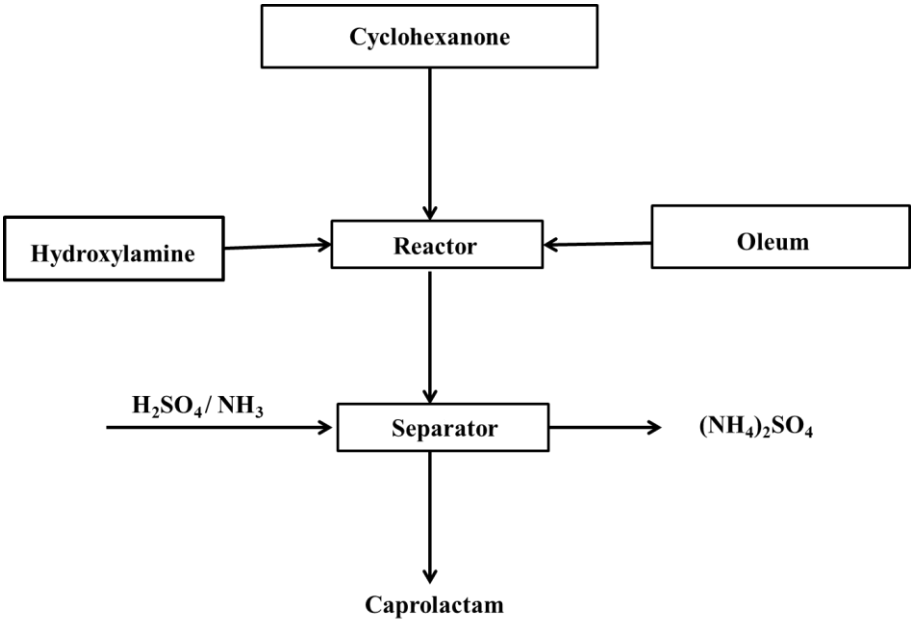

Scheme 5-2: Illustration of the industrial production steps for caprolactam

From the scale of waste generated through this production step, caprolactam could be described as the secondary product rather than the main product. The poor selectivity to caprolactam through this production process, coupled with stringent environmental requirements, requires an improved or alternative process.

To avoid the waste stream, solid acid catalysts have been used for the oxidation of cyclohexanone using ammonia. Amongst early solid acid catalysts investigated for this step are the amorphous TiO_2/SiO_2 matrix [5] and B_2O_3/Al_2O_3. The crystalline titanosilicate zeolite TS-1 with the MFI framework topology was found to be more active for the conversion of cyclohexanone and equally highly selective to the oxime, compared to the amorphous titania-silica matrix[4].

In view of the well-known shape selectivity of zeolites in catalytic reactions, it is not surprising that there have been several reports on the application of zeolites for the production of caprolactam. Basically, efforts have been focused on two main processes: the first is the selective conversion of cyclohexanone to oxime, to ensure maximum production of the monomer for caprolactam. The second process of focus is the selective transformation of the oxime to caprolactam. In both of these steps, the hazardous use of oleum is always avoided.

The first step of caprolactam production requires redox sites, and a number of crystalline titanium based materials such as titanium-silicalite (TS-1) [6-11], titanium-zeolite beta (Ti-Beta) [12, 13], titanium-USY[14] and titanium- mesoporous silicas, such as Ti-SBA and Ti-MCM, have been well studied for the selective transformation of cyclohexanone to the corresponding oxime. Much progress and success have indeed been recorded in this aspect.

In the second part, several process parameters such as reaction conditions, reactor type, and composition of reacting species and medium of reaction have all been

studied with the view to optimizing selectivity to caprolactam. The roles of the catalyst design process, acidity and morphology have also been widely studied and reported [15-21].

Recently, there have been some considerable efforts to design a bifunctional solid catalyst that will combine both the redox and acidic sites for the direct conversion of cyclohexanone to caprolactam in a one-pot low temperature reaction in a liquid medium. Thomas and Raja[22] have prepared a bifunctional nanoporous material based on an aluminophosphate zeolite (AlPO5), to achieve which, they substituted different combinations of metal atoms into the zeolite structure. These include Mn/Mg, Fe/Mg, Mn/Zn and Fe/Zn, where the substitution of divalent Mg and Zn for aluminium in the AlPO structure rendered the material acidic. The redox sites were induced by the substitution of trivalent manganese, iron and colbalt. These bifunctional catalysts showed excellent activity in the conversion of cyclohexanone directly to caprolactam (with a selectivity of 80% archived for the Mn/Mg-AlPO-5 system) at a low temperature of $80^{O}C$ in a solvent free medium.

In a similar report, Anil Kumar and Hoelderich [23] demonstrated the role of Nb substituted MCM-41 in the direct conversion of cyclohexanone to caprolactam. An increased yield of caprolactam was reported with increasing Nb concentration in the MCM-41 structure - an observation attributed to the increased acid strength of the catalyst.

In an earlier investigation using a bifunctional catalyst for the direct formation of caprolactam from cyclohexanone, the role of the zeolite pore geometry was elucidated by Raja *et al* [24] using both transition metal substituted AlPO-36 and AlPO-18. Under the same reaction conditions the large pore transition metal substituted AlPO-36 was found to be more efficient in the direct conversion of

cyclohexanone to the caprolactam. This observation was attributed to the inability of the cyclohexanone oxime to access the small pore of the substituted AlPO-18.

This chapter aims to explore further the possibility of this one-pot transformation of cyclohexanone to caprolactam in a low temperature liquid phase process. The co-incorporation of aluminium and titanium into the siliceous MFI framework was investigated. This system was chosen for the relative ease of synthesising a phase pure product. The titanium is envisaged to act as the redox site (Si^{4+}-O-Ti^{4+}) while the aluminium would induce the desired acidity (Si^{4+}-OH-Al^{3+}) for the transformation of the intermediate oxime to the end product. Due to the importance of the pore geometry, emphasized earlier [24], the use of chitosan as a macro templating agent was involved in the synthesis process, with the aim of creating a bifunctional zeolite with multi-modal pore structure.

5.2 Experimental procedure

5.2.1 Synthesis procedure

The zeolite precursor was prepared from a clear solution of silicon, aluminium and titanium sources, following standard procedures. In a typical batch, distilled water and tetrapropylammonium hydroxide (template) were mixed together. To this mixture, aluminium isopropoxide (aluminium source) was added and stirred at room temperature until completely dissolved. Subsequently, tetraethyl orthosilicate (the source of silica) was added and the mixture was stirred for one hour. Separately, titanium (IV) ethoxide was dissolved in isopropanol, with stirring, for 10 minutes. The titanium solution was then added dropwise to the silicon-aluminium solution previously prepared. The entire solution was aged at room temperature for 3 hours

with constant stirring. For the samples containing chitosan, the powder was added after the precursor had been aged for 1 hour. For crystallization, the zeolite precursor was put into a Teflon lined steel autoclave, sealed and placed in an oven at a temperature of 170 ^{O}C for 2 days.

Table 5.1: Mass composition of the zeolite precursor for this work

Water	TPAOH	AlPrO	TEOS	TEOT	IPA
13.85g	8.14 g	0.145 g	10.44 g	0.16 g	3ml

After crystallization, the autoclave was quenched in cold water and the samples retrieved by centrifugation. The solid samples were washed several times with deionized water, until the pH of the filtrate was near neutral. Afterwards they were dried at 110 ^{O}C overnight, cooled to room temperature and crushed to a fine powder in an agate mortar.

Calcination was conducted at 650 ^{O}C in static air to remove both the template and the chitosan. The calcination furnace was ramped to the calcination temperature at a rate of 2 ^{O}C/min and held for 12 hours. Figure 5.1 gives the temperature profile for the calcination step.

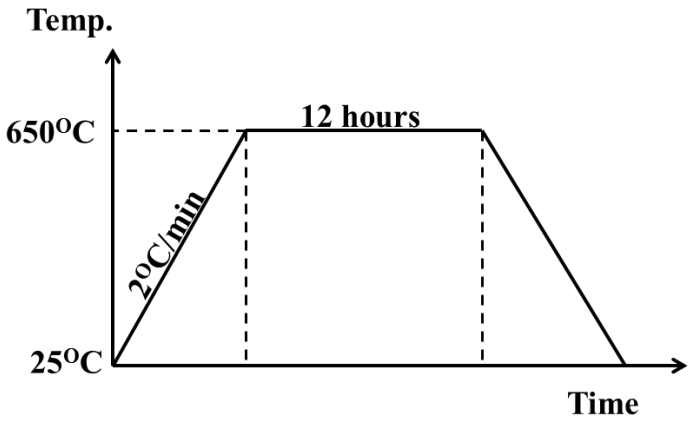

Figure 5.1: Calcination temperature programme profile

5.2.2 Sample notations

The nomenclature used for the samples synthesized in this chapter follows the notation *HAT-X-Y-Zg*, where HAT is an acronym for Hierarchical Aluminium Titanium, X is the silicon to aluminium ratio, Y represents the silicon to titanium ratio and Z is the mass of chitosan powder included in the synthesis precursor.

5.2.3 Characterization

After calcination, the whiteness of the powder samples obtained indicates the removal of the chitosan included during the synthesis step. Following the calcination, the samples were subjected to various characterization techniques to ascertain the phase, purity, crystallinity, morphology, coordination state of the T-atoms, acidity and textural properties, as described in chapter two.

The samples were then evaluated for liquid phase ammoximation and Beckmann rearrangement of cyclohexanone and gas phase Beckmann rearrangement as well as methanol to hydrocarbon reactions.

5.3 Phase identification and phase purity determination by XRD

Figure 5.2 gives the XRD patterns of the samples after calcination. The patterns are typically those of a zeolite with the MFI framework topology. There are no extra peaks which can be attributed to impure or dense silica phases in the form of quartz or crystobalite. These observations confirm that the materials are indeed MFI based zeolite. They also confirm the purity of the phase and the sharpness of the peaks

shows that the samples have a high degree of crystallinity. This observation also confirms that the coexistence of both aluminium and titanium in a one-pot synthesis does not negatively impact on the crystallinity and purity of the resulting materials, further evidence of which can be seen from the XRD patterns of the two reference samples without titanium (one synthesized without chitosan and the other with chitosan) given in figure 5.3, with XRD patterns similar to those in figure 5.2.

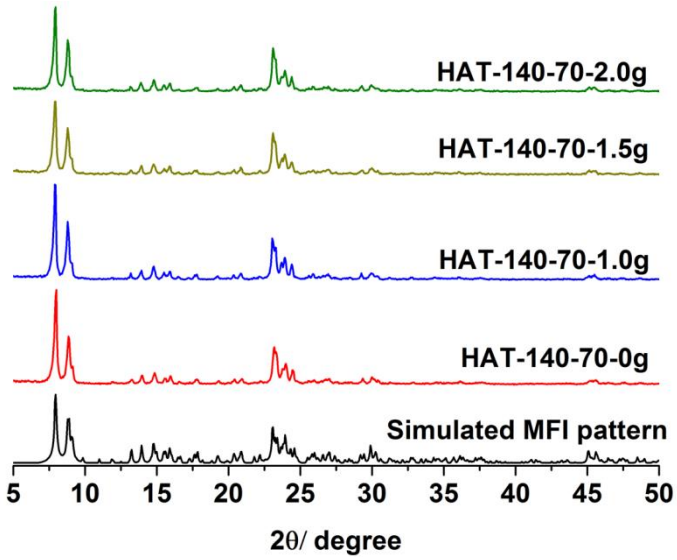

Figure 5.2: XRD patterns of samples synthesized with both aluminium and titanium in the starting precursor, and with different amount of chitosan

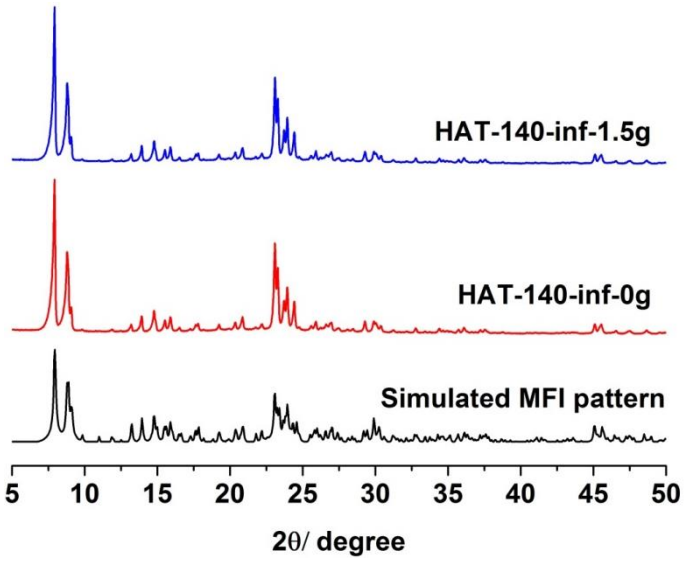

Figure 5.3: XRD patterns of samples synthesized with aluminium but without titanium (with and without chitosan)

5.4 Coordination state of titanium, silicon and aluminium

The coordination state of the T-atoms (Ti, Al and Si) is investigated here. Here, as in previous chapters, spectroscopy techniques have been employed to gain complete insight into the coordination environment of these elements.

Figure 5.4, shows the FTIR spectra, where all the samples exhibit a very strong and identical peak at 960 cm^{-1}, indicating the presence of titanium in an isolated four fold coordination site.

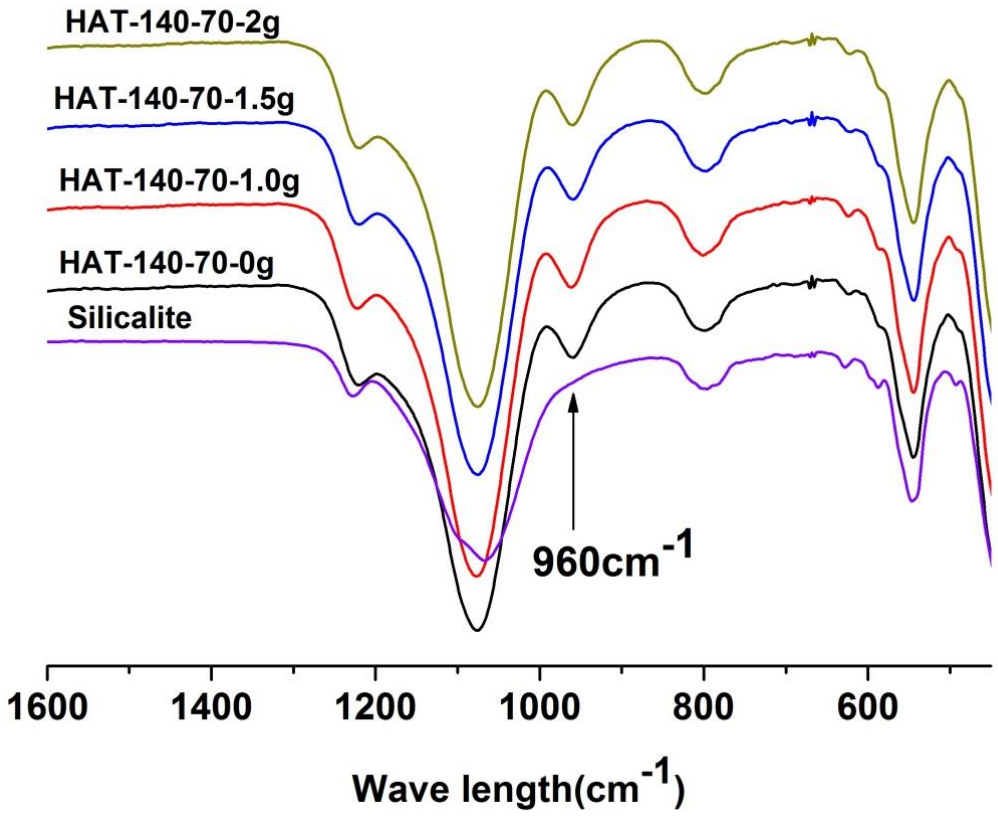

Figure 5.4: FTIR spectra of all samples showing titanium in the framework position, as indicated by the 960 cm^{-1} vibration bands (arrowed)

Figure 5.5 is the DRUV-Vis spectra of all the aluminium containing TS-1 zeolites synthesized with different amount of chitosan powder. All the samples exhibit a very strong and sharp absorption peak at wavelength of 210 nm, which is characteristic of

tetrahedraly coordinated titanium. Some octahedral titanium phase is, however, noticeable in some of the samples. For instance, the sample HAT-inf-70-0g (Si/Al=∞, Si/Ti=70, chitosan in precursor=0 g) which is pure TS-1, and those samples with both aluminium and titanium synthesized with 1 and 2 g chitosan in their precursors (HAT-140-70-1g & HAT-140-70-2g) all have the 210 nm peak as the only clear peak. However, in addition to the 210 nm peak, a weak absorption band can also be seen between 300 and 370 nm for the samples synthesized without chitosan (HAT-140-70-0g) and that synthesized with 1.5 g (HAT-140-70-1.5g) chitosan. This weak band is an indication of titanium in an octahedral coordination state in these samples.

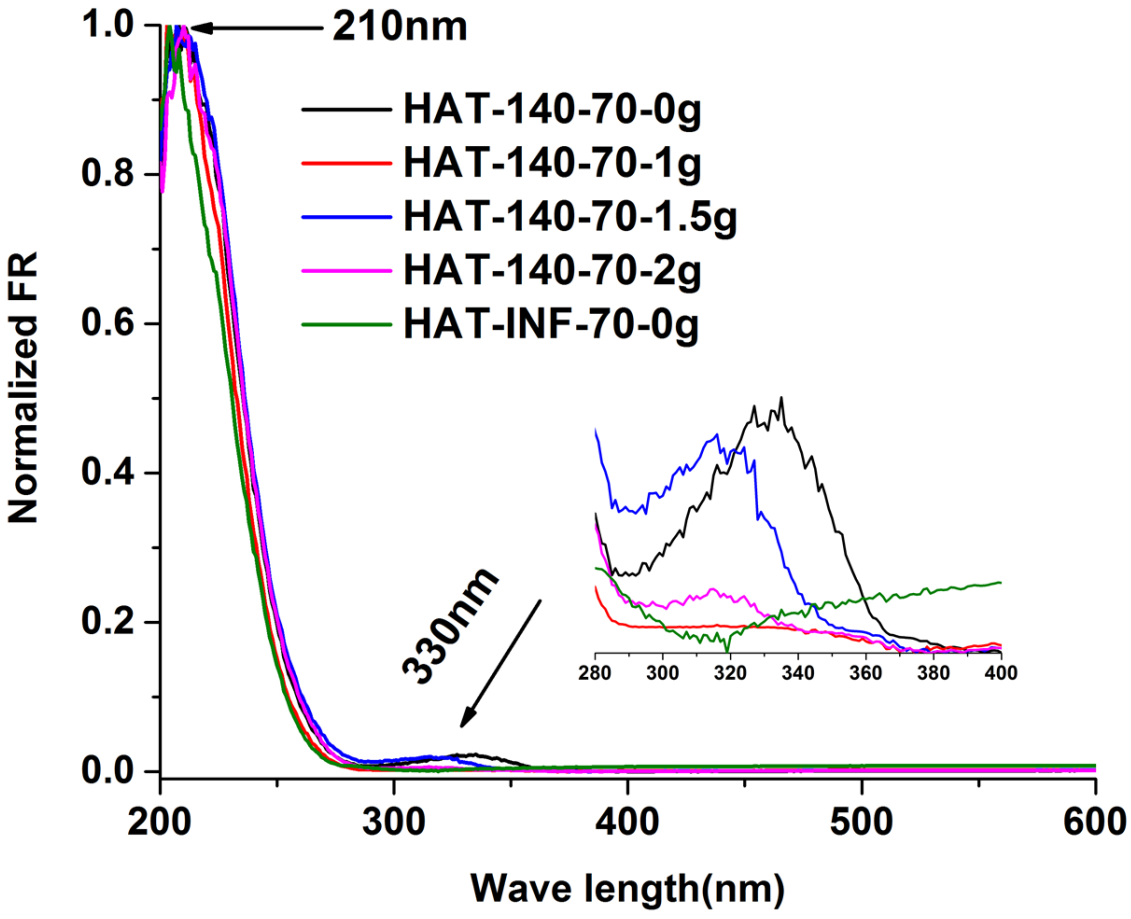

Figure 5.5: UV-Vis Spectra showing coordination state of titanium in the zeolite framework

The UV-Raman is particularly useful for quantification analysis when the UV enhanced 1125 cm^{-1} band is taken into consideration. The Raman spectra of all the synthesized samples, each compared to those of silicalite and anatase, are presented in figures 5.6 and 5.7.

The spectra in figure 5.6 corroborate the findings from the UV-Vis analysis presented earlier in figure 5.5. The two samples which displayed weak bands in the region 300 - 330 nm in the UV-Vis experiment can be seen to have vibration bands corresponding to that of anatase in the Raman analysis. This observation is a confirmation that all of the titanium atoms in the starting precursor were not completely inserted into the framework of these two samples.

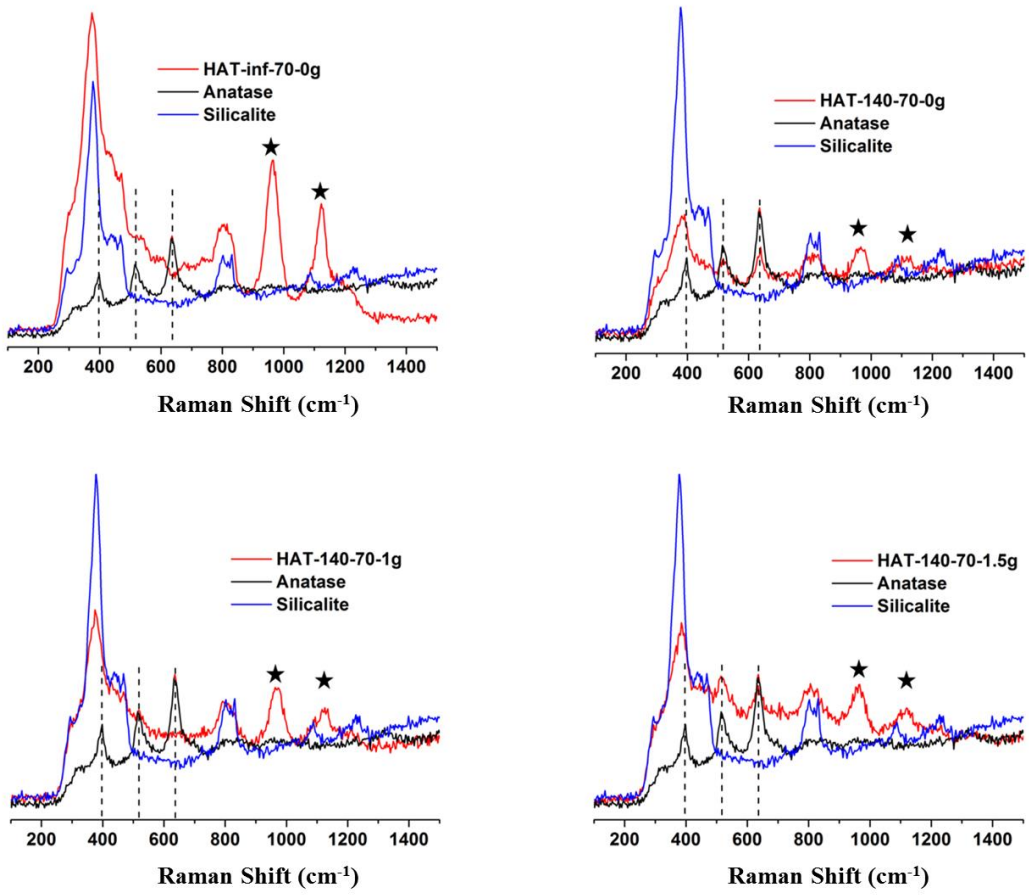

Figure 5.6: Raman spectra of synthesised samples compared to anatase and silicalite (broken lines denote anatase peak positions and stars indicate tetrahedral titanium position)

Apart from this observation, all the samples synthesized with titanium in the starting gel showed the Raman bands at both 960 cm^{-1} and 1125 cm^{-1}, which as discussed in chapter three, are known to be an indication of tetrahedraly coordinated titanium [25-28]. The intensity of these two bands, however, varies from one sample to another. The band at 1125 cm^{-1} is known to be a resonant Raman band and the ratio of this band to that at 960 cm^{-1} can produce useful information on the relative amounts of titanium successfully incorporated into the framework of each sample.

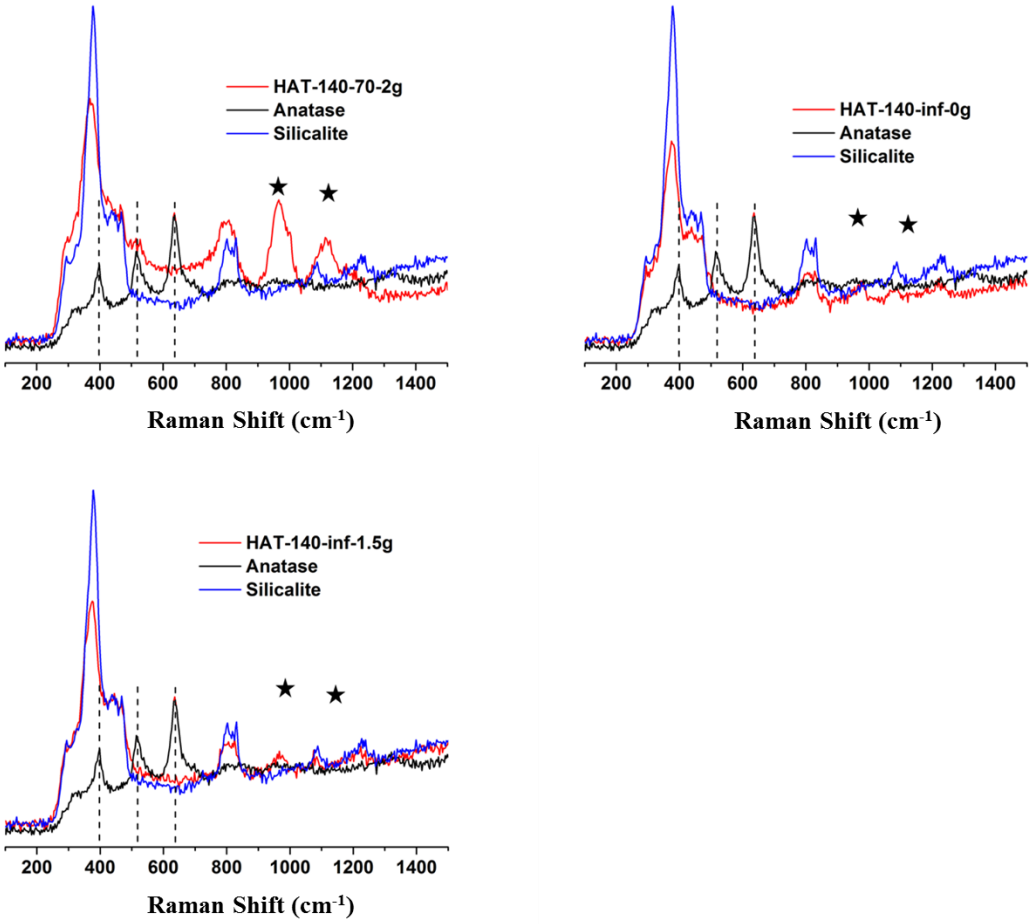

Figure 5.7: Raman spectra of synthesised samples compared to anatase and silicalite (broken lines denote anatase peak positions and stars indicate tetrahedral titanium position)

As expected, the two samples synthesized with no titanium in the starting precursor (HAT-140-inf-0g and HAT-140-inf-1.5g) both show no Raman band (figure 5.7) attributable to framework titanium. These two samples prove that aluminium makes

no contribution to the intensity or position of the two titanium framework bands and that the observations thus far are a consequence of the titanium present.

Table 5.2: Summary of the intensity of 960 cm^{-1} and 1125 cm^{-1} Raman bands

	I_{960}	I_{1125}	I_{1125}/ I_{960}
HAT-140-inf-0g	-	-	-
HAT-140-inf-1.5g	-	-	-
HAT-140-70-0g	787	721.7	0.92
HAT-140-70-1g	989.5	835.8	0.85
HAT-140-70-1.5g	1014.54	835.8	0.82
HAT-140-70-2g	1184.5	913.02	0.77
HAT-inf-70-0g	1852	1408.6	0.76

5.5 NMR characterisation

The coordination environment of silicon and aluminium in the framework was investigated using solid state NMR. As noted in chapter four, for zeolites like ZSM-5, two silicon environments have generally been observed and reported by earlier authors [29-32]. These are the Si(0Al) and Si(1Al) where the Si atom is respectively surrounded by four other silicon tetrahedra and, three silicon tetrahedral and one aluminium tetrahedron.

Figure 5.8 (top) displays the solid state ^{29}Si NMR spectra of the samples synthesized with both aluminium and titanium with different chitosan addition. These spectra fit well with those obtained and described by other workers[29, 30]. The major peak at -112.6 ppm indicates that most of the silicon is neighboured by other silicon tetrahedra while the shoulder at -106.8 ppm is that of silicon coexisting with three other silicon and one aluminium tetrahedra as neighbours.

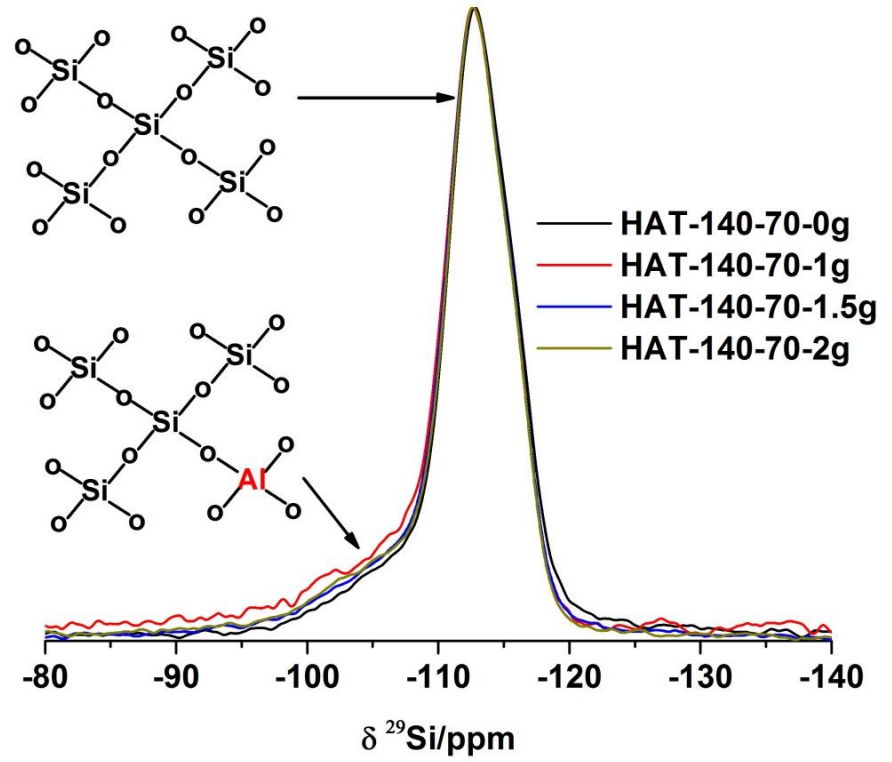

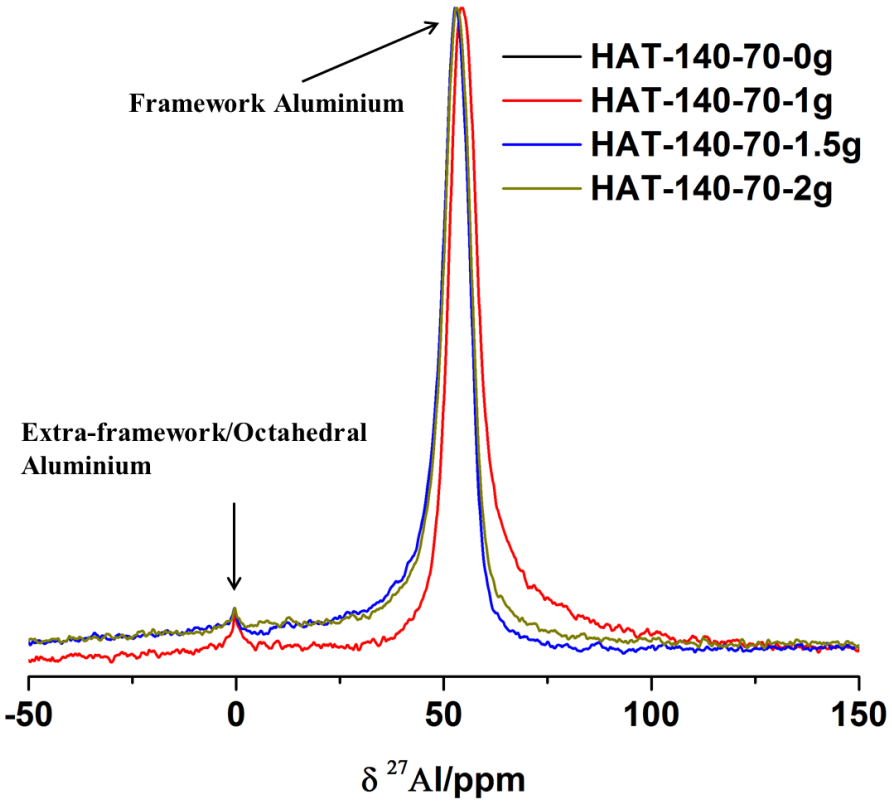

Figure 5.8: NMR spectra of Al-TS-1 with different amounts of chitosan in the synthesis precursor (Top) silicon; (Bottom) aluminium

From figure 5.8 (bottom), two aluminium environments can be seen. The major peak at *ca* 50 ppm corresponds to tetrahedral aluminium in the zeolite framework while that at *ca* 0 ppm corresponds to non-framework or octahedral aluminium species. In general, most of the aluminium atoms are incorporated into the framework.

5.6 Acidity of the samples by *in situ* FTIR

IR spectroscopy can be used for the determination of Brønsted acid sites either with or without the use of probe molecules. IR bands at certain wavelengths are finger prints for certain types of acidity or acidity arising from different sources.

As discussed in chapters two and four, the band in the region 3600 – 3610 cm^{-1} is a finger print for framework associated acidity, i.e. the bridging OH in zeolites. Also, as discussed previously, this band is often obscured in the presence of moisture, thus the sample is often subjected to dehydration to have a clearer appreciation of this band. The evolution of the two OH bands with increasing *in situ* temperature is demonstrated in figure 5.9.

For all the samples, two distinct bands (ca 3600 and 3710 cm^{-1}), which correspond to Brønsted (Si-OH-Al) and terminal silanol (Si-OH) respectively can be seen. These observed bands prove the presence of acidity in all of the samples; in particular, the Brønsted site corroborates the insertion of aluminium into the framework. Figure 5.10 compares the spectra of the bifunctional samples at the dehydration temperature of 823 K. The band at ca 3600 cm^{-1} for the sample synthesized without chitosan (HAT-140-70-0g) appears to be more intense than the rest of the samples - this might suggest higher acidity in this sample than the others.

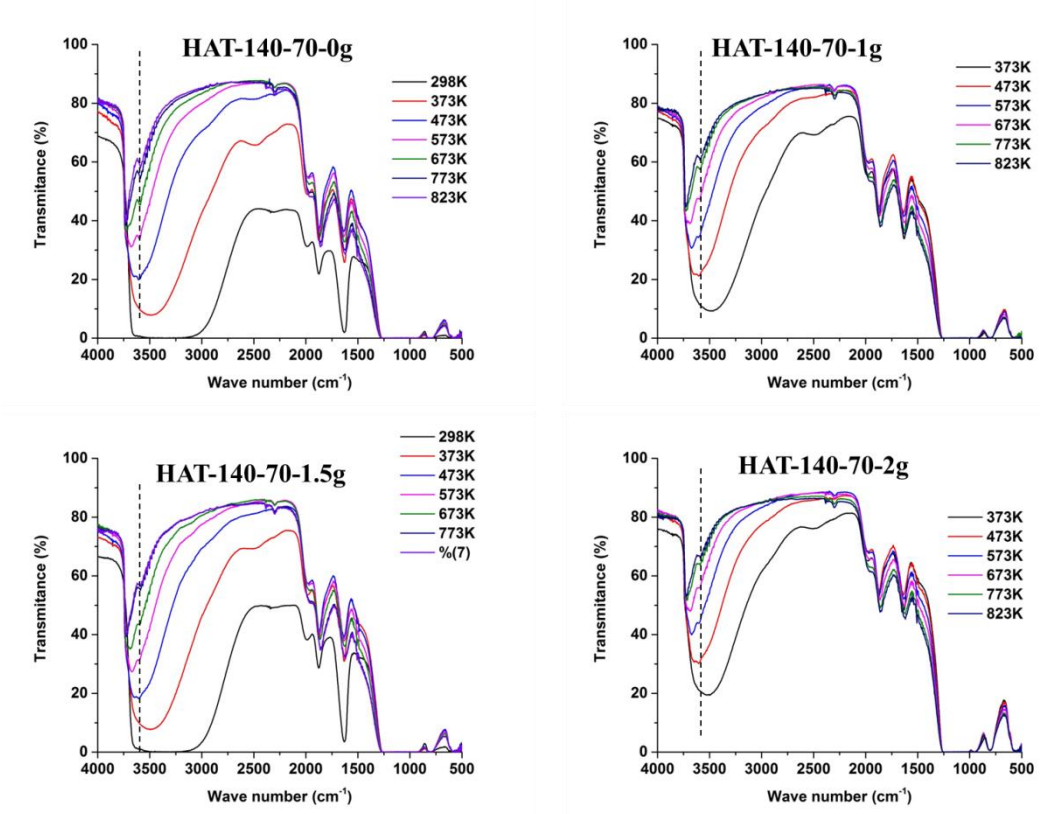

Figure 5.9: *In situ* FTIR spectra showing emergence of the Brønsted acid site (indicated by the dashed lines) with dehydration temperature

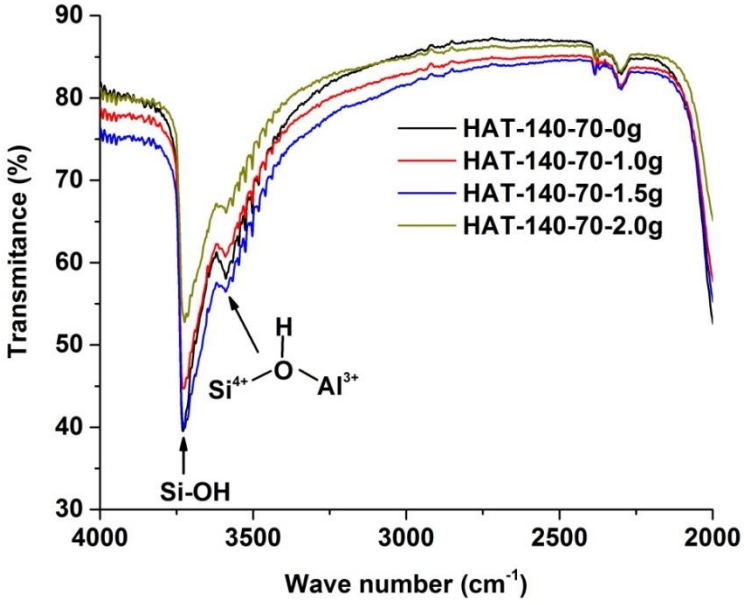

Figure 5.10: Comparison of the FTIR spectra of all samples dehydrated at 823 K

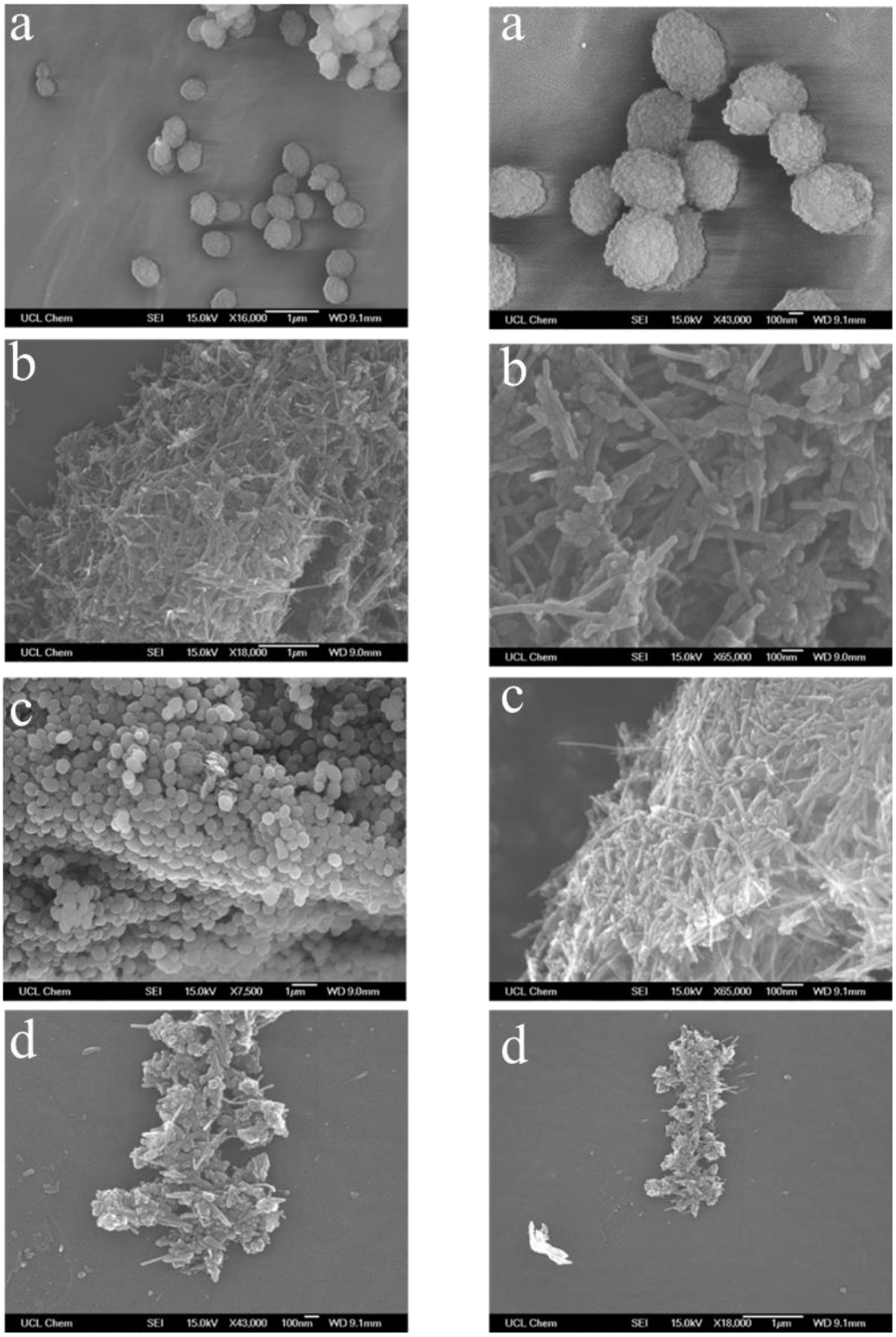

Figure 5.11: SEM micrographs showing the morphology of (a)HAT-140-70-0g, (b)HAT-140-70-1g, (c) HAT-140-70-1.5g, (d) HAT-140-70-2g. (left column is at different magnification from the right column or of a different area of the sample)

5.7 Investigation of the morphology by SEM

The images in figure 5.11 are those from the SEM of the titanium and aluminium containing samples synthesized with different chitosan powder in the synthesis precursor. The sample without chitosan in the starting gel shows aggregated particles that form into a fairly uniform sphere of particles approximately 200 nm in size, which is the only morphological appearance observed in this sample, even after extensive imaging of different regions. In the samples synthesized in the presence of chitosan, the same morphology observed in the sample described above was also observed. However, in addition and with greater prominence, strands of particles were also observed. A detailed inspection of this morphology indicates that the zeolite particles form into these strands on the chitosan particles and remain as such upon removal of the chitosan by calcination. The thickness of these strands decreases with increasing chitosan content in the synthesis medium.

5.8 Textural properties

The nitrogen adsorption isotherms for these samples are given in figure 5.12 below. The isotherms of all the samples exhibit a hysteresis loop, indicating the presence of pores that are larger than microporous. Such hysteresis is typical of type H3, according to a recent IUPAC reclassification [33] and as discussed in chapter two. According to reference [33], this loop may arise from non-rigid aggregates of plate-like particles and/or from macropore networks that are incompletely filled by the pore condensate. This explanation is consistent with the observation from the SEM micrograph in figure 5.11 where the zeolite crystals were observed to exist as spheres or strands of agglomerated particles.

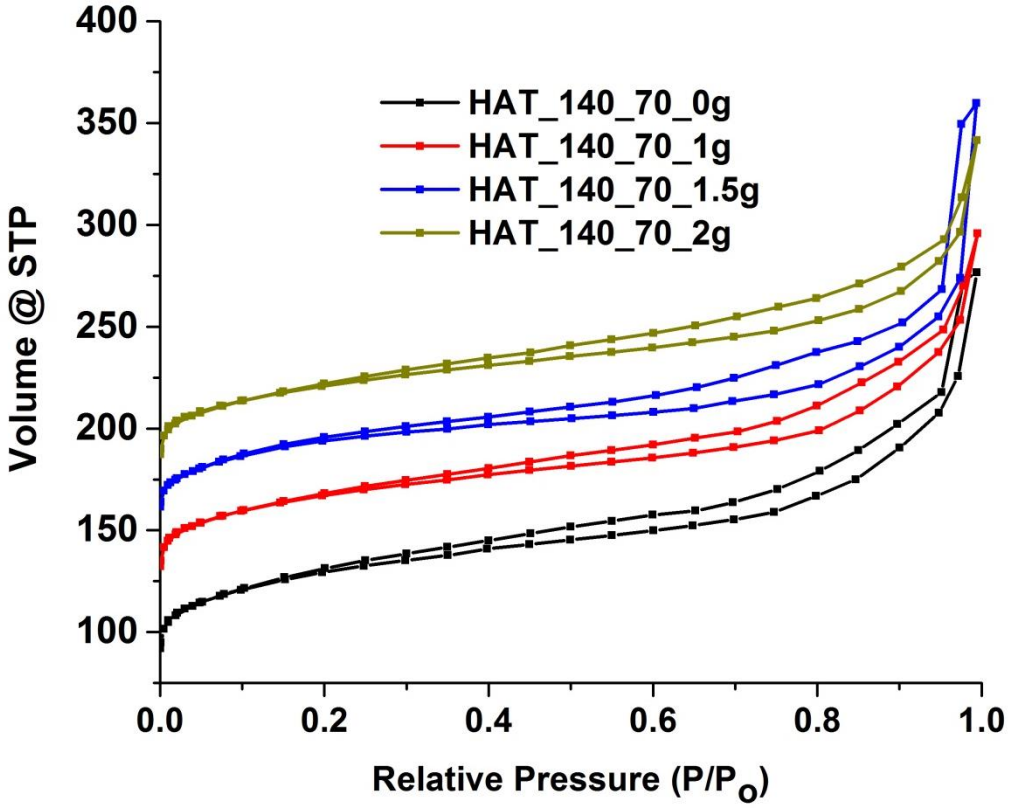

Figure 5.12: Nitrogen adsorption isotherms showing the type H3 hysteresis loop for all the samples

5.9 Catalytic evaluation

Three different reactions were conducted on each of the synthesized catalysts in this chapter. It was envisaged that the coexistence of the aluminium and titanium would impose bifunctional (acid and redox) active sites on the catalyst. To evaluate this potential, the direct conversion of cyclohexanone to caprolactam in a one stream liquid phase was attempted. As noted earlier, this reaction was selected because of the economic importance of the caprolactam as well as the fact that redox site is needed for the first step while an acid site will be required for the second. The schematic representation of the reaction steps for the conversion of cyclohexanone to caprolactam over a bifunctional titanium-aluminium zeolite catalyst is given in scheme 5-3 below.

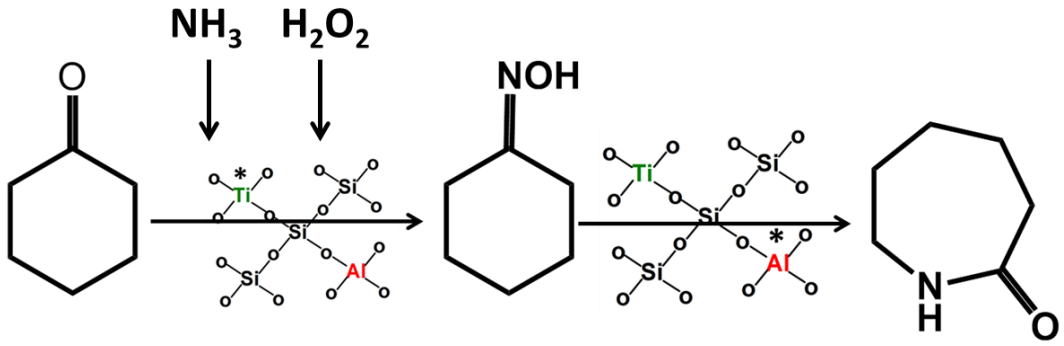

Scheme 5-3: Schematic representation of the reaction steps of cycloheaxanone to caprolactam convrsion. The active site for each step is astericked

5.9.1 Cyclohexanone ammoximation and Beckmann rearrangement

This reaction was conducted in a batch reactor. The reactor consists of a specially designed 50ml flask with allowance for slow and constant injection of hydrogen peroxide. Cyclohexanone, ammonia, the solvent (if used) and catalyst were charged into the reactor (see table 5.3 for composition). This mixture was heated slowly to the desired reaction temperature, before gradually injecting the peroxide over 2 hours. Upon complete injection of the peroxide, the reaction was allowed to proceed for additional 2 hours, after which the glass reactor was cooled rapidly to room temperature in an ice bath. The reactor content was filtered to separate the catalyst from the reaction mixture. The analysis of the reaction mixture was conducted with a GC equipped with an FID using the internal standard method, for which mesitylene was used.

Table 5.3: Reaction feed composition

Feed	Quantity
Cyclohexanone	1.05 mL
Ammonia (28 wt%)	1.00 mL
H_2O_2 (30 wt%)	1.00 mL
Solvent	5.00 mL
Mesitylene (Internal standard)	0.05 mL
Catalyst	100 mg

Figure 5.13 shows the results of the reaction conducted at different temperatures with butanol as the solvent. The titanium centres were very active for the first step, as evident from the conversion and selectivity of the cyclohexanone feed to the oxime; but in all of the catalysts, no caprolactam was detected. Cyclohexanone conversion peaked at 343 K for all the catalysts, and further increasing the temperature to 353 K resulted in a decline in the conversion. The selectivity to oxime, however, varies with the samples. For instance, the samples HAT-140-70-0g and HAT-140-70-1g both show a constant drop in oxime selectivity with increasing reaction temperature. In the case of HAT-140-70-1.5g, the oxime concentration increased with temperature up to 343 K, followed by a fall at 353 K, while HAT-140-70-2g consistently produced more oxime up to the maximum reaction temperature investigated here.

Following the detection of no caprolactam from reactions over any of the catalysts, it was considered that the product desorption might be obstructed by the solvent. Hence, lighter solvents in ethanol and methanol were investigated at 353 K and the results are presented in figure 5.14.

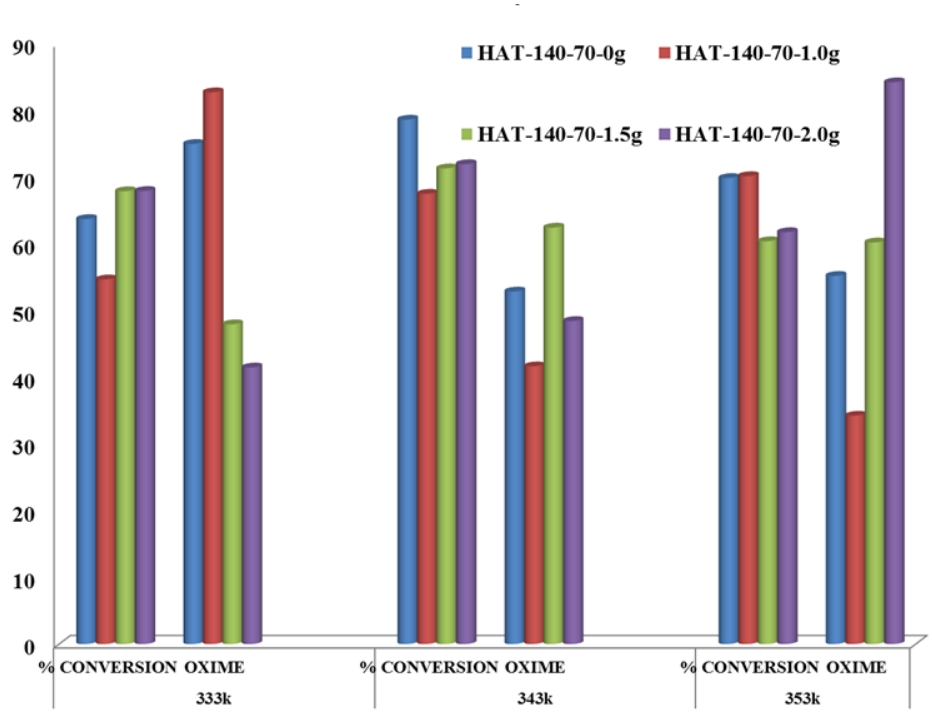

Figure 5.13: Effect of reaction temperature on cyclohexanone conversion and product distribution over the synthesized catalysts

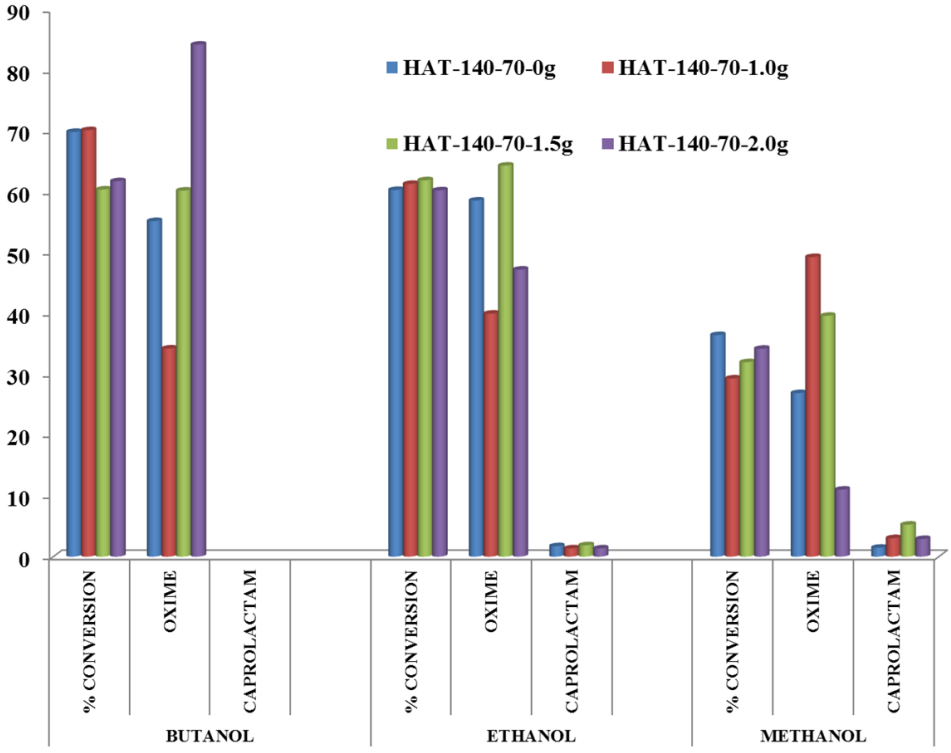

Figure 5.14: Effect of solvent on conversion and product distribution

Amongst the solvents investigated, methanol produced the least conversion and had the lowest selectivity to oxime. However the most amount of caprolactam was achieved in this solvent, which may lead to the conclusion that methanol favours the selectivity to Caprolactam, but the extremely low yield of this component means this conclusion must be treated with caution.

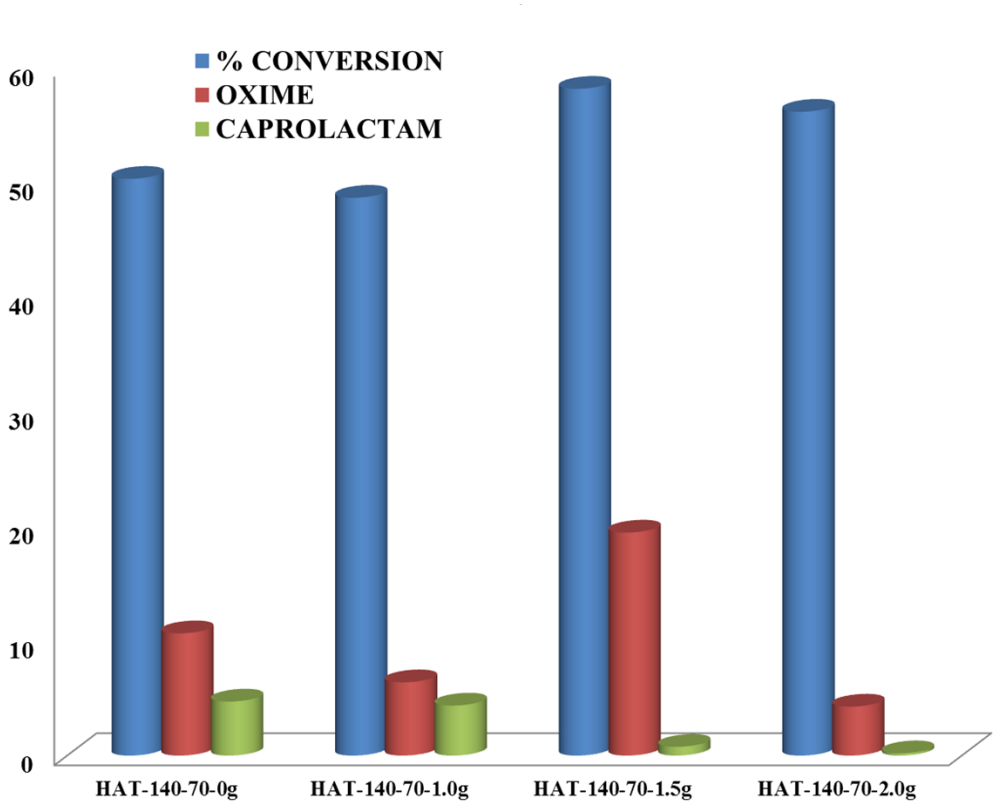

Figure 5.15: Cyclohexanone conversion and product distibution over different catalysts in a solvent free medium; (reaction temperature: 353 K, time: 4 hours)

The emergence of caprolactam in methanol and ethanol, in particular with more in methanol suggests that the lighter solvent may favour more caprolactam. To investigate this hypohesis, the reaction was conducted in a solvent free medium. The conversion of cyclohexanone in this reaction (i.e the solvent free medium) was higher than that obtained in methanol, comparable to that of ethanol and slightly lower than in butanol. The product distribution differs considerably from that

obtained in the solvent media. As presented in figure 5.15, the yield of caprolactam is still considerably lower than anticipated and at the same time, selectivity to oxime has been greatly diminished when compared to the results in the solvent medium.

The low yield of caprolactam in this experiment proves that the solvent used is perhaps not the crucial factor. Contrary to the observation for caprolactam, selectivity to oxime appears to be solvent dependent. In the solvent medium all the reacting species were in a single phase, allowing for more efficient transport over the catalysts, whereas, in the solvent free medium, they are in two different phases (organic and inorganic), which may favour faster decomposition of the peroxide and ammonia particularly at high temperature.

High selectivity to oxime was achieved over all of the catalysts in the solvent medium. The oxime produced was expected to be the material for caprolactam production. However, following the poor yield of the caprolactam, which should have been produced by the acid site in the catalyst, it was decided to conduct direct reaction of oxime over ZSM-5 and other commercial acid zeolites in the liquid phase, which we will expect to shed light on the role of the acid site in this reaction.

Table 5.4: Catalytic conversion of cyclohexanone oxime over different solid acid zeolite

	HAT-140-inf-0g	ZSM-5	Beta	Mordenite
Conversion (%)	0	0	0	0
Caprolactam (%)	*NPD	NPD	NPD	NPD

*NPD means no product detected

As shown in table 5.4, none of these commercial zeolites with purely acidic sites show any activity in the liquid phase conversion of the oxime to caprolactam. These results show that, there are no problems with the activity of the acid sites of the bifunctional zeolites investigated in this work. It may be postulated, especially based on the experiment of the purely acid site zeolites, that the acid sites required for this

reaction might not be activated in a liquid medium. Another possible explanation for the poor yield of caprolactam over the bifunctional catalysts investigated could be that their pores are not large enough to be accessed by the oxime, as demonstrated earlier for AlPO-36 and AlPO-18 systems of bifunctional catalyst [24]. But the poor performance of the larger pore zeolites Beta and Mordenite in the conversion of the oxime would effectively rule out this possibility.

To ascertain the active nature or otherwise of the acid sites of the bifunctional zeolites, two different gas phase experiments requiring acid sites were designed. The first involves the Beckmann rearrangement of cyclohexanone oxime to caprolactam and the second the conversion of methanol to hydrocarbons. These experiments will give insight into the activity of the acid sites of these bifunctional samples.

5.9.2 Gas-phase Beckmann rearrangement

The feed composition consists of 10 wt% cyclohexanone oxime in ethanol. The reactor catalyst bed was loaded with 200 mg of catalyst preformed and screened into 300 micron size. Catalyst activation was conducted at 500 ^{O}C for one hour under nitrogen flow and the reaction carried out at 350 ^{O}C over 4 hours. The product was collected in a tube placed in an ice bath. As before, the products were analysed using a GC equipped with an FID, with component identification achieved by comparing the retention time of standard compounds to that of the product and quantification conducted by the internal standard technique using mesitylene.

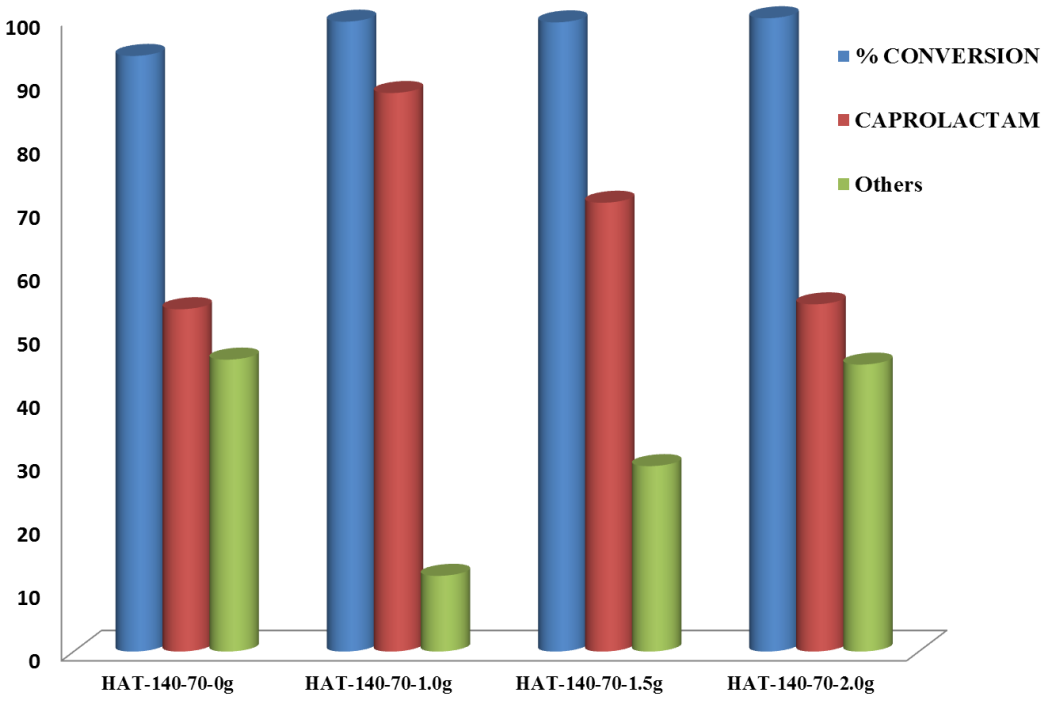

Figure 5.16: Gas phase Beckmann rearrangement of cyclohexanone oxime to caprolactam at WHSV=2hr^{-1}

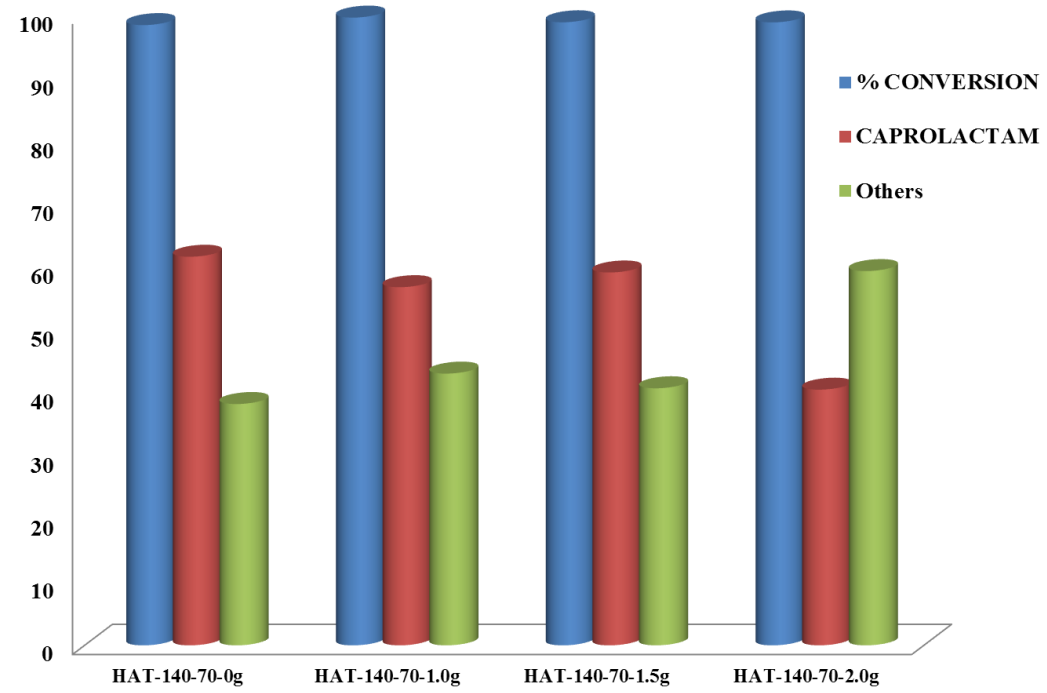

Figure 5.17: Gas phase Beckmann rearrangement of cyclohexanone oxime to caprolactam at WHSV=1hr^{-1}

The active nature of the acid site of these bifunctional catalysts is demonstrated in figure 5.16. All of the catalysts show very good activity in the conversion of cyclohexanone oxime to caprolactam - the conversion exceeds 90% for all the catalysts. The catalysts synthesized with chitosan in the precursor display better conversion and higher selectivity to caprolactam compared to that without chitosan. Increasing the chitosan in the starting precursor from 1 to 2 g resulted in decreased selectivity to caprolactam (but still higher than for the plain sample) and production of more 'others' products.

Reduction of the contact time of the reacting species with the catalyst bed had no effect on the conversion but exerts significant influence on the product selectivity (see figure 5.17). At shorter contact times (WHSV of $1hr^{-1}$), the selectivity to caprolactam was significantly influenced.

Table 5.5: Summary of MTH reaction products over the bifuctional catalysts

	HAT-140-70-0g	HAT-140-70-1g	HAT-140-70-1.5g	HAT-140-70-2g	HAT-140-inf-0g	HAT-140-inf-1.5g
Liquid products	Distribution of liquid Products					
Xylene	27.60	19.64	23.22	23.81	30.23	29.16
E-toluene	11.08	8.74	12.14	12.11	13.37	13.07
Diethylbenzene	1.02	1.73	1.11	1.52	1.11	1.99
Trimethylbenzene	47.17	49.45	50.01	50.46	45.80	45.88
Durene	13.13	20.44	13.52	12.10	9.59	9.90

5.9.3 Methanol to hydrocarbon conversion

As noted in chapter four, the methanol to hydrocarbon (MTH) reaction is an acid catalysed reaction where methanol is converted to a range of hydrocarbon products. Typical products that may be formed during the MTH reaction are given in chapter four of this work.

The gas phase reaction was conducted under the same reaction conditions described in the previous section. The liquid products were trapped while the gaseous products were allowed to evolve. The liquid products were analysed following the procedure described earlier in chapter four.

From the distribution of the liquid products emerging from each catalyst, no influence of the titanium coexisting with the aluminium could be observed. There was no significant variation in the products distribution as in table 5.5 for all the catalysts containing both titanium and aluminium in the framework. The catalysts synthesized from precursors with no chitosan had more yield of liquid products as compared to those with chitosan, which may be attributed to the decrease in the acidity imposed on these samples by the chitosan as discussed earlier and presented in figure 5.10. The pure aluminium silicalite (ZSM-5), however, shows a different pattern in the product selectivity. In these samples, higher xylene selectivity was achieved compared to those with both titanium and aluminium. The composition of the trimethylbenzene products in pure ZSM-5 was, however, lower than that obtained for the bifunctional counterpart.

5.10 Post reaction catalyst analysis

5.10.1 Coke analysis

The amount of residual coke left on each of the catalysts was investigated after the reactions. As discussed in chapter four, the quantity of coke was determined via the thermal analysis technique using TGA. About 10 - 15 mg of each sample was heated in the instrument up to 1000 ^{O}C and the weight lost due to the release of volatiles and residual coke in or on the catalyst was monitored.

Figure 5.18 (a and b) gives the thermograph for the catalysts thermally treated after the gas phase Beckmann rearrangement of cyclohexanone oxime. The thermographs show that all of the catalyst can be regenerated at about 600 ^{O}C, which implies that no stable coke was formed in or on the catalyst during this reaction.

A summary of the amount of coke per 200 mg of each catalyst is given in table 5.6. The catalysts subjected to longer contact time with the reaction mixtures show more coke, which is to be expected as the longer contact time implies that the catalysts are involved in more reaction processes and, hence, the likelihood of more coke being deposited increases.

Figure 5.19 is the thermograph of the catalysts used for the MTH reaction. Unlike in the Beckmann reaction where there was not much difference in the amount of coke deposited on all the catalysts, the sample without chitosan shows significantly more coke content during the MTH reaction. This observation can be attributed to the relatively stronger acidity (see FTIR spectra of figure 5.10) of this sample compared to the others.

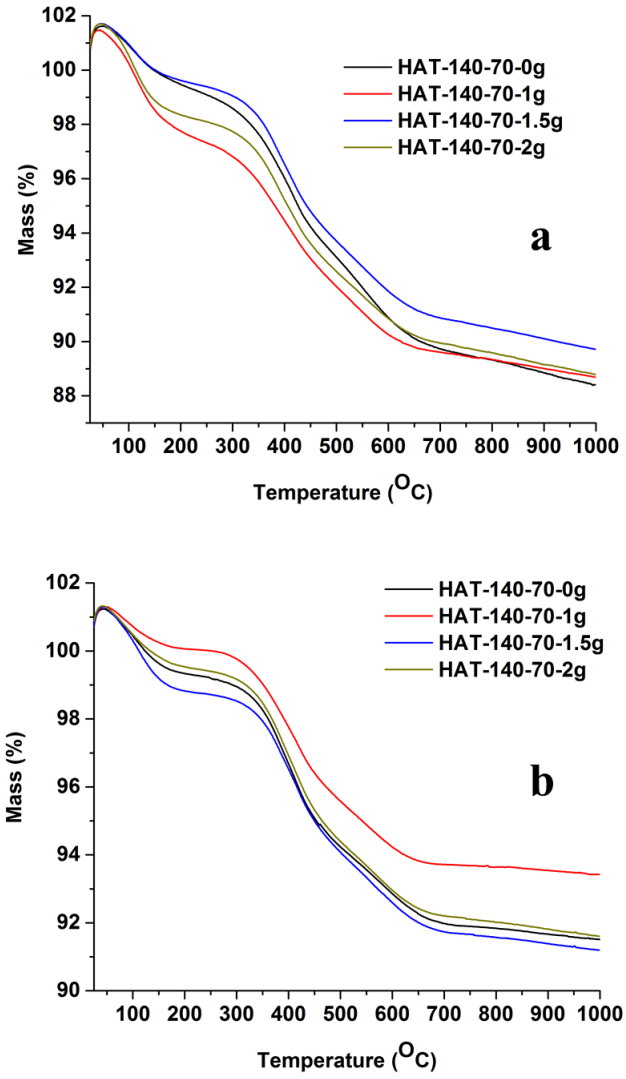

Figure 5.18: TGA Thermograph of catalysts used in the gas phase Beckmann reaction at WHSV of (a) $2hr^{-1}$ and (b) $1hr^{-1}$

Table 5.6: Total amount of coke produced per 200 mg of catalyst during gas phase Beckmann reaction at different WHSV

	Total Coke generated/200mg catalyst (mg)	
Catalyst/WHSV	$1hr^{-1}$	$2hr^{-1}$
HAT-140-70-0g	16.98	23.20
HAT-140-70-1g	13.16	22.63
HAT-140-70-1.5g	17.61	20.57
HAT-140-70-2g	16.79	22.42

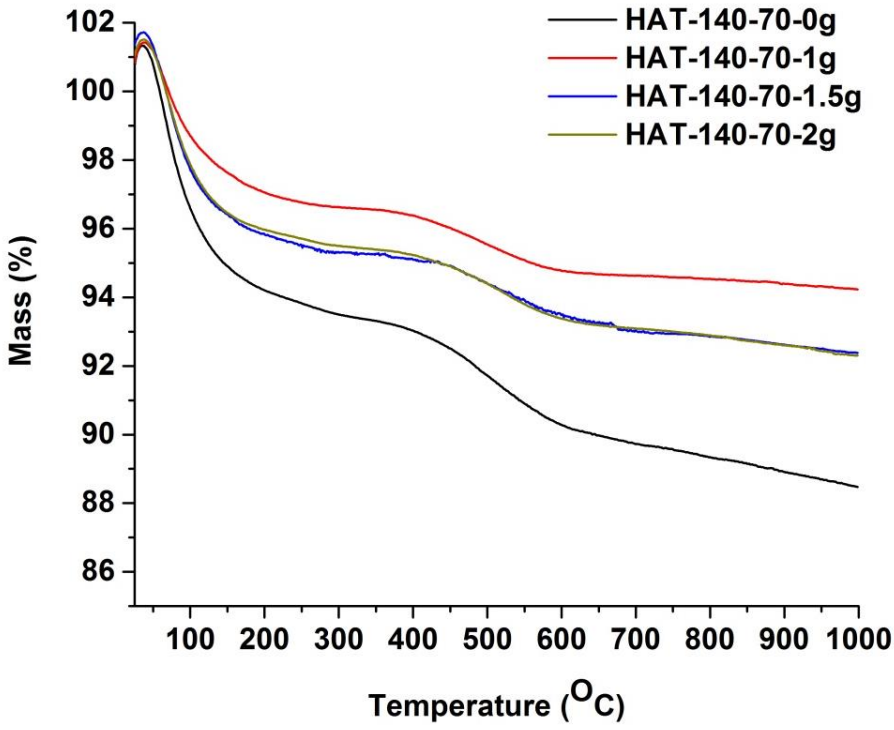

Figure 5.19: TGA Thermograph of catalysts used in the methanol to hydrocarbon reaction

Table 5.7: Coke produced per 200 mg of catalyst during MTH reaction, WHSV=2hr^{-1}, Reaction time=4hr, Temperature = 350 ^{O}C

	Initial weight (mg)	Final weight (mg)	Coke (mg)	Coke per mg	Total coke/200mg
HAT-140-70-0g	12.67	11.21	1.46	0.12	23.05
HAT-140-70-1g	13.76	12.97	0.79	0.06	11.54
HAT-140-70-1.5g	12.08	11.16	0.92	0.08	15.24
HAT-140-70-2g	13.31	12.28	1.02	0.08	15.40

5.10.2 Nature of coke

As in chapter four, the nature of the residual coke in each of the catalysts post reaction can be determined through the Raman technique, which is particularly sensitive to carbon and the carbon source. The Raman analysis of the post Beckmann reaction catalysts is given in figure 5.20. The intensity of the band at approximately

1613 cm^{-1}, which is attributed to hydrogen deficient carbon, can be seen to grow increasingly intense as the WHSV was increased from (a)1$hr^{-1}$to (b) 2hr^{-1}

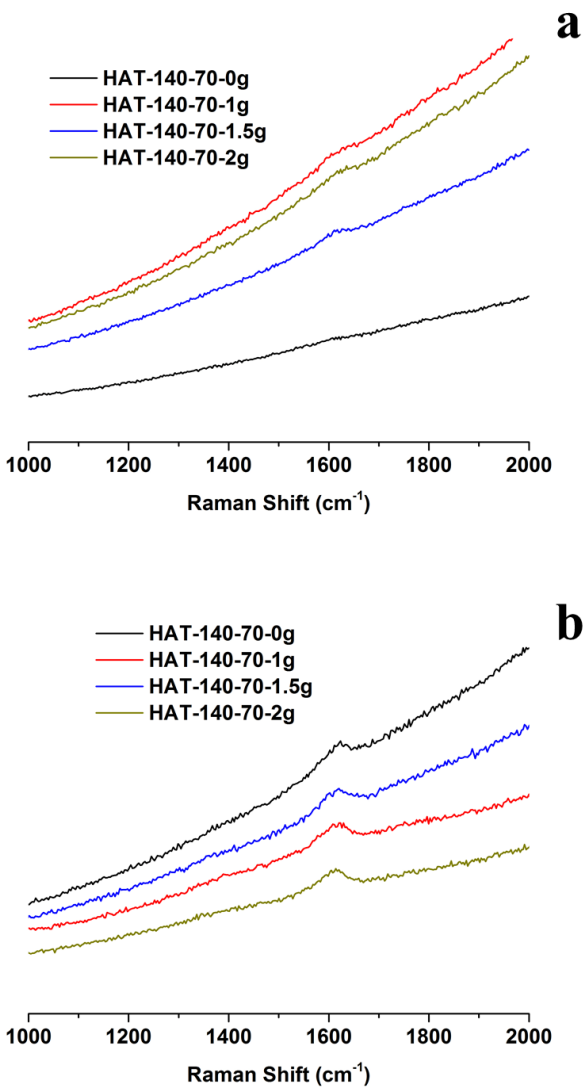

Figure 5.20: Raman spectrum of spent catalyst from the gas phase Beckmann rearrangement at WHSV of (a) 1$hr^{-1}$and (b) 2hr^{-1}

Contrary to the coked catalysts from the Beckmann reaction, where only the 1613 cm^{-1} peak was detected, the coked catalysts from the MTH reaction showed two distinct carbon bands. In addition to the band at 1613 cm^{-1}, which is that of hydrogen deficient carbon from aromatic compounds, another band at 1394 cm^{-1}

(figure 5.21) can be seen. This second band is characteristic of olefinic carbon species, which are less devoid of hydrogen.

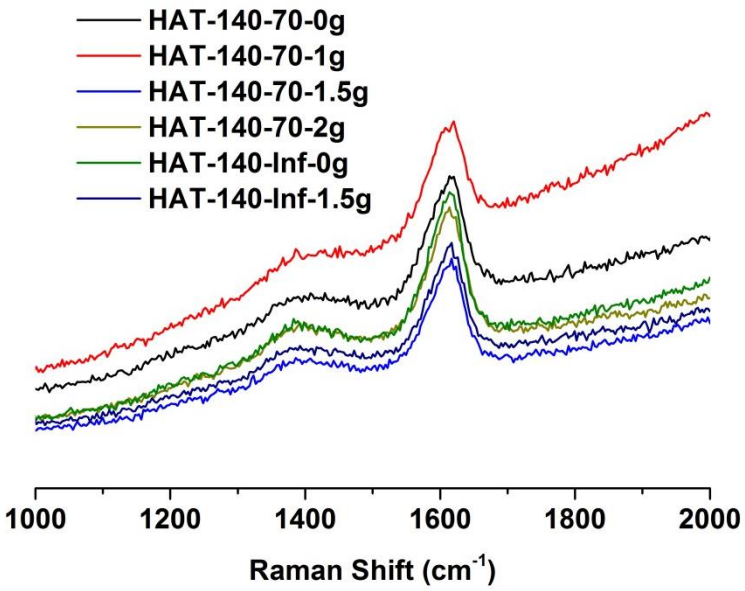

Figure 5.21: Raman spectra of spent catalysts from the gas phase methanol to hydrocarbon reaction

5.10.3 Catalyst regeneration

The post MTH reaction catalysts were subjected to different temperatures in static air in an attempt to free them from the deposited coke species. No sign of the Raman bands, that signify the presence of carbon was detected in any of the catalysts after they were subjected to a temperature of 600 ^{O}C, which is consistent with the TGA thermographs presented earlier in Figure 5.19. This result shows that a temperature just above 600 ^{O}C should be sufficient to remove all the coke species and free the catalysts' active sites. Notably, however, the olefinic carbon band can be seen to have completely vanished even at a much lower regeneration temperature of 450 ^{O}C, while, at the same temperature, the aromatic band has diminished considerably.

The most significant observation of this regeneration cycle was the appearance of the anatase band in those samples which were originally devoid of this titanium phase prior to the reactions. One possible explanation for this observation could be that the framework titanium is being leached out during the gas phase reaction. Another possibility could be the leaching or transformation of the tetrahedral framework titanium into the extra framework anatase during regeneration. The likelihood of the latter is, however, debateable as the fresh catalyst was subjected to post synthesis calcination in the same temperature range without any noticeable phase transformation.

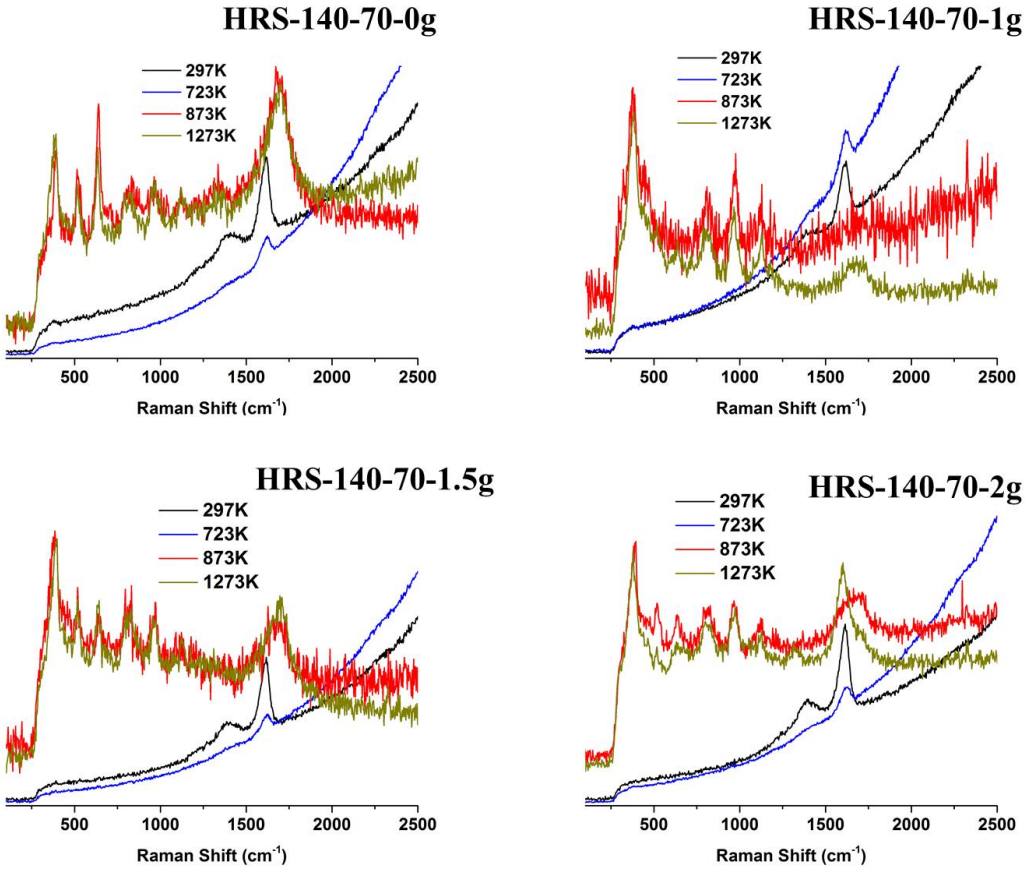

Figure 5.22: Raman spectra of spent catalysts from the MTH reaction treated at different temperatures.

5.11 Summary and conclusions

Bifunctional zeolite catalysts based on the MFI topology were successfully synthesized. The redox site was created by tetrahedral incorporation of tetravalent titanium into the zeolite framework, while the acid sites were created by substitution of trivalent aluminium in the siliceous framework of the MFI zeolite. These were achieved by one-pot hydrothermal synthesis.

Powder diffraction patterns confirmed that the synthesized zeolites were crystalline and phase pure with the MFI topology. The morphology showed aggregated spherical particles in the plain samples, while those synthesized in the presence of chitosan displayed aggregated particles forming rod shapes. Vibrational spectroscopy techniques showed some of the titanium were not in the tetrahedral position for certain samples, just as observed for the aluminium through the solid state NMR technique.

All the samples showed good catalytic activity in the liquid phase ammoximation and the gas-phase Beckmann reaction as well as the methanol to hydrocarbon reactions. The initial objective of one-stream, low temperature, liquid phase production of caprolactam from cyclohexanone was, however, not achieved, which was attributed to the failure to activate the acid sites of the catalysts in the liquid medium, as their activity was proven in subsequent gas-phase reactions. Another possible explanation for this observation could be that the caprolactam is not readily desorbed from the catalyst pores or active sites upon formation.

Post reaction analysis of the spent catalysts showed two types of coke species in the catalysts from the MTH reaction, while those used for the Beckmann reaction exhibited just one carbon species. The amount of carbon deposited was observed to

increase with the contact time between the catalyst and the feed. Some of the framework titanium, however, appears to have leached out of the framework position and converted into the anatase phase during high temperature catalyst regeneration; this can be appreciated by the appearance of Raman peaks attributable to the presence of the anatase phase or octahedrally coordinated titanium.

References

1. C.N. Satterfield, *Heterogeneous catalysis in industrial practice,* Second edition, McGraw-Hill, **1991**.

2. G.A. Mills, H. Heinemann, T.H. Milliken, A.G. Oblad, I*nd. Eng. Chem.*, **1953**, *45*, 134-137

3. R. Beerthuis, G. Rothenberg, N.R. Shiju, *Green Chem.*, **2015**, *17*, 1341-1361

4. A. Thangaraj, S. Sivasankar, P. Ratnasamy, *Journal of Catalysis*, **1991**, *131*, 394-400

5. N. R. Shiju, M. Anilkumar, W. F. Hoelderich, D. R. Brown, *J. Phys. Chem. C*, **2009**, *113*, 7735-7742

6. M. Tamura, W. Chaikittisilp, T. Yokoi, T. Okubo, *Microporous and Mesoporous Materials*, **2008**, *112*, 202-210

7. M. Moliner, A. Corma, *Microporous and Mesoporous Materials*, **2014**, *189*, 31-40

8. Y.K. Hwang, J.S. Chang, S.E. Park, D.S. Kim, Y.U. Kwon, S.H. Jhung, J.S. Hwang, M.S. Park, *Angew Chem Int Ed Engl*, **2005**, *44*, 556-60

9. C. Shen, Y.J. Wang, C. Dong, G.S. Luo, *Chemical Engineering Journal*, **2014**, *235*, 75-82

10. G. Liu, J. Wu, H. Luo, *Chinese Journal of Chemical Engineering*, **2012**, *20*, 889-894

11. J. Lin, F. Xin, L. Yang, Z. Zhuang, *Catalysis Communications*, **2014**, *45*, 104-108

12. J.C. Van Der Waal, M.S. Rigutto, H. Van Bekkum, *Applied Catalysis A: General*, **1998**, *167*, 331-342

13. A. Corma, M.A. Camblor, P. Esteve, A. Martinez, J. Perez-Pariente, *Journal of Catalysis*, **1993**, *145*, 151-158

14. Y. Wang, A. Zhang, Q. Xu, R. Chen, *Applied Catalysis A: General*, **2001**, *214*, 167-177

15. E.G. Vaschetto, G.A. Monti, E.R. Herrero, S.G. Casuscelli, G.A. Eimer, *Applied Catalysis A: General*, **2013**, *453*, 391-402

16. D. Zhang, R. Wang, X. Yang, *Catalysis Communications*, **2011**, *12*, 399-402

17. F. Meng, Y. Wang, L. Wang, R. Yang, T. Zhang, *Journal of Molecular Catalysis A: Chemical*, **2011**, *335*, 105-111

18. M. Anilkumar, W.F. Höelderich, *Journal of Catalysis*, **2008**, *260*, 17-29

19. M. Anilkumar, W.F. Hoelderich, *Catalysis Today*, **2012**, *198*, 289-299

20. H. Wei, N. Zhang, T. Zhao, Y. Liu, Y. Wen, X. Wang, B. Li, *RSC Adv.*, **2015**, *5*, 3642-3647

21. C. Yin, R. Ni, X. Bao, Y. Chen, *Microporous and Mesoporous Materials*, **2015**, *202*, 133-137

22. J.M. Thomas, R. Raja, *Proc Natl Acad Sci USA*, **2005**, *102*, 13732-6

23. M. Anilkumar, W.F. Hoelderich, *Applied Catalysis B: Environmental*, **2015**, *165*, 87-93

24. R. Raja, G. Sankar, J.M. Thomas, *J. Am. Chem. Soc.*, **2001**, *123*, 8153-8154

25. F. Zhang , X. Guoa, X. Wang , G. Li , J. Zhou, J. Yu, C. Li, *Catalysis letters*, **2001**, *72*, 235-239

26. S. Bordiga, A. Damin, F. Bonino, G. Ricchiardi, A. Zecchina, R. Tagliapietra, C. Lamberti, *Physical Chemistry Chemical Physics*, **2003**, *5*, 4390

27. Q. Guo, K. Sun, Z. Feng, G. Li, M. Guo, F. Fan, C. Li, *Chemistry*, **2012**, *18*, 13854-60

28. C. Li, G. Xiong, Q. Xin, J. Liu, P. Ying, Z. Feng, J. Li, W. Yang, Y. Wang, G. Wang, X. Liu, M.X. Wang, E. Min, *Angew Chem Int Ed*, **1999**, *38*, 2220-2222

29. A. Nearchou, A. Sartbaeva, *CrystEngComm*, **2015**, *17*, 2496-2503

30. E. Lippmaa, M. Magi, A. Samoson, M. Tarmak, G. Engelhardt, *J. Am. Chem. Soc*, **1981**, *103*, 4992-4996

31. J. Klinowski, *Progress in NMR Spectroscopy*, **1984**, *16*, 237-309

32. J.M. Thomas, *Microporous and Mesoporous Materials*, **2007**, *104*, 5-9

33. M. Thommes, K. Kaneko, A.V. Neimark, J.P. Olivier, F. Rodriguez-Reinoso, J. Rouquerol, K.S.W. Sing, *Pure and Applied Chemistry*, **2015**, *87*, 1051-1069

Chapter 6: Summary, conclusion and future works

6.1 Summary and conclusion

First, we investigated the potential use of chitosan as an inert macro templating agent for the direct synthesis of a hierarchical titano-silicate (TS-1) zeolite. The study afforded us the opportunity to monitor the effect of the addition of the chitosan on the physical and chemical features of the TS-1 zeolite. Using X-ray diffraction, it was observed that the presence of chitosan in the synthesis precursor of the TS-1 had no influence on the crystallinity and phase purity of the resulting zeolite. In addition to the tetrahedrally bound framework titanium atoms in the TS-1 zeolite structure, Raman, UV-Vis and XAS techniques showed some extra-framework titanium species were present. Nitrogen adsorption measurements on the synthesized TS-1 samples showed the existence of pores in the meso- and macropore range in the samples, leading to the conclusion that chitosan is a potential macro-templating candidate.

The catalytic versatility of theses samples was subsequently investigated for cyclohexene and styrene epoxidation. All the chitosan templated samples showed better catalytic conversion in both reactions, but displayed lower selectivity to the epoxide products. The results of the selectivity over each sample showed that the method through which the samples were synthesized was important. For instance, the samples derived from the partially dried (PD) synthesis technique showed better selectivity to epoxide in the cyclohexene oxidation reaction, compared to those derived through the fully dried (FD) technique. Reaction conditions were also shown

to be important in epoxide selectivity - reactions conducted at lower temperatures or for short times resulted in improved selectivity for epoxide product. The product distribution of the styrene epoxidation reaction showed strong dependence on the solvent employed. In this reaction acetonitrile tends to favour selectivity to benzaldehyde, while acetone favours styrene oxide.

The next study focused on the application of the chitosan in a three dimensional (3D) frame structure as a macro-template. First, the chitosan powder was transformed into the scaffold and the scaffold used as a rigid macro-template for the synthesis of the alumino-silicate ZSM-5 zeolite. SEM characterization showed the scaffolds were porous with distinct pore networks. The zeolite crystals were observed to crystallize within these pores, and the resulting zeolites exhibit step growth morphology. X-ray diffraction of all the scaffold templated samples showed good crystallinity and phase purity, while Solid State NMR showed that the aluminium atoms exist predominantly in the framework position, even though some extra framework aluminium was detected. The acidity of all the samples was proven through *in situ* FTIR. Samples templated with scaffolds that were made out of high chitosan concentration showed a lower number of Brønsted acid sites. This Brønsted acidity could, however, be improved by increasing the aluminium content in the starting precursor. The role of the scaffold as a macro-template was also demonstrated by nitrogen adsorption measurements which showed two distinct pore distributions at ca 20 Å and 50 Å (corresponding to the microporous and mesoporous sites respectively) for the templated samples. All the samples synthesized here displayed good catalytic activity for the methanol to hydrocarbon reaction. The selectivity of the samples depends on several parameters, such as the chitosan weight percentage,

the amount of zeolite precursor impregnated into the scaffold and the silicon to aluminium ratio of the sample.

In the final part of this study, the focus was on the synthesis of samples that will combine both redox and acid functionalities. A combination of characterization techniques (FTIR, Raman, UV-VIS and NMR) confirmed the coexistence of both titanium and aluminium in tetrahedral framework positions. These bifunctional catalysts showed distinct activity for the redox and acid functionalities, but could not be used to catalyse the reactions consecutively. This observation was attributed to the possibility of the acid sites not been activated in the liquid phase.

6.2 Future works

We have shown that chitosan can be successfully used as a macro-template to synthesize hierarchically porous zeolites with the MFI structure. Other steps could be taken in order to better understand the role of the chitosan during the hydrothermal synthesis step. First, the chitosan could be densified by subjecting it to hydrothermal treatment prior to mixing it with the zeolite precursor. Secondly, to obtain the truly 3D scaffold zeolite, which was the focus of chapter 4 of this work, other synthesis conditions may be explored. One such condition could be the impregnation of the scaffold with the zeolite precursor, followed by freeze drying and subjecting the system to vapour phase synthesis techniques to prevent swelling of the scaffold. The chitosan scaffold could also be made into different shapes or into beads for direct addition to the precursor. Hierarchical zeolites prepared using chitosan as macro-templates clearly have great promise in catalytic science.

Appendices

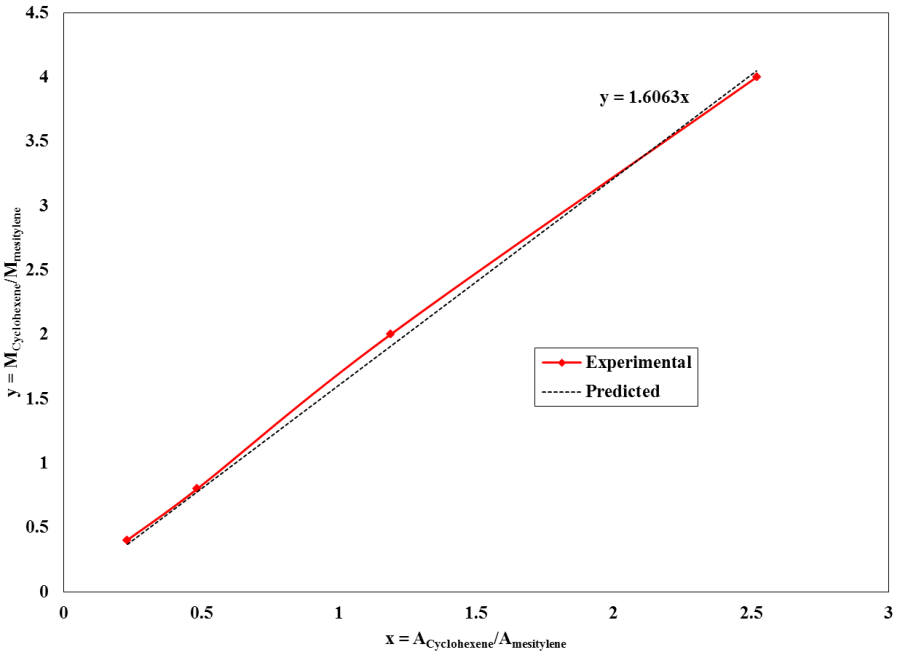

Appendix 1: Calibration curve of cyclohexene

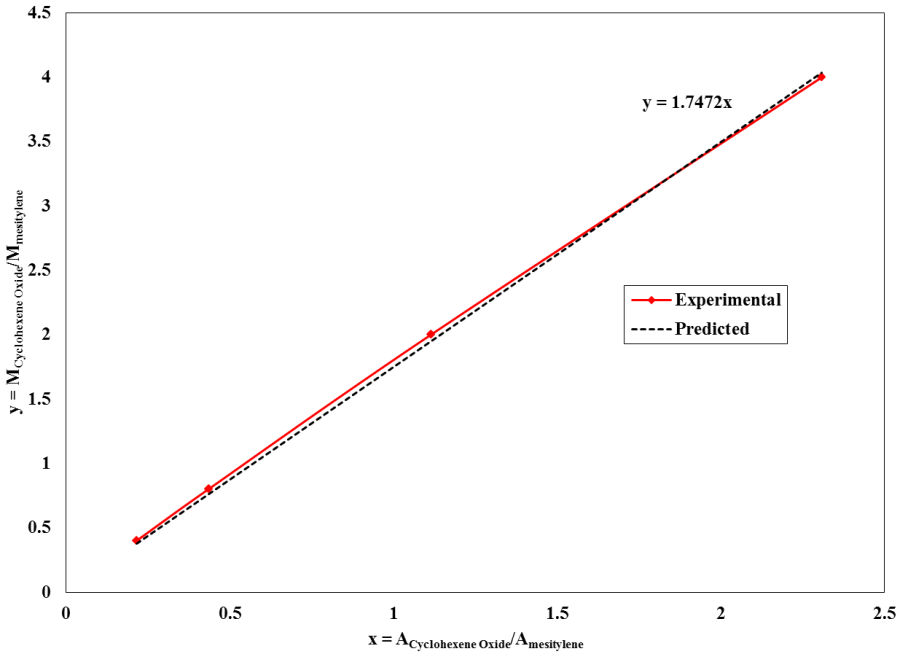

Appendix 2: Calibration curve of cyclohexene oxide

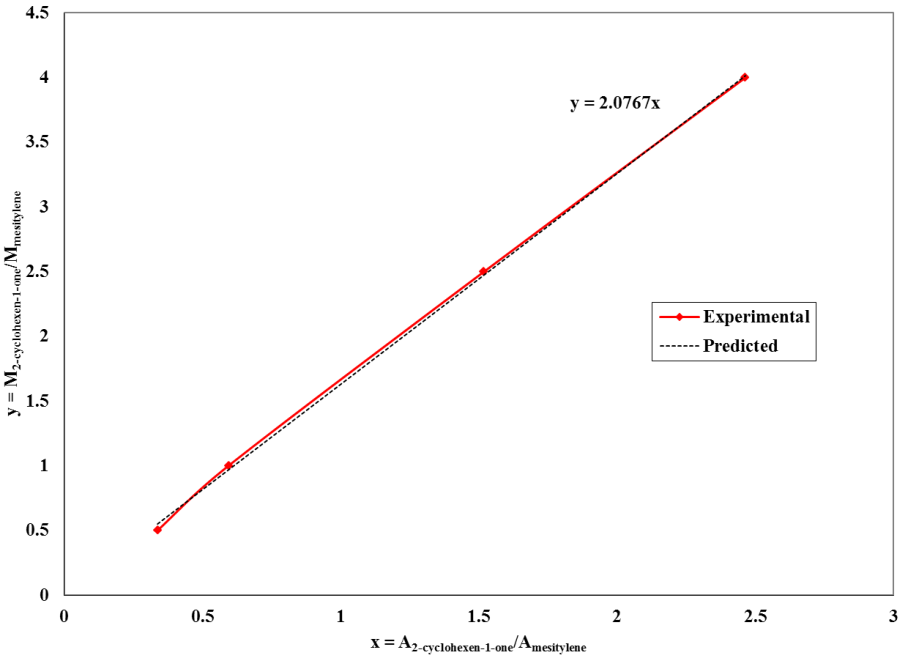

Appendix 3: Calibration curve of 2-cyclohexen-1-one

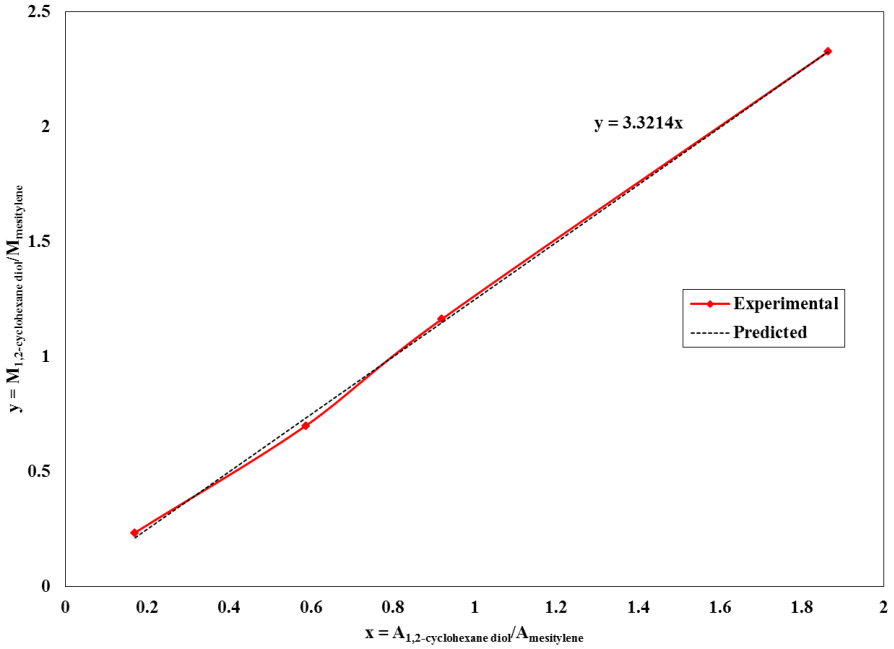

Appendix 4: Calibration curve of 1,2-cyclohexane diol

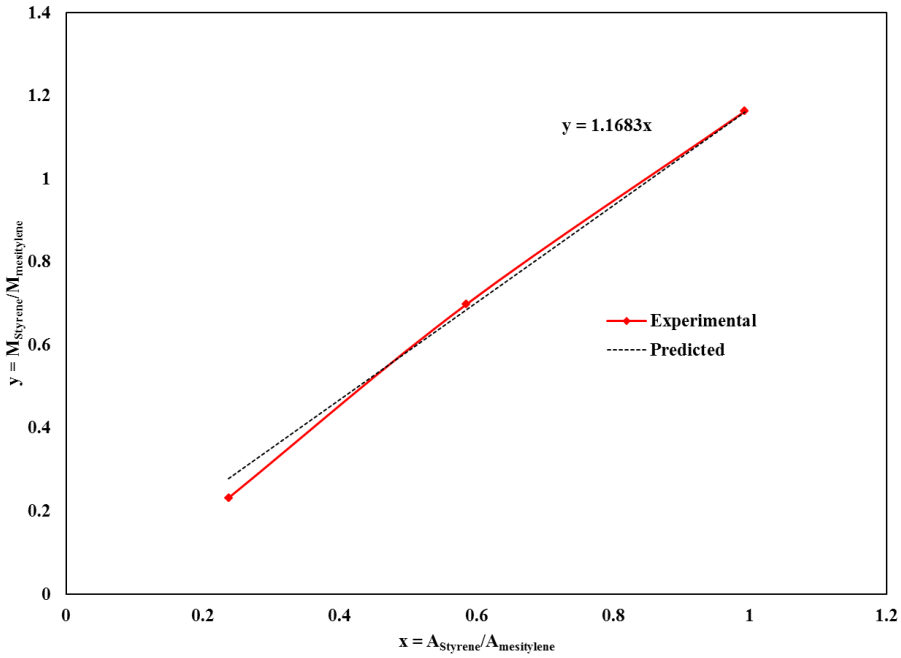

Appendix 5: Calibration curve of styrene

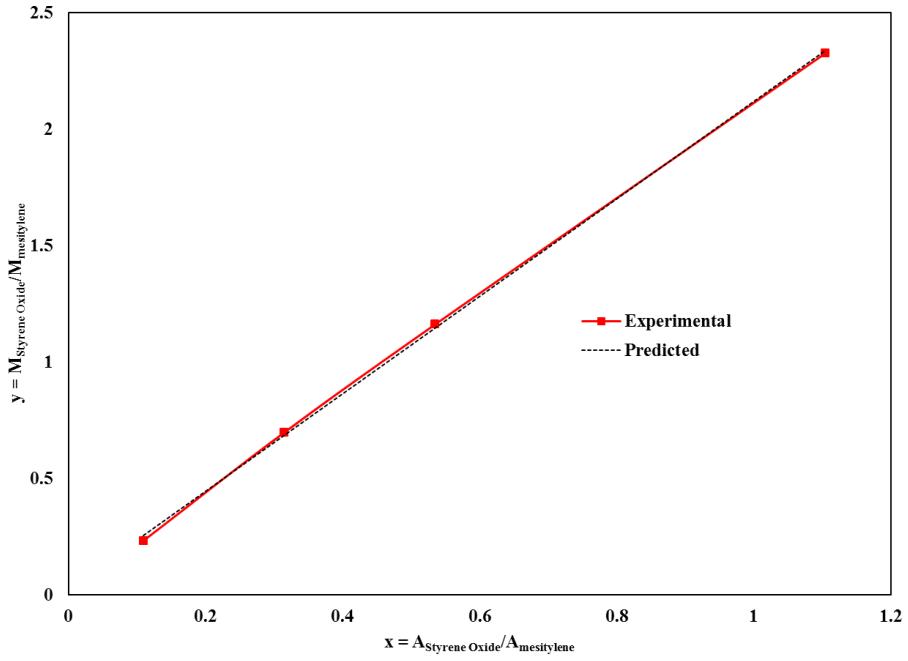

Appendix 6: Calibration curve of styrene oxide

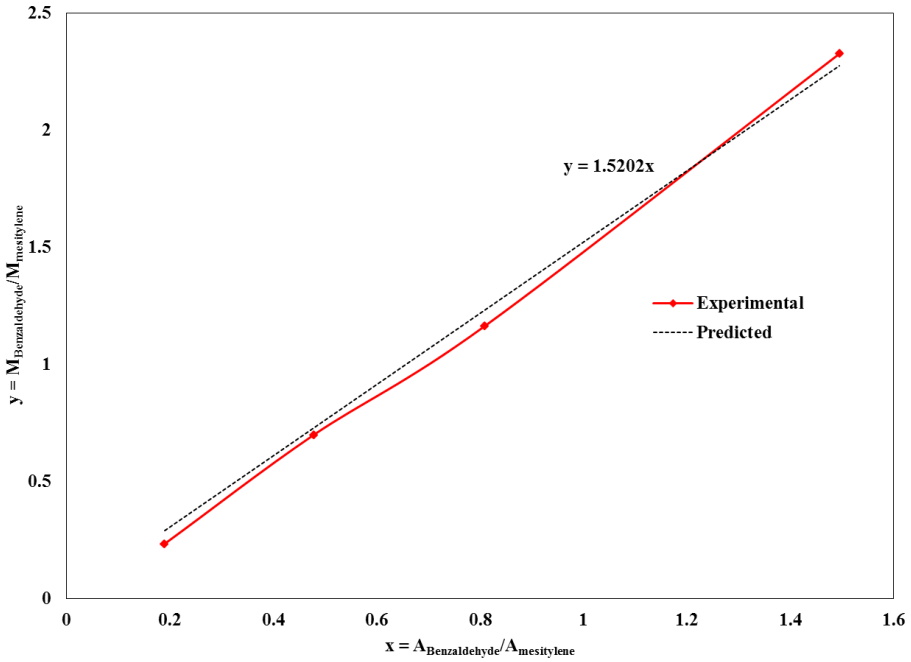

Appendix 7: Calibration curve of benzaldehyde

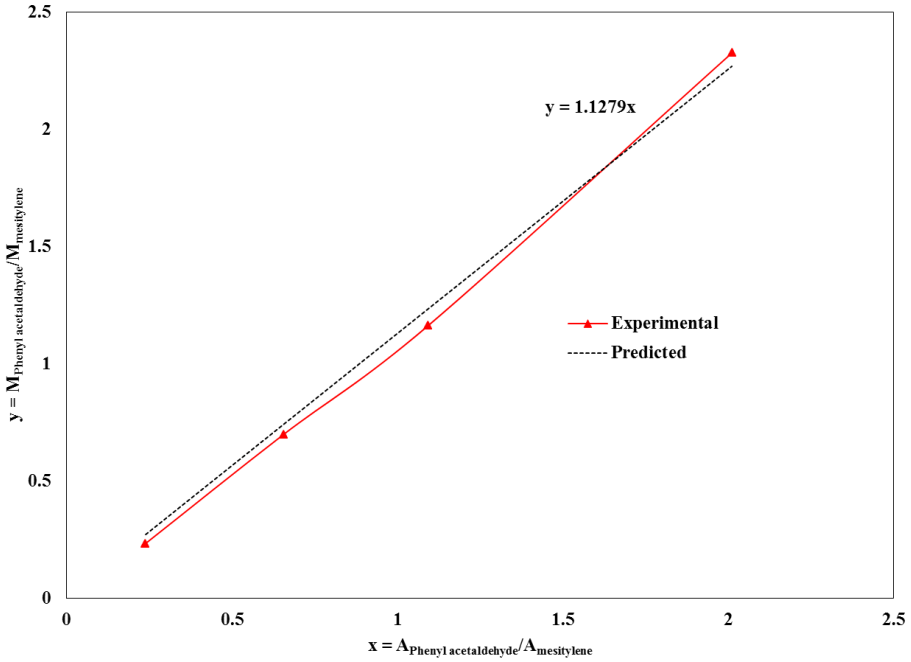

Appendix 8: Calibration curve of phenyl acetaldehyde

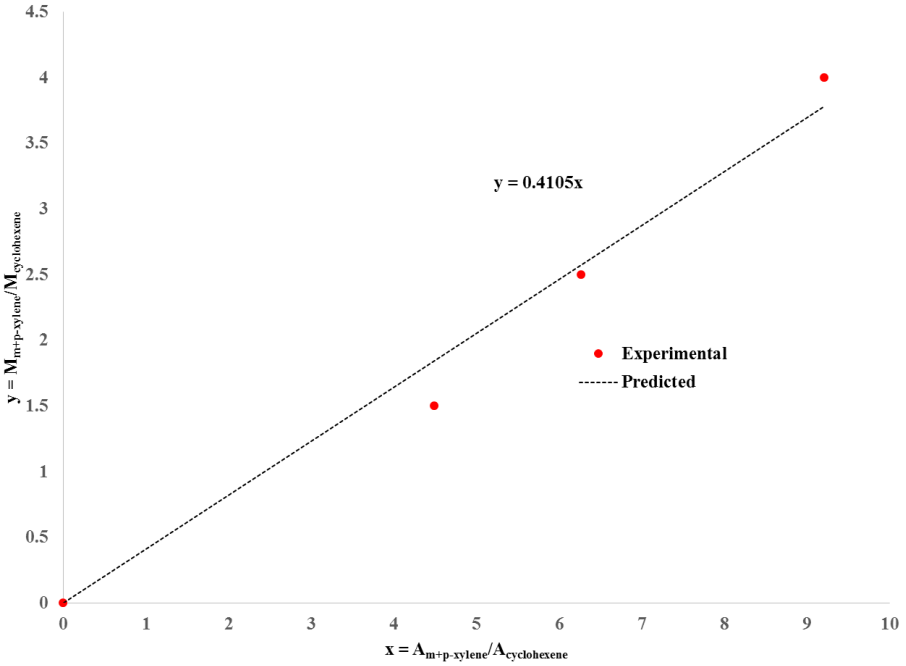

Appendix 9: Calibration curve of m- and p-xylene

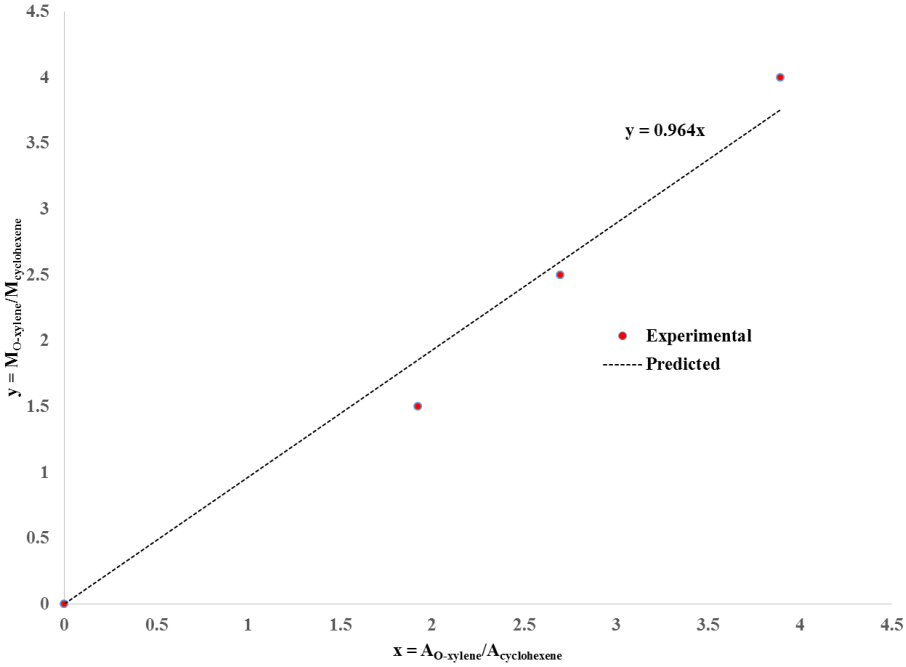

Appendix 10: Calibration curve of O-xylene

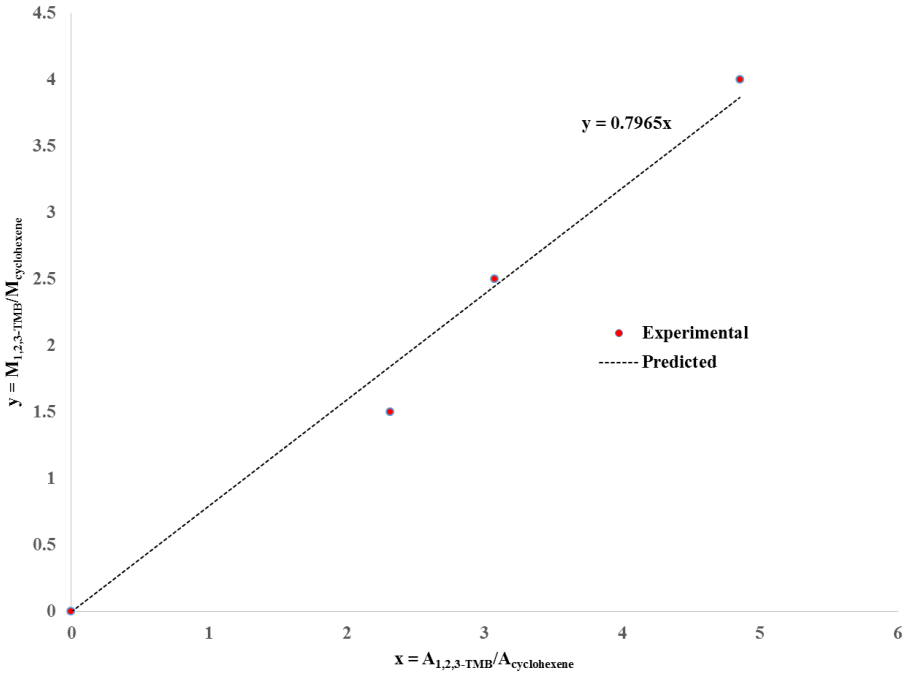

Appendix 11: Calibration curve of 1,2,3-trimethyl benzene

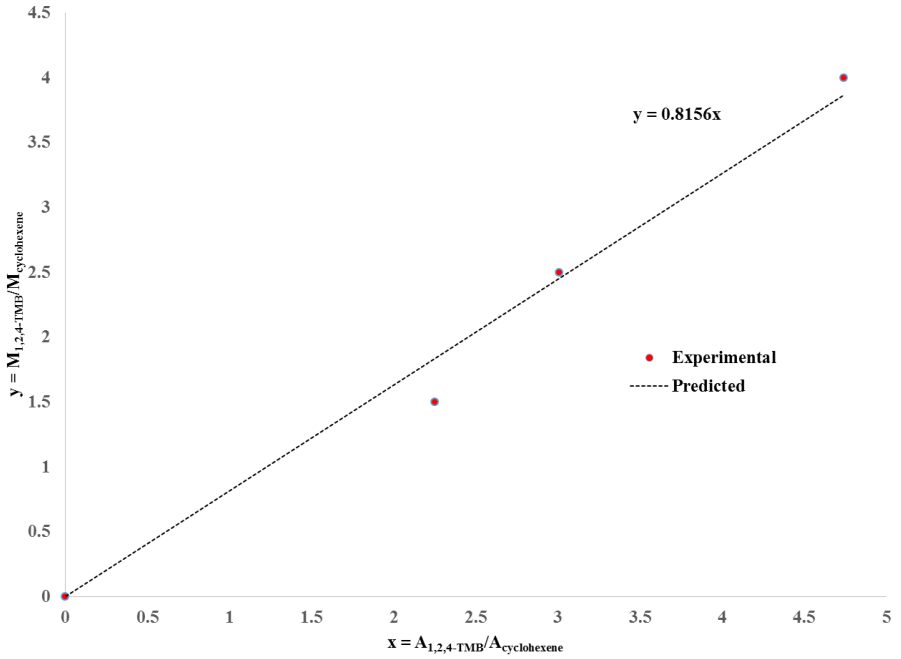

Appendix 12: Calibration curve of 1,2,4-trimethyl benzene

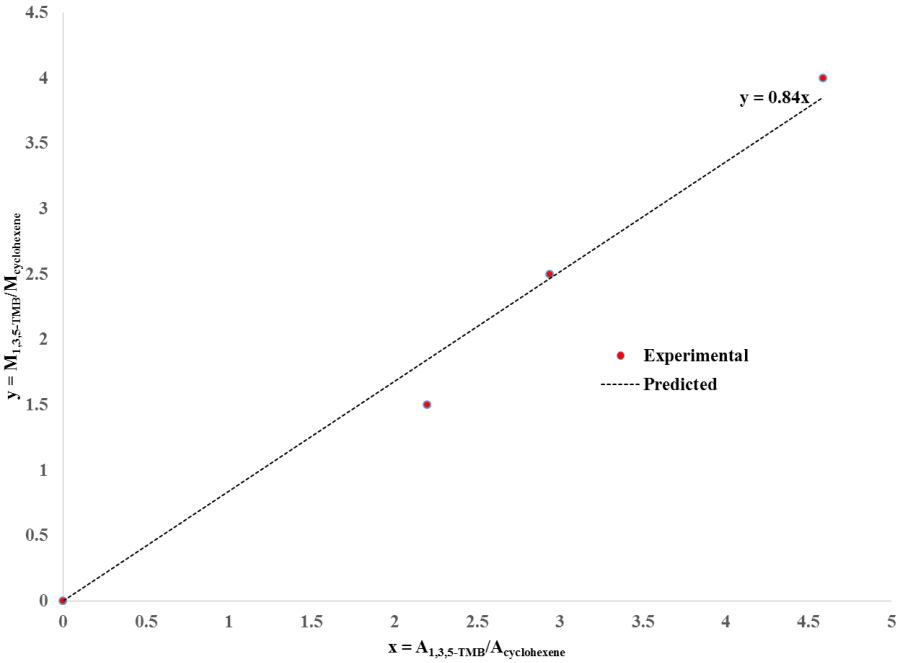

Appendix 13: Calibration curve of 1,3,5-trimethyl benzene

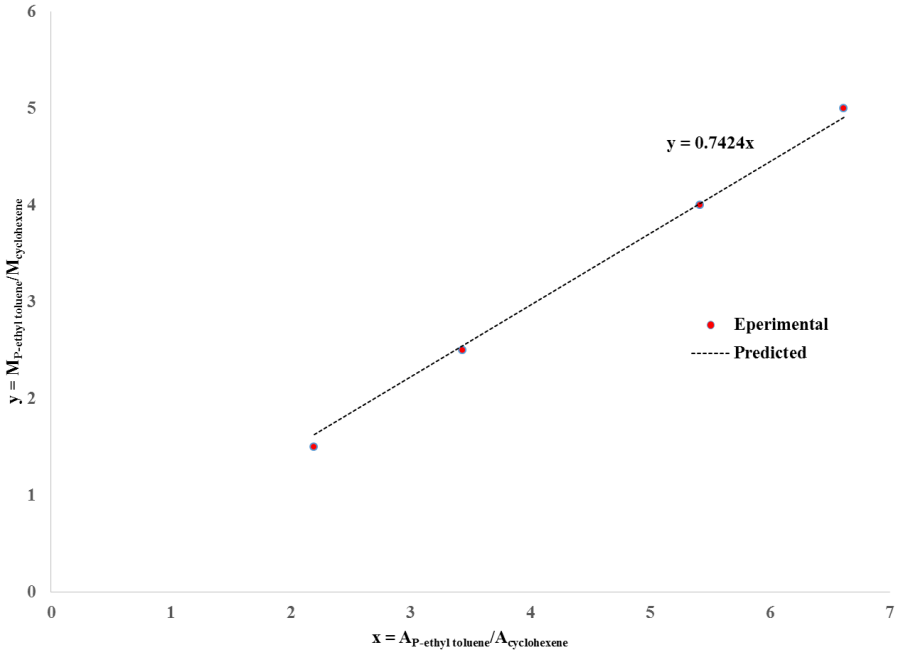

Appendix 14: Calibration curve of p-ethyl toluene

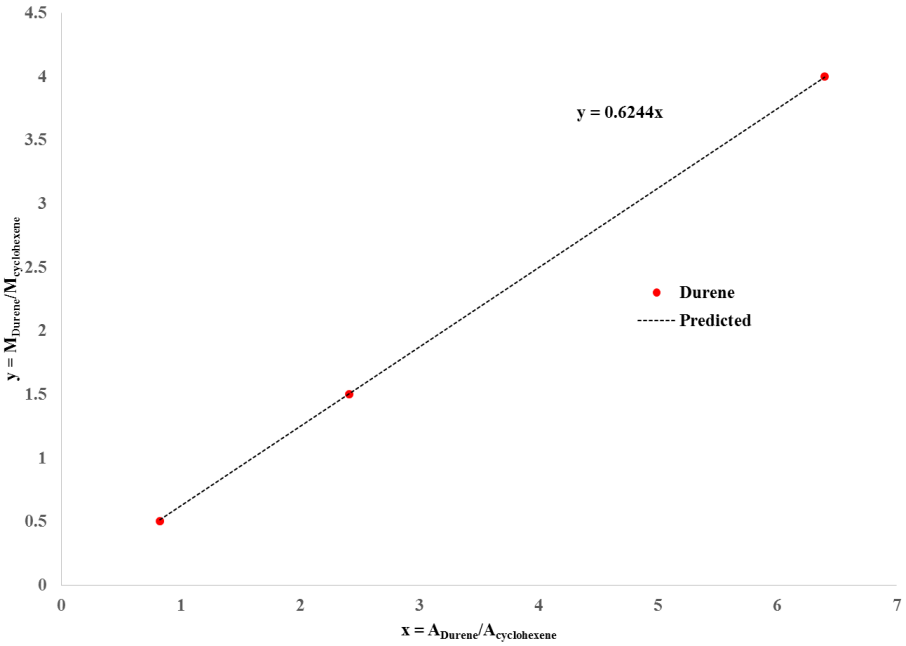

Appendix 15: Calibration curve of Durene

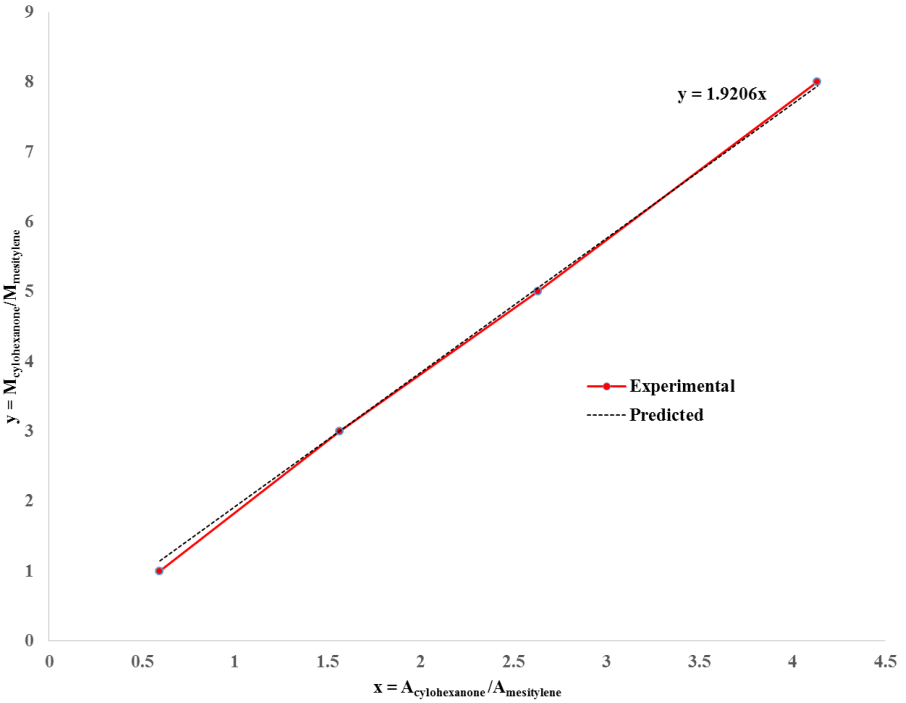

Appendix 16: Calibration curve of cyclohexanone

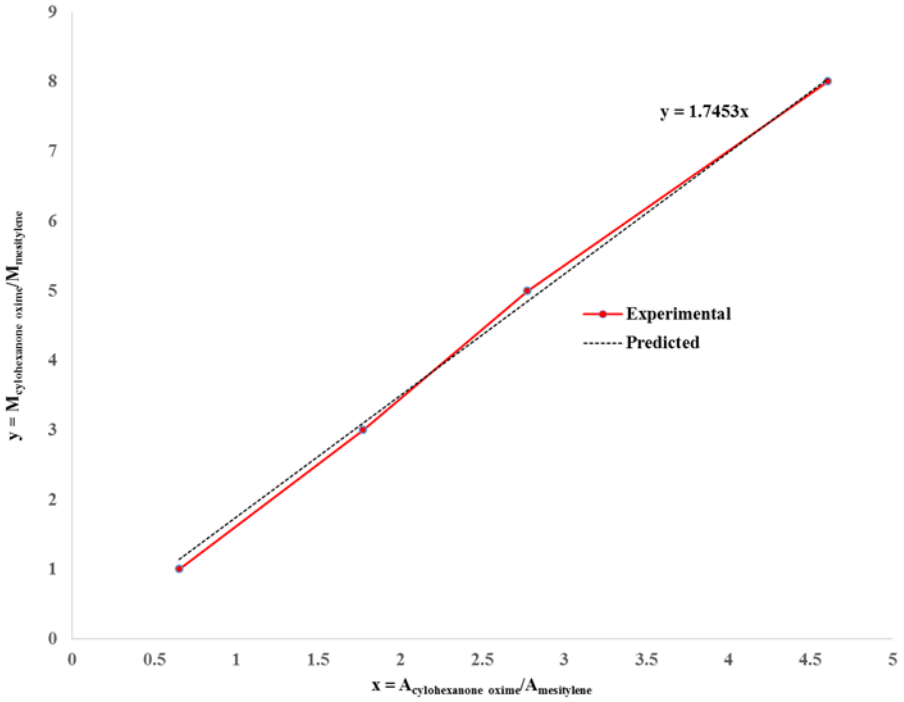

Appendix 17: Calibration curve of cyclohexanone oxime

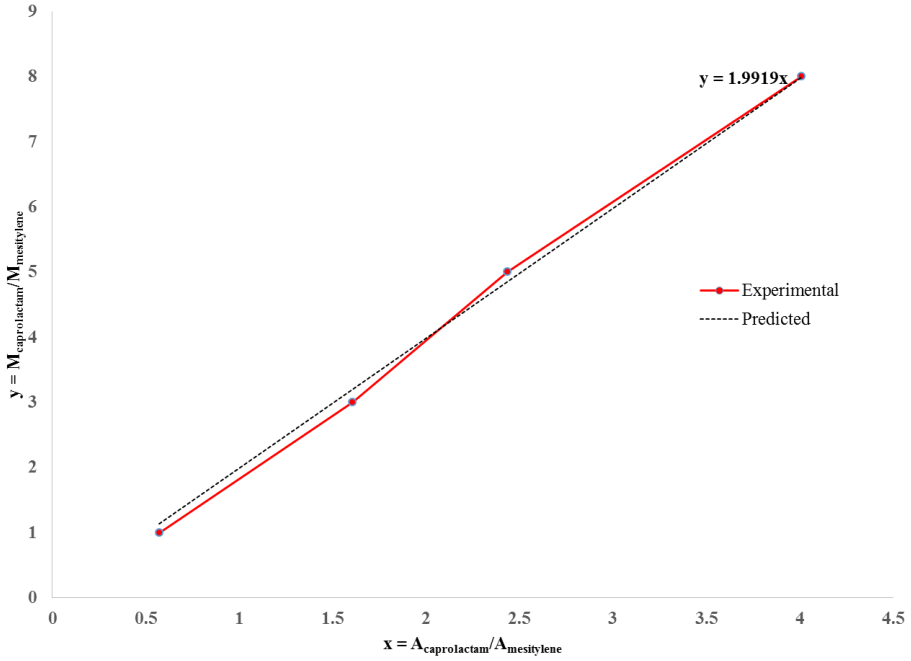

Appendix 18: Calibration curve of caprolactam

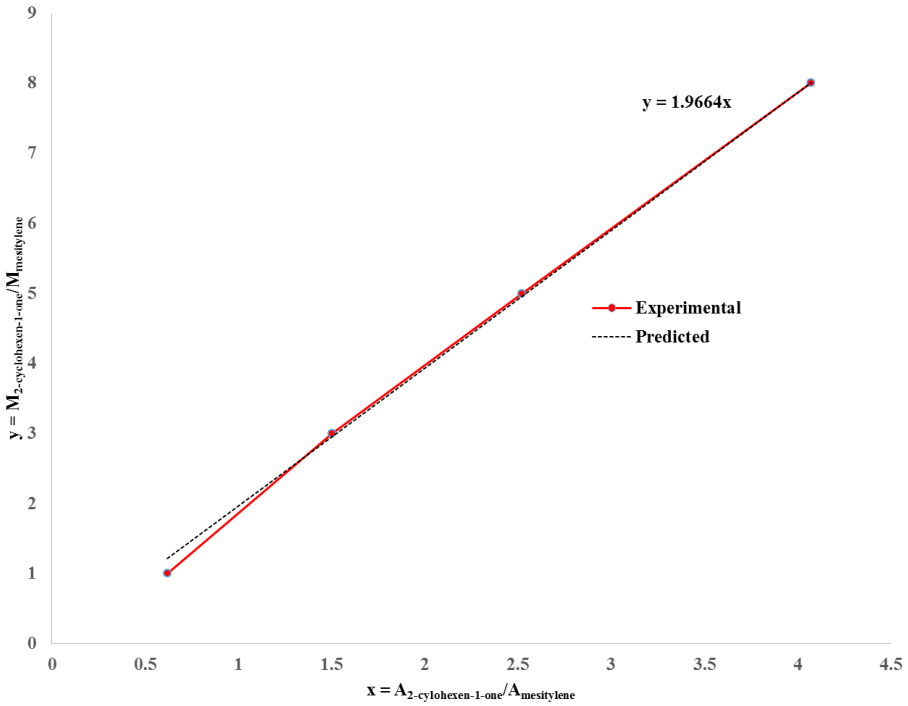

Appendix 19: Calibration curve of 2-cyclohexen-1-one

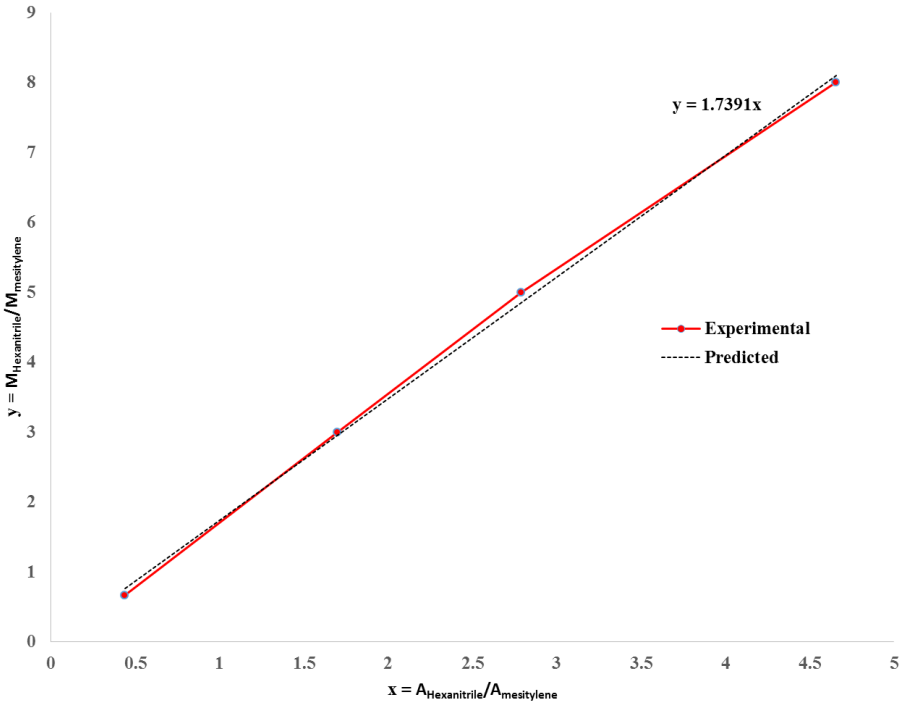

Appendix 20: Calibration curve of hexanitrile

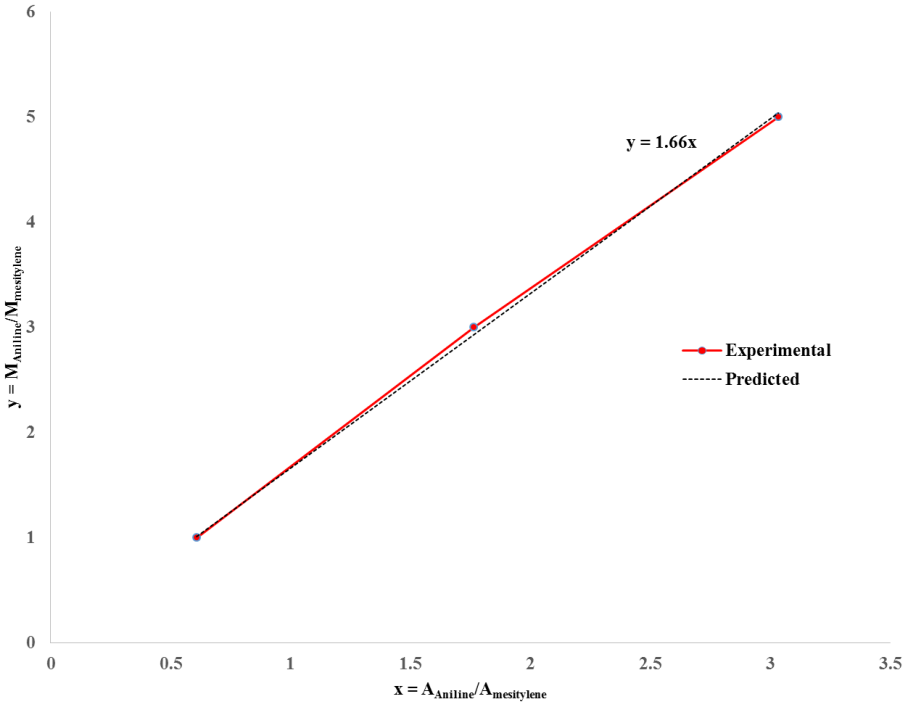

Appendix 21: Calibration curve of aniline